Implémentation et applications d'algorithmes fondés sur la théorie de la fonctionnelle de la densité dépendante du temps dans les logiciels à la base des fonctions gaussiennes et ondelettes

Bhaarathi Natarajan

UNIVERSITÉ DE GRENOBLE

THÈSE

Pour obtenir le grade de

DOCTEUR DE L'UNIVERSITÉ DE GRENOBLE

Spécialité : **Chimie physique**

Arrêté ministérial : 7 Août 2006

Présentée par

Bhaarathi Natarajan

Thèse dirigée par **Mark Earl Casida**
et codirigée par **Thierry Deutsch**

préparée au sein **Département de Chimie Moléculaire (DCM)**
et de **Chimie et Science du Vivant (CSV)**

Implementation, Testing, and Application of Time-Dependent Density-Functional Theory Algorithms for Gaussian- and Wavelet-based Programs

Thèse soutenue publiquement le **Laboratoire de Chimie Théorique**, devant le jury composé de :

Prof. Éric Suraud

Laboratoire de Physique Théorique - IRSAMC University Paul Sabatier Toulouse 3 118 Route de Narbonne, 31062 Toulouse cedex , Président

Prof. Dietrich Förster

CPMOH, University of Bordeaux 1, 351 Cours de la Liberation, 33405 Talence, France, Rapporteur

Prof. Jürg Hutter

Physical Chemistry Institute, University of Zurich, Winterthurerstrasse 190, CH-8057 Zurich, Switzerland, Rapporteur

Dr. Valérie Véniard

Laboratoire des Solides Irradiés, École Polytechnique, 91128 Palaiseau Cedex, France, Examinateur

Dr. Miguel Alexandre Lopes Marques

Laboratoire de Physique de la Matière Condensée et Nanostructures, Université Lyon 1 et CNRS, 43 blv. du 11 novembre 1918, 69622 Villeurbanne Cedex, France, Examinateur

Mark E. Casida

Laboratoire de Chimie Théorique, Département de Chimie Moléculaire (DCM), Université Joseph Fourier, Grenoble, France , Directeur de thèse

Thierry Deutsch

Institut Nanosciences et Cryogénie, SP2M/L-Sim, CEA cedex 9, 38054 Grenoble, FRANCE , Co-Directeur de thèse

Dedicated to my *parents*.

ABSTRACT

The interaction of light with matter is a well-established domain of physical science. For a chemical physicist, this interaction may be used as a probe (spectroscopy) or to induce chemical reactions (photochemistry.) Photochemical reaction mechanisms are difficult to study experimentally and even the most sophisticated modern femtosecond spectroscopic studies can benefit enormously from the light of theoretical simulations. Spectroscopic assignments often also require theoretical calculations. Theoretical methods for describing photoprocesses have been developed based upon wave-function theory and show remarkable success when going to sophisticated higher-order approximations. However such approaches are typically limited to small or at best medium-sized molecules. Fortunately time-dependent density-functional theory (TD-DFT) has emerged as a computationally-simpler method which can be applied to larger molecules with an accuracy which is often, but not always, similar to high-quality wave-function calculations. Part of this thesis concerns overcoming difficulties involving the approximate functionals used in present-day TD-DFT. In particular, we have examined the quality of conical intersections when the Ziegler-Wang noncollinear spin-flip approach is used and have shown that the spin-flip approach has merit as a particular solution in particular cases but is not a general solution to improving the description of conical intersections in photochemical simulations based upon TD-DFT. Most of this thesis concerns algorithmic improvements aimed at either improving the analysis of TD-DFT results or extending practical TD-DFT calculations to larger molecules. The implementation of automatic molecular orbital symmetry analysis in deMon2k is one contribution to improving the analysis of TD-DFT results. It also served as an introduction to a major programming project. The major methodological contribution in this thesis is the implementation of Casida's equations in the wavelet-based code BigDFT and the subsequent analysis of the pros and cons of wavelet-based TD-DFT where it is shown that accurate molecular orbitals are more easily obtained in BigDFT than with deMon2k but that handling the contribution of unoccupied orbitals in wavelet-based TD-DFT is potentially more problematic than it is in a gaussian-based TD-DFT code such as deMon2k. Finally the basic equations for TD-DFT excited state gradients are derived. The thesis concludes with some perspectives about future work.

RÉSUMÉ

L'interaction entre la matiére et le rayonnement est un domaine bien établi de la physique. Pour un physico-chimiste, cette interaction peut être utilisée comme une sonde (spectroscopie) ou pour provoquer des réactions chimiques (photo-chimie). Les mécanismes des réactions photochimiques sont difficiles à étudier expèrimentalement et même les études les plus sophistiquées de spectroscopies femtosecondes peuvent bénéficier énormément des simulations théoriques.Les résultats spectroscopiques d'ailleurs ont souvent besoin des calculs théoriques pour l'analyse de leurs spectres. Les méthodes théoriques pour décrire les processus photochimiques ont été principalement développées en utilisant le concept de la fonction d'onde à N corps et ont eu des succès remarquables. Cependant de telles approches sont généralement limitées à des petites ou moyennes molécules. Heureusement la théorie de la fonctionnelle de la densité dépendant du temps (TD-DFT) a émergé comme une méthode simple de calcul pouvant être appliquée à des molécules plus grandes, avec une précision qui est souvent, mais pas toujours, semblable à la précision provenant des méthodes basés sur la fonction d'onde à N électrons. Une partie de cette thèse consiste à surmonter les difficultés des approximations utilisées de nos jours en TD-DFT. En particulier, nous avons examiné la qualité des intersections coniques quand l'approche du retournement de spin non collinéaire de Ziegler-Wang est utilisée et nous avons montré que l'approche du retournement de spin, parfois ,améliore dans des cas particuliers, mais que c'est n'est pas une solution générale pour mieux décrire les intersections coniques dans les simulations photochimiques basées sur la TD-DFT. La plupart des parties de cette thèse traite d'améliorations algorithmiques, soit pour améliorer l'analyse des résultats de la TD-DFT, soit pour étendre les calculs de TD-DFT à de grandes molécules. L'implémentation de l'analyse automatique des symétries des orbitales moléculaires dans deMon2k est une contribution pour améliorer l'analyse des résultats de la TD-DFT. Cela a aussi servi comme une introduction au projet de programmation majeur. La contribution méthodologique principale dans cette thèse est l'implémentation des équations de Casida dans le code BigDFT fondé sur le formalisme des ondelettes. Cette implémentation a aussi permis une analyse détaillée des arguments positifs et négatifs de l'utilisation de la TD-DFT fondée sur les ondelettes. On montre qu'il est plus facile d'obtenir des orbitales moléculaires précises qu'avec deMon2k. Par contre, la contribution des orbitales inoccupées est plus problématiques qu'avec un code de gaussienne comme deMon2k. Finalement, les équations de base des gradients

analytiques des états excités sont dérivées pour la TD-DFT. La thèse se termine avec quelques perspectives de travaux futurs.

PUBLICATIONS

1. Miquel Huix-Rotllant, Bhaarathi Natarajan, Andrei Ipatov, C. Muhavini Wawire, Thierry Deutsch, and Mark E. Casida, *Phys. Chem. Chem. Phys.*, **12**, 12811-12825 (2010). "Assessment of Noncollinear Spin-Flip Tamm-Dancoff Approximation Time-Dependent Density-Functional Theory for the Photochemical Ring-Opening of Oxirane"

2. Mark E. Casida, Bhaarathi Natarajan, and Thierry Deutsch, in *Fundamentals of Time-Dependent Density-Functional Theory*, edited by Miquel A. L. Marques, N. T. Maitra, Fernando Noguiera, E. K. U. Gross, and Angel Rubio **(Springer: in press).** "Non-Born-Oppenheimer Dynamics and Conical Intersections", http://arxiv.org/abs/1102.1849

3. Bhaarathi Natarajan, Luigi Genovese, Mark E. Casida, Thierry Deutsch, Olga N. Burchak, Christian Philouze, and Maxim Y. Balakirev, *Chem. Phys.*, **under review** "Wavelet-Based Linear-Response Time-Dependent Density-Functional Theory", http://arXiv:1108.3475v1

4. Bhaarathi Natarajan, Mark E. Casida, Luigi Genovese, and Thierry Deutsch, in *Theoretical and Computational Developments in Modern Density Functional Theory*, edited by A. K. Roy **(in press)**. "Wavelets for Density-Functional Theory and for Post Dependent Density-Functional Theory Calculations", http://arXiv:1110.4853v1

I can no other answer make, but, thanks, and thanks.

— William Shakespeare

ACKNOWLEDGMENTS

The work in this thesis is very much an overlapping project between two different departments (Physics and Chemistry) in two different institutes (CEA and University of Grenoble.) Consequently, there are many people I would like to thank, without whom I would never have reached this level of academic achievement. First among them are my supervisors Mark E. Casida and Thierry Deutsch, both of whom are extremently patient, knowledgeable and hard-working, yet always approachable. Especially I am very grateful to Mark for his expert advice and all his time and support. Mark's wide knowledge and his logical way of thinking have been of great value for me. His perpetual energy and enthusiasm in research have motivated all his students, including me. In addition, Mark is always accessible and willing to help his students with their research with his deep personal understanding. As a result, research life became smooth and rewarding for me. A special thanks to Dr. Luigi Genovese for fruitful discussions and for showing me the minute details of the BigDFT code.

During this work I have discussed with many experts for whom I have great regard, and I wish to extend my warmest thanks to all those who have helped me with my work, especially Andreas Köster, Souvrav Pal, Claude Paul, Klaus Hermann, and Damian Castile

Many other people have been helpful with practical advice and assistance during different periods of my PhD studies, among which I am infinitely grateful to Kim Casida, for her love and affection, Arpan Krishna Deb for very welcome coffee breaks, Radhika Ramadoss, and Anusha Muthukumar.

In addition, I would like to express my gratitude to the Nanoscience Foundation, and CEA for their financial and admistrative support over the last three years, without which I would never have been able to undertake this research project.

Finally, I am eternally indebted to my friends and family. Most importantly are my parents, their encouragement, understanding and guidance has been steadfast and I will be forever grateful for their support. I am also thankful to my close friends for keeping me grounded and helping me to unwind, especially over this period of thesis studies.

CONTENTS

LIST OF TABLES

ACRONYMS

For the readers convenience we give a list of the abbreviations used in this thesis in alphabetical order:

AA adiabatic approximation

ABS absorption

ADF Amsterdam density-functional

ALDA adiabatic LDA

AO atomic orbitals

APW augmented plane wave

a.u atomic units

AX avoided crossing

BO Born-Oppenheimer

CASSCF complete active space self-consistent field

CC coupled cluster

CDFT-CI constrained density-functional theory-CI

CFSE crystal field stabilization energy

CFT crysal field theory

CI configuration interaction

CIS configuration interaction singles

crmult coarse grid multiplier

CX conical intersection

DC derivative nonadiabatic coupling vector

DFT density-functional theory

DIIS discret inversion in the iterative subspace

DM density matrix

DMC diffusion Monte Carlo

DMSO dimethyl sulphur dioxide

DZVP double-zeta-valance polarization

EXX exact exchange

FD finite difference

FE finite element

FLUO fluorescence

frmult fine grid multiplier

FWHM full-width at half-maximum

GGA generalized gradient approximation

GTH Goedecker-Teter-Hutter

GTOs Gaussian-type orbitals

Ha Hartree energy

HF Hartree-Fock

HGH Hartwigsen-Goedecker-Hutter

HK Hohenberg-Kohn

HOMO highest occupied molecular orbital

HS high-spin

ISF interpolating scaling function

ISX intersystem crossing

KS Kohn-Sham

LCAO linear-combination of atomic orbital

LDA local density approximation

LFT ligand field theory

LGOs ligand group orbitals

LMTO linear muffin-tin orbital

LS low-spin

LUMO lowest unoccupied molecular orbital

MBPT many-body perturbation theory

MCSCF multi-configurational self-consistent field

MO molecular orbitals

MP Møller-Plesset

MRA multiresolution analysis

MRCI multireference configuration interaction

NVR noninteracting v-representability

OEP optimized effective potential

PES potential energy surfaces

PHOS phosphorescence

QMC quantum Monte Carlo

RI resolution-of-identity

ROKS restricted open-shell Kohn-Sham

RPA random-phase approximation

S singlet

SCF self-consistent field

SCO spin crossover

SF spin-flip

SI international System

SIC self-interaction correction

SOS sum-over-states

SP spin-preserving

T triplet

TD time-dependent

TDA Tamm-Dancoff approximation

TD-DFT time-dependent density-functional theory

TOTEM two-orbital two-electron model

LR linear-response

TRK Thomas-Reiche-Kuhn

TS transition state

TZVP triple-zeta-valance polarization

UGD unscaled gradient difference vector

xc exchange-correlation

Part I

THEORETICAL MOTIVATION

1 BACKGROUND MATERIAL

Many molecular-quantum-mechanics research seminars, theses, and reviews have began by quoting a remark made by Paul Dirac:

> "The underlying physical laws necessary for the mathematical theory of a larger part of physics and the whole of chemistry are thus completely known, and the difficulty is only that the exact application of these laws leads to equations much too complicated to be soluble." [Proceedings of the Royal Society of London. Series A, Containing Papers of a Mathematical and Physical Character, Vol. **123**, No. 792 (6 April 1929)] [1]

While this remark is as true now as it was then (we are still unable to afford exact solutions to the equations), the development of supercomputers has enabled increasingly accurate solutions to be obtained. Presented in this chapter are: (i) the equations of the molecular quantum mechanics which explain the majority of chemistry referred to by Dirac, (ii) the basis upon which we approximate their solution, and (iii) the ways in which we seek to improve such approximations. In the context of this thesis, emphasis is placed on DFT, and TD-DFT treatments are introduced for completeness and for later discussion.

1.1 SYNOPSIS

The spirit of this thesis is very much that attributed to Dirac. The goal is to find more efficient accurate ways to solve the Schrödinger equation in order to extract chemically-useful information. Part of the answer involves improving the numerical methods used in present-day electronic structure calculations and part of the answer involves seeking practical approximations. The purpose of this synopsis is to explain–in broad strokes–the specific approach to be taken during my thesis work and the general organization of my thesis.

The approach taken in my work is to use DFT for ground states and LR TD-DFT for electronic excited states. The emphasis on DFT, rather than wave-function-based approaches, is a question of efficiency. DFT calculations simply scale better with system size than do wave-function methods of comparable accuracy. LR-TD-DFT is now a well-established

1 The quote is typically given out of context as presented here. The rest of the text actually goes on to speak about the need for approximations: "It therefore becomes desirable that approximate practical methods of applying quantum mechanics should be developed, which can lead to an explanation of the main features of complex atomic systems without too much computation."

way to extract information about electronic excited states. Nevertheless much contemporary effort is currently being devoted to improving DFT and TD-DFT, both from the point of view of commonly-used underlying approximations and from the point of view of improved numerical algorithms. The focus of this thesis is on TD-DFT rather than conventional ground-state DFT. Algorithms and approximations are proposed, tested, and (in some cases) applied to previously unstudied systems. High-lights include:

- Testing an implementation of SF LR-TD-DFT for the computation of potential energy surfaces (PES) with comparison against multireference wave-function methods at an accuracy comparable to that of multireference methods.
- Implementation and exploration of wavelet-based LR-TD-DFT calculations.

The thesis is "by articles," meaning that it includes entire published articles or articles submitted for publication. The reason for doing so is that some of the work was only possible because of the contributions of several co-authors and this seemed the best way to acknowledge them. Each article is prefaced with an introduction placing the work in the context of this thesis and describing my contribution to that article. Of course, this type of thesis has the drawback that many of the articles retain redundant introductory material. Notation may also sometimes differs from article to article. That is inevitable when choosing this type of format and the readers are thanked ahead of time for their understanding and indulgence.

The thesis is mainly divided into four parts. Part I (Chapters 1– 3) consists of background material. Chapter 1 consists of an "elementary" review of "textbook material" needed to keep the thesis self-contained and accessible to (say) a new doctoral student. Chapters 2 and 3 review, respectively, the state of the art for TD-DFT investigations of photochemistry and wavelet algorithms for solving the Kohn-Sham (KS) equations of DFT.

Part II (Chapters 4 and 5) are original scientific contributions which are either already published articles or have been submitted for publication. The performance of the deMon2k implementation of SF-LR-TD-DFT is investigated in Chapter 4 for its ability to describe key PES features needed for a realistic description of photochemical reactions. Chapter 5 describes our implementation, testing, and application of LR-TD-DFT in the wavelet code BigDFT. Implementation details are given in appendix C following the theoretical details in appendix A.

Part III (Chapters 6 presents on-going research. Chapter 6 describes my personal experience implementing the molecular-orbital symmetry labeling in the Grenoble version of deMon2k whose documentation is described in appendix B and its successful application to

$[Fe(H_2O)_6]^{2+}$–a common example in inorganic chemistry books discussing ligand field theory but also a molecule with rare T_h symmetry.

Part IV (Chapter 7) concludes and points out how our work might best be continued in the future.

Appendix D presents the equations that we have worked out for implementing analytic gradients for TD-DFT excited states in deMon2k and in BigDFT.

1.2 ATOMIC UNITS

We use a system of Hartree energy (Ha) atomic units (a.u) throughout this dissertation unless otherwise denoted. Atomic units are based upon Gaussian rather than *international System (SI)* units, so that factors of $4\pi\epsilon_0$ never appear. There are also Rydberg atomic units but they rarely work anymore. In atomic units,

$$e = m_e = \hbar = 1$$

where e is the elementary charge on the proton, m_e is the electron mass, and $\hbar$ Planck's constant divided by 2π. Conversion to other units can be obtained by dimensional analysis. For example, distance is in units of $\hbar^2/m_e e^2$ and called the Bohr radius a_0, and energy is in units of e^2/a_0 and is called Ha (E_h). The equations expressed in SI units Coulomb's constant $1/4\pi\epsilon_0$ also have magnitude 1.

1.2.1 *Naming Excited States*

There are various notations for the electronic states of a molecule and the transitions between them. The most widely used nomenclatures are the enumerative one and Kasha's.

The enumerative nomenclature is based on the energetic order of the states and their multiplicities. The electronic state with the lowest energy defines the ground state, and the adiabatic energies of the other states determine the corresponding labels. Thus, in this notation the singlet ground state is denoted by S_0, whereas the excited states are expressed by the successive numbers S_1, S_2, S_3,...,S_n. A similar formula is used for the triplet states, which are denoted by T_1, T_2,...,T_n. The excitations are expressed by $S_0 \rightarrow S_1$, where the arrow indicates the direction of excitation. It is worthwhile to mention that, since the nature of the states can change along the PES, the enumerative nomenclature can sometimes lead to confusion.

Kasha's nomenclature only specifies the nature of the state involved in the transition. The symbols π,σ, and n characters are used to denote unsaturated, sigma and non-bonding occupied orbitals, respectively. The same symbols with an added "$*$" (π^*, σ^*) are used to refer to the corresponding antibonding orbitals. As in the former case, the excitations are expressed as $\pi \rightarrow \pi^*$. With this nomenclature the states

present smooth energetic profiles along the PES. We will use both nomenclatures indistinctively throughout this thesis. For the sake of shortness, excitations will either be denoted as π, π^* or $\pi - \pi^*$. Basically the enumerative nomenclature labels adiabatic PESs while Kasha's notation labels diabatic PES.

1.3 CLASSICAL BEGINNINGS

The classical mechanics which is so strongly associated with the name of Isaac Newton grew out of our everyday experience with balls, pendulums, boats on water–macroscopic objects of all kinds– and the realization that these laws also describe the motion of heavenly bodies. However classical mechanics fails miserably when describing objects as small as atoms and molecules. In 1911, Rutherford [281] proposed that an atom must contain a small massive center called the nucleus. He believed the nucleus contained all the positive charge of the atom and was surrounded by orbiting electrons with equal and opposite charge which moved around the nucleus much like planets around the sun. Later, Bohr [47] suggested that electrons could not spiral inwards out of these orbits by emitting continuous radiation as they were only allowed to emit quanta. This Rutherford-Bohr model mixes the classical physics idea of electrons as particles in orbits with concepts of energy quanta, and while this model successfully explains the emission spectrum of hydrogen atom, it is incorrect. Nevertheless, it was the introduction of quantum theory to chemistry, and this was where quantum mechanics began to take over.

Quantum mechanics offers chemists the possibility of simulating and hence understanding molecular structure, spectroscopy, and reactivity. However, only the two particle hydrogen atom (H) has a closed solution and only a few other systems may be considered to have essentially numerically exact solutions (e.g., H_2^+ and He). The rest of this chapter tries to give an elementary introduction to the basic quantum mechanics used in this thesis and to practical approximation needed for treating nontrivial problems.

Quantum mechanics was born when two important theories come together to give a clear explanation of the hydrogen spectrum. Louis de Broglie postulated that every particle had a wavelength associated with its momentum p,

$$\lambda = \frac{h}{p}$$

As nonemitting charged entities, electrons are restricted to orbits with integral wavelengths,

$$2\pi r = n\lambda$$

so their angular momentum is quantized

$$2\pi r = \frac{nh}{p} \Rightarrow pr = n\hbar$$

By combining these relations with the equation balancing centrifugal and Coulombic forces,

$$\frac{p^2}{mr} = \frac{e^2}{(4\pi\epsilon_0)r^2}$$

we have two equations in two unknowns which may be solved to give

$$\begin{aligned} p &= \frac{me^2}{(4\pi\epsilon_0)n\hbar} \\ r &= \frac{(4\pi\epsilon_0)n^2\hbar^2}{me^2}, \end{aligned} \tag{1.1}$$

since

$$E = \frac{p^2}{2m} - \frac{e^2}{(4\pi\epsilon_0)r},$$

then

$$E = -\frac{m^2e^2}{2(4\pi\epsilon_0)^2n^2\hbar^2} = -\frac{m^2e^2}{8\epsilon_0^2n^2h^2}.$$

In Gaussian units this is

$$E = -\frac{m^2e^2}{2n^2\hbar^2}$$

and in atomic units

$$E = -\frac{1}{2n^2}.$$

The energy gaps between these stable orbitals compose the hydrogen spectrum. Beyond the hydrogen atom, quantum mechanics cannot be solved exactly but numerical solutions of H_2^+ and He are essentially exact.

Using the de Broglie wavelength, Erwin Schrödinger substituted the momentum of an electron for the frequency term in the classical wave equation and derived his famous differential equation. For the hydrogen atom, the Schrödinger equation reads (in a.u)

$$\left(-\frac{1}{2}\nabla^2 - \frac{1}{r}\right)\psi(\mathbf{r}) = \epsilon\psi(\mathbf{r}), \tag{1.2}$$

The Schrödinger equation defines kinetic $\langle\psi| - \frac{1}{2}\nabla^2|\psi\rangle$ and potential $\langle\psi| - \frac{1}{r}|\psi\rangle$ energies in terms of electronic wave functions, $\psi(\mathbf{r})$. P. A. M. Dirac showed that Werner Heisenberg's initial matrix mechanics form of quantum mechanics is in fact just an alternative linear algebra form of Schrödinger's later wave mechanics formulation of quantum mechanics.

1.4 THE HAMILTONIAN

First of all, I am going to describe the Hamiltonian of an N-electron M-nuclei system. In principle the Hamiltonian contains all the physics

of this many-body system. By solving the Schrödinger equation with this Hamiltonian, we should then be able to derive all the observable quantities. Its form is,

$$\begin{aligned}\hat{\mathbf{H}} &= \sum_i \left(-\frac{1}{2}\nabla_i^2\right) + \sum_\alpha \left(-\frac{1}{2M_\alpha}\nabla_\alpha^2\right) + \\ &\frac{1}{2}\sum_{i\neq j}\frac{1}{\mathbf{r}_{ij}} + \frac{1}{2}\sum_{\alpha\neq\beta}\frac{Z_\alpha Z_\beta}{\mathbf{R}_{\alpha\beta}} - \sum_{i,\alpha}\frac{Z_\alpha}{|\mathbf{r}_i - \mathbf{R}_\alpha|}\,. \end{aligned} \tag{1.3}$$

The first term is the electronic kinetic energy operator, where ∇_i^2 is the Laplacian acting over the electronic coordinates $\{\mathbf{r_i}\}$ with an electronic mass m. The second term is the operator corresponding to the kinetic energy of the nuclei, where ∇_α^2 is the Laplacian acting over the nuclear coordinates $\{\mathbf{R}_\alpha\}$ with the mass of nuclei M_α. The third and fourth terms are the pairwise electrostatic electron-electron and nucleus-nucleus interactions respectively, where, $\mathbf{r}_{ij} = |\mathbf{r}_i - \mathbf{r}_j|$ and $\mathbf{R}_{ij} = |\mathbf{R}_i - \mathbf{R}_j|$ are the electron-electron and nucleus-nucleus separations of the pairs which are being considered, and Z_α represents the charge of the αth nucleus. Finally, the fifth term corresponds to the electron-nuclear attraction.

From the Hamiltonian given above, is clear that the number of independent variables in the corresponding Schrödinger's equation is determined by the number of particles involved. Therefore, an exact solution to such kind of equation is *not* possible for realistic systems. Hence, when dealing with this kind of problems, people very often try to work them out by applying different successive approximations in order to model the physics of the system, which, in some cases, can compromise the accuracy of the final result or at least provide results that are not general. In some cases, this leads to empirical models (i.e., models containing external parameters) which will work well for only a few kinds of systems and external conditions. (Note, however, that empirical methods are largely avoided in this thesis, which favours a first-principles density-functional theory approach.)

Very frequently, the first approximation that people do is the adiabatic (or Born-Oppenheimer (BO) [48]) approximation. This one is usually not very critical in terms of loss of accuracy, and instead simplifies considerably our problem so, next, I am going to present a short description of what it is about.

1.5 BORN-OPPENHEIMER APPROACH

If we divide the system into light particles (electrons) and heavy ones (atomic nuclei) and think classically, in thermodynamic equilibrium the mean value for the kinetic energy of both kind of particles is of the same order [49, 50] but, due to the large mass difference between nucleons (i.e., protons+neutrons) and electrons, the electronic speed very much exceeds nuclear speeds (by approximately two orders of

magnitude.) Then, for every modification in the position of the atomic nuclei an almost instantaneous rearrangement of the electrons occurs, following the new nuclear positions. This allows us to consider, at least to a first approximation, the movement of the electrons as if they were in field of *fixed* nuclei. While studying the movement of the nuclei, on the contrary only the potential originating from the mean electronic spatial distribution (not an instantaneous one) must be taken into account. When this physical approximation is formulated in quantum mechanics, it is known as the *adiabatic* or *BO approximation*.

In the BO approximation, the nuclear Schrödinger equation is written as,

$$\left(-\sum_{\alpha}\frac{1}{2M_{\alpha}}\nabla_{\alpha}^{2}+V_{0}(\mathbf{R})\right)\Phi(\mathbf{R})=\epsilon\Phi(\mathbf{R})\,, \tag{1.4}$$

where $\mathbf{R}=\{\mathbf{R}_{\alpha}\}$ is the set of all the nuclear coordinates and $V_0(\mathbf{R})$ the clamped-ion energy of the system, which is often referred to as the *Born-Oppenheimer potential energy surface*, and ϵ are the atomic eigenvalues. In practice, $V_0(\mathbf{R})=E_0(\mathbf{R})+V_{nn}(\mathbf{R})$ is the ground-state energy of a system of interacting electrons moving in the field of fixed nuclei, which obeys the Schrödinger equation

$$H_{e}^{BO}(\mathbf{r};\mathbf{R})\phi_{n}(\mathbf{x};\mathbf{R})=E_{n}(\mathbf{R})\phi_{n}(\mathbf{x};\mathbf{R})\,. \tag{1.5}$$

where the Hamiltonian–which acts on to the electronic variables and depends only parametrically on $\mathbf{R}$–reads

$$H_{e}^{BO}(\mathbf{r};\mathbf{R})=-\frac{1}{2}\sum_{i}\nabla_{i}^{2}+\frac{1}{2}\sum_{i\neq j}\frac{1}{\mathbf{r}_{ij}}-\sum_{i,\alpha}\frac{Z_{\alpha}}{|\mathbf{r}_{i}-\mathbf{R}_{\alpha}|}\,, \tag{1.6}$$

plus the nuclear-nuclear repulsion energy,

$$V_{nn}(\mathbf{R})=\sum_{\alpha<\beta}\frac{Z_{\alpha}Z_{\beta}}{|\mathbf{R}_{\alpha}-\mathbf{R}_{\beta}|}\,. \tag{1.7}$$

This could be mistaken as a simple rearrangement of equation (1.3), but it is important to notice that now the electronic part is decoupled from the rest and can be solved independently, using the set of nuclear positions $\mathbf{R}$, only as parameters. Explicit inclusion of the coupling of the electronic and nuclear degress of freedom beyond the Born-Oppenheimer approximation and present in the full Schrödinger equation is important for simulations of some types of photoprocess.

1.5.1 *Density As Basic Variable*

Within the BO approximation,

$$V_{0}(\mathbf{R})=E_{0}(\mathbf{R})+V_{nn}(\mathbf{R})\,. \tag{1.8}$$

while the nuclear-nuclear repulsion $V_{nn}(\mathbf{R})$ is a relatively simple object, the electronic energy $E_0(\mathbf{R})$ for nuclei frozen in the configuration $\mathbf{R}$ is still very complicated. *A priori* $E_0(\mathbf{R})$ depends upon $\phi(\mathbf{x};\mathbf{R})$ where $\mathbf{x} = \{\mathbf{x}_i\}$ and $\mathbf{x}_i = (\mathbf{r}_i, \sigma_i)$ are the space plus spin coordinates of N electrons. Nevertheless chemists have long analyzed chemical reactivity in terms of atomic charges–which is to say, in terms of the charge density

$$\rho(\mathbf{r}_1;\mathbf{R}) = \sum_{\sigma} \int |\phi_0(\mathbf{x}_1;\mathbf{R})|^2 d\mathbf{x}_2 d\mathbf{x}_3 ... d\mathbf{x}_N \,. \tag{1.9}$$

Why should this work? Part of the answer is that the electron-nuclear attraction depends only upon the charge density,

$$V_{ne}(\mathbf{R}) = -\int \rho(\mathbf{r};\mathbf{R}) \left(\sum_{\alpha} \frac{Z_\alpha}{|\mathbf{r} - \mathbf{R}_\alpha|} \right) d\vec{r}, \tag{1.10}$$

as does the classical electron-electron repulsion energy

$$V_{ee}(\mathbf{R}) = \frac{1}{2} \int \frac{\rho(\mathbf{r_1};\mathbf{R})\rho(\mathbf{r_2};\mathbf{R})}{|\mathbf{r}_1 - \mathbf{r}_2|} d\mathbf{r}_1 d\mathbf{r}_2 \,. \tag{1.11}$$

For atoms, we can also obtain the electronic kinetic energy from the virial theorem [268] as

$$\begin{aligned} T_e(\mathbf{R}) &= \langle \phi_0(\mathbf{R}) | -\frac{1}{2} \sum \nabla_i | \phi_0(\mathbf{R}) \rangle \\ &= -\frac{1}{2} V_{ne}(\mathbf{R}) \,. \end{aligned} \tag{1.12}$$

Indeed $T_e(\mathbf{R}) + V_{ne}(\mathbf{R}) + V_{ee}(\mathbf{R})$ accounts for most of $E_0(\mathbf{R})$ but it it still not an accurate-enough approximation for most problems in chemical and solid-state physics.

A solution in principle was given by E. Bright Wilson [36], who pointed out that (i) integration over ρ gives the number of electrons, N, (ii) the cusps in ρ give the nuclear positions, $\mathbf{R}$, and (iii) the derivatives of ρ at the cusps give the nuclear charges, $\{Z_\alpha\}$. Hence the ground-state density of a molecule contains all of the information necessary to reconstruct the electronic Hamiltonian $H_e^{BO}(\mathbf{r};\mathbf{R})$ and hence to determine all of the electronic properties of the system by "just" solving the electronic Schrödinger equation. In particular, the ground-state energy is a functional of the ground-state charge density

$$E_0(\mathbf{R}) = E_0(\mathbf{R})[\rho_0(\vec{r};\mathbf{R})] \,. \tag{1.13}$$

In 1964, Hohenberg and Kohn provided a more general mathematical proof of this same result, so beautifully motivated by E. Bright Wilson. The Hohenberg-Kohn (HK) theorems and the Kohn–Sham formulation of density–functional theory (DFT) are the subject of the next section.

1.6 INTRODUCTION TO DFT

Over the last 45 years DFT has become one of the standard methods for calculations in several branches of physics and chemistry. Among all the other approaches to electronic structure calculations, such as configuration interaction (CI), coupled cluster (CC) and Møller-Plesset (MP) perturbation theory, the rather special place of DFT becomes directly clear from the fundamentals, as first formulated in 1964 by Hohenberg and Kohn [172].

1.6.1 *The First Hohenberg-Kohn Theorem*

> Every observable quantity of a stationary quantum mechanical system is determined by the ground-state density alone.

In other words, the aim of DFT is not to obtain a good approximation to the ground-state wave function of the system, but rather to find the energy of the system as a functional of the density, without any reference to the wave function. This proof, that all observables of a many electron system are unique functionals of the electron density, provides the theoretical basis for DFT.

Consider a nonrelativistic N-electron system in the Born-Oppenheimer approximation. The Hamiltonian $\hat{H}$ in the Schrödinger equation

$$\hat{H}_e \Psi(\mathbf{x_1}, \mathbf{x_2}, ...\mathbf{x_n}) = E\Psi(\mathbf{x_1}, \mathbf{x_2}, ..., \mathbf{x_n}) \,, \tag{1.14}$$

consists of the kinetic energy $\hat{T}$, the nuclear-electron interaction $\hat{v}_{ne}$, and the electron-electron interaction $\hat{v}_{ee}$.

In the HK theorem the one-to-one mapping between the electron density ρ

$$\rho(\mathbf{r}_1) = \sum_{\sigma_1 = \uparrow\downarrow} N \int |\Psi(\mathbf{x}_1, \mathbf{x}_2, ..., \mathbf{x}_n)|^2 d\mathbf{x}_2 ..., d\mathbf{x}_n \,, \tag{1.15}$$

and the external potential $\hat{v} = \sum_i v(\mathbf{r}_i)$ (which is typically just the nuclear attraction $v(\mathbf{r}_i) = -\sum_i \sum_\alpha \frac{Z_\alpha}{\mathbf{r}_{i\alpha}}$ or could be more general) is proved. The mapping

$$\hat{v} \xrightarrow{\text{Eq. (1.14)}} \Psi \xrightarrow{\text{Eq. (1.15)}} \rho \,, \tag{1.16}$$

is rather simple and straight forward. Each $\hat{v}$ connects to a wave function, Ψ, by solving Schrödinger equation (1.14), and the corresponding density ρ can be found by integrating the square of the wavefunction Eq. (1.15).

The proof of the mapping in other direction (that ρ determines $\hat{v}$)

$$\hat{v} \xleftarrow{a} \Psi \xleftarrow{b} \rho \,, \tag{1.17}$$

is done in two steps. In each case, the proof is by contradiction: (a) If $\hat{v}$ and $\hat{v}'$ differ by more than a constant C, they will not lead to the same wavefuction Ψ.
(b) If the ground state Ψ of $\hat{H}$ and Ψ' of $\hat{H}'$ are different, they cannot lead to the same density ρ.

Let us first prove the lemma (a). For a *nondegenerate* ground state it follows that,

$$\begin{aligned} \left(\hat{T}+\hat{v}_{ee}+\hat{v}_{ne}\right)|\Psi\rangle &= E_{gs}|\Psi\rangle\,, \qquad (1.18)\\ \left(\hat{T}+\hat{v}_{ee}+\hat{v}'_{ne}\right)|\Psi'\rangle &= E'_{gs}|\Psi'\rangle\,, \qquad (1.19)\end{aligned}$$

Now we assume that $\Psi = \Psi'$, and one gets

$$(\hat{v}-\hat{v}')|\Psi\rangle = (E_{gs}-E'_{gs})|\Psi\rangle\,, \qquad (1.20)$$

which immediately leads to $\hat{v} = \hat{v}' + C$ at least where $\Psi \neq 0$, in contradiction with the assumption made in (a).

We now prove the lemma (b). Using the variational principle, in the case for (b) one proves that if $\Psi \neq \Psi'$. This implies that $\rho(\mathbf{r}) \neq \rho'(\mathbf{r})$. Without loss of generality we may choose Ψ and Ψ' such that

$$\begin{aligned} E_{gs} &= \langle\Psi|\hat{H}|\Psi\rangle < \langle\Psi'|\hat{H}|\Psi'\rangle\,,\\ &= \langle\Psi'|\hat{H}'+\hat{v}-\hat{v}'|\Psi'\rangle\,,\\ &= E'_{gs}+\int \rho'(\mathbf{r})[v(\mathbf{r})-v'(\mathbf{r})]\,d\mathbf{r}\,. \qquad (1.21)\end{aligned}$$

and similarly

$$\begin{aligned} E'_{gs} &= \langle\Psi'|\hat{H}'|\Psi'\rangle < \langle\Psi|\hat{H}'|\Psi\rangle\,,\\ &= \langle\Psi|\hat{H}+\hat{v}'-\hat{v}|\Psi\rangle\,,\\ &= E_{gs}+\int \rho(\mathbf{r})[v'(\mathbf{r})-v(\mathbf{r})]\,d\mathbf{r}\,. \qquad (1.22)\end{aligned}$$

Assuming that $\rho(\mathbf{r}) \neq \rho'(\mathbf{r})$, the combination of the equations (1.21) and (1.22) leads to the following contradiction

$$E_{gs}+E'_{gs} < E_{gs}+E'_{gs}\,. \qquad (1.23)$$

Therefore the maps between $\hat{v}$, Ψ and ρ are bijective (i.e., one-to-one).

$$\hat{v} \longleftrightarrow \Psi \longleftrightarrow \rho\,, \qquad (1.24)$$

and as a consequence of the bijective map $\Psi \longleftrightarrow \rho$, every observable O of the system is a unique functional of the density

$$\langle\Psi[\rho]|\hat{O}|\Psi[\rho]\rangle = O[\rho]\,. \qquad (1.25)$$

1.6.2 *The Second Hohenberg-Kohn Theorem*

> The exact ground-state density of a system in a particular external potential can be found by minimization of the energy functional.

As a direct consequence of Eq. (1.24), the map $\rho \to \hat{v}$ indicates that ρ determines the external potential as well as the total number of electrons, and thus the entire Hamiltonian. Therefore, in addition, the first HK theorem tells us that for the energy functional of a system in a particular external potential v_0

$$E_{v_0}[\rho] = \langle \Psi[\rho] | \hat{T} + \hat{v}_{ee} + \hat{v}_0 | \Psi[\rho] \rangle \,, \tag{1.26}$$

the exact ground-state density can be found by minimization of $E_{v_0}[\rho]$,

$$E_0 = \min_\rho E_{v_0}[\rho] \,. \tag{1.27}$$

The part of the energy functional, $F_{HK}[\rho]$, which does not involve the external potential is a *universal* density functional

$$\begin{aligned} E_{HK}[\rho] &= E_{v_0}[\rho] = F_{HK}[\rho] + \int v_0(\mathbf{r})\rho_0(\mathbf{r})\,d\mathbf{r} \,, \\ F_{HK}[\rho] &= \langle \Psi[\rho] | \hat{T} + \hat{v}_{ee} | \Psi[\rho] \rangle \,. \end{aligned} \tag{1.28}$$

1.6.3 *v-Representability And The Levy Constrained Search Formalism*

When we proved the Hohenberg-Kohn theorem above, we made the assumption that the density is *v-representable*. By this is meant that the density comes from the anti-symmetric ground state wave function associated with some potential $v(\mathbf{r})$. Why is this important? The reason is that we want to use the variational character of the energy functional

$$E_0 \leqslant E_{v_0}[\rho] \,, \tag{1.29}$$

To find the ground state energy, which assumes that ρ is a v-representable density. If our trial density that we put in this functional turns out to be non-v-representable, the variational principle is no longer valid. One would think that most "reasonable" densities would be v-representable, but many "reasonable" densities have actually been shown to be non-v-representable [221, 224]. The Levy constrained search formulation provides a way around the problem of v-representability and in the same way presents a constructive proof of the HK theorem,

The minimization of $E_{v_0}[\rho]$ can be written as

$$\langle \Psi_0 | \hat{T} + \hat{W} | \Psi_0 \rangle + \int d\mathbf{r}\, v(\mathbf{r})\rho(\mathbf{r}) \leqslant \langle \Psi_{\rho_0} | \hat{T} + \hat{W} | \Psi_{\rho_0} \rangle + \int d\mathbf{r}\, v(\mathbf{r})\rho(\mathbf{r}) \,,$$

(1.30)

or

$$\langle \Psi_0 | \hat{T} + \hat{W} | \Psi_0 \rangle \leqslant \langle \Psi_{\rho_0} | \hat{T} + \hat{W} | \Psi_{\rho_0} \rangle \,. \tag{1.31}$$

Here Ψ_0 is the ground state wave function and Ψ_{ρ_0} is any other wave function yielding the same density. We recognize this as the HK functional, F_{HK}.

It turns out that the ground state wave function of density $\rho(\mathbf{r})$ can be defined as the wave function which yields $\rho(\mathbf{r})$ and minimizes the HK functional. Levy constrained search formulation of the HK theorem [221, 224, 220, 222] which states that we can divide our search for the ground state energy into two steps, we minimize $E_{v_0}[\rho]$ first over all wave functions giving a certain density, and then over all N-representable densities

$$\begin{aligned} E_0 &= \min_\Psi \langle \Psi | \hat{T} + \hat{W} + \hat{V} | \Psi \rangle \\ &= \min_\rho \left(\min_{\Psi \to \rho} \langle \Psi | \hat{T} + \hat{W} + \hat{V} | \Psi \rangle \right) \\ &= \min_\rho \left(\min_{\Psi \to \rho} \langle \Psi | \hat{T} + \hat{W} + \hat{V} | \Psi \rangle + \int d\mathbf{r} v_{ext}(\mathbf{r}) \rho(\mathbf{r}) \right) \end{aligned} \tag{1.32}$$

N-representable means is that ρ can be obtained from an anti-symmetric wave function, and that it fulfills the following three conditions: It should be positive, it should integrate to N, and it should be finite. This is obviously a much weaker condition that v-representability and any reasonable density fulfills it. The word "constrained" in the Levy constrained search method comes from the fact that the Ψs that we search among are constrained to give the density ρ.

1.6.4 *The Kohn-Sham Equations*

Unfortunately the Hohenberg-Kohn theorem does not provide us with a practical scheme for doing DFT calculations. It does not tell us how to perform the map $\rho \to \Psi$ in practice, and only defines F_{HK} formally. Approximating F_{HK} is the basis for orbital-free DFT. Unfortunately sufficient accurate approximation for F_{HK} have proven difficult to develop.

Instead practical approximations are based on a different exact formalism, namely that given, a little later in 1965 by *Kohn and Sham* [206]:

> The ground-state density of the interacting practicle system can be calculated as the ground-state density of an auxiliary non-interacting system

In other words, the central (non-interacting v-representabile) assumption in the KS scheme is that, for each interacting electron system with

external potential $v_0(\mathbf{r})$, a local potential $v_{s,0}(\mathbf{r})$ (the Kohn-Sham potential) exists such that the density $\rho_s(\mathbf{r})$ of the non-interacting system equals the density $\rho_s(\mathbf{r})$ of the interacting system, $\rho_s(\mathbf{r}) = \rho(\mathbf{r})$.

Consequently, if this is true, this KS potential $v_{s,0}(\mathbf{r})$ must, according to the first HK theorem $[(v_s(\mathbf{r}) \longleftrightarrow \Psi_s(\mathbf{r}) \longleftrightarrow \rho_s(\mathbf{r}))]$ be unique, in the sense that it is a unique functional of the density: $v_s[\rho](\mathbf{r})$. The Schrödinger equation for such a system of non-interacting electrons ($\hat{v}_{ee} = 0$), which move in an external potential $\hat{v}_{s,0}$ reads

$$\left(-\frac{1}{2}\nabla^2 + v_{s,0}(\mathbf{r})\right)\phi_{i\sigma}(\mathbf{r}) = \epsilon_i\phi_{i\sigma}(\mathbf{r})\,. \tag{1.33}$$

and the density of such a system is determined by the N lowest energy orbitals

$$\rho_s(\mathbf{r}) = \sum_{i\sigma} n_{i\sigma}|\phi_{i\sigma}(\mathbf{r})|^2\,. \tag{1.34}$$

The kinetic energy of this non-interacting KS system is given by

$$T_s[\rho] = \sum_{i\sigma}\sum_{i\sigma} n_{i\sigma}\langle\phi_{i\sigma}| - \frac{1}{2}\nabla^2|\phi_{i\sigma}\rangle\,. \tag{1.35}$$

In order to arrive at a useful expression for the KS potential, $v_{s,0}(\mathbf{r})$, we write the total energy expression for the interacting system in the following way,

$$E[\rho] = T_s[\rho] + \int v_0(\mathbf{r})\rho(\mathbf{r})d\mathbf{r} + \frac{1}{2}\int\int\frac{\rho(\mathbf{r})\rho(\mathbf{r}')}{|\mathbf{r}-\mathbf{r}'|}d\mathbf{r}d\mathbf{r}' + E_{xc}[\rho]\,, \tag{1.36}$$

hereby introducing an exchange-correlation (xc) energy functional $E_{xc}[\rho]$,

$$E_{xc}[\rho] = F_{HK}[\rho] - T_s[\rho] - \frac{1}{2}\int\int\frac{\rho(\mathbf{r})\rho(\mathbf{r}')}{|\mathbf{r}-\mathbf{r}'|}d\mathbf{r}d\mathbf{r}'\,. \tag{1.37}$$

The HK theorem ensures that the energy functional $E[\rho]$ is stationary for small variations $\delta\rho(\mathbf{r})$ around the exact density $\rho_0(\mathbf{r})$

$$\frac{\delta E[\rho]}{\delta\rho(\mathbf{r})}|_{\rho=\rho_0} = 0\,, \tag{1.38}$$

this leads to

$$\frac{\delta F_{HK}[\rho]}{\delta\rho(\mathbf{r})}|_{\rho=\rho_0} = -v_0(\mathbf{r})\,. \tag{1.39}$$

similarly for the non-interacting system we find

$$\frac{\delta T_s[\rho]}{\delta\rho(\mathbf{r})}|_{\rho=\rho_0} = -v_{s,0}(\mathbf{r})\,. \tag{1.40}$$

Differentiating now Eq. (1.37) with respect to $\rho(\mathbf{r})$ yields

$$v_{s,0}(\mathbf{r}) = v_0(\mathbf{r}) + \int\frac{\rho(\mathbf{r}')}{|\mathbf{r}-\mathbf{r}'|}d\mathbf{r}' + \frac{\delta E_{xc}}{\delta\rho(\mathbf{r})}\,, \tag{1.41}$$

which is often denoted in shorthand as

$$v_{s,0}(\mathbf{r}) = v_0(\mathbf{r}) + v_H(\mathbf{r}) + v_{xc}(\mathbf{r})\,. \tag{1.42}$$

The xc potential is given by,

$$v_{xc}(\mathbf{r}) = \frac{\delta E_{xc}}{\delta \rho(\mathbf{r})}\,. \tag{1.43}$$

Hence with Eq. (1.33) we find

$$\left[-\frac{1}{2}\nabla^2 + v_0(\mathbf{r}) + \int \frac{\rho(\mathbf{r}')}{|\mathbf{r}-\mathbf{r}'|}d\mathbf{r}' + \frac{\delta E_{xc}}{\delta \rho(\mathbf{r})}\right]\phi_{i\sigma}(\mathbf{r}) = \epsilon_i \phi_{i\sigma}(\mathbf{r})\,, \tag{1.44}$$

Since the KS potential depends on the density, the Eqs. (1.41) and (1.44) have to be solved self-consistently. And therefore, once an approximation for the E_{xc} has been made, the KS equations provide a way for calculating the density $\rho(\mathbf{r})$, and from that such as the energy of the system.

1.6.5 *Approximations For The Exchange-Correlation Functional*

The KS equation holds independently of any approximation on the functional $E_{xc}[\rho]$, thus it would give the exact ground-state properties of an interacting system if the exact functional were known. In practice the success of DFT is due to the fact that $E_{xc}[\rho]$ can be reasonably approximated by a local or nearly local functional of the density. The first and most widespread approximation to $E_{xc}[\rho]$ is the LDA proposed in the original KS paper, which assumes that the xc energy of a real system behaves locally as that of a uniform electron gas. The xc functional in this case can be expressed as

$$E_{xc}^{LDA}[\rho] = \int \epsilon_{xc}^{hom}(\rho(\mathbf{r}))\rho(\mathbf{r})d\mathbf{r}\,, \tag{1.45}$$

where $\epsilon_{xc}^{hom}(\rho)$ is the xc energy per electron of the homogeneous electron gas at density $\rho(\mathbf{r})$. The exchange contribution can be evaluated analytically [242], while the correlation part has been obtained by parameterizing the results of Monte Carlo simulations [76, 265, 320]. The LDA is exact in the limit of high density (where the kinetic energy dominates) or of slowly-varying density distributions. In fact experience has shown that accurate results are obtained well beyond this theoretical range of validity. Typically the LDA yields a good accuracy in reproducing experimental structural and vibrational properties of strongly bound systems, but usually overestimates bonding energies and underestimates bond lengths. As a first improvement beyond the LDA, the generalized gradient approximation (GGA) has been introduced:

$$E_{xc}^{GGA}[\rho] = \int \epsilon_{xc}^{GGA}(\rho(\mathbf{r}), |\nabla\rho(\mathbf{r})|)\rho(\mathbf{r})d\mathbf{r}\,, \tag{1.46}$$

which depends also on the norm of the local density gradient, $\nabla\rho(\mathbf{r})$. Several expressions for ϵ_{xc}^{GGA} have been considered. The three most popular parametrizations are that of Becke (B88) [41], Perdew and Wang (PW91) [264], and Perdew, Burke, and Enzerhof (PBE) [266]. GGA significantly improves upon the LDA to predict the binding energies of real materials. There are other types of xc functionals which are explicitly orbital-dependent; among them we mention the self-interaction correction (SIC) methods, the optimized effective potential (OEP), the exact exchange (EXX) and hybrid functionals such as B3LYP. Some of these functionals provide a remarkable improvement of the accuracy for some systems, but in general they also introduce a significant increase in computational cost.

1.7 INTRODUCTION TO TD-DFT

The extension of DFT to deal with the time-dependent Schrödinger equation and excited-state properties has been achieved with the formulation of time-dependent density-functional theory (TD-DFT) [241], a theory which has been mathematically estabilished by the theorem of Runge and Gross [280]. In this approach the complex many-body time-dependent Schrödinger equation is replaced by a set of (coupled) time-dependent single-particle equations. For this reason this method is computationally much more suitable than cumbersome many-body techniques and in practice, it is one of the possible choice in order to treat strongly non-linear phenomena in realistic systems. Furthermore, for many applications, very simple approximations to TD-DFT, such as the adiabatic LDA (ALDA) [35] have shown an unexpected accuracy.

To cope with a wide range of applications, different practical implementations of linear-response (LR) TD-DFT are available. In its most general form, the TD-DFT linear-response problem can be expressed in terms of a Dyson-like equation [60]. This equation describes how to compute a generalized susceptibility, whose poles are the excitation energies of the system. Through this response function it is possible to calculate the linear response of any local observable to any local external perturbation. The polarizability which gives the optical absorption spectra, can also be obtained in this way. Nevertheless, since in general the computational cost of constructing and solving the Dyson-like problem is very high, there are more efficient and widespread ways to solve TD-DFT equations when only optical properties are required.

The Dyson-like equation for susceptibility has been reformulated by Casida [60] into an eigenvalue problem, whose eigenvalues and eigenvectors are used to build the optical absorption spectra. The construction of Casida's equations requires the prior diagonalization of the full ground-state problem, this operation may be very demanding, especially for large basis sets. The eigenvalue problem is then

efficiently solved by iterative techiniques [192, 298]. Nevertheless, within this approach only a limited number of the low-lying eigenvalues can be obtained. This leads to a limitation of the energy range accessible. Furthermore, the density of excitation energies in a given energy range increases linearly with the system size, thus making it difficult if not impossible to calculate them individually for very large systems.

Some of the drawbacks of Casida's approach have been overcome by directly solving the TD-DFT equations in the time domain. For linear response purpose it is necessary to integrate this equations by adding a properly-chosen small external perturbing potential [334, 333]. Real-time TD-DFT is suitable for calculating the optical spectra in a large energy range and the full diagonalization of the ground-state Hamiltonian is completely avoided, since it is necessary to propagate the occupied states only. The basic operations required to integrate TD-DFT equations are the same as an iterative ground-state calculation, unfortunately they have to be performed many many more times. For this reason the overall scalability of this method is basically the same as that of a ground-state calculation, but the prefactor is much larger.

To summarize this overview of TD-DFT, two main open issues for a wide applicability of this methodology: One is related to the accuracy of the available xc functionals, which has to be improved in order to treat, e.g., excitons in solids or Rydberg states in finite systems. The other concerns the enhancement of the algorithmic performance of the method, which is essential for the application TD-DFT to realistic systems, indeed we need to build large models to simulate e.g., biochromophores embedded in their biological environment or dye-sensitized solar cells, just to mention two important examples. In this thesis we will deal with this second issue. We will introduce a new approach to solve TD-DFT equations in the linear regime.

1.7.1 *The Time-Dependent Hohenberg-Kohn-Sham Formalism*

The derivation for the TD KS equations is, compared to the static case, much more complicated, and it was first formulated in 1984 by Runge and Gross [280]. The formalism of Runge and Gross has many, atleast superficial parallels with the ground state DFT formalism of Hohenberg, Kohn and Sham [172, 206]. For recent reviews on time-dependent density functional theory, see [110, 150, 60, 151, 52, 318, 307, 61, 88, 238, 239, 53, 107, 73, 63, 64, 65]. The Runge-Gross theorem is,

> Given the initial state at t_0, the single particle potential $v(\mathbf{r}, t)$ leading to a given density $\rho(\mathbf{r}, t)$ is uniquely determined up to an arbitrary additive function of time, so that the map $v(\mathbf{r}, t) \to \rho(\mathbf{r}, t)$ is invertible

As a consequence of the bijective map $v(\mathbf{r},t) \longleftrightarrow \rho(\mathbf{r},t)$, every observable $O(t)$ is a unique functional of, and can be calculated from, the density $\rho(\mathbf{r},t)$.

$$O[\rho](t) = \langle \Phi[\rho](t)|\hat{O}(t)|\Phi[\rho](t)\rangle \,. \tag{1.47}$$

In a general TD situation such a proof starts from the time-dependent Schrödinger equation,

$$i\frac{\partial}{\partial t}\Psi(t) = \hat{H}(t)\Psi(t)\,, \tag{1.48}$$

in which the Hamiltonian $\hat{H}(t) = \hat{T} + \hat{W} + \hat{v}(t)$, consists of a kinetic energy part $\hat{T}$, some particle-particle interaction $\hat{W}$, and the single-particle potential $\hat{v}(t)$.

If the time-dependent Schrödinger equation Eq. (1.48) is solved for a fixed initial state Ψ_0, at time t_0, and several potentials $v(\mathbf{r},t)$, we obtain the map $v(\mathbf{r},t) \to \Psi(t)$. From the wavefunction we get the density by $\rho(\mathbf{r},t) = \langle\Psi(t)|\hat{\rho}(\mathbf{r})|\Psi(t)\rangle$, which defines the map $\Psi(t) \to \rho(\mathbf{r},t)$, and in which the density operator $\hat{\rho}(\mathbf{r})$ is given by

$$\hat{\rho}(\mathbf{r}) = \sum_{k=1}^{N} \delta(\mathbf{r} - \mathbf{r}_k)\,. \tag{1.49}$$

In order now to prove that there exists a TD version of the first HK theorem, one has to show that the map $v(\mathbf{r},t) \to \Psi(t) \to \rho(\mathbf{r},t)$ is invertible up to a purely time-dependent additive function $\alpha(t)$ and under the requirement that the potential is expandable in a Taylor series around $t = t_0$. Despite this phase factor which appears in the wave functions, $\Psi(t) = e^{-i\alpha(t)}\Phi[\rho](t)$, the expectation value of any observable is often a functional of the density alone, because the phase frequently cancels out in Eq. (1.47).

The proof is fully given in Ref. [280] and a short outline is given here. If two potentials $v(\mathbf{r},t)$ and $v'(\mathbf{r},t)$ differ by more than a purely time-dependent function $\alpha(t)$, there must exist some non-negative integer k for which

$$\frac{\partial^k}{\partial t^k}[v(\mathbf{r},t) - v'(\mathbf{r},t)]|_{t=t_0} \neq \text{const. in } \mathbf{r} \tag{1.50}$$

The thing to prove now is that the densities $\rho(\mathbf{r},t)$ and $\rho'(\mathbf{r},t)$, which correspond to the potentials $v(\mathbf{r},t)$ and $v'(\mathbf{r},t)$ are different, if Eq. (1.50) is fulfilled for $k \geqslant 0$.

Since we start from the same fixed initial state wave function Ψ_0 it should be noted that the particle $\rho(\mathbf{r},t)$, and also current $\mathbf{j}(\mathbf{r},t)$ densities are of course identical at the initial time t_0, and start therefore to differ infinitesimally later than t_0. This proof consists of two steps:

(a). The time evolution of the current density if given by the equation of motion

$$i\frac{\partial \mathbf{j}(\mathbf{r},t)}{\partial t} = \langle \Phi(t)|[\hat{\mathbf{j}}, \hat{H}(t)]|\Phi(t)\rangle\,, \tag{1.51}$$

where the current operator $\hat{\mathbf{j}}(\mathbf{r})$ is given by

$$\hat{\mathbf{j}}(\mathbf{r}) = \frac{1}{2i}\sum_{k=1}^{N}\left(\nabla_{\mathbf{r}_k}\delta(\mathbf{r}-\mathbf{r}_k) + \delta(\mathbf{r}-\mathbf{r}_k)\nabla_{\mathbf{r}_k}\right)\,, \tag{1.52}$$

Since $\Phi(t)$ and $\Phi'(t)$ evolve from the same initial state Φ_0, Eq. (1.51) gives

$$\begin{aligned} i\frac{\partial}{\partial t}[\mathbf{j}(\mathbf{r},t) - \mathbf{j}'(\mathbf{r},t)]|_{t=t_0} &= \langle \Phi_0|[\hat{\mathbf{j}}(\mathbf{r}), \hat{H}(t_0)]|\Phi_0\rangle\,, \\ &= i\rho(\mathbf{r},t_0)\nabla[v(\mathbf{r},t_0) - v'(\mathbf{r},t_0)]\,. \end{aligned} \tag{1.53}$$

Working out the commutator in Eq. (1.53) (for $k = 0$ and $k > 0$ in Eq. (1.50) shows after some straightforward algebra that $\mathbf{j}(\mathbf{r},t)$ and $\mathbf{j}'(\mathbf{r},t)$ will become different infinitesimally later than t_0.

(b). To arrive at the corresponding densities, the continuity equation is used

$$\frac{\partial \rho(\mathbf{r},t)}{\partial t} = -\nabla\cdot\mathbf{j}(\mathbf{r},t)\,, \tag{1.54}$$

in which the result of (a) has to be inserted to finally find that also $\rho(\mathbf{r},t)$ and $\rho'(\mathbf{r},t)$ will become different infinitesimally later than t_0.

Based on the Runge and Gross theorem, we can construct a TD KS scheme.

> The time-dependent density $\rho(\mathbf{r},t)$ of the interacting particle system can be calculated as the density $\rho_s(\mathbf{r},t)$ of an auxiliary non-interacting (KS) system with the local potential $v_s(\mathbf{r},t)$.

Thus the exact TD density of the interacting system can be computed from

$$\rho(\mathbf{r},t) = \rho_s(\mathbf{r},t) = \sum_{i=1}^{N}|\phi_i(\mathbf{r},t)|^2\,, \tag{1.55}$$

where the TD-KS (TD-DFT) orbitals are obtained by solving the time-dependent Schrödinger equation of the non-interacting particle system

$$i\frac{\partial}{\partial t}\phi_j(\mathbf{r},t) = \left(-\frac{1}{2}\nabla^2 + v_s[\rho](\mathbf{r},t)\right)\phi_j(\mathbf{r},t)\,, \tag{1.56}$$

in which the single-particle KS potential is given by

$$v_s[\rho](\mathbf{r},t) = v(\mathbf{r},t) + \int\frac{\rho(\mathbf{r}',t)}{\mathbf{r}-\mathbf{r}'}d\mathbf{r}' + v_{xc}(\mathbf{r},t)\,, \tag{1.57}$$

and Eq. (1.57) formally defines the exchange-correlation potential $v_{xc}(\mathbf{r},t)$.

1.7.2 *Adiabatic Approximation*

As in the ground-state DFT formalism, the TD-KS equations require a suitable approximation for the xc potential in order to be applied in practice. The exact v_{xc} depends non-locally on the density both in the spatial and in the time variables (memory dependence). Fortunately, by disregarding memory dependence, we obtain an approximation which is not too bad and that has been successfully applied in many cases. This approach, called the adiabatic approximation (AA), can be written formally as

$$v_{xc}^{adia}[\rho](\mathbf{r},t) = v_{xc}^{GS}[\rho_t](\mathbf{r},t)\,, \tag{1.58}$$

where v_{xc}^{GS} is the ground-state xc functional calculated at the instantaneous density, ρ_t at time t. An example is the TD-LDA in the limit of an external potential $v(\mathbf{r},t)$, which varies slowly in time, the time-dependent local density approximation (TD-LDA) is used to calculate this xc potential $v_{xc}(\mathbf{r},t)$. Amazingly just like LDA in the case of time-independent DFT, the TD-LDA seems to work well beyond its domain of justification. Therefore $v_{xc}(\mathbf{r},t)$ is approximated by the same xc potential as in time-independent DFT, but now using the TD density at a particular time t, rather than the TD density.

Thus, evaluated with the density at a particular time t, the xc potential is approximated by,

$$v_{xc}[\rho_t](\mathbf{r},t) = \frac{\delta E_{xc}[\rho_t]}{\delta \rho_t(\mathbf{r})}\,, \tag{1.59}$$

where $\rho_t(\mathbf{r})$ is $\rho(\mathbf{r},t)$ evaluated at fixed t, and it should be noted that, in this approximation, all retardation memory effects are neglected, and an instantaneous reaction of the SCF to changes in ρ is assumed. Each ground-state functional such as LDA, GGA or hybrid can yield a corresponding adiabatic approximation. In the limit of an external potential that varies slowly in time, the AA becomes exact if the true xc ground-state functional is known. In practice the results are also affected by the faults of the ground-state approximations, such as the lack of spatial non-locality of LDA or GGA. Nevertheless, despite the crudeness of AA, optical spectra calculated within this approach are often nearly as accurate as the results of more demanding many-body approaches [261]. More importantly AA TD-DFT is easier to implement and apply than are the many-body approaches, making AA TD-DFT an obvious choice for calculations on larger more complex systems. There are several known failures of the AA, due to either lack of memory or spatial non-locality. Among them we mention the optical properties of solids and long conjugated molecules, double excitations, and charge-transfer excitations. These faults of AA and the attempts to solve them are reviewed in [53].

All applications of TD-DFT in this thesis will use the AA.

1.7.3 *Linear-Response Theory*

The majority of applications of TD-DFT concern the calculation of optical absorption spectra using linear-response theory and within the dipole approximation. The results of such calculations can be compared with the findings of standard spectroscopic experiments, where the external perturbing field is weak. In this section we will summarize the general results of LR theory, with emphasis on its application to optical absorption spectra. Linear-response theory is a straightforward consequence of the time-dependent Schrödinger equation in a perturbative treatment. For convenience, the equations will be considered in the frequency representation, obtained by Fourier transforming time-dependent quantities.

Given a many-particle system, the purpose of LR theory is to study the variation of a given physical observable due to the application of a weak external perturbation. As it is usual in quantum mechanics, both the observable and the perturbation are represented by Hermitian operators. The fundamental quantity in TD LR theory is the generalized susceptibility which in the frequency domain (Lehmann representation) can be written [118]

$$\begin{aligned}\chi(\mathbf{r},\mathbf{r}',\omega) \;=\; \sum_n \Bigg[& \frac{\langle\Psi_0|\hat{\psi}^\dagger(\mathbf{r})\hat{\psi}(\mathbf{r})|\Psi_n\rangle\langle\Psi_n|\hat{\psi}^\dagger(\mathbf{r}')\hat{\psi}(\mathbf{r}')|\Psi_0\rangle}{\omega-(E_n-E_0)+i\eta} \\ & -\frac{\langle\Psi_0|\hat{\psi}^\dagger(\mathbf{r}')\hat{\psi}(\mathbf{r}')|\Psi_n\rangle\langle\Psi_n|\hat{\psi}^\dagger(\mathbf{r})\hat{\psi}(\mathbf{r})|\Psi_0\rangle}{\omega+(E_n-E_0)+i\eta}\Bigg] \,, \end{aligned} \tag{1.60}$$

where η is an infinitesimal positive number, Ψ_0 and Ψ_n are respectively the ground- and excited-state wave functions corresponding to the energies E_0 and E_n, and $\hat{\psi}^\dagger(\mathbf{r})$ and $\hat{\psi}(\mathbf{r})$ are field operators. The operator $\hat{\psi}^\dagger(\mathbf{r})\hat{\psi}(\mathbf{r})$ is the second-quantized version of the density operator $\hat{\rho}(\mathbf{r}) = \sum_{i=1}^{N}\delta(\mathbf{r}-\mathbf{r_i})$, where N is the number of electrons. The poles of Eq. (1.60) correspond to the excitation energies of the system. Using Eq. (1.60) the Fourier transform of the response of the expectation value of a local operator, $\hat{A}$, to a local time-dependent perturbation $v'_{ext}(\mathbf{r},t)$ reads:

$$A'(\omega) = \int A(\mathbf{r})\chi(\mathbf{r},\mathbf{r}',\omega)v'_{ext}(\mathbf{r}',\omega)d\mathbf{r}d\mathbf{r}' \,. \tag{1.61}$$

In case of an independent-particle system Ψ_0 and Ψ_n become Slater determinants of single-particle orbitals, $\phi_i(\mathbf{r})$, corresponding to the energies ϵ_i and Eq. (1.60) can be written as

$$\chi_{KS}(\mathbf{r},\mathbf{r}',\omega) = \sum_{ij}(n_j-n_i)\frac{\phi_j^*(\mathbf{r})\phi_i(\mathbf{r})\phi_i^*(\mathbf{r}')\phi_j(\mathbf{r}')}{\epsilon_j-\epsilon_i+\omega+i\eta} \,, \tag{1.62}$$

where n_j and n_i are orbital occupation numbers. This equation is particulary useful in TD-DFT since it is used to calculate the KS

susceptibility. It is important to notice that, if i and j are both occupied or both empty levels,then the corresponding contribution to χ vanishes. A particularly important linear response function is the dynamic polarizability

$$\alpha_{ij}(\omega) = \int r_i \chi(\mathbf{r}, \mathbf{r}', \omega) r'_j d\mathbf{r} d\mathbf{r}' , \tag{1.63}$$

where r_i and r'_j are the components of the position operators $\mathbf{r}$ and $\mathbf{r}'$. If we consider the linear-response of the dipole to the external perturbation $v'_{ext}(\mathbf{r}, \omega) = -\mathcal{E}(\omega) \cdot \mathbf{r}$ in which $\mathcal{E}(\omega)$ is a weak electric field, we can write the polarizability as

$$a(\omega) = \frac{1}{3} Tr a\alpha(\omega) = \sum_n \frac{f_n}{(E_n - E_0)^2 - \omega^2} , \tag{1.64}$$

where the spectroscopic oscillator strengths are

$$f_n = \frac{2}{3}(E_n - E_0) \left(|\langle \Psi_0 | \hat{x} | \Psi_n \rangle|^2 + |\langle \Psi_0 | \hat{y} | \Psi_n \rangle|^2 + |\langle \Psi_0 | \hat{z} | \Psi_n \rangle|^2 \right) , \tag{1.65}$$

and $\hat{x}, \hat{y}$ and $\hat{z}$ are the components of the position operator. Eq. (1.64) is a straight-forward consequence of Eq. (1.60) and of Eq. (1.63). The dynamic polarizability is particularly important since it is closely related to the absorption of electromagnetic radiation in the dipole approximation. Indeed for a molecular system we can write the molar extinction coefficient as

$$\varepsilon(\omega) \propto \omega Im(\alpha(\omega + i\eta)) , \tag{1.66}$$

This relation can be obtained in the context of the semi-classical theory of the interaction radiation-matter using the *dipole approximation* and *Fermi's golden rule*. Since this result has been used in the thesis we will sketch here the demonstration. First of all we remind the reader that the absorption coefficient ε is defined by the relation $I(z) = I_0 e^{-\varepsilon c z}$, where I indicates the intensity of an electromagnetic beam propagating along z. We also remind the reader that the density of radiation energy is given by $\rho = \mathcal{E}^2/8\pi$, where $\mathcal{E}$ is the norm of the electric field associated with the wave. The intensity I is provided by the product $c\rho$ where c is the speed of light. Using these relations, the energy per unit of time (power) which is provided to the system under investigation by the light beam can be written as

$$\frac{dU}{dt} = c\frac{dU}{dz} = \frac{Vc}{8\pi}\frac{d\mathcal{E}^2}{dz} = -\frac{Vc}{8\pi}\varepsilon\mathcal{E}^2 , \tag{1.67}$$

where V denotes the volume. This equation can be inverted to obtain

$$\varepsilon = -\frac{8\pi}{Vc\mathcal{E}^2}\frac{dU}{dt} , \tag{1.68}$$

In order to estabilish a connection with microscopic theory we rewrite eq. (1.67) as

$$\frac{dU}{dt} = \sum_{if} \omega_{fi} W_{if} \,, \tag{1.69}$$

where i and f indicate occupied and unoccupied (virtual) energy levels, ω_{fi} is their difference in energy and W_{if} is the transition probability per unit of time between levels i and f. To go further we have now to evaluate W_{fi} using quantum mechanics. We will consider the simple case of a single electron subject to an external potential $v_{ext}(\mathbf{r})$ and to electromagnetic radiation. The Hamiltonian for this system can be expressed as

$$\hat{H} = \frac{1}{2}(-i\nabla - \frac{\mathbf{A}}{c})^2 + v_{ext}(\mathbf{r}) \,, \tag{1.70}$$

where $\mathbf{A}$ is the vector potential associated with the elctromagnetic wave. Using the Coulomb gauge $\nabla \cdot \mathbf{A} = 0$ and discarding the quadratic term in the vector potential, Eq. (1.70) can be simplified as

$$H = -\frac{1}{2}\nabla^2 + v_{ext}(\mathbf{r}) + \frac{i}{c}\mathbf{A} \cdot \nabla \,, \tag{1.71}$$

where the last term of the Hamiltonian can be treated perturbatively. For an electromagnetic wave propagating along z, the vector potential can be chosen to be

$$\mathbf{A}(z,t) = \mathbf{A}_0 e^{i(kz-\omega t)} \,, \tag{1.72}$$

where k is the wave number and ω is frequency. In general, if the wavelength λ of the radiation is large compared with the dimension of the system under investigation, the vector potential can be expanded in powers of $kz = 2\pi/\lambda z$

$$\mathbf{A}(z,t) = \mathbf{A}_0 e^{i\omega t}[1 + ikz - \frac{1}{2}(kz)^2 + ...] \,. \tag{1.73}$$

By limiting the expansion to the first term, namely by discarding the dependence on the position, we obtain the dipole approximation. Using Fermi's golden rule, the transition probability per unit of time between two levels i (occupied) and f (unoccupied) is given by

$$W_{if} = \frac{2\pi}{c^2}[\mathbf{A}_0 \cdot \langle \Psi_f | \nabla | \Psi_i \rangle]^2 \delta(\omega_{fi} - \omega) \,. \tag{1.74}$$

Through the identity $[\mathbf{r}, H] = \nabla$, the term $\langle \Psi_f | \nabla | \Psi_i \rangle$ can be expressed as

$$\langle \Psi_f | \nabla | \Psi_i \rangle = -\omega_{fi} \langle \Psi_f | \mathbf{r} | \Psi_i \rangle \,, \tag{1.75}$$

and Eq. (1.74) can be finally writted as

$$W_{if} = 2\pi[\mathcal{E}_0 \cdot \langle \Psi_f | \mathbf{r} | \Psi_i \rangle]^2 \delta(\omega_{fi} - \omega) \,, \tag{1.76}$$

where we used the relation $\mathcal{E}_0 = (i\omega_{fi}/c)\mathbf{A}_0$. Now W_{if} is ready to be inserted in Eq. (1.69) to obtain the molar extinction coefficient through Eq. (1.68).

1.7.4 *Linear-Response TD-DFT And Dyson-Like Equation*

According to Eq. (1.61) the perturbation v'_{ext} introduces a first-order change in the electronic density that can be expressed for an interacting system as,

$$\delta\rho(\mathbf{r},\omega) = \int \chi(\mathbf{r},\mathbf{r}',\omega)\delta v'_{ext}(\mathbf{r}',\omega)d\mathbf{r}' , \tag{1.77}$$

where χ is the generalized susceptibility defined in Eq. (1.61). By construction, the noninteracting Kohn-Sham equations (1.56) have the same time-dependent density as the many-body problem. For this reason, the response of the density $\rho'(\mathbf{r},\omega)$ is also the same. In this case the equations are a bit more subtle, since the effective potential also depends on the internal variables. Indeed the response of the density can be written as

$$\rho'(\mathbf{r},\omega) = \int \chi_{KS}(\mathbf{r},\mathbf{r}',\omega)v'_{KS}(\mathbf{r}',\omega)d\mathbf{r}' , \tag{1.78}$$

where

$$v'_{H_{xc}}(\mathbf{r},\omega) = v'_{H}(\mathbf{r},\omega) + v'_{ext}(\mathbf{r},\omega) , \tag{1.79}$$

In Eq. (1.79) we have introduced the first-order response of the Hartree + xc potential induced by the application of v'_{ext}

$$v'_{H_{xc}}(\mathbf{r},\omega) = v'_{H}(\mathbf{r},\omega) + v'_{xc}(\mathbf{r},\omega) = \int f_{H_{xc}}(\mathbf{r},\mathbf{r}',\omega)\rho'(\mathbf{r}',\omega)d\mathbf{r}' , \tag{1.80}$$

The kernel f is defined by

$$f_{H_{xc}}(\mathbf{r},\mathbf{r}',\omega) = \int \frac{\delta v_{H_{xc}}(\mathbf{r},t)}{\delta\rho(\mathbf{r}',t')} e^{i\omega(t-t')} d(t-t') , \tag{1.81}$$

where the right-hand term is a functional of ground-state density only, whose LR we are calculating, in the AA, Eq. (1.81) does not depend explicitly on frequency because the xc contribution to the kernel is local in time

$$f_{xc}^{adia}(\mathbf{r},\mathbf{r}',t-t') = \frac{\delta v_{xc}(\mathbf{r})}{\delta\rho(\mathbf{r}')}|_{\rho=\rho_0}\delta(t-t') , \tag{1.82}$$

By equating the density response in Eq. (1.77), we obtain a Dyson-like equation for the TD-DFT linear-response, namely,

$$\chi(\mathbf{r},\mathbf{r}',\omega) = \chi_{KS}(\mathbf{r},\mathbf{r}',\omega) + \int\int \chi_{KS}(\mathbf{r},\mathbf{r}_1,\omega)f(\mathbf{r}_1,\mathbf{r}_2,\omega)\chi(\mathbf{r}_2,\mathbf{r}',\omega)d\mathbf{r}_1 d\mathbf{r}_2 . \tag{1.83}$$

The poles of the response function χ are excitation energies of the interacting system and the residues are the corresponding oscillator strength. The kernel K is responsible for the corrections to the non-interacting KS susceptibility. Indeed if we set $f_{H_{xc}} = 0$ we obtain exactly $\chi = \chi_{KS}$. The optical spectra can be obtained from the Dyson-like equation through Eq. (1.63).

1.7.5 *Casida's Equation*

For frequency-dependent and -independent kernels, Casida has reformulated the calculation of the poles (namely the transition energies) of the response function χ into a generalized Hermitian eigenvalue problem [60]. Ref. [60] also explicitly considers frequency-dependent kernels. This approach with frequency-independent kernels is widespread in the quantum chemistry community and is implemented in many ab initio codes. It is particularly suitable to calculate absorption spectra, although it is not possible to access broad energy ranges. The starting point to derive Casida's equations is Eq. (1.78) where $v_{H'_{xc}}$ in turn depends linearly upon the response of the density through Eq. (1.80). By explicitly substituting the KS susceptibility in Eq. (1.78), we notice that the factorization allows for a direct integration of the product of the response function and of the first-order change in the potential. The induced density change can then be written as

$$\rho'(\mathbf{r},\omega) = \sum_{ij} P'_{ij}\phi_i(\mathbf{r})\phi_j^*(\mathbf{r})\,, \tag{1.84}$$

in which the expansion coefficients are given by

$$P'_{ij}(\omega) = \frac{n_j - n_i}{\epsilon_j - \epsilon_i + \omega + i\eta}\int \phi_i(\mathbf{r})\left[v'_{KS}(\mathbf{r},\omega) + v_{appl}(\mathbf{r},\omega)\right]\phi_j^*(\mathbf{r})d\mathbf{r}\,. \tag{1.85}$$

Theses coefficients are different from zero only if they connect virtual states with occupied states and vice versa. By inserting explicitly ρ' in the form of Eq. (1.84) in Eq. (1.80) and by using this last equation to evaluate Eq. (1.85), we obtain the linear system

$$\sum_{kl}\left[\frac{\omega - (\epsilon_k - \epsilon_l)}{n_j - n_i}\delta_{ik}\delta_{jl} - K_{ij,kl}\right]P'_{kl}(\omega) = \int \phi_i(\mathbf{r})v'_{appl}(\mathbf{r},\omega)\phi_j^*(\mathbf{r})d\mathbf{r}\,, \tag{1.86}$$

where

$$K_{ij,kl}(\omega) = \int\int \phi_i^*(\mathbf{r})\phi_j(\mathbf{r})f_{Hxc}(\mathbf{r},\mathbf{r}',\omega)\phi_k^*(\mathbf{r}')\phi_l(\mathbf{r}')d\mathbf{r}d\mathbf{r}'\,, \tag{1.87}$$

is the coupling matrix and $f_{KS}(\mathbf{r},\mathbf{r}',\omega)$ is the exchange-correlation kernel given by Eq. (1.81). Equation (1.86) describes the dynamic response to a dynamic perturbation. At an excitation energy, this response becomes infinite even for an infinisimally small v'_{appl}. This means we may find the excitation energies by seeking the zero eigenvalues of the matrix in brackets on the lefthand side of Eq. (1.86). The resultant equation can be written in the final form of Casida's equation

$$\hat{\Omega}F_I = \omega_I F_I\,, \tag{1.88}$$

where

$$\hat{\Omega}_{ij,kl} = (\epsilon_l - \epsilon_k)^2 + 2\sqrt{(n_i - n_j)(\epsilon_j - \epsilon_i)}K_{ij,kl}\sqrt{(n_k - n_l)(\epsilon_l - \epsilon_k)}, \tag{1.89}$$

is a Hermitian matrix. The eigenvalues of Eq. (1.88) provide the excitation energies of the system; the eigenvectors, instead, can be used to obtain the spectroscopic oscillator strengths and to assign the symmetry of each transition. First of all, in order to solve Casida's equations, it is necessary to diagonalize the ground-state Hamiltonian in order to obtain all (or at least many of) the empty KS states. This operation has an unfavorable scaling, which makes this approach not particularly appropriate for large basis sets, such as plane-waves. It is essential to take advantage of iterative krylov-space techniques such as Davidson diagonalization, [92] that do not require the explicit calculation and storage of the full matrix. Indeed the full power of the iterative techniques exmes only when combined with the fact that the coupling matrix can be evaluated using techniques, which are already well established for ground-state calculations, such as the auxiliary function expansion method for localized basis sets [30] or fast Fourier transforms in plane-wave/wavelet implementations. In this scheme the computational cost is significantly reduced. The real drawback of this approach is that iterative techniques allow for the calculation of only a limited number of the lowest eigenvalues. Furthermore serious problems can arise when particularly large systems have to be treated. Indeed, by increasing the size of the system, the density of transitions in a given energy range increases as well.

2

STATE OF THE ART

The light-matter interaction is one of the fundamentals in physics and chemistry. Light (i.e., the electromagnetic field) is a versatile tool to initiate, probe, and control physical and chemical processes. Photochemistry can be defined as the study of chemical reactions involving electronically-excited states typically generated by photon absorption. Generally this process means that energy is exchanged, something that can lead to both increase and decrease of energy in the chemical system. The effect is determined by the size of the energy quanta exchanged, and can range from a change in angular momentum for the overall rotation of the molecule to a complete disruption of all chemical bonds. In this chapter the main interest is in the effects after interacting with photons that carry sufficient energy to match the gap between the ground state and the lowest electronically excited states.

With the rapid development of theories and computer power, theoretical chemistry has found more and more applications in understanding molecular reactions and chemical processes [28, 299]. Its results no longer only serve as the complement for the information obtained by chemical experiments, but also can in many cases predict hitherto unobserved chemical phenomena and guide the design of new drugs and materials. Starting from Hartree-Fock (HF) method with BO approximation, various quantum mechanics methods with improved accuracy or efficiency have been developed in studying different systems. In the *ab initio* post HF methods, such as multireference configuration interaction (MRCI) [327, 200, 201], CC [203], MP (MP2, MP3, MP4, etc.) [19, 202], and quantum chemistry composite methods (G2, G3, CBS, etc.) [96, 85], included electron correlation in a more accurate way than HF and high accuracy was expected. While these traditional electronic structure theories are based on the complicated many-electron wavefunction, DFT employs electronic density as the basic quantity. It is now among the most popular and versatile methods to study relative small or medium-size molecules as well as condensed phases and gives quite satisfactory results often at a level of accuracy comparable to, say, MP2 at a relatively low computational costs compared to MP2. Moreover, multi-configurational self-consistent field (MCSCF) method and TD-DFT, the theoretical study can be extended from the electronic ground states to the excited states. Not only the geometries and energies on PESs can be determined accurately, many other important properties, such as electronic charge distributions, dipoles and higher multipole moments, vibrational frequencies, reactivity or spec-

troscopic quantities, can also be calculated with satisfactory precison, thus providing us more insights into chemical systems.

In the BO approximation, the PES of a molecule can be defined as the surface described by the potential energy function of the molecule with respect to the molecular geometry. The surface dimension depends on the number of atoms of the molecule (1 for diatomic and 3N-6 for a nonlinear polyatomic molecules with N being the number of atoms). An additional energy axis is needed to graph the PES, so the (3N-6)-D surface lives in a (3N-6+1)-D space. Due to the large number of dimensions of these polyatomic surfaces, they are commonly known as hyper-surfaces. The hyper-surface are described by the Schrödinger equation, whose solution gives the molecular energy as a function of the nuclear coordinates. However, the Schrödinger equation has an infinite number of solutions, which correspond to the different electronic states of the molecule, and each state has its own hyper-surface. The topology of the hyper-surface drives all the processes of the molecule in that particular electronic state. The PES topology of the excited states is different from that of the ground state, and therefore, the regions (geometries) that the molecule can access are different too. Consequently, there are processes that can only take place in excited states.

To study the reactions or processes a molecule may undergo a chemical reaction, one has to study the topology of the PESs that can be involved in such processes. In these studies the stable conformations of molecules are represented by valleys in the 2 or 3 dimensional sketches of PES, and the height of the "mountain passes" between valleys indicate the difficulty of the reaction. This so-called static description of the reactivity of molecules can be improved by carrying out dynamics studies, which are based on the solution of time-dependent nuclear Schrödinger equation. The latter provides the position of the nuclei (potential energy) and the kinetic energy of the molecule at a given time in a given state. The importance of dynamics calculations for this thesis chapter relies on the fact that they can describe non-stationary processes. Those processes are especially relevant in photophysics because photon absorptions provide an extra energy to molecules which starts a sequence of non-stationary events that are commonly known as deactivation process. The most important parameters of the deactivations are the excited state lifetimes and branching ratios. With the potential and kinetic energies, one can determine both the "trajectory" a molecule will follow, i.e., the reaction that may take place and the time needed to do so, i.e., the reaction lifetime. If different products are formed, a set of trajectories can determine the probability with which each product can be formed (branching ratio), which includes the probability of regenerating the initial structure. The average of all trajectories and regions of the PES that a molecule can access one gets an accurate description of the reactivity and behaviour of

the molecule upon photon absorption. Thus, one gets enough data to describe the experimental results.

Dynamics simulations are an indispensable tool for the description of reactions in photophysics, however they are computationally challenging due to its high cost. As it will be shown, in this thesis chapter we have tried to reach a compromise between computational feasibility and results accuracy. This can be done by rationalizing the dynamics simulations carried out at a computationally feasible level with a high level PES.

There are different types of molecular dynamics simulations and they can be classified depending on the way the nuclear motion is treated. Two main groups, namely classical and quantum dynamics methods, define the boundaries of the molecular dynamics framework. These two methodologies present some limitations especially when dealing with non-adiabatic processes of large systems. A large variety of methods are addressed in this chapter. The full classical and quantum dynamics methods are explained first together with some of their limitations. Later, different methods with mixed classical-quantum character, especially TD-DFT based methods, are explained.

Various methodologies and level of theories have been reviewed with more emphasis on the theory behind rather than in the chemistry behind them. The methodologies will not be explained in great detail but will be plainly overviewed. Further insight will be given into those parts which are more relevant for the understanding of the results or have implications for the choice of methodology.

2.1 COMMENTS ON MY CONTRIBUTION TO THIS ARTICLE

The article included in this chapter entitled "Non-Born-Oppenheimer dynamics and conical intersections" authored by my thesis director Mark E. Casida and co-authored by myself along with my joint-supervior Thierry Deutsch is an invited article for the second edition of the book *Fundamentals of Time-Dependent Density Functional Theory* edited by Miguel Marques, Neepa T. Maitra, Fernando Nogueira, E. K. U. Gross, and Angel Rubio to be published in time for the next Benasque School in January 2012 where it will be distributed among the students and used as a reference. Mark and I, have discussed the outline of this review article but most of the writing was done by Mark. Since this was my first experience with the writing of a review article, I learned quite a lot about the problems of transforming information from an expert point of view to make it accessible to an introductory reader just beginning to study this wide-spread subject area.

The chapter begins with a review of the literature on molecular dynamics and the theoretical description of PESs for describing photophysical and photochemical processes, in Section (2.2). This is followed by a description of some general methods of calculation of excited

state dynamics using wave-function theory in Section (2.3) including the algorithms developed that are able to search for a CX from the Hessian and gradient of the electronic energy for a state, using the reaction pathway approach to photochemistry. TD-DFT is explained in Section (2.4), as a natural alternative technique to wave-function theory-based techniques and example results are given. Some conclusions about the calculations presented in this chapter are given in Section (2.5). It is hoped that the calculations presented in this chapter will provide a basis for the further investigation of other parts of the excited potential energy surfaces presented in the thesis, in particular as regards our investigation of photoexcited oxirane PESs presented in Chapter (4). My contribution focused mainly on my favourite part *searching algorithms for CX* (Sec. 2.3.3). Plus most of the TD-DFT section (Sec. 2.4) make use of the results from our already published SF article [177] in which I was one of the active authors. Thanks to Thierry for his valuable comments and for proof-reading.

NON-BORN-OPPENHEIMER DYNAMICS AND CONICAL INTERSECTIONS

M. E. CASIDA, B. NATARAJAN, AND T. DEUTSCH

- To be appear in *Fundamentals of Time-Dependent Density-Functional Theory* edited by M. A. L. Marques, N. T. Maitra, F. M. Nogueira, E. K. U. Gross, and A. Rubio. Lecture Notes in Physics, **837** , Springer (2012).
- http://arxiv.org/abs/1102.1849.

2.2 INTRODUCTION

The area of excited-state dynamics is receiving increasing attention for a number of reasons. First the importance of photochemical processes in basic energy sciences, improved theoretical methods and the associated theoretical understanding of photochemical processes. Then there is the advent of femtosecond (and now attosecond) spectroscopy allowing access to more detailed experimental information about photochemical processes. Since photophysical and chemical processes are more complex than thermal (i.e., ground state) processes, simulations quickly become expensive and even unmanageable as the model system becomes increasingly realistic. With its combination of simplicity and yet relatively good accuracy, TD-DFT has been finding an increasingly important role to play in this rapidly developing field. After reviewing some basic ideas from photophysics and photochemistry, this chapter will cover some of the strengths and weaknesses of TD-DFT for modeling photoprocesses. The emphasis will be on going beyond the BO approximation.

There are distinct differences between how solid-state physicists and chemical physicists view photoprocesses. We believe that some of this is due to fundamental differences in the underlying phenomena being studied but that much is due to the use of different approximations and the associated language. Ultimately anyone who wants to work at the nanointerface between molecules and solids must come to terms with these differences, but that is not our objective here. Instead we will adopt the point of view of a chemical physicist (or physical chemist)—see e.g., [247].

The usual way to think about molecular dynamics is in terms of the potential energy surfaces that come out of the BO separation. In thermal processes, vibrations are associated with small motions around PES minima. Chemical reactions are usually described as going over passes (transition states) on these hypersurfaces as the system moves

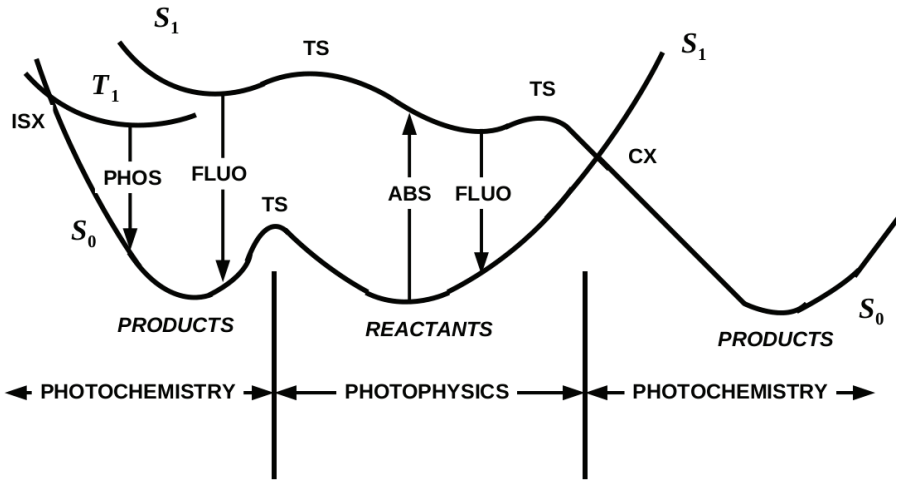

Figure 2.1: Schematic representation of potential energy surfaces for photophysical and photochemical processes: S_0, ground singlet state; S_1, lowest excited singlet state; T_1, lowest triplet state; absorption (ABS), fluorescence (FLUO), phosphorescence (PHOS), intersystem crossing (ISX), conical intersection (CX), transition state (TS).

from one valley (reactants) to another (products). Photoprocesses are much more complicated (see Fig. 2.1). Traditionally they include not only process that begin by absorption of a photon, but also any process involving electronically excited states, such as chemiluminescence (e.g., in fireflies and glow worms) where the initial excitation energy is provided by a chemical reaction. The Franck-Condon approximation tells us that the initial absorption of a photon will take us from one vibronic state to another without much change of molecular geometry, thus defining a Franck-Condon region on the excited-state potential energy surfaces. The molecule can return to the ground state by emitting a photon of the initial wavelength or, depending upon vibronic coupling and perturbations from surrounding molecules, the molecule may undergo radiationless relaxation to a lower energy excited state before emitting or it may even decay all the way to the ground state without emitting. If emission takes place from a long-lived excited state of the same spin as the ground state, then we speak of fluorescence. If emission takes place from an excited-state with a different spin due to intersystem crossing, then we speak of phosphorescence. If it is unsure whether the emission is fluorescence or phosphorescence, then we just say the molecule luminesces. Because of the large variety of de-excitation processes, excited molecules usually return too quickly to their ground state for the molecular geometry to change much. We then speak of a photophysical process because no chemical reaction has taken place. Thus fluorescence is usually described as an excited molecule relaxing slightly to a nearby minimum on the

excited-state potential energy surface where it is momentarily trapped before it emits to the ground state. It follows that the photon emitted during fluorescence is Stokes shifted to a lower energy than that of the photon initially absorbed.

Photochemical reactions occur when the excited molecule decays to a new minimum on the ground state surface, leading to a new chemical species (product). This may have positive value as a way for synthesizing new molecules or negative value because of photodegradation of materials or because of photochemically-induced cancers. Either way the photochemical reaction must occur quickly enough that it can compete with other decay processes. Photochemical reactions almost always occur via photochemical funnels where excited-state and ground-state surfaces come together, either almost touching (avoided crossing) or crossing (conical intersection.) These funnels play a role in photochemical reactions similar to transition states for thermal reactions. However it must be kept in mind that these funnels may be far from the Franck-Condon region on the excited-state potential energy surface, either because there is an easy energetically-"downhill" process or because, unless the absorption wavelength can be carefully tuned to a known vertical excitation energy, the system will typically arrive in an electronically-excited state with excess dynamical energy which can be used to move from one excited-state potential energy surface valley over a transition state to funnels in another basin of the excited-state potential energy surface. While conical intersections are forbidden in diatomic molecules, they are now believed to be omnipresent in the photochemistry of polyatomic molecules. Traditional simple models involve symmetry constraints which correspond to a potential energy surface cut, typically revealing an avoided crossing rather than the nearby CX corresponding to a less symmetric geometry. A particularly striking example is provided by experimental and theoretical evidence that the fundamental photochemical reaction involved in vision passes through a CX [271]. For these reasons, modern photochemical modeling often involves some type of dynamics and, when this is not possible, at least focuses on finding conical intersections that can explain the reaction.

While a single-reference electronic structure method may be adequate for describing photophysical processes, the usual standard for describing photochemical processes is a multireference electronic structure method such as the CASSCF method. (See [165] for a review of modern quantum chemical methods.) This is because the first approximation to the wave function along a reaction pathway is as a linear combination of the wave functions of the initial reactants and the final products. Since CASSCF is both computationally heavy and requires a high-level of user intervention, a simpler method such as TD-DFT would be very much welcome. Early work in TD-DFT in quantum chemistry foresaw increasing applications of TD-DFT in photochemical

modeling. For example, avoided crossings between cross-sections of excited-state potential energy surfaces may be described with TD-DFT because of the multireference-like nature of TD-DFT excited states [69]. However great attention must also be paid to problems arising from the use of approximate functionals [61]. In particular, the TD-DFT TDA [170] was found to give improved shapes of excited-state potential energy surfaces [71, 82], albeit at the price of losing oscillator strength sum rules. A major advance towards serious investigations of TD-DFT for describing photoprocesses came with the implementation of analytical derivatives for photochemical excited states in many electronic structure programs [56, 55, 180, 86, 282]. This made it possible to relax excited-state geometries and to calculate Stokes shifts within the framework of TD-DFT. In fact, TD-DFT has become a standard part of the photochemical modeler's toolbox. It is typically used for calculating absorption spectra and exploring excited-state potential energy surfaces around the Franck-Condon region. TD-DFT also serves as a rapid way to gain the chemical information needed to carry out subsequent CASSCF calculations. (See e.g., [99, 100, 97, 296, 98] for some combined femtosecond spectroscopy/theoretical studies of photochemical reactions which make good use of TD-DFT.) It would be nice to be able to use a single method to model entire photochemical processes. The advent of mixed TD-DFT/classical surface-hopping Tully-type dynamics [301, 328, 302, 305, 306, 32] is giving us a way to extend the power of TD-DFT to the exploration of increasingly complicated photochemical processes.

The rest of this chapter is organized as follows: The next section reviews non-Born-Oppenheimer phenomena from a wave-function point of view, with an emphasis on mixed quantum/classical dynamics. This sets the stage for our discussion of TD-DFT for non-Born-Oppenheimer dynamics and conical intersections in Sec. 2.4. We sum up in Sec. 2.5.

2.3 WAVE-FUNCTION THEORY

Most likely anyone who has made it this far into this chapter has seen the BO approximation at least once, if not many times. However it is relatively rare to find good discussions that go beyond the BO approximation [103, 75]. This section tries to do just this from a wave-function point of view, in preparation for a discussion of TD-DFT approaches to the same problems in the following section. We first begin by reviewing (again!) the BO approximation, but this time with the point of view of identifying the missing terms. We then discuss mixed quantum/classical approximations, and end with a discussion of the pathway method and ways to find and characterize conical intersections. (Mixed quantum/quantum and quantum/semiclassical methods are also interesting, but have been judged beyond the scope of this chapter.) We shall use Hartree atomic units ($\hbar = m_e = e = 1$)

thoughout and adopt the convention in this section that electronic states are labeled by small Latin letters, while nuclear degrees of freedom are labeled by capital Latin letters.

2.3.1 *Born-Oppenheimer Approximation And Beyond*

As is well-known, the BO approximation relies on a separation of time scales: Since electrons are so much lighter and so move so much faster than nuclei, the electrons may be thought of as moving in the field of nuclei which are "clamped" in place and the nuclei move in a field which is determined by the mean field of the electrons. The BO approximation provides a precise mathematical formulation of this physical picture. Our interest here is in where the BO approximation breaks down and what terms are needed to describe this breakdown.

Consider a molecule composed of M nuclei and N electrons. Denote the nuclear coordinates by $\bar{\mathbf{R}} = (\mathbf{R}_1, \mathbf{R}_2, \ldots, \mathbf{R}_M)$ and electronic coordinates by $\bar{\mathbf{r}} = (\mathbf{r}_1, \mathbf{r}_2, \ldots, \mathbf{r}_N)$. The full Hamiltonian, $\hat{H}(\bar{\mathbf{R}}, \bar{\mathbf{r}}) = \hat{T}_n(\bar{\mathbf{R}}) + \hat{H}_e(\bar{\mathbf{r}}; \bar{\mathbf{R}}) + V_{nn}(\bar{\mathbf{R}})$, is the sum of an electronic Hamiltonian, $\hat{H}_e(\bar{\mathbf{r}}; \bar{\mathbf{R}}) = \hat{T}_e(\bar{\mathbf{r}}) + V_{en}(\bar{\mathbf{r}}; \bar{\mathbf{R}}) + V_{ee}(\bar{\mathbf{r}})$, with its electronic kinetic energy, $\hat{T}_e$, electron-nuclear attraction, V_{en}, and electron-electron repulsion, V_{ee}, with the missing nuclear terms—namely the nuclear kinetic energy, $\hat{T}_n$, and the nuclear-nuclear repulsion, V_{nn}. Solving the TD Schrödinger equation,

$$\hat{H}(\bar{\mathbf{R}}, \bar{\mathbf{r}})\tilde{\Psi}(\bar{\mathbf{R}}, \bar{\mathbf{x}}, t) = i\frac{d}{dt}\tilde{\Psi}(\bar{\mathbf{R}}, \bar{\mathbf{x}}, t)\,, \tag{2.1}$$

is a formidable $(N + M)$-body problem. ($\bar{\mathbf{x}}$ denotes inclusion of electron spin. We have decided to omit nuclear spin for simplicity. Note, however, that explicit inclusion of nuclear spin can sometimes be important — for example, the properties of *ortho*- and *para*-hydrogen.) That is why the Born-Oppenheimer expansion (which is not yet the Born-Oppenheimer approximation!),

$$\Phi(\bar{\mathbf{R}}, \bar{\mathbf{x}}, t) = \sum_j \Psi_j(\bar{\mathbf{x}}; \bar{\mathbf{R}})\chi_j(\bar{\mathbf{R}}, t)\,, \tag{2.2}$$

is used, where the electronic wave functions are solutions of the time-independent electronic problem in the field of clamped nuclei,

$$\hat{H}_e(\bar{\mathbf{r}}; \bar{\mathbf{R}})\Psi_j(\bar{\mathbf{x}}; \bar{\mathbf{R}}) = E_j^e(\bar{\mathbf{R}})\Psi_j(\bar{\mathbf{x}}; \bar{\mathbf{R}})\,. \tag{2.3}$$

Inserting the Born-Oppenheimer expansion Eq. (2.2) into the full Schrödinger equation Eq. (2.1), left multiplying by $\Psi_i^*(\bar{\mathbf{x}}; \bar{\mathbf{R}})$, and integrating over $\bar{\mathbf{x}}$ gives the TD Schrödinger equation for the nuclear degrees of freedom,

$$\left[\hat{T}_n(\bar{\mathbf{R}}) + V_i(\bar{\mathbf{R}})\right]\chi_i(\bar{\mathbf{R}}, t) + \sum_j \hat{V}_{i,j}(\bar{\mathbf{R}})\chi_j(\bar{\mathbf{R}}, t) = i\frac{\partial}{\partial t}\chi_i(\bar{\mathbf{R}}, t)\,. \tag{2.4}$$

Here, $V_i(\bar{\mathbf{R}}) = E_i^e(\bar{\mathbf{R}}) + V_{nn}(\bar{\mathbf{R}})$, is the *adiabatic* PES for the ith electronic state. [Notice that this is a different use of the term "adiabatic" than in the TD-DFT "adiabatic approximation" for the exchange-correlation (xc) functional.] The remaining part, $\hat{V}_{i,j}(\bar{\mathbf{R}})$, is the hopping term which couples the ith and jth potential energy surfaces together. It should be kept in mind that the Born-Oppenheimer expansion Eq. (2.2) is exact and hence so is Eq. (2.4). As is well known, the BO approximation neglects the hopping terms,

$$\left[\hat{T}_n(\bar{\mathbf{R}}) + V_i(\bar{\mathbf{R}})\right] \chi_i(\bar{\mathbf{R}}, t) = i\frac{\partial}{\partial t}\chi_i(\bar{\mathbf{R}}, t)\,. \tag{2.5}$$

We, on the other hand, are interested in precisely the terms neglected by the BO approximation. The hopping term is given by,

$$\hat{V}_{i,j}(\bar{\mathbf{R}})\chi_j(\bar{\mathbf{R}}, t) = -\sum_I \frac{1}{2m_I}\left[G_{i,j}^{(I)}(\bar{\mathbf{R}}) + 2\mathbf{F}_{i,j}^{(I)}(\bar{\mathbf{R}})\cdot\nabla_I\right]\chi_j(\bar{\mathbf{R}}, t)\,, \tag{2.6}$$

where,

$$\begin{aligned} G_{i,j}^{(I)}(\bar{\mathbf{R}}) &= \int d^3\,\bar{x}_1 \cdots \int d^3\,\bar{x}_N \Psi_i^*(\bar{\mathbf{x}};\bar{\mathbf{R}})\left[\nabla_I^2 \Psi_j(\bar{\mathbf{x}};\bar{\mathbf{R}})\right] \\ &= \langle i|\nabla_I^2|j\rangle\,, \end{aligned} \tag{2.7}$$

is the scalar coupling matrix and,

$$\begin{aligned} \mathbf{F}_{i,j}^{(I)}(\bar{\mathbf{R}}) &= \int d^3\,\bar{x}_1 \cdots \int d^3\,\bar{x}_N \Psi_i^*(\bar{\mathbf{x}};\bar{\mathbf{R}})\left[\nabla_I \Psi_j(\bar{\mathbf{x}};\bar{\mathbf{R}})\right] \\ &= \langle i|\nabla_I|j\rangle\,, \end{aligned} \tag{2.8}$$

is the derivative coupling matrix [75]. Note that the derivative coupling matrix is also often denoted $\mathbf{d}_{i,j}^I$ and called the nonadiabatic coupling vector [103]. Here we have introduced a compact notation for some complicated objects: Both the scalar and derivative coupling matrices are simultaneously a function of the nuclear coordinates, a matrix in the electronic degrees of freedom, and a vector in the nuclear degrees of freedom, and a matrix in the electronic degrees of freedom. However the derivative coupling matrix is also a vector in the three spatial coordinates of the Ith nucleus.

Interestingly the scalar coupling matrix and derivative coupling matrix are not independent objects. Rather, making use of the resolution of the identity for the electronic states, it is straightforward to show that,

$$\begin{aligned} \sum_k \left(\delta_{i,k}\nabla_I + \mathbf{F}_{i,k}^{(I)}(\bar{\mathbf{R}})\right)\cdot\left(\delta_{k,j} + \nabla_I \mathbf{F}_{k,j}^{(I)}(\bar{\mathbf{R}})\right) &= \nabla_I^2 + G_{i,j}^{(I)}(\bar{\mathbf{R}}) + \\ & 2\mathbf{F}_{i,j}^{(I)}(\bar{\mathbf{R}})\cdot\nabla_I\,. \end{aligned} \tag{2.9}$$

We may then rewrite the TD nuclear equation (2.4) as,

$$\begin{aligned} -\left\{\sum_I \frac{1}{2m_I}\right. & \left.\left[\sum_k \left(\delta_{i,k}\nabla_I + \mathbf{F}_{i,k}^{(I)}(\bar{\mathbf{R}})\right)\cdot\left(\delta_{k,j}\nabla_I + \mathbf{F}_{k,j}^{(I)}(\bar{\mathbf{R}})\right)\right]\right\}\chi_j(\bar{\mathbf{R}}, t) \\ & + V_i(\bar{\mathbf{R}})\chi_i(\bar{\mathbf{R}}, t) = i\frac{\partial}{\partial t}\chi_j(\bar{\mathbf{R}}, t)\,, \end{aligned} \tag{2.10}$$

which is known as the group BO equation [75]. Evidently this is an equation which can be solved within a truncated manifold of a few electronic states in order to find fully quantum mechanical solutions beyond the BO approximation.

More importantly for present purposes is that Eq. (2.10) brings out the importance of the derivative coupling matrix. The derivative coupling matrix can be rewritten as,

$$\mathbf{F}^{(I)}_{i,j}(\bar{\mathbf{R}}) = \frac{\langle i| \left[\nabla_I \hat{H}_e(\bar{\mathbf{R}})\right] |j\rangle - \delta_{i,j}\nabla_I E^e_i(\bar{\mathbf{R}})}{E^e_j(\bar{\mathbf{R}}) - E^e_i(\bar{\mathbf{R}})}. \tag{2.11}$$

Since this equation is basically a force-like term, divided by an energy difference, we see that we can neglect coupling between adiabatic potential energy surfaces when (i) the force on the nuclei is sufficiently small (i.e., the nuclei are not moving too quickly) and (ii) when the energy difference between potential energy surfaces is sufficiently large.

These conditions often break down in funnel regions of photochemical reactions. There is then a tendency to follow diabatic surfaces, which may be defined rigorously by a unitary transformation of electronic states (when it exists) to a new representation satisfying the condition, $\mathbf{F}^{(I)}_{i,j}(\bar{\mathbf{R}}) \approx 0$. The advantage of the diabatic representation (when it exists, which is not always the case) is that it eliminates the off-diagonal elements of the derivative coupling matrix in the group BO equation [Eq. (2.10)], hence eliminating the need to describe surface hopping. At a more intuitive level, the character of electronic states tends to be preserved along diabatic surfaces because

$$\langle i|\frac{dj}{dt}\rangle = \dot{\mathbf{R}} \cdot \langle i|\nabla j\rangle = \dot{\mathbf{R}} \cdot \mathbf{F}_{i,j} \approx 0 \tag{2.12}$$

in this representation. For this reason, it is usual to trace diabatic surfaces informally in funnel regions by analyzing electronic state character, rather than seeking to minimize the nonadiabatic coupling vector. Avoided crossings of adiabatic surfaces are then described as due to configuration mixing of electronic configurations belonging to different diabatic surfaces.

2.3.2 *Mixed Quantum/Classical Dynamics*

Solving the fully quantum-mechanical dynamics problem of coupled electrons and nuclei is a challenge for small molecules and intractable for larger molecules. Instead it is usual to use mixed quantum/classical methods in which the nuclei are described by Newtonian classical mechanics while the electrons are described by quantum mechanics. Dividing any quantum system into two parts and then approximating one using classical mechanics is the subject of on-going research [210]. In general, no rigorous derivation is possible and wave-function phase

information (e.g., the Berry phase) is lost which may be important in some instances. Nevertheless mixed quantum/classical approximations are intuitive: Most nuclei (except perhaps hydrogen) are heavy enough that tunneling and other quantum mechanical effects are minor, so that classical dynamics is often an *a priori* reasonable first approximation. Of course, rather than thinking of a single classical trajectory for the nuclear degree of freedom, we must expect to think in terms of ensembles (or "swarms") of trajectories which are built to incorporate either finite temperature effects or to try to represent quantum mechanical probability distributions or both. The purpose of this subsection is to introduce some common mixed quantum/classical methods.

The most elementary mixed quantum/classical approximation is Ehrenfest dynamics. According to Ehrenfest's theorem [109], Newton's equations are satisfied for mean values in quantum systems, $d\langle\hat{\mathbf{r}}\rangle/dt = \langle\hat{\mathbf{p}}\rangle/m$ and $d\langle\hat{\mathbf{p}}\rangle/dt = -\langle\nabla V\rangle$. Identifying the position of the nuclei with their mean value, we can then write an equation, $m_I\ddot{\mathbf{R}}_I(t) = -\nabla_I V(\bar{\mathbf{R}}(t))$, whose physical interpretation is that the nuclei are moving in the mean field of the electrons. Here

$$V(\bar{\mathbf{R}}(t)) = \langle\Psi(\bar{\mathbf{R}},t)|\hat{H}_e(\bar{\mathbf{R}}(t))|\Psi(\bar{\mathbf{R}},t)\rangle + V_{nn}(\bar{\mathbf{R}}(t))\,, \tag{2.13}$$

where the electronic wave function is found by solving the TD equation,

$$\hat{H}_e(\bar{\mathbf{x}},\bar{\mathbf{R}}(t))\Psi(\bar{\mathbf{x}};\bar{\mathbf{R}},t) = i\frac{\partial}{\partial t}\Psi(\bar{\mathbf{x}};\bar{\mathbf{R}},t)\,. \tag{2.14}$$

While Ehrenfest dynamics has been widely and often successfully applied, it suffers from some important drawbacks. The first drawback is that the nuclei always move on average potential energy surfaces, rather than adiabatic or diabatic surfaces, even when far from funnel regions where the nuclei would be expected to move on the surface of a single electronic state. While this is serious enough, since it suggests errors in calculating branching ratios (i.e., relative yields of different products in a photoreaction), a more serious drawback is a loss of microscopic reversibility. That is, the temporal variation of the mean potential energy surface depends upon past history and can easily be different for forward and reverse processes.

A very much improved scheme is the fewest switches method of Tully [313, 158]. Here the nuclei move on well-defined adiabatic potential energy surfaces,

$$m_I\ddot{\mathbf{R}}_I(t) = -\vec{\nabla}_I V_i(\bar{\mathbf{R}}(t))\,, \tag{2.15}$$

and the electrons move in the field of the moving nuclei,

$$\hat{H}_e(\bar{\mathbf{r}};\bar{\mathbf{R}}(t))\Psi(\bar{\mathbf{x}},t) = i\frac{d}{dt}\Psi(\bar{\mathbf{x}},t)\,. \tag{2.16}$$

To determine the probability that a classical trajectory describing nuclear motion hops from one electronic PES to another, we expand

$$\Psi(\bar{x}, t) = \sum_m \Psi_m(\bar{x}; \bar{\mathbf{R}}(t)) C_m(t) \,, \tag{2.17}$$

in solutions of the time-independent Schrödinger equation,

$$\hat{H}(\bar{r}; \bar{\mathbf{R}}(t)) \Psi_m(\bar{x}; \bar{\mathbf{R}}(t)) = E_m(\bar{\mathbf{R}}(t)) \Psi_m(\bar{x}; \bar{\mathbf{R}}(t)) \,. \tag{2.18}$$

The probability of finding the system on surface m is then given by, $P_m(t) = |C_m(t)|^2$. The coefficients may be obtained in a dynamics calculation by integrating the first-order equation,

$$\dot{C}_m(t) = -iE_m(t) C_m(t) - \sum_n \langle m | \frac{dn}{dt} \rangle C_n(t) \,. \tag{2.19}$$

A not unimportant detail is that the nonadiabatic coupling elements need not be calculated explicitly, but instead can be calculated using the finite difference (FD) formula,

$$\langle m(t + \Delta t/2) | \dot{n}(t + \Delta t/2) \rangle = \frac{\langle m(t) | n(t + \Delta t) \rangle - \langle m(t + \Delta t) | n(t) \rangle}{2\Delta t} \,. \tag{2.20}$$

In practice, it is also important to minimize the number of surface hops or switches in order to keep the cost of the dynamics calculation manageable. [Tully also suggests (p. 1066 of Ref. [313]) that too rapid switching would lead to trajectories behaving incorrectly *as if* they were on an average PES.] Tully accomplished this by introducing his fewest-switches algorithm which is a type of Monte Carlo procedure designed to correctly populate the different potential energy surfaces with a minimum of surface hopping. Briefly, the probability of jumping from surface m to surface n in the interval $(t, t + \Delta t)$ is given by $g_{m \to n}(t, \Delta t) = \dot{P}_{m,n}(t) \Delta t / P_{m,m}(t)$ where $P_{m,n}(t) = C_m(t) C_n^*(t)$. A random number ξ is generated with uniform probability on the interval $(0, 1)$ and compared with $g_{m \to n}(t, \Delta t)$. The transition $m \to n$ occurs only if $P_n^{(m-1)} < \xi < P_n^{(m)}$ where $P_n^{(m)} = \sum_{l=1,m} P_{n,l}$ is the sum of the transition probabilities for the first m states. Additional details of the algorithm, beyond the scope of this chapter, involve readjustment of nuclear kinetic energies and the fineness of the numerical integration grid for the electronic part of the calculation with respect to that of the grid for the nuclear degrees of freedom.

It is occasionally useful to have a simpler theory for calculating the probability of PES hops which depends only on the potential energy surfaces and not on the wave functions. Such a theory was suggested by Landau [211] and Zener [339] (see also Wittig [330]). Their work predates the modern appreciation of the importance of conical intersections and so focused on surface hopping at avoided

crossing (AX). The Landau-Zener model assumes that surface hopping occurs only on the surface where the two diabatic surfaces cross that give rise to the AX where the surface hopping occurs. After some linearizations and an asymptotic limit, it is possible to arrive at a very simple final formula,

$$P = \exp\left(-\frac{\pi^2 \Delta E_{adia}^2}{h(d|\Delta E_{dia}|/dt)}\right), \tag{2.21}$$

for the probability of hopping between two potential energy surfaces. This formula is to be applied at the point of closest approach of the two PES where the energy difference is ΔE_{adia}. However $d|\Delta E_{dia}|/dt$ is evaluated as the maximum of the rate of change of the *adiabatic* energy difference as the AX is approached. While not intended to be applied to conical intersections, it is still applicable in photodynamics calculations in the sense that trajectories rarely go exactly through a CX.

2.3.3 *Pathway Method*

Dynamics calculations provide a swarm of reaction trajectories. The "pathway method" provides an alternative when dynamics calculations are too expensive or a simplified picture is otherwise desired, say, for interpretational reasons. The pathway method consists of mapping out minimum energy pathways between the initial Franck-Condon points obtained by vertical excitations and excited-state minima or conical intersections. Although analogous to the usual way of finding thermal reaction paths, it is less likely to be a realistic representation of true photoprocesses except in the limit of threshold excitation energies since excess energy is often enough to open up alternative pathways over excited-state transition states. While the necessary ingredients for the photochemical pathway method are similar to those for thermal reactions, conical intersections are a new feature which is quite different from a thermal transition state. This section provides a brief review for finding and characterizing conical intersections.

The notion of a CX arises from a relatively simple argument [337]. The PES of a molecule with f internal degrees of freedom is an f-dimensional hypersurface in an $(f+1)$-dimensional space (the extra dimension is the energy axis). If two potential energy surfaces simply cross "without seeing each other", then the crossing space is characterized by the constraint

$$E_i(\bar{\mathbf{R}}) = E_j(\bar{\mathbf{R}}), \tag{2.22}$$

making the crossing space $(f-1)$-dimensional. However in quantum mechanics, we also have the additional constraint,

$$H_{i,j}(\bar{\mathbf{R}}) = 0. \tag{2.23}$$

This makes the crossing space $(f-2)$-dimensional. This means that there will be two independent directions in hyperspace in which the two potential energy surfaces will separate. These two directions define a branching plane. Within the 3-dimensional space defined by the energy and the branching plane, the CX appears to be a double cone (see Fig. 2.6), the point of which represents an entire $(f-1)$-dimensional space. Of course, $f = 1$ for a diatomic and no CX is possible. This is the origin of the well-known AX rule for diatomics. Here we are interested in larger molecules where the low dimensionality of the branching space in comparison with the dimensionality of the parent hyperspace can make the conical intersection hard to locate and characterize.

In the pathway method, the system simply goes energetically downhill until two potential energy surfaces have the same energy Eq. (2.22). The resultant intersection space must be analyzed and the branching plane extracted so that the surface crossing region can be properly visualized and interpreted. In order to do so, let us recall a result from elementary calculus. Imagine a trajectory, $\bar{\mathbf{R}}(\tau)$, depending upon some parameter τ within the CX surface. Then $\nabla\mathcal{C}(\bar{\mathbf{R}})$ must be perpendicular to the conical intersection for any constraint function $\mathcal{C}(\bar{\mathbf{R}}) = 0$ because,

$$0 = \frac{d\mathcal{C}(\bar{\mathbf{R}}(\tau))}{d\tau} = \nabla\mathcal{C}(\bar{\mathbf{R}}) \cdot \frac{d\bar{\mathbf{R}}}{d\tau}. \tag{2.24}$$

and we can always choose $d\bar{\mathbf{R}}/d\tau \neq 0$. Taking the gradient of Eq. (2.23) defines the derivative coupling vector, $\mathbf{f}_{i,j} = \nabla H_{i,j}(\bar{\mathbf{R}})$, while taking the gradient of Eq. (2.22) defines the gradient difference vector, $\mathbf{g}_{i,j} = \nabla E_i(\bar{\mathbf{R}}) - \nabla E_j(\bar{\mathbf{R}})$. Together the derivative nonadiabatic coupling vector (DC) and unscaled gradient difference vector (UGD) are referred to as the branching vectors which characterize the branching plane. [Note that the derivative coupling vector is essentially the numerator of the derivative coupling matrix expression given in Eq. (2.11). This confusion of nomenclature is unfortunate but present in the literature.]

The condition that $d\bar{\mathbf{R}}/d\tau$ be perpendicular to the branching plane provides a constraint for use in the exploration of the CX hyperspace when seeking the minimum energy CX or the first-order saddle point in conical intersection. In particular, there has been considerable effort devoted to the problem of developing efficient algorithms for finding minimum energy points within the CX space [204, 27, 276, 336, 104, 184]. Furthermore, an automated systematic exploration method for finding minimum energy conical intersections has been very recently developed [229]. First-order saddle points and the corresponding minimum energy pathways both within the CX hypersurface may be useful reference points when mapping out a surface, and an optimization method was developed for such points within the CX hypersurface [292]. Some of the minimum energy CX optimizers use the branching

plane conditions explicitly to keep the degeneracy of the two adiabatic states during optimizations [236, 40, 22], making explicit use of both the derivative coupling vector and gradient difference vector at every step. Most well-estabilished optimization algorithms assume smoothness of the function to be optimized. Since the PES necessarily has a discontinuous first derivative in the vicinity of a conical intersection, the above-mentioned algorithms for finding minimum energy conical intersections have required access to the UGD and DC. The gradient difference vector can easily be obtained from analytical gradients, if available, or by numerical energy differentiation if analytical gradients are not yet available. However ways for finding the derivative coupling vector are not yet available for all methods since implementation of an analytical derivative method is often regarded as a prerequisite [230]. Some approaches make use of a penalty function to get around the need to calculate the derivative coupling vector and these have proven very useful for finding minimum energy CX regions without the need for the derivative coupling vector [219]. This is especially important for methods such as renormalized CC theories and TD-DFT or free-energy methods for which the electronic wave function is not completely defined, considerably complicating the problem of how to calculate derivative coupling vector matrix elements. However, convergence of penalty function methods is in general slower than methods which make explicit use of the branching plane constraints, especially if tight optimization of the energy difference, $(E_i - E_j)$, is desired [196].

2.4 TD-DFT

The last section discussed the basic theory of non-Born-Oppenheimer dynamics and conical intersections from a wave-function point of view. We now wish to see to what extent we can replace wave-function theory with what we hope will be a simpler DFT approach. As usual in DFT, we seek both the guiding light of formal rigor and pragmatic approximations that work. We will take a more or less historical approach to presenting this material. In this section, upper case Latin indices designate electronic states, while lower case Latin indices designate orbitals.

One of the early objectives of TD-DFT was to allow simulations of the behavior of atoms and clusters in intense laser fields, well beyond the LR regime and too complex to be handled by comparable wave-function methods. The closely related topic of ion-cluster collisions was studied early on using TD-DFT in a very simplified form [335]. The Ehrenfest method was the method of choice for TD-DFT simulations coupling electronic and nuclear degrees of freedom in this area. The

gradient of the potential (2.13) is calculated with the help of the Hellmann-Feynman theorem as,

$$\vec{\nabla}_I V(\bar{\mathbf{R}}(t)) = \langle \Psi(\bar{\mathbf{R}}, t) | \vec{\nabla}_I \hat{H}_e(\bar{\mathbf{R}}(t)) | \Psi(\bar{\mathbf{R}}, t) \rangle + \vec{\nabla}_I V_{nn}(\bar{\mathbf{R}}(t)) \,. \quad (2.25)$$

Note that the first integral on the right hand side only involves the (time-dependent) charge density — at least in the usual TD-DFT adiabatic approximation. Among the notable work done with this approximation is early studies of the dynamics of sodium clusters in intense laser fields [58], the development of the TD electron localization function [54], and (more recently) the study of electron-ion dynamics in molecules under intense laser pulses [195]. Besides limitations associated with the TD-DFT adiabatic approximation, the TD-DFT Ehrenfest method suffers from the same intrinsic problems as its wave-function sibling—namely that it is implicitly based on an average PES and so does not provide state-specific information, and also suffers from problems with microscopic irreversibility.

To our knowledge, the first DFT dynamics on a well-defined excited-state PES was not based upon TD-DFT but rather on the older multiplet sum method of Ziegler, Rauk, and Baerends [340, 91]. This was the work of restricted open-shell Kohn-Sham (ROKS) formalism of Irmgard Frank *et al*. [126] who carried out Car-Parinello dynamics for the open-shell singlet excited state ${}^1(i, a)$ using the multiplet sum method energy expression,

$$E_s = 2E[\Phi^{a\uparrow}_{i\uparrow}] - E[\Phi^{a\uparrow}_{i\downarrow}] \,, \quad (2.26)$$

where $\Phi^{a\tau}_{i\sigma}$ is the KS determinant with the $i\sigma$ spin-orbital replaced with the $a\tau$ spin-orbital. Such a formalism suffers from all the formal difficulties of the multiplet sum method, namely that it is just a first-order estimate of the energy using a symmetry-motivated zero-order guess for the excited-state wave function and assumes that DFT works best for states which are well-described by single determinants. Nevertheless appropriate use of the multiplet sum method can yield results similar to TD-DFT. A recent application of this method is to the study of the mechanism of the electrocyclic ring opening of diphenyloxirane [128].

The implementation of TD-DFT excited-state derivatives in a wide variety of programs not only means that excited-state geometry optimizations may be implemented, allowing the calculation of the Stokes shift between absorption and fluorescence spectra, but that the pathway method can be implemented to search for conical intersections in TD-DFT. Unless nonadiabatic coupling matrix elements can be calculated within TD-DFT (*vide infra*), then a penalty method should be employed as described in the previous section under the pathway method. This has been done by Levine, Ko, Quenneville, and Martinez using conventional TD-DFT [218] and by Minezawa and Gordon using spin-flip TD-DFT [249]. We will come back to these calculations later in this section.

The most recent approach to DFT dynamics on a well-defined excited-state PES is Tully-type dynamics [313, 158, 312] applied within a mixed TD-DFT/classical trajectory surface-hopping approach. Surface-hopping probabilities can be calculated from PES alone within the Landau-Zener method Eq. (2.21), however a strict application of Tully's method requires nonadiabatic coupling matrix elements as input. Thus a key problem to be addressed is how to calculate nonadiabatic coupling matrix elements within TD-DFT. Initial work by Craig, Duncan, and Prezhdo used a simple approximation which neglected the xc-kernel [84]. A further approximation, commented on by Maitra [232], has been made by Craig and co-workers [84, 156] who treated the electronic states as determinants of Kohn-Sham orbitals which are propagated according to the TD KS equation. This means that neither the excitation energies nor the associated forces could be considered to be accurate.

The first complete mixed TD-DFT/classical trajectory surface-hopping photodynamics method was proposed and implemented by Tapavicza, Tavernelli, and Röthlisberger [301] in a development version of the CPMD code. It was proposed that the nonadiabatic coupling matrix elements be evaluated within Casida's *ansatz* [60] which was originally intended to aid with the problem of assigning excited states by considering a specific functional form for an approximate excited-state wave function. Note that numerical integration of Eq. (2.19) to estimate the coefficients, $C_m(t)$, for the true system of interacting electrons also involves making assumptions about the initial interacting excited state. Casida's *ansatz* is a more logical choice for this than is a simple single determinant of KS orbitals. For the TDA, the Casida *ansatz* takes the familiar form, $\Psi_I = \sum_{ia\sigma} \Phi_{i\sigma}^{a\sigma} X_{ia\sigma}$. In fact, matrix elements between ground and excited states may be calculated exactly in a Casida-like formalism because of the response theory nature of Eq. (2.11) [79, 174, 288]. Test results show reasonable accuracy for nonadiabatic coupling matrix elements as long as conical intersections are not approached too closely [29, 174, 305, 306, 288]. One likely reason for this is the divergence of Eq. (2.11) when $E_I = E_J$. Hu and Sugino attempted to further improve the accuracy of nonadiabatic coupling matrix elements by using average excitation energies [173]. The problem of calculating nonadiabatic coupling matrix elements between two excited states is an open problem in TD-DFT, though the ability to calculate excited-state densities [130] suggests that such matrix elements could be calculated from double response theory using Eq. (2.11). The idea is that adding a second TD electric field *in addition* to the first perturbation which allows the extraction of excited-state densities, should allow the extraction of the excited-state absorption spectrum using LR theory in much the same way that this is presently done for the ground state. To our knowledge, this has

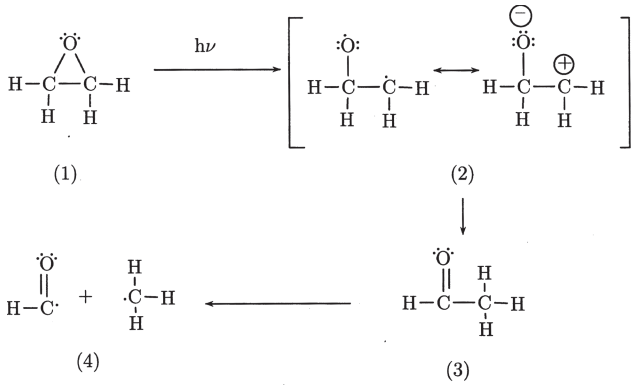

Figure 2.2: Mechanism proposed by Gomer and Noyes in 1950 for the photochemical ring opening of oxirane. Reprinted with permission from [302]. Copyright 2008, American Institute of Physics.

never yet been done. But were it to be done, the extension to the derivative coupling matrix through Eq. (2.11) should be trivial.

Soon after the implementation of mixed TD-DFT/classical trajectory surface-hopping photodynamics in CPMD, a very similar method was implemented in TURBOMOL and applied [328, 250, 32]. A version of TURBOMOL capable of doing mixed TD-DFT/classical trajectory surface-hopping photodynamics using analytic nonadiabatic coupling matrix elements has recently appeared [288] and has been used to study the photochemistry of vitamin-D [303]. Time-dependent density-functional tight-binding may be regarded as the next step in a multiscale approach to the photodynamics of larger systems. From this point of view, it is interesting to note that mixed TD-DFT-tight binding/classical trajectory surface-hopping photodynamics is also a reality [251]. Given the increasingly wide-spread nature of implementations of mixed TD-DFT/classical trajectory surface-hopping photodynamics, we can only expect the method to be increasingly available to and used by the global community of computational chemists.

Before going further, let us illustrate the state-of-the-art for TD-DFT when applied to non-Born-Oppenheimer dynamics and conical intersections. We will take the example of the photochemical ring opening of oxirane (structure I in Fig. 2.2). While this is not the "sexy application" modeling some biochemical photoprocess, the photochemistry of oxiranes is not unimportant in synthetic photochemistry and, above all, this is a molecule where it was felt that TD-DFT "ought to work" [82]. A first study showed that a main obstacle to photodynamics is the presence of triplet and near singlet instabilities which lead to highly underestimated and even imaginary excitation energies as funnel regions are approached. This is illustrated in Fig. 2.3 for C_{2v} ring opening. While the real photochemical process involves asymmetric CO ring-opening rather than the symmetric C_{2v} CC ring-opening,

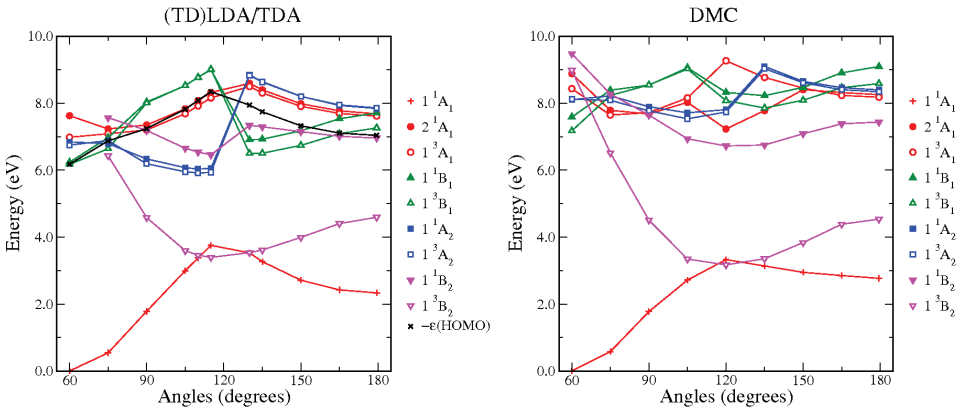

Figure 2.3: Comparison of TDA TD-LDA and diffusion Monte Carlo curves for C_{2v} ring opening of oxirane. Reprinted with permission from [82]. Copyright 2007, American Institute of Physics.

results for the symmetric pathway have the advantage of being easier to analyze. The figure shows that applying the TDA strongly attenuates the instability problem, putting most curves in the right energy range. Perhaps the best way to understand this is to realize that, whereas time-dependent Hartree-Fock (TD-HF), is a nonvariational method and hence allows variational collapse of excited states, TDA TD-HF is the same as configuration interaction singles (CIS) which is variational. There is however still a cusp in the ground state curve as the ground state configuration changes from σ^2 to $(\sigma^*)^2$. According to a traditional wave-function picture, these two states, which are each double excitations relative to each other should be included in configuration mixing in order to obtain a proper description of the ground state PES in the funnel region [82, 177].

Figure 2.4 shows an example of mixed TDA TDPBE/classical trajectory surface-hopping calculations for the photochemical ring-opening of oxirane with the initial photoexcitation prepared in the $^1(n, 3p_z)$ state. Part (b) of the figure clearly shows that more than one PES is populated after about 10 fs. The Landau-Zener process is typical of the dominant physical process which involves an excitation from the HOMO nonbonding lone pair on the oxygen initially to a $3p_z$ Rydberg orbital. As the reaction proceeds, the ring opens and the target Rydberg orbital rapidly changes character to become a CO σ^* antibonding orbital (Fig. 2.5). Actual calculations were run on a swarm of 30 trajectories, confirming the previously proposed Gomer-Noyes mechanism [144] (Fig. 2.2), but also confirming other experimental by-products and giving unprecedented state-specific reaction details such as the orbital description briefly described above.

The oxirane photochemical ring-opening passes through a CX, providing a concrete example of a CX to study with TD-DFT. We now

return to the study by Levine, Ko, Quenneville, and Martinez of conical intersections using conventional TD-DFT [218] who noted that strict conical intersections are forbidden by the TD-DFT adiabatic approximation for the simple reason that there is no coupling matrix element [Eq. (2.23)] to zero out between the ground and excited states. Figure 2.6 shows a CASSCF conical intersection close to the oxirane photochemical funnel. Also shown are the TDA TD-DFT surfaces calculated with the same CASSCF branching coordinates. Interestingly the CASSCF and TD-DFT conical intersections look remarkably similar. However closer examination shows that the TD-DFT "conical intersection" is actually two *intersecting* cones rather than a true CX, confirming the observation of Levine *et al*. This was analyzed in detail in [302] where it was concluded that the problem is that we are encountering effective noninteracting v-representability. True NVR means that there is no noninteracting system whose ground state gives the ground state density of the interacting system. This only means that there is some excited state of the noninteracting system with integer occupation number which gives the ground state density of the interacting system. What we call effective NVR is when the LUMO falls below the HOMO (or, in the language of solid-state physics, there is a "hole below the Fermi level"). This is exactly what frequently happens in the funnel region.

Spin-flip (SF) TD-DFT [295, 291, 322] offers one way to circumvent some of the problems of effective NVR in funnel regions. This is because we can start from the lowest triplet state which has fewer effective NVR problems and then use SFs to obtain both the ground state and a doubly-excited state. Analytic derivatives are now available for some types of SF-TD-DFT [290]. Figure 2.7 shows that SF-TD-DFT works fairly well for treating the AX in the C_{2v} ring-opening pathway of oxirane. Minezawa and Gordon also used SF-TD-DFT to locate a conical intersection in ethylene [249]. However Huix-Rotllant, Natarajan, Ipatov, Wawire, Deutsch, and Casida found that, although SF-TD-DFT does give a true CX in the photochemical ring opening of oxirane, the funnel is significantly shifted from the position of the CASSCF conical intersection [177]. The reason is that the key funnel region involves an active space of more than orbitals which is too large to be described accurately by SF-TD-DFT.

There are other ways to try to build two- and higher-excitation character into a DFT treatment of excited states. Let us mention here only MRCI/DFT [148], constrained density-functional theory-CI (CDFT-CI) [332], and mixed TD-DFT/many-body theory methods based upon the Bethe-Salpeter equation [278] or the related polarization propagator approach [62, 176] or the simpler dressed TD-DFT [233, 74, 149, 243, 244, 178] approach.

All of these may have the potential to improve the DFT-based description of funnel regions in photochemical reactions. Here however we must be aware that we may be in the process of building a theory

which is less automatic and requires the high amount of user intervention typical of present day CASSCF calculations. This is certainly the case with CDFT-CI which has already achieved some success in describing conical intersections [193].

2.5 PERSPECTIVES

Perhaps the essence of dynamics can be captured in a simple sentence: "You should know from whence you are coming and to where you are going." Of course this rather deterministic statement must be interpreted differently in classical and quantum mechanics. Here however we would like to think about its meaning in terms of the development of DFT for applications in photoprocesses. Theoretical developments in this area have been remarkable in recent years, opening up the possibility for a more detailed understanding of femtosecond (and now also attosecond) spectroscopy. In this chapter we have tried to discuss the past, the present, and a bit of the future.

The past treated here has been the vast area of static investigation and dynamic simulations of photophysical and photochemical processes. We have first described more traditonal wave-function techniques. We have also mentioned and made appropriate references to important work on early DFT work involving Ehrenfest TD-DFT and ROKS DFT dynamics. Our emphasis has been on photochemical processes involving several potential energy surfaces, partly because of our own personal experiences, but also because photo*chemical* processes start out as photo*physical* processes in the Franck-Condon region and then rapidly become more complicated to handle.

The present-day status of DFT photodynamics is perhaps best represented by the recent availability of mixed TD-DFT and TD-DFTB/classical surface-hopping dynamics codes as well as serious efforts to investigate and improve the quality of the TD-DFT description of photochemical funnel regions. First applications have already shown the utility of this theory and we feel sure that other applications will follow as programs are made broadly available to computational scientists. Finally we have ended the last section with some speculations about the future concerning the need for explicit double- and higher-excitations to correctly describe funnel regions.

As expected, we could not treat everything of relevance to the chapter title. Roi Baer's recent work indicating that Berry phase information is somehow included in the ground-state charge density is most intriguing [39]. Also on-going work on multicomponent DFT capable of treating electrons and nuclei on more or less the same footing [207, 208] would seem to open up new possibilities for developing useful non-Born-Oppenheimer approximations within a DFT framework. We are sure that still other potentially relevant work has

been unfortunately omitted either because of space limitations or for other reasons.

Do we know where this field is going? Certainly non-Born-Oppenheimer photodynamics using some form of DFT is currently a hot and rapidly evolving area. Exactly what lies in store may not yet be clear, but what we do know is that we are going to have fun getting there!

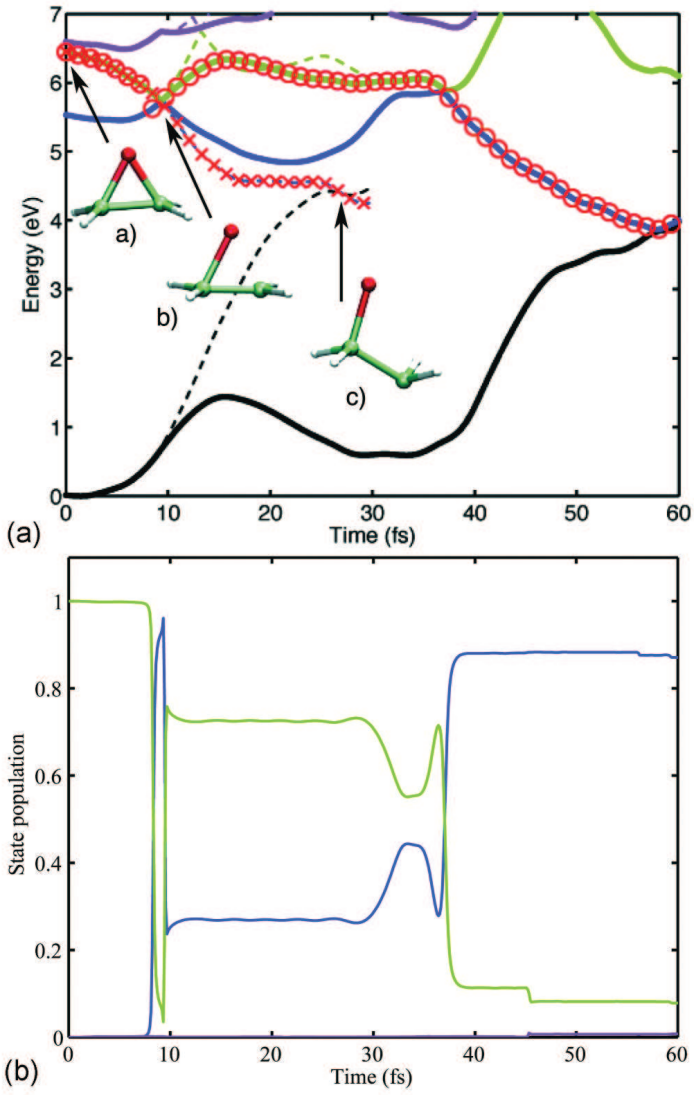

Figure 2.4: (a) Cut of potential energy surfaces along reaction path of a Landau-Zener (dashed line) and a fewest-switches (solid line) trajectory (black, S_0; blue, S_1; green, S_2; magenta, S_3). Both trajectories were started by excitation into the $^1(n, 3p_z)$ state, with the same geometry and same initial nuclear velocities. The running states of the Landau-Zener and the fewest-switches trajectory are indicated by the red crosses and circles, respectively. The geometries of the Landau-Zener trajectory are shown at time a) 0, b) 10, and c) 30 fs. (b) State populations (black, S_0; blue, S_1; green, S_2; magenta, S_3) as a function of the fewest-switches trajectory in (a). Reprinted with permission from [302]. Copyright 2008, American Institute of Physics.

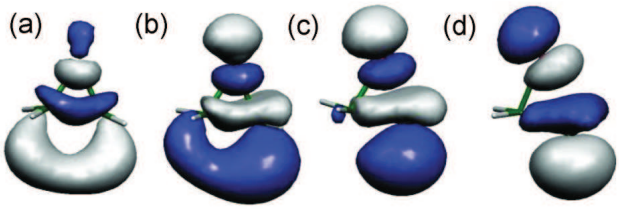

Figure 2.5: Change of character of the active state along the reactive Landau-Zener trajectory, shown in Fig. 2.4. Snapshots were taken at times (a) 2.6, (b) 7.4, (c) 12.2, and (d) 19.4 fs. For (a) and (b), the running state is characerized by a transition from the HOMO to the LUMO plus one (LUMO+1), while for (c) and (d) it is characterized by a HOMO-LUMO transition due to orbital crossing. Note that the HOMO remains the same oxygen nonbonding orbital throughout the simulation. Reprinted with permission from [302]. Copyright 2008, American Institute of Physics.

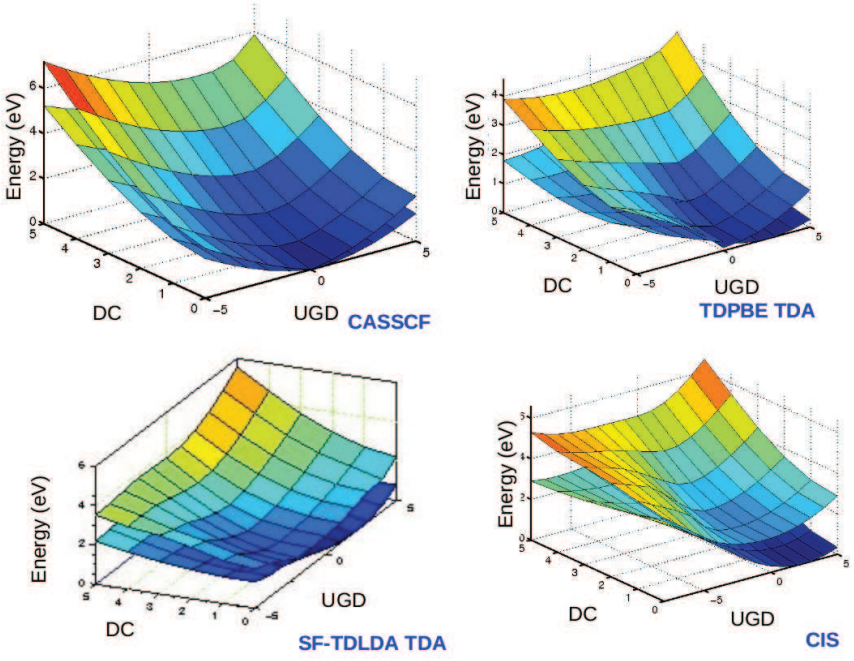

Figure 2.6: Comparison of the S_0 and S_1 potential energy surfaces calculated using different methods for the CASSCF branching coordinate space. Reproduced from [177] by permission of the PCCP Owner Societies.

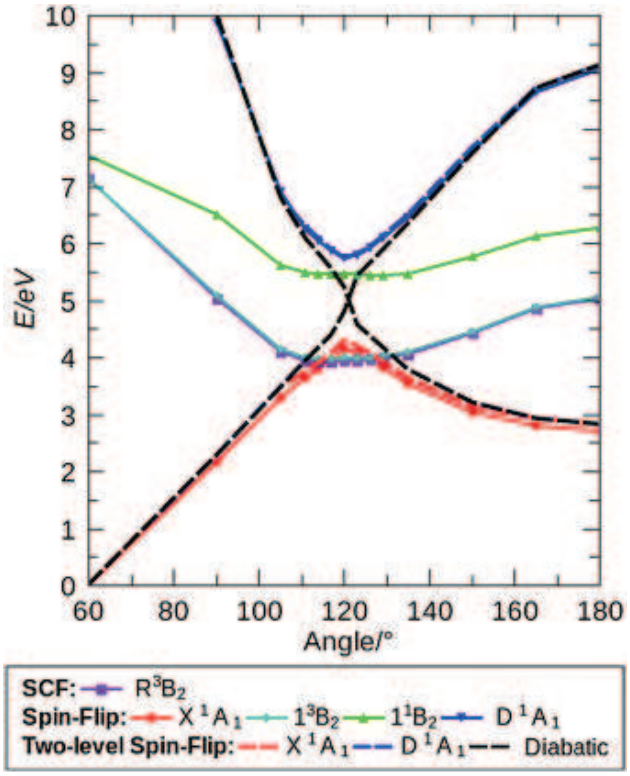

Figure 2.7: C_{2v} potential energy curves: full calculation (solid lines), two-orbital model (dashed lines). Reproduced from [177] by permission of the PCCP Owner Societies.

3

WAVELETS FOR DFT

Most of the low-energy physics, chemistry and biology can be explained by the quantum mechanics of electrons and ions. First-principles methods based on DFT [206, 172] have proven to be an accurate and reliable tool in understanding and predicting a wide variety of physical and chemical properties [183]. Traditional *ab initio* methods are however extremely expensive in terms of computational as well as memory requirements. Typically, the computer time scales as N^3 where N is the number of electrons in the system, restraining the system sizes that can be examined. In order to treat grand challenge problems, such as the computational description of excited-state dynamics, a significant increase in computational power is required or new methods have to be devised with better scaling properties. One such method based on wavelets is described in this chapter of the thesis.

While the name "wavelets" is relatively young (early 80's) the basic ideas have been around for a long time in different forms ranging from abstract analysis to signal processing and theoretical physics. They incorporate the feature of having multiple scales, so very different resolutions can be used in different parts of space in a mathematically rigorous manner. The main contribution of the wavelet field as such has been to bring together a number of similar ideas from different disciplines and create synergy between these techniques. The result is a flexible and powerful toolbox of algorithmic techniques combined with a solid underlying theory. In short, the concept of multiresolution analysis (MRA) underlines the theory of wavelets. The idea is simple and ancient: separate the information to be analyzed into a "principal" part and a "residual" part.

For solving the electronic Schrödinger equation numerically, a finite basis set is used for representing the wavefunction. Usually, this basis consists of Gaussian-type orbitals (GTOs), which offer computational advantages by virtue of the Gaussian product theorem. Hence, the truncation of the full infinite basis is an approximation. Since the computational problem sizes of the methods used scale with a power law with respect to the basis set size, the selection of the actual basis set is therefore a compromise. There are hierarchical series of basis sets, such as the correlation-consistent sets of Dunning [331, 198, 108], which allow systematic convergency towards the basis set limit and furthermore allows the usage of extrapolation techniques.

Using KS equations one needs to find a way to represent the wavefunctions and the density function numerically with a limited number

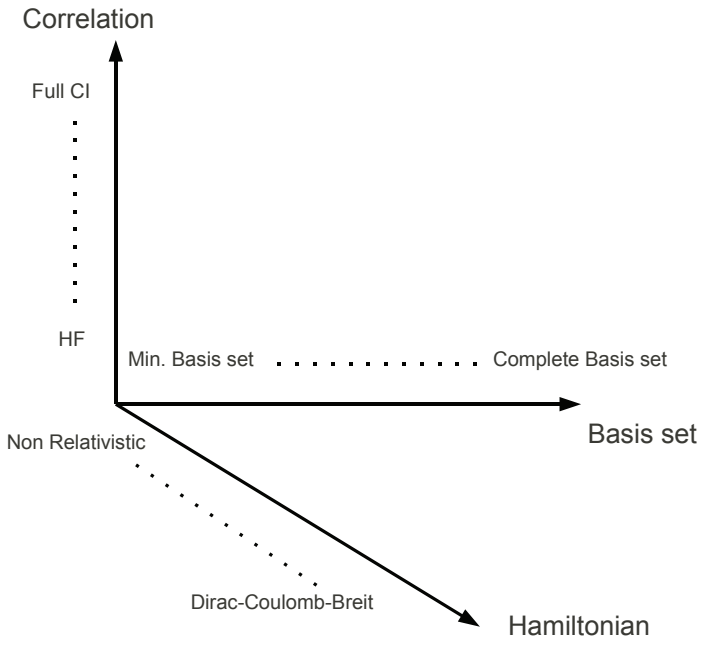

Figure 3.1: Schematic overview of the three axes of hierarchical approximations in the *ab initio* electronic structure theory.

of floating point numbers. This is usually done by choosing a basis set consisting of N functions $\phi_n(r)$ with $n = 1....,N$ where this N is now greater than or equal to the number of electrons in the system. As we pointed out before that the computations with infinite bases are impracticable in actual calculations and, truncated, but large basis set expansions are necessary to obtain accurate results. Because of computer limitations, these basis sets are rarely large enough to provide to reach the required chemical accuracy in molecules of chemical interest. The error resulting from this trunctation is difficult to assess, and the way it affects the results largely depends on the physical properties under calculation. As shown in Figure 3.1, the computational resources are limited to an appropriate level of accuracy. The choices are the truncation of the basis set, treating the electron correlation approximately and accounting for relativistic effects by using different Hamilton operators.

Like the plane waves in Fourier analysis, wavelets are a basis for expanding square-integrable function space $\mathcal{L}^2(\mathcal{R})$. But unlike the harmonic functions, wavelets have dual localization in both real and reciprocal space. In this chapter wavelets will be introduced starting from the perspective of a chemical physicist/physical chemist. We are not going to derive wavelets in any formal way, but we will strive for mathematical correctness through the properties of wavelets. We merely wish to make wavelets plausible, by giving a simple view of what they do and how they work.

3.1 COMMENTS ON MY CONTRIBUTION TO THIS ARTICLE

The review article "Wavelets for Density-Functional Theory and Post Density-Functional Theory Calculations" is an outcome of our response to an invitation to propose a research contribution to the book *Theoretical and Computational Developments in Modern Density Functional Theory* edited by Amlan K. Roy to be published by Nova Science Publishers. Through this review article we aim to give some guidelines (based on my experiences) to help novices get started with wavelets. This article builds on previous reviews but differs in attempting to include more practical advice and covers some recent and ongoing development.

Section (3.3) gives an overview of multiresolution analysis and wavelet theory with a brief historical note. The third-order interpolating wavelet is introduced together with some important concepts necessary to understand wavelet analysis. Section (3.4) introduces the theoretical framework of DFT and TD-DFT. In continuation, Sections (3.6) and (3.7) talks about some aspects related to its numerical implementation. Implementation aspects of the Poisson solver in the subsections (3.7.5) and (3.7.6) is treated in detail. Section (3.8) is an introduction partly to LR-TD-DFT and proceeds with explaining the way of setting up Casida's equation in a wavelet basis set. Section (3.9) validates our implemented version of LR-TD-DFT in BigDFT against the GTO-based program deMon2k and an application to the CO molecule is discussed. Throughout this project, I acted as an principal author, whereas Mark's contribution to the results section (Sec: 3.9) and Thierry's comments and discussion on wavelets theory section (Sec: 3.3) were highly appreciated.

WAVELETS FOR DENSITY-FUNCTIONAL THEORY AND POST DENSITY-FUNCTIONAL THEORY CALCULATIONS

BHAARATHI NATARAJAN, MARK E. CASIDA, LUIGI GENOVESE AND THIERRY DEUTSCH

- To be appear in *Theoretical and Computational Developments in Modern Density Functional Theory* edited by A. K. Roy, Nova-science publishers (2012).
- http://arXiv:1110.4853v1.

3.2 INTRODUCTION

The broad meaning of "adaptivity" is the capacity to make something work better by alternation, modification, or remodeling. Concepts of adaptivity have found widespread use in quantum chemistry, ranging from the construction of Gaussian-type orbital (GTO) basis sets, see e.g., the development of correlation consistent bases [108, 198, 331], to linear scaling methods in DFT [223, 93, 140, 205, 248, 260], selective CI methods [179, 112] and local correlation methods based on many-body perturbation theory (MBPT) or CC theory [286, 287]. This chapter is about a specific adaptive tool, namely wavelets as an adaptive basis set for DFT calculations which can be automatically placed when and where needed to handle multiresolution problems with difficult boundary conditions.

Let us take a moment to contrast the wavelet concept of adaptivity with other types of adaptivity. In other contexts, the adaptive procedure is typically based on a combination of physical insights together with empirical evidence from numerical simulations. A rigorous mathematical justification is usually missing. This may not be surprising: Familiar concepts lose a lot of their original power if one tries to put them in a rigorous mathematical framework. Therefore, we will not shoulder the monumental and perhaps questionable task of providing a rigorous mathematical analysis of all the adaptive approaches used nowadays throughout quantum chemistry. Instead we will concentrate on the mathematical analysis of a particular electronic structure method which lends itself to a rigorous mathematical analysis and application of adaptivity. In contrast with other adaptive methods, MRA with wavelets can be regarded as an additive subspace correction and their wavelet representations have a naturally built-in adaptivity which comes through their ability to express directly and separately components of the desired functions living on different scales.

This combined with the fact that many operators and their inverses have nearly sparse representations in wavelet coordinates may eventually lead to very efficient schemes that rely on the following principle: Keep the computational work proportional to the number of significant coefficients in the wavelet expansions of the sought-after solution. As there are a lot of different wavelet bases with different properties (length of support, number of vanishing moments, symmetry, etc.) in each concrete case we can choose the basis that is most appropriate for the intrinsic complexity of the desired solution. This fact makes the wavelet-based schemes a very sophisticated and powerful tool for compact representations of rather complicated functions. The expected success of wavelet transforms for solving electronic structure problems in quantum mechanics are due to three important properties: (a) the ability to choose a basis set providing good resolution where it is needed, in those cases where the potential energy varies rapidly in some regions of space, and less in others; (b) economical matrix calculations due to their sparse and banded nature; and (c) the ability to use orthonormal wavelets, thus simplifying the eigenvalue problem. Of course, this might lead to adaptive methods which are fully competitive from a practical point of view, for example, working with a systematic basis instead of GTO bases requires from the onset larger basis sets and the benefit of systematic improvement might be a distant prospect. However, we have the more realistic prospect that our rigorous analysis provides new and hopefully enlightening perspectives on standard adaptive methods, which we reckon cannot be obtained in another way.

On the other hand advances in computational technology opened up new opportunities in quantum mechanical calculation of various electronic structures, like molecules, crystals, surfaces, mesoscopic systems, etc. The calculations can only be carried out either for very limited systems or with restricted models, because of their great demands on computational and data storage resources. Independent particle approximations, like the HF based [162, 124, 293, 279] algorithms with single determinant wave functions, leave out the electron correlation and need operation and storage capacity of order N^4, if N is the total number of electrons in the system. If inclusion of the electron correlation is necessary, CI or CC methods can be applied, with very high demand of computational resources ($\mathcal{O}(N^6)$ to $\mathcal{O}(N)$). An alternative way is to use MBPT. The second order perturbation calculations can be carried out within quite reasonable time and resource limits, but the results are usually unsatisfactory, they just show the tendencies, while the 4th order MBPT needs $\mathcal{O}(N^7)$ to $\mathcal{O}(N^8)$ operations. All these algorithms use the N-electron wave function as a basic quantity.

Another branch of methods use electron density as the primary entity. Pioneers of this trend, like Thomas [309], Fermi [115, 116],

Frenkel [127] and Sommerfeld [297] developed the statistical theory of atoms and the LDA. The space around the nuclei is separated into small regions, where the atomic potential is approximated as a constant, and the electrons are modeled as a free electron gas of Fermi-Dirac statistics [101, 117, 127]. Dirac included electron correlation [102], which improved the results. After the HK theorems had appeared [172], and Kohn and Sham had offered a practically applicable method [206] based on their work, many scientists were motivated to work on the theory, and DFT developed into one of the most powerful electronic structure methods.

Despite the success of density functional theory, it has some drawbacks. The exact formula of the exchange-correlation potential is not known, thus chemical intuition and measured data are necessary in order to approximate it, and the kinetic energy functional is hard to calculate. Powerful approximating formulas are available (see, e.g. [106]), like the Thomas–Fermi functional based gradient and generalized gradient expansions, where the energy functionals are expressed as a power series of the gradient of the density (the first such suggestion was [166].)

Considering the historical development of sophisticated N-electron methods, a typical trend can be observed. Starting with a very simple model, new details are introduced in order to improve the results. This scheme is followed in the linear muffin-tin orbital (LMTO) method [21] where the interatomic regions is replaced by the spherical orbital of an atomic potential around the nuclei. Similarly, the linearized augmented plane wave (APW) [329] and the plane wave pseudopotential approach [263] describe the details of the crystal potential differently in different spatial regions. Although they are rather successful, for applying any of these models, chemical intuition is needed, free parameters, like the radius of the bordering sphere between the two types of potentials, and the boundary conditions have to be set. A systematic method, which can handle the different behaviors of the electron structures at different spatial domains, or either at different length scale [269], is the longterm requirement of any physical chemist.

Basis sets are commonly used in all electron structure calculations, as the wave function is usually expanded as linear combination of some kind of basis functions. Thus the operator eigenvalue problem is reduced to an algebraic matrix eigenvector problem. The resulting algebraic equations are easier to solve, well-known algorithms and subroutine libraries are available, however, the difficulty of choosing the proper basis set arises. If linear-combination of atomic orbital (LCAO) is used, the atomic basis functions are Slater or Gaussian-type of functions [270, 272], the selection of atomic orbitals needs chemical intuition, which is a result of long experience, and can not be algorithmized. Both basis sets are non-orthogonal, and lack the explicit

convergence properties [326]. Moreover, calculation of operator matrix elements with Slater-type orbitals is complicated, their integrals have to be treated numerically. Although integrals of Gaussian functions are analytically known, the Gaussian-type basis does not reflect the nuclear cusp condition of Kato [194], which reflects on singularities of the N-electron wave function in the presence of Coulomb-like potentials. Since then it turned out that for high precision numerical calculations it is essential to satisfy these requirements. However, while the nuclear cusp condition is relatively easy to fulfill by Slater-type orbitals (STO), the electron-electron cusp is extremely hard to represent. In general, GTO-based/STO-based DFT codes gives reliable results with a relatively small number of basis functions, making them optimal for large scale computations where high accuracy is less crucial. On the other hand there is no consistent way to extend these basis sets and thereby converge the results with respect to the size of the basis.

The second type of basis set covers the system-independent functions such as plane waves [263] or wavelets [26]. The main advantage of these basis sets, is that their size can be systematically increased until the result of the calculation has converged, and are generally considered to be more accurate than the former type. The number of basis function required to obtain convergence is normally *so large* that direct solution of the matrix eigenvalue problem within the entire basis space is *not* possible. Instead one has to use iterative methods to determine the lowest (occupied) part of the spectrum [263]. In solid state physics, where more or less periodic systems are studied, choosing plane wave basis sets is rather usual. These basis functions are system independent and easily computable, but the results are not always convincing and the number of necessary basis functions is almost untreatable. (Theoretically, plane waves could also be used for describing molecules, since the two-electron integrals and the expectation values are connected to the Fourier transform, thus they are easily computable, and this could balance the large number of necessary basis functions.) The reason, why so many plane waves are needed is that the wave functions around the nuclei need very high frequency terms, i.e. high resolution level, for reproducing the nuclear cusps. In the framework of Fourier analysis, the whole space has to be expanded at the same resolution, despite the fact that in most of the space low frequency terms would be sufficient.

Fully-numerical "basis-set free" HF calculations of atoms have been known since the 1960s (Vol. 1, pp. 322-326 and Vol. 2, pp. 15-30 of Ref. [294] and Refs. [120, 121, 122, 237]) and have proven helpful in constructing efficient finite basis sets for molecular calculations. In the late 1980s, Axel Becke used a fully-numerical DFT program for diatomics to show that many of the problems of DFT calculations at that time were due not to the functionals used, but rather to numerical

artifacts of the DFT programs of the 1970s [164].) Since that time, fully-numerical DFT codes have been implemented for polyatomic molecules using the finite difference (FD) method, with PARSEC from the chemists point of view or OCTOPUS from the view point of physicsts being a notable examples.

BIGDFT the pseudo potential code for bigger systems based as it is on traditional Hohenberg-Kohn-Sham DFT [172, 206], could only calculate ground-state properties with an eye to order-N DFT. As a step to increase the applicability of the code we formulated the wavelet-based LR-TD-DFT and here we support our first implementation for calculating electronic excitation spectra [256]. Electronic excitation spectra can be calculated from TD-DFT [280] using time-dependent linear-response theory [267, 60]. Casida formulated LR-TD-DFT (often just refered to as TD-DFT) so as to resemble the LR TD-HF equations already familiar to quantum chemists [60]. That method was then rapidly implemented in a large number of electronic structure codes in quantum chemistry, beginning with the DEMON family of programs [186] and the TURBOMOL program [35]. Among the programs that implemented "Casida's equations" early on was the FD method DFT program PARSEC [44] and they may also be found in the FD method DFT program OCTOPUS [73]. See Ref. [217] for a recent FD method implementation of TD-DFT. Since a wavelet-based program offers certain advantages over these other FD method DFT programs, it was deemed important to also implement LR-TD-DFT in BIGDFT.

In the next section we give a detailed description of the idea behind the multiresolution analysis and wavelets, with a historical note. Sec. 3.4 and Sec. 3.5, briefly present the theoretical introduction to DFT and TD-DFT, and Sec. 3.6, talks about the well-known Krylov space methods for solving eigenvalue equations involved in our implementation. Sec. 3.7 and Sec. 3.8, give the numerical implementation of DFT and how we have implemented TD-DFT from the aspects of theoretical and algorithmic point of view on wavelets based pseudopotential electronic structure code BIGDFT, and in Section 3.9 we give the results of detailed comparisons between TD-DFT excitation spectra calculated with BIGDFT and with the implementation of Casida's equations in the GTO-based program DEMON2K. Conclusions are drawn for future applications in the field of chemistry and some of the other problems are reviewed to draw chemists' greater attention to wavelets and to gain more benifits from using the wavelet technique.

3.3 WAVELET THEORY

The mathematics of wavelets is a fairly new technique, it can generally be used where one traditionally uses Fourier techniques. They incorporate the feature of having multiple scales, so very different resolutions can be used in different parts of space in a mathemati-

cally rigorous manner. This matches many systems in nature well, for example molecules where the atomic orbitals are very detailed close to the cores, while they only vary slowly between them. Wavelet analysis can quite generally be viewed as a local Fourier analysis. From the wavelet expansion, or wavelet spectrum, of a function, f, it can be inferred not only how fast f varies, i.e. which frequencies it contains, but also where in space a given frequency is located. This property has important applications in both data compression, signal/image processing and noise reduction [258]. Wavelet methods are also employed for solving partial differential equations [87, 187], and in relation to electronic structure methods a complete DFT program based on interpolating wavelets has been developed [2].

3.3.1 *The Story Of Wavelets*

Most historical versions of wavelet theory however, despite their source's perspective, begin with Joseph Fourier. In 1807, a French mathematician, Joseph Fourier, discovered that all periodic functions could be expressed as a weighted sum of basic trigonometric functions. His ideas faced much criticism from Lagrange, Legendre, and Laplace for lack of mathematical rigor and generality, and his papers were denied publication. It took Fourier over 15 years to convince them and publish his results. Over the next 150 years his ideas were expanded and generalized for non-periodic functions and discrete time sequences. The fast Fourier transform algorithm, devised by Cooley and Tukey in 1965 placed the crown on Fourier transform, making it the king of all transforms. Since then Fourier transforms have been the most widely used, and often misused, mathematical tool in not only electrical engineering, but in many disciplines requiring function analysis. This crown however, was about to change hands. Following a remarkably similar history of development, the wavelet transform is rapidly gaining popularity and recognition.

The first mention of wavelets was in a 1909 dissertation by Hungarian mathematician Alfred Haar. Haar's work was not necessarily about wavelets, as "wavelets" would not appear in their current form until the late 1980s. Specifically, Haar focused on orthogonal function systems, and proposed an orthogonal basis, now known as the Haar wavelet basis, in which functions were to be transformed by two basis functions. One basis function is constant on a fixed interval, and is known as the scaling function. The other basis function is a step function that contains exactly one zero–crossing (vanishing moment) over a fixed interval (more on this later).

The next major contribution to wavelet theory was from a 1930s French scientist Paul Pierre Lévy. More correctly, Lévy's contribution was less of a contribution and more of a validation. While studying the ins and outs of Brownian motion in the years following Haar's

publication, Lévy discovered that a scale–varied Haar basis produced a more accurate representation of Brownian motion than did the Fourier basis. Lévy, being more of a physicist than mathematician, moved on to make large contributions to our understanding of stochastic processes.

Contributions to wavelet theory between the 1930s and 1970s were slight. Most importantly, the windowed Fourier transform was developed, with the largest contribution being made by another Hungarian named Dennis Gabor. The next major advancement in wavelet theory is considered to be that of Jean Morlet in the late 1970s.

Morlet, a French geophysicist working with windowed Fourier transforms, discovered that fixing frequency and stretching or compressing (scaling) the time window was a more useful approach than varying frequency and fixing scale. Furthermore, these windows were all generated by dilation or compression of a prototype Gaussian. These window functions had compact support both in time and in frequency (since the Fourier transform of a Gaussian is also a Gaussian.) Due to the small and oscillatory nature of these window functions, Morlet named his functions as "wavelets of constant shape". In 1981, Morlet worked with Croatian–French physicist Alex Grossman on the idea that a function could be transformed by a wavelet basis and transformed back without loss of information, thereby outlining the wavelet transformation. It is of note that Morlet initially developed his ideas with nothing more than a handheld calculator.

In 1986, Stéphane Mallat noticed a publication by Yves Meyer that built on the concepts of Morlet and Grossman. Mallat consulted Meyer, and the result of said consultation was Mallat's publication of multiresolution analysis. Mallat's MRA connected wavelet transformations with the field of digital signal processing. Specifically, Mallat developed the wavelet transformation as a multiresolution approximation produced by a pair of digital filters. The scaling and wavelet functions that constitute a wavelet basis are represented by a pair of finite impulse response filters, and the wavelet transformation is computed as the convolution of these filters with the input function. The importance of Mallat's contribution cannot be overstated. Without the fast computational means of wavelet transformation provided by the MRA, then wavelets, undoubtedly, would not be the effective and widely used signal processing tools that they are today.

In 1988, a student of Alex Grossman, named Ingrid Daubechies, combined the ideas of Morlet, Grossman, Mallat, and Meyer by developing the first family of wavelets as they are known today. Named the Daubechies wavelets, the family consists of 8 separate wavelet and scaling functions (more on this later). With the development of pair Daubechies wavelet and scaling functions which are orthogonal, continuous, regular, and compactly supported, the foundations of the modern wavelet theory were laid. The last ten years mostly witnessed

a search for other wavelets with different properties and modifications of the MRA algorithms. In 1992, Albert Cohen, Jean Feauveau and Daubechies constructed the compactly supported biorthogonal wavelets, which are preferred by many researchers over the orthonormal basis functions, whereas R. Coifman, Meyer and Victor Wickerhauser developed wavelet packers, a natural extension of MRA.

3.3.2 *Multiresolution Analysis*

A suitable gateway to the theory of wavelets is through the idea of MRA. A detailed description of MRAs can be found in Keinert [197], from which a brief summary of the key issues are given in the following.

A multiresolution analysis is an infinite nested sequence of subspaces $L^2(\mathbb{R})$

$$V_j^0 \subset V_j^1 \subset \ldots \subset V_j^n \subset \ldots \tag{3.1}$$

with the following properties

- V_j^∞ is dense in L^2
- $f(x) \in V_j^n \iff f(2x) \in V_j^{n+1} \qquad 0 \leqslant n \leqslant \infty$
- $f(x) \in V_j^n \iff f(x - 2^{-n}l) \in V_j^n \,;\, 0 \leqslant l \leqslant (2^n - 1)$
- There exists a function vector φ of length $j+1$ in L^2 such that

  $$\{\varphi_j(x) : 0 \leqslant k \leqslant j\}$$

  forms a basis for V_j^0.

This means that if we can construct a basis of V_j^0, which consists of only $j+1$ functions, we can construct a basis of any space V_j^n, by simple compression (by a factor of 2^n), and translations (to all grid points at scale n), of the original $j+1$ functions, and by increasing the scale n, we are approaching a complete basis of L^2. Since $V_j^n \subset V_j^{n+1}$ the basis functions of V_j^n can be expanded in the basis of V_j^{n+1}

$$\varphi_l^n(x) \overset{\text{def}}{=} 2^{n/2}\varphi(2^n x - l) = \sum_l h^{(l)} \varphi_l^{n+1}(x)\,. \tag{3.2}$$

where the $h^{(l)}$s are the so-called filter vector that describes the transformation between different spaces V_j^n.

The MRA is called orthogonal if

$$\langle \varphi_0^n(x), \varphi_l^n(x) \rangle = \delta_{0l} I_{j+1}\,, \tag{3.3}$$

where I_{j+1} is the $(j+1) \times (j+1)$ unit matrix, and $j+1$ is the length of the function vector. The orthogonality condition means that the functions are orthogonal both within one function vector and through

all possible translations on one scale, but not through the different scales.

Complementary to the nested sequence of subspaces V_j^n, we can define another series of spaces W_j^n that complements V_j^n in V_j^{n+1}

$$V_j^{n+1} = V_j^n \oplus W_j^n \tag{3.4}$$

where there exists another function vector ϕ of length $j+1$ that, with all its translations on scale n forms a basis for W_j^n. Analogously to Eq. (3.2) the function vector can be expanded in the basis of V_j^{n+1}

$$\phi_l^n(x) \overset{\text{def}}{=} 2^{n/2}\phi(2^n x - l) = \sum_l g^{(l)}\phi_l^{n+1}(x)\,. \tag{3.5}$$

with filter matrices $g^{(l)}$. The functions ϕ also fulfill the same orthogonality condition as Eq. (3.3), and if we combine Eq. (3.1) and Eq. (3.4) we see that they must be orthogonal with respect to different scales. Using Eq. (3.4) recursively we obtain

$$V_j^n = V_j^0 \oplus W_j^0 \oplus W_j^1 \oplus \ldots \oplus W_j^{n-1}\,. \tag{3.6}$$

which will prove to be an important relation.

3.3.3 *Wavelets*

There are many ways to choose the basis functions φ and ϕ (which define the spanned spaces V_j^n and W_j^n), and there have been constructed functions with a variety of properties, and we should choose the wavelet family that best suits the needs of the problem we are trying to solve. (Wavelets are often denoted by ψ in the literature but the choice has been made here to denote them by ϕ so as to avoid confusion with the KS orbitals.) Otherwise, we could start from scratch and construct the new family, one that is custum-made for the problem at hand. Of course, this is not a trivial task, and it might prove more efficient to use an existing family, even though its properties are not right on cue.

There is a one-to-one correspondence between the basis functions φ and ϕ, and the filter matrices $h^{(l)}$ and $g^{(l)}$ used in the two-scale relation equations Eq. (3.2) and Eq. (3.5), and most well-known wavelet families are defined only through their filter coefficients.

In the following we are taking a different, more intuitive approach, for defining the *scaling space* V_j^n as the space of piecewise polynomial functions

$$\begin{aligned} V_j^n \overset{\text{def}}{=} \{f :\ & \text{all polynomials of degree} \leqslant j \\ & \text{on the interval} (2^{-n}l, 2^{-n}(l+1)) \\ & \text{for} 0 \leqslant l < 2^n, f \text{ vanishes elsewhere}\}\,. \end{aligned} \tag{3.7}$$

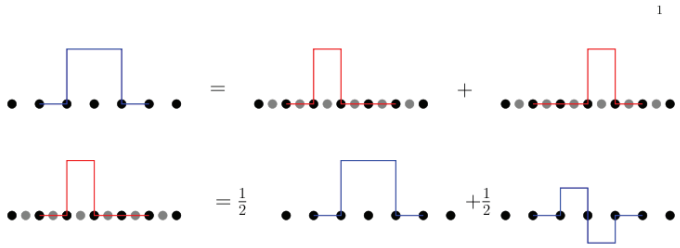

Figure 3.2: Wavelets (bottom) and scaling function (top).

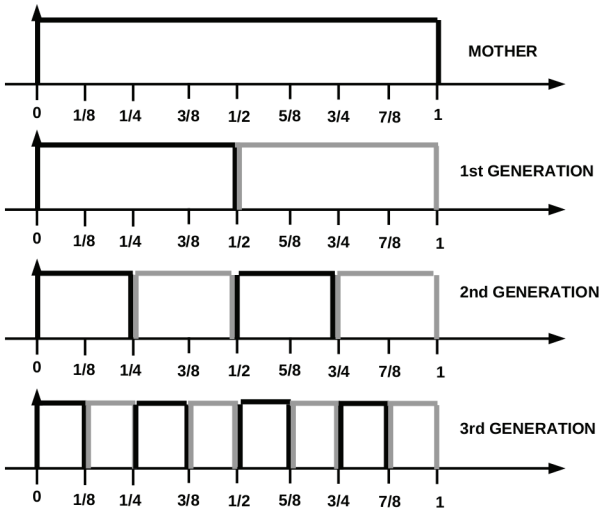

Figure 3.3: Haar scaling functions.

It is quite obvious that one polynomial of degree j on the interval $[0, 1]$ can be exactly reproduced by two polynomials of degree j, one on the interval $[0, \frac{1}{2}]$ and the other on the interval $[\frac{1}{2}, 1]$. The spaces V_j^n hence fulfills the MRA condition Eq. (3.1), and if the polynomial basis is chosen to be orthogonal, the V_j^n constitutes an orthogonal basis.

3.3.4 *An Example: Simple Haar Wavelets*

The basic wavelet ideas that we need can be easily explained using Haar wavelets [155]. These are simply the box functions shown in Fig. 3.3. We begin with a compact "mother scaling function", in this case the Haar function,

$$\varphi(x) = \begin{cases} 0 & ; \quad x > 1 \\ 1 & ; \quad 0 < x < 1 \\ 0 & ; \quad x < 0 \end{cases} . \tag{3.8}$$

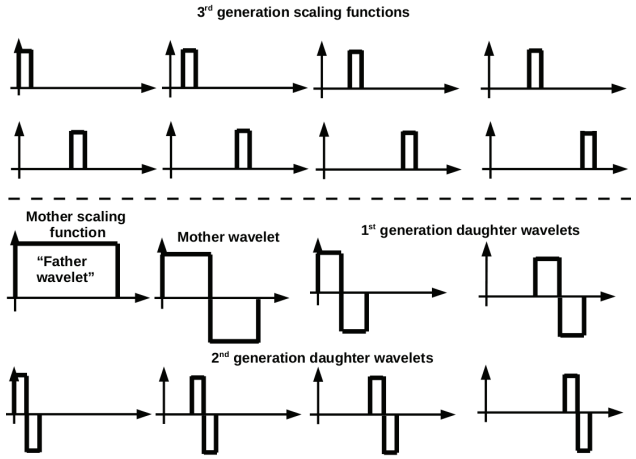

Figure 3.4: Haar scaling functions and the corresponding wavelets.

Translations, $\{\varphi_i(x) = \varphi(x-i)\}$, of this mother function produces a crude basis set. Its relation to the grid of integers is obvious. Successively more refined basis sets may be generated by repeated application of the scaling operation consisting of contracting the functions to half their size in the x direction. The kth generation of scaling function is given by $\left\{\varphi_i^{(k)}(x) = \varphi(2^k x - i)\right\}$. Each generation has a fixed resolution related to an underlying grid with the same resolution. Let us now try to construct a multiresolution basis set. This is accomplished by (say) beginning with the third generation wavelets and taking sums and differences of adjacent functions until the eight third generation scaling functions have been replaced with the eight wavelets shown in Fig. 3.4. Notice how each generation of daughter wavelets is related to the mother wavelet by scaling, $\phi_i^{(k)}(x) = \phi(2^k x - i)$. Notice also how the mother and two generations of daughter wavelets plus the mother scaling function (occasionally refered to as the "father wavelet") constitute a multiresolution basis set equivalent to the original third generation scaling basis set. Thus an arbitrary function, $f(x)$, expressible in the original scaling basis,

$$f(x) = \sum_{i=1}^{8} \varphi_i^{(3)}(x) s_i^{(3)}, \tag{3.9}$$

has the wavelet transform,

$$f(x) = \varphi_0^{(0)}(x) s_0^{(0)} + \phi_0^{(0)}(x) d_0^{(0)} + \sum_{i=0,1} \phi_i^{(1)}(x) d_i^{(1)} + \sum_{i=0,3} \phi_i^{(2)}(x) d_i^{(2)}. \tag{3.10}$$

Since the basis set is multiresolution, we may choose to add more grid points in some region of space and go locally to higher order wavelet expansions. It is also not always necessary to carry out a full

wavelet transform, but rather it may be useful to just carry out a partial transform giving a linear combination of wavelets with several scaling functions at a time. The extension to three dimensions is accomplished by using products of one-dimensional scaling functions and wavelets. Haar wavelets are just one type of wavelet basis set. It happens to be pedagogically useful but is not particularly useful for computations.

3.3.5 *Wavelet Basis*

The *wavelet space* W_j^n is defined, according to Eq. (3.4), as the orthogonal complement of V_j^n in V_j^{n+1}. The wavelet basis functions of W_j^n are hence piece-wise polynomials of degree $\leqslant j$ on each of the two intervals on scale $n+1$ that overlaps with one interval on scale n. These piece-wise polynomials are then made orthogonal to a basis of V_j^n and to each other. The construction of the wavelet basis follows exactly [16] where a simple Gram-Schmidt orthogonalization was employed to construct a basis that met the necessary orthogonality conditions.

One important property of the wavelet basis is the number of vanishing moments. The j-th continuous moment of a function ϕ is defined as the integrals

$$\mu_j \overset{\text{def}}{=} \int_0^1 x^j \phi(x) dx\,, \tag{3.11}$$

and the function ϕ has M vanishing moments if

$$\mu_j = 0, \quad k = 0, ..., M-1$$

The vanishing moments of the *wavelet* functions gives information on the approximation order of the *scaling* functions. If the wavelet function ϕ has M vanishing moments, any polynomial of order $\leqslant M-1$ can be exactly reproduced by the scaling function φ, and the error in representing an arbitrary function in the scaling basis is of M-th order. By construction, x^i is in the space V_j^0 for $0 \leqslant i \leqslant j$, and since $W_j^0 \perp V_j^0$, the first $k+1$ moments of ϕ_j^0 must vanish.

3.3.6 *The Scaling Basis*

The construction of the scaling functions is quite straightforward, $j+1$ suitable polynomials are chosen to span any polynomial of degree j on the unit interval. The total basis for V_j^n is then obtained by appropriate dilation and translation of these functions. Of course, any polynomial basis can be used, the simplest of them the standard basis $\{1, x, ..., x^j\}$. However, this basis is not orthogonal on the unit interval. In the following, two choices of orthogonal scaling functions will be

presented, and even though they span exactly the same spaces V_j^n there are some important numerical differences between the two.

In order to construct a set of orthogonal polynomials we could proceed in the same manner as for the wavelet functions and do a Gram-Schmidt orthogonalization of the standard basis $\{1, x, ..., x^j\}$. If this is done on the interval $x \in [-1, 1]$ we end up with the Legendre polynomials $\{L_k\}_{k=0}^j$. These functions are usually normalized such that $L_k(1) = 1$ for all j. To make the *Legendre scaling functions* φ_k^L we transform the Legendre polynomials to the interval $x \in [0, 1]$, and L^2 normalize

$$\varphi_k^L(x) = \sqrt{2k+1} L_k(2x-1), \quad x \in [0,1]\,. \tag{3.12}$$

The basis for the space V_j^n is then made by proper dilation and translation of φ_k^L. Alpert et al. [16] presented an alternative set of scaling functions with interpolating properties. These *interpolating scaling functions* φ_k^I are based on the Legendre scaling functions $\{\varphi_k^L\}_{k=0}^j$, and the roots $\{y_k\}_{k=0}^j$ and weights $\{w_k\}_{k=0}^j$ of the Gauss-Legendre quadrature of order $j+1$, and are organized in the linear combinations

$$\varphi_k^I(x) = \sqrt{w_k} \sum_{i=0}^{j_p} \varphi_i^L(y_k)\varphi_i^L(x), \quad x \in [0,1]\,, \tag{3.13}$$

Again the basis of V_j^n is made by dilation and translation of ϕ_k^I. The construction of φ_k^I gives them the interpolating property

$$\varphi_k^I(y_i) = \frac{\delta_{ki}}{\sqrt{w_i}}\,. \tag{3.14}$$

which will prove important for numerical efficiency.

A detailed discussion on the properties of interpolating wavelets can be found in Donoho [89], but the case of interpolating wavelets is somewhat different. An important property of interpolating wavelets is the smoothness of any function represented in this basis. This property stems from general Lagrange interpolation. In the wavelet case the interpolating property applies within one scaling function vector only, which means that functions represented in this basis can be discontinous in any merging point between the different translations on any scale.

3.3.7 *Interpolating Scaling Functions*

Since the general introduction to wavelets were already made, we will now concentrate our description on the level 3 interpolating scaling function (ISF) introduced by Deslauriers and Dubuc, and described in detail in Ref. [226]. Its main advantage is that it is fast and easy to perform nonlinear operations on functions represented in this basis,

as long as the operation is local in shape. It also represents 3rd order polynomials exactly which means that it behaves very smoothly.

We introduced the projection operator P^n that projects an arbitrary function $f(x)$ onto the basis $\{\varphi^n_{j,l}\}$ of the scaling space V^n (in the remaining of this text the subscript k of the scaling and wavelet spaces will be omitted, and it will always be assumed that we are dealing with a kth order polynomial basis.)

$$f(x) \approx P^n f(x) \underset{=}{\text{def}} f^n(x) = \sum_{l=0}^{2^n-1} \sum_{j=0}^{k} s^{n,f}_{j,l} \varphi^n_{j,l}(x)\,, \tag{3.15}$$

where the expansion coefficients $s^{n,f}_{j,l}$, the so-called *scaling* coefficients, are obtained by the usual integral

$$s^{n,f}_{j,l} \underset{=}{\text{def}} \langle f, \varphi^n_{j,l}\rangle = \int_0^1 f(x)\varphi^n_{j,l}(x)dx\,, \tag{3.16}$$

If this approximation turns out to be too crude, we double our basis set by increasing the scale and perform the projection P^{n+1}. This can be continued until we reach a scale N where we are satisfied with the overall accuracy of f^N relative to the true function f.

In a perfect world, the projection in Eq. (3.16) could be done exactly, and the accuracy of the projection would be independent of the choice of polynomial basis. In the real world the projections are done with Gauss-Legendre quadrature and the expansion coefficients $s^{n,f}_{j,l}$ of $f(x)$ are obtained as

$$\begin{aligned} s^{n,f}_{j,l} &= \int_{2^{-nl}}^{2^{-n(l+1)}} f(x)\varphi^n_{j,l}(x)dx \\ &= 2^{-n/2}\int_0^1 f(2^{-n}(x+l))\varphi^0_{j,0}(x)dx \\ &\approx 2^{-n/2}\sum_{q=0}^{k_q-1} w_q f(2^{-n}(y_q+l))\varphi^0_{j,0}(y_q) \end{aligned} \tag{3.17}$$

where $\{w_q\}_{q=0}^{k_q-1}$ are the weights and $\{y_q\}_{q=0}^{k_q-1}$ the roots of the Legendre polynomial L_{k_q} used in k_qth order quadrature.

By approximating this integral by quadrature we will of course not obtain the exact expansion coefficients. However, it would be nice if we could obtain the exact coefficients whenever our basis is flexible enough to reproduce the function exactly, that is if $f(x)$ is a polynomial of degree $\leqslant k$. The Legendre quadrature holds a $(2k-1)$ rule which states that the k-order quadrature is exact whenever the integrand is a polynomial of order $2k-1$. By choosing the $k_q = k+1$ order quadrature we will obtain the exact coefficient whenever $f(x)$ is a polynomial of degree $\leqslant (k+1)$ when projecting on the basis of orderk Legendre polynomials.

In the multidimensional (d-dimensional) case the expansion coefficients are given by multidimensional quadrature

$$s_{jl}^{nf} = 2^{-dn/2} \sum_{q_1=0}^{k} \sum_{q_2=0}^{k} \dots \sum_{q_d=0}^{k} f(2^{-n}(y_q + l)) \Pi_{i=1}^{d} w_{q_i} \varphi_{j_p,0}^{0}(y_{q_i}), \tag{3.18}$$

using the following notation for the vector of quadrature roots

$$y_q \underset{=}{\text{def}} (y_{q_1}, y_{q_2}, \dots, y_{q_d}), \tag{3.19}$$

This quadrature is not very efficient in multiple dimensions since the number of terms scales as $(k+1)^d$. However, if the function f is separable and can be written as $f(x_1, x_2, \dots, x_d) = f_1(x_1) f_2(x_2) \dots f_d(x_d)$, then Eq. (3.18) can be simplified to

$$s_{jl}^{nf} = 2^{-dn/2} \Pi_{i=1}^{d} \sum_{q_i=0}^{k} f_i(2^{-n}(y_{q_i} + l_i)) w_{q_i} \varphi_{j_i,0}^{0}(y_{q_i}), \tag{3.20}$$

which is a product of small summations and scales only as $d(k+1)$.

The Legendre polynomials show very good convergence for polynomial functions $f(x)$, and are likely to give more accurate projections. However, most interesting functions $f(x)$ are not simple polynomials, and the accuracy of the Legendre scaling functions versus a general polynomial basis might not be very different.

By choosing the quadrature order to be $k+1$ a very important property of the interpolating scaling functions emerges, stemming from the specific construction of these functions [Eq. (3.13)], and the use of the $k+1$ order quadrature roots and weights. The interpolating property [Eq. (3.14)] inserts a Kronecker delta whenever the scaling function is evaluated in a quadrature root, which is exactly the case in the quadrature sum. This reduces Eq. (3.17) to

$$s_{jl}^{n,f} = \frac{2^{-n/2}}{\sqrt{w_j}} f(2^{-n}(x_j + l)), \tag{3.21}$$

which obviously makes the projection $k+1$ times more efficient.

In multiple dimensions this property becomes even more important, since it effectively removes all the nested summations in Eq. (3.18) and leaves only one term in the projection

$$s_{jl}^{nf} = f(2^{-n}(y_j + l)) \Pi_{i=1}^{d} \frac{2^{-n/2}}{\sqrt{w_{j_i}}}, \tag{3.22}$$

This means that in the interpolating basis the projection is equally effective regardless of the separability of the function f.

3.4 DENSITY FUNCTIONAL THEORY

A method to resolve the electronic structure is by using variational principle

$$E[\Psi] = \frac{\langle \Psi | \hat{H} | \Psi \rangle}{\langle \Psi | \Psi \rangle}, \tag{3.23}$$

Where $\langle \Psi | \hat{H} | \Psi \rangle = \int d\mathbf{r} \Psi^*(\mathbf{r}) \hat{H} \Psi(\mathbf{r})$, Ψ denotes the electronic wave function and $\hat{H}$ the Hamiltonian. The energy computed from a guess Ψ is an upper bound to the true ground state energy E_0. Full minimization of the functional $E[\Psi]$ will give the true ground state Ψ^{gs} and energy $E_0 = E[\Psi^{gs}]$.

Density-functional theory states that the many electron problem can be replaced by an equivalent set of self-consistent one-electron equations, the Kohn-Sham equations

$$\hat{h}\psi_i^\sigma(\mathbf{r}) = \left(-\frac{1}{2}\nabla^2 + \hat{v}_{psp}(\mathbf{r}) + \hat{v}_H(\mathbf{r}) + \hat{v}_{xc}^\sigma(\mathbf{r}) \right) \psi_i^\sigma(\mathbf{r}) = \epsilon_i^\sigma \psi_i^\sigma(\mathbf{r}). \tag{3.24}$$

The eigenfunctions ψ_i^σ are the one-electron wave functions that correspond to the minimum of the KS energy functional. In these wave functions, i is the orbital index and σ denotes the spin, which can be either up $\uparrow$ or down $\downarrow$ (spin α or β.)

The Hamiltonian $\hat{H}$ consists of four different parts: a part related to the kinetic energy of the electrons, the pseudopotentials $\hat{v}_{psp}$, the Hartree potential $\hat{v}_H$ and the exchange correlation potential $\hat{v}_{xc}$. The interaction of the positively charged nuclei with the electrons is described using the pseudopotential $\hat{v}_{psp}$ instead of using the full Coulombic potential. The pseudopotential usually consists of both a local and a non-local part

$$\hat{v}_{psp}(\mathbf{r}) = v_{loc}(r) + \sum_l |l\rangle \hat{v}_l(r, r') \langle l|. \tag{3.25}$$

The Hartree potential $\hat{v}_H$ describes the interaction between electrons and is given by

$$\hat{v}_H(\mathbf{r}) = \int d\mathbf{r}' \frac{\rho_\uparrow(\mathbf{r}) + \rho_\downarrow(\mathbf{r}')}{|\mathbf{r} - \mathbf{r}'|}. \tag{3.26}$$

Finally, the exchange correlation potential $\hat{v}_{xc}$ describes the nonclassical interaction between the electrons and is given by the functional derivative of an exchange correlation energy functional

$$\hat{v}_{xc}^\sigma(\mathbf{r}) = \frac{\delta E_{xc}(\rho_\uparrow, \rho_\downarrow)}{\delta \rho_\sigma(\mathbf{r})}. \tag{3.27}$$

In these equations ρ^σ is the electron spin density, defined as

$$\rho_\sigma(\mathbf{r}) = \sum_i n_i^\sigma |\psi_i^\sigma(\mathbf{r})|^2, \tag{3.28}$$

where n_i^σ is the occupation number, i.e. the number of electrons in orbital *i*. In case of LDA (which we use throughout this chapter) where there is no longer a distinction between spin up and spin down, orbitals can contain at most two electrons.

3.5 TIME-DEPENDENT DENSITY FUNCTIONAL THEORY

This section contains a brief review of the basic formalism of TD-DFT which is already well-known from the literature [280]. The TD single particle KS equations are,

$$\left(-\frac{1}{2}\nabla^2 + v_{eff}[\rho](\mathbf{r},t)\right)\psi_{i\sigma}(\mathbf{r},t) = i\frac{\partial}{\partial t}\psi_{i\sigma}(\mathbf{r},t) \tag{3.29}$$

Here, the wave functions $\psi_i(\mathbf{r},t)$ and $v_{eff}[\rho](\mathbf{r},t)$ explicitly depend on time, whereas,

$$v_{eff}[\rho](\mathbf{r},t) = \sum_a v_{ion}(\mathbf{r}-\mathbf{R}_a) + \int \frac{\rho(\mathbf{r}',t)}{|\mathbf{r}-\mathbf{r}'|}d\mathbf{r}' + v_{xc}[\rho](\mathbf{r},t)\,. \tag{3.30}$$

Using the AA, (which is local in time)

$$\begin{aligned} v_{xc}[\rho](\mathbf{r},t) &\approx \frac{\delta E_{xc}[\rho_t]}{\delta\rho_t(\mathbf{r})} \\ \frac{\delta v_{xc}[\rho](\mathbf{r},t)}{\delta\rho(\mathbf{r}',t')} &\approx \delta(t-t')\frac{\delta^2 E_{xc}[\rho_t]}{\delta\rho_t(\mathbf{r})\delta\rho_t(\mathbf{r}')}\,, \end{aligned} \tag{3.31}$$

and using the LDA,

$$E_{xc}[\rho] = \int \rho(\mathbf{r})\epsilon_{xc}(\rho(\mathbf{r}))d\mathbf{r}\,. \tag{3.32}$$

The method that we wish to use here is Casida's approach [60]. This section explains the deriving equations of LR-TD-LDA method.

The TD perturbation to the external potential can be written as,

$$\delta v_{eff}[\rho](\mathbf{r},t) = \delta v_{appl}(\mathbf{r},t) + \delta v_{SCF}[\rho](\mathbf{r},t)\,, \tag{3.33}$$

where,

$$v_{SCF}[\rho](\mathbf{r},t) = \int \frac{\rho(\mathbf{r}',t)}{|\mathbf{r}-\mathbf{r}'|}d\mathbf{r}' + v_{xc}[\rho](\mathbf{r}',t)\,, \tag{3.34}$$

The LR of the density matrix (DM) can be written in terms of generalised susceptibility χ as below,

$$\delta\mathbf{P}_{ij\sigma}(\omega) = \sum_{kl\tau}\chi_{ij\sigma,kl\tau}(\omega)\delta v^{eff}_{kl\tau}(\omega)\,, \tag{3.35}$$

After some mathematical steps, one can end-up with the sum-over-states (SOS) representation of χ,

$$\chi_{ij\sigma,kl\tau}(\omega) = \delta_{ik}\delta_{jl}\delta_{\sigma\tau}\frac{\lambda_{lk\tau}}{\omega-(\omega_{kl\tau})}\,, \tag{3.36}$$

where $\lambda_{lk\tau} = n_{l\tau} - n_{k\tau}$ the difference in occupation numbers and $\omega_{kl\tau} = \epsilon_{k\tau} - \epsilon_{l\tau}$ the difference between the eigenvalues of kth and lth states. In the basis of KS orbitals $\{\psi_{i\sigma}\}$, we can re-write the LR-DM equation as,

$$\delta \mathbf{P}_{ij\sigma}(\omega) = \frac{\lambda_{ji\sigma}}{\omega - \omega_{ij\sigma}} \left[\delta v^{appl}_{ij\sigma}(\omega) + \delta v^{SCF}_{ij\sigma}(\omega)\right] \tag{3.37}$$

Now the term δv^{SCF} is complicated because it itself depends on the response of the DM.

$$\delta v^{SCF}_{ij\sigma}(\omega) = \sum \mathbf{K}_{ij\sigma,kl\tau} \delta \mathbf{P}_{kl\tau}(\omega)\,, \tag{3.38}$$

Where,

$$\mathbf{K}_{ij\sigma,kl\tau} = \frac{\partial v^{SCF}_{ij\sigma}}{\partial \mathbf{P}_{kl\tau}}\,, \tag{3.39}$$

whose integral form is,

$$\mathbf{K}_{ij\sigma,kl\tau} = \int\int \psi^*_{i\sigma}(\mathbf{r})\psi_{j\sigma}(\mathbf{r}) \quad \left[\frac{1}{|\mathbf{r}-\mathbf{r}'|} + \frac{\delta^2 E_{xc}[\rho]}{\delta\rho_\sigma(\mathbf{r})\delta\rho_\tau(\mathbf{r}')}\right] \psi_{k\tau}(\mathbf{r}')\psi^*_{l\tau}(\mathbf{r}')d\mathbf{r}d\mathbf{r}'\,, \tag{3.40}$$

If the response is due to a real spin-independent external perturbation, δv^{appl}, then we can restrict ourselves to the real density response and the coupling matrix is symmetric.

After some algebra, the real parts of the DM elements $\mathfrak{Re}\,\delta\mathbf{P}(\omega)$ can be given as,

$$\sum_{kl\tau}\left[\frac{\delta_{ik},\delta_{jl}\delta_{\sigma\tau}}{\lambda_{kl\tau}\omega_{lk\tau}}(\omega^2 - \omega^2_{lk\tau}) - 2\mathbf{K}_{ij\sigma,kl\tau}\right]\mathfrak{Re}\,(\delta\mathbf{P}_{kl\tau})(\omega) = \delta v^{appl}_{ij\sigma}(\omega) \tag{3.41}$$

Here the real part of $\mathfrak{Re}\,\delta\mathbf{P}_\sigma(\omega)$ means the Fourier transform of the real part of $\mathfrak{Re}\,\delta\mathbf{P}_\sigma(t)$. Thus the real part of the first-order DM obtained from the solution of the above linear equations gives access to the frequency-dependent polarizabilities. This leads to the following eigenvalue equation from which the excitation energies and oscillator strengths can be obtained.

$$\hat{\Omega}\vec{F}_I = \omega_I^2\vec{F}_I\,, \tag{3.42}$$

where,

$$\Omega_{ij\sigma,kl\tau} = \delta_{ik}\delta_{jl}\delta_{\sigma\tau}\omega^2_{kl\tau} + 2\sqrt{\lambda_{ij\sigma}\omega_{ji\sigma}}\mathbf{K}_{ij\sigma,kl\tau}\sqrt{\lambda_{kl\tau}\omega_{lk\tau}} \tag{3.43}$$

Here, the desired excitation energies are equal to ω_I and the oscillator strengths f_I are obtained from the eigenvectors $\vec{F}_I$. The frequency-dependent polarizability is directly related to vertical excitation energies, oscillator strength and transition dipole moments μ_I,

$$\alpha(\omega) = \sum_I \frac{f_I}{{\omega_I}^2 - \omega^2} = \frac{2}{3}\sum_I \frac{\omega_I\mu_I^2}{{\omega_I}^2 - \omega^2} \tag{3.44}$$

3.6 KRYLOV SPACE METHODS

The methods described in this article involve solving two very large eigenvalue problems. One of these is the matrix form of the KS orbital equation [Eq. (3.24)] while the other is the LR-TD-DFT equation [Eq. (3.42)]. The first is very large because the wavelet basis set is very large while the other is very large because it is of the order of the number of unoccupied orbitals times the number of unoccupied orbitals on each side. It is important to realize that special methods must be and are being used to solve these very large eigenvalue problems. In particular, BIGDFT make use of the block Davidson variant of the Krylov space method to solve the Kohn-Sham equation while BIGDFT and most other codes solving the LR-TD-DFT equation [Eq. (3.42)] also make use of the block Davidson method. Krylov methods and the block Davidson method are briefly described in this section.

Krylov space methods may be traced back to a paper in the early 1930s written by the Russian mathematician Alexei Nikolaevich Krylov. The main idea is that to solve a matrix problem involving a matrix $\mathbf{A}$, it is frequently never actually necessary to construct the matrix $\mathbf{A}$ because iterative solutions only require a reasonable first guess followed by repeated action of the *operator* $\hat{A}$ on a vector. A number of such methods are known with Lanczos diagonalization and the discret inversion in the iterative subspace (DIIS) [275] as particularly well-known examples in theoretical chemical physics. Given a vector $\vec{x}$, the Krylov space of order r is given by,

$$\mathcal{K}_r(\mathbf{A}, \vec{x}) = \text{span}\left\{\vec{x}, \mathbf{A}\vec{x}, \mathbf{A}^2\vec{x}, \cdots, \mathbf{A}^r\vec{x}\right\} . \tag{3.45}$$

The Davidson diagonalization method [92] for solving the matrix eigenvalue problem

$$\mathbf{A}\vec{x} = a\vec{x}, \tag{3.46}$$

is deceptively simple. Suppose that we want the lowest eigenvalue and eigenvector and we have an intial guess vector, $\vec{x}^{(0)}$. Then we can always write,

$$\vec{x} = \vec{x}^{(0)} + \delta\vec{x}, \tag{3.47}$$

is the component of the exact solution which is orthogonal to the intial guess vector. Simple algebra then gives a formula highly reminiscent of Rayleigh-Schrödinger perturbation theory but exact,

$$\delta\vec{x} = \left[\mathbf{Q}(a\mathbf{1} - \mathbf{A})\mathbf{Q}\right]^{-1}(\mathbf{A} - a\mathbf{1})\,\vec{x}^{(0)} , \tag{3.48}$$

where,

$$\mathbf{Q} = \mathbf{1} - \vec{x}^{(0)}\vec{x}^{(0)\dagger} , \tag{3.49}$$

projects onto the subspace orthogonal to the guess vector. Solving Eq. (3.48) requires us to overcome two difficulties. The first is that we need a guess for the eigenvalue a, but this is easily remedied by taking $a^{(0)} = \vec{x}^{(0)\dagger}\mathbf{A}\vec{x}^{(0)}/\vec{x}^{(0)\dagger}\vec{x}^{(0)}$ and then iterating. The greater problem is to invert the matrix $[\mathbf{Q}(a\mathbf{1} - \mathbf{A})\mathbf{Q}]$. It actually turns out that a highly accurate inversion is not really needed (and actually can cause some problems.) Instead it is better just to replace this difficult inversion with,

$$\delta\vec{x} = (a\mathbf{1} - \mathbf{D})^{-1}\,(\mathbf{A} - a\mathbf{1})\,\vec{x}^{(0)}\,, \tag{3.50}$$

where $\mathbf{D}$ is some diagonal matrix, hence easy to invert. Orthogonalizing $\delta\vec{x}$ to $\vec{x}^{(0)}$ and normalizing produces $\vec{x}^{(1)}$, which is the next basis vector in our Krylov space. Setting up and diagonalizing the 2×2 matrix of $\mathbf{A}$ in this basis and taking the lowest eigenvalue gives us the next estimate $a^{(1)}$. If application of Eq. (3.48) is close to zero then we have solved the eigenvalue problem Eq. (3.46), otherwise we have a new $\delta\vec{x}$ with which to generate $\vec{x}^{(2)}$ and so on and so forth until convergence. The block Davidson method [255] extends the Davidson method to the lowest several eigenvalues and eigenvectors.

Davidson diagonalization works well when started from a reasonably good initial guess, otherwise the Lanczos method may be advantageous. One of the most recent incarnations of the Lanczos method is the Liouville-Lanczos method for solving the LR-TD-DFT problem [321, 277, 33, 235].

3.7 NUMERICAL IMPLEMENTATION OF DFT IN BIGDFT

Computational physics/chemistry is the transformation and implementation of scientific theory into efficient algorithms which requires both theoretical and experimental skill. The transformation of a new theory into an efficient algorithm requires understanding of programming concepts, mathematical and physical intuition and theoretical insight, whereas the production of the computer code is much like experimentation, requiring debugging, testing and organisation to yield a highly efficient product. It is also an adaptation of new scientific theory into computer code exploiting the advances in compiler, programming language and hardware technology. The aim is to make an affordable algorithm to enable efficient computation, portability of code, ease of adaptability and to document the science. To make such an afforable algorithm requires an intuitive understanding of the physics to be implemented, much experimentation with optimisation and debugging of the developing code, a suitable choice of programming language, as well as a basic overview of the nature of the platforms for which the code is intended.

The KS scheme of DFT greatly reduces the complexity of ground state electronic structure calculations by recasting the many-body

problem into a (self-consistent) single-particle problem. For real atomistic modeling, however, the KS equations are still difficult to solve and further approximate techniques are required. In general it is important, though, that these approximations can be controlled in such a way that the associated error does not exceed (and indeed be much less than) the error introduced by the xc-functional. While DFT accounts for approximately 90% of all quantum chemical calculations being performed, the sometimes unpredictable nature of results and the inability to systematically improve the quality of calculation may mean that a place for the conventional correlated techniques remains in the quantum chemist's tool kit. In this work the detailed description of DFT program BIGDFT has been given. BIGDFT [2] has been developed as an European project (FP6-NEST) from 2005 to 2008, and is a wavelet-based pseudopotential implementation of DFT and TD-DFT. For complimentary purpose, Gaussian based quantum chemistry DFT code DEMON2K [9] is also used but we are not going to discuss the numerical implementation of DEMON2K here and we restrict ourselves to use DEMON2K for validating our recent implementation of LR-TD-DFT in BIGDFT. However in the following sections, we are going to recast how the fundamental computational operations were performed in BIGDFT.

3.7.1 *Daubechies Wavelets*

Before embarking on our own endeavours, we should make some reference to related work. First, it should be acknowledged that a considerable amount of work has been done already in pursuit of a wavelet implementation for the electronic structure calculations [132, 133, 134, 136, 95, 137]. The object of using wavelets as a basis set is to associate an expansion coefficient to each of the piece-wise wavelets. The expansion coefficients are free to vary from one wavelet function to the next. This feature enables wavelets to be highly localised continuous functions of a fractal nature with finite supports. The Daubechies wavelets have no available analytic forms, and they are not readily available in sampled versions. They are defined effectively by the associated dilation coefficients. These express a wavelet in high resolution and a scaling function in the low resolution–which has the same width and which stretches to zero–as a linear combination of the more densely packed and less dispersed scaling functions that form a basis for the two resolution level in combination.

The fact that the Daubechies wavelets are known only via their dilation coefficients is no impediment to the discrete wavelet transform. This transform generates the expansion coefficients associated with the wavelet decomposition of a data sequence. In this perspective, the dilation coefficients of the wavelets and of the associated scaling

functions are nothing but the coefficients of a pair of quadrature mirror filters that are applied succesively.

As described above Daubechies family consists of two fundamental functions: the scaling function $\phi(x)$ and the wavelet $\varphi(x)$ (see Fig. 3.5.) The full basis set can be obtained from all translations by a certain grid spacing h of the scaling and wavelet functions centered at the origin. These functions satisfy the fundamental defining (refinement) equations,

$$\begin{aligned} \phi(x) &= \sqrt{2} \sum_{j=1-m}^{m} h_j \phi(2x-j)\,, \\ \varphi(x) &= \sqrt{2} \sum_{j=1-m}^{m} g_j \phi(2x-j)\,. \end{aligned} \tag{3.51}$$

which relate the basis functions on a grid with spacing h and another one with spacing $h/2$. The coefficients, h_j and g_j, consitute the so-called "filters" which define the wavelet family of order m. These coefficients satisfy the relations, $\sum_j h_j = 1$ and $g_j = (-1)^j h_{-j+1}$. Eq. (3.51) is very important since it means that a scaling-function basis defined over a fine grid of spacing $h/2$ may be replaced by combining a scaling-function basis over a coarse grid of spacing h with a wavelet basis defined over the fine grid of spacing h. This then gives us the liberty to begin with a coarse description in terms of scaling functions and then add wavelets only where a more refined description is needed. In principle the refined wavelet description may be further refined by adding higher-order wavelets where needed. However in BIGDFT we restricted ourselves to just two levels: coarse and fine associated respectively with scaling functions and wavelets.

For a three-dimensional description, the simplest basis set is obtained by a tensor product of one-dimensional basis functions. For a two resolution level description, the coarse degrees of freedom are expanded by a single three dimensional function, $\phi^0_{i_1,i_2,i_3}(\mathbf{r})$, while the fine degrees of freedom can be expressed by adding another seven basis functions, $\phi^\nu_{j_1,j_2,j_3}(\mathbf{r})$, which include tensor products with one-dimensional wavelet functions. Thus, the Kohn-Sham wave function $\psi(\mathbf{r})$ is of the form

$$\psi(\mathbf{r}) = \sum_{i_1,i_2,i_3} c^0_{i_1,i_2,i_3} \phi^0_{i_1,i_2,i_3}(\mathbf{r}) + \sum_{j_1,j_2,j_3} \sum_{\nu_1}^{7} c^\nu_{j_1,j_2,j_3} \phi^\nu_{j_1,j_2,j_3}(\mathbf{r})\,. \tag{3.52}$$

The sum over i_1,i_2,i_3 runs over all the grid points contained in the low-resolution regions and the sum over j_1,j_2,j_3 runs over all the points contained in the (generally smaller) high-resolution regions. Each wave function is then described by a set of coefficients $\{c^\nu_{j_1,j_2,j_3}\}$, $\nu = 0,...,7$. Only the nonzero scaling function and wavelet coefficients are

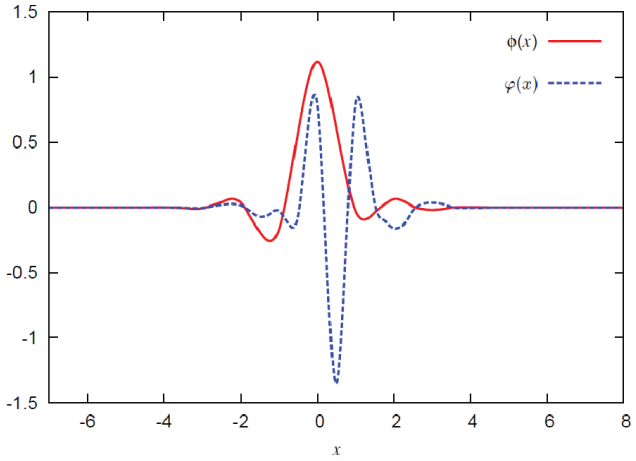

Figure 3.5: Daubechies scaling function $\phi(x)$ and wavelet $\varphi(x)$ of order 16.

stored. The data is thus compressed. The basis set being orthogonal, several operations such as scalar products among different orbitals and between orbitals and the projectors of the nonlocal pseudopotential can be directly carried out in this compressed form.

3.7.2 *Treatment Of Kinetic Energy*

The matrix elements of the kinetic energy operator among the basis functions of our mixed representation (i.e., scaling functions with scaling functions, scaling function with wavelets and wavelets with wavelets) can be calculated analytically [43]. For simplicity, let us illustrate the application of the kinetic energy operator onto a wavefunction ψ that is only expressed in terms of scaling functions.

$$\psi(x,y,z) = \sum_{i_1,i_2,i_3} s_{i_1,i_2,i_3}\phi(x/h-i_1)\,\phi(y/h-i_2)\,\phi(z/h-i_3)$$

The result of the application of the kinetic energy operator on this wavefunction, projected to the original scaling function space, has the expansion coefficients

$$\hat{s}_{i_1,i_2,i_3} = -\frac{1}{2h^3}\int \phi(x/h-i_1)\,\phi(y/h-i_2)\,\phi(z/h-i_3)\times \\ \times\nabla^2\psi(x,y,z)\mathrm{d}x\mathrm{d}y\mathrm{d}z\,.$$

Analytically the coefficients s_{i_1,i_2,i_3} and $\hat{s}_{i_1,i_2,i_3}$ are related by a convolution

$$\hat{s}_{i_1,i_2,i_3} = \frac{1}{2}\sum_{j_1,j_2,j_3} K_{i_1-j_1,i_2-j_2,i_3-j_3}s_{j_1,j_2,j_3} \tag{3.53}$$

where

$$K_{i_1,i_2,i_3} = T_{i_1}T_{i_2}T_{i_3}, \tag{3.54}$$

where the coefficients T_i can be calculated analytically via an eigenvalue equation:

$$\begin{aligned} T_i &= \int \phi(x) \frac{\partial^2}{\partial x^2} \phi(x-i) dx \\ &= \sum_{\nu,\mu} 2h_\nu h_\mu \int \phi(2x-\nu) \frac{\partial^2}{\partial x^2} \phi(2x-2i-\mu) dx \\ &= \sum_{\nu,\mu} 2h_\nu h_\mu 2^{2-1} \int \phi(y-\nu) \frac{\partial^2}{\partial y^2} \phi(y-2i-\mu) dy \\ &= \sum_{\nu,\mu} h_\nu h_\mu 2^2 \int \phi(y) \frac{\partial^2}{\partial y^2} \phi(y-2i-\mu+\nu) dy \\ &= \sum_{\nu,\mu} h_\nu h_\mu \, 2^2 \, T_{2i-\nu+\mu} \end{aligned}$$

Using the refinement equation Eq. (3.51), the values of the T_i can be calculated analytically, from a suitable eigenvector of a matrix derived from the wavelet filters [43]. For this reason the expression of the kinetic energy operator is *exact* in a given Daubechies basis.

Since the 3-dimensional kinetic energy filter K_{i_1,i_2,i_3} is a product of three one-dimensional filters Eq. (3.54) the convolution in Eq. (3.53) can be evaluated with $3N_1N_2N_3L$ operations for a three-dimensional grid of $N_1N_2N_3$ grid points. L is the length of the one-dimensional filter which is 29 for our Daubechies family. The kinetic energy can thus be evaluated with linear scaling with respect to the number of nonvanishing expansion coefficients of the wavefunction. This statement remains true for a mixed scaling function-wavelet basis where we have both nonvanishing s and d coefficients and for the case where the low and high resolution regions cover only parts of the cube of $N_1N_2N_3$ grid points.

3.7.3 *Treatment Of Local Potential Energy*

In spite of the striking advantages of Daubechies wavelets the initial exploration of this basis set [315] did not lead to any algorithm that would be useful for practical electronic structure calculations. This was due to the fact that an accurate evaluation of the local potential energy is difficult in a Daubechies wavelet basis.

By definition, the local potential $v(\mathbf{r})$ can be easily known on the nodes of the uniform grid of the simulation box. Approximating a potential energy matrix element $v_{i,j,k;i',j',k'}$

$$v_{i,j,k;i',j',k'} = \int d\mathbf{r} \phi_{i',j',k'}(\mathbf{r}) v(\mathbf{r}) \phi_{i,j,k}(\mathbf{r})$$

by

$$v_{i,j,k;i',j',k'} \approx \sum_{l,m,n} \phi_{i',j',k'}(\mathbf{r}_{l,m,n}) v(\mathbf{r}_{l,m,n}) \phi_{i,j,k}(\mathbf{r}_{l,m,n})$$

gives an extremely slow convergence rate with respect to the number of grid points used to approximate the integral because a single scaling function is not very smooth, i.e., it has a rather low number of continuous derivatives. A. Neelov and S. Goedecker [257] have shown that one should not try to approximate a single matrix element as accurately as possible but that one should try instead to approximate directly the expectation value of the local potential. The reason for this strategy is that the wavefunction expressed in the Daubechy basis is smoother than a single Daubechies basis function. A single Daubechies scaling function of order 16 (i.e., the corresponding wavelet has 8 vanishing moments) has only 2 continuous derivatives. More precisely its index of Hölder continuity is about 2.7 and the Sobolev space regularity with respect to $p = 2$ is about 2.91 [213]. A single Daubechies scaling function of order 16 has only 4 continuous derivatives. By suitable linear combinations of Daubechies 16 one can however exactly represent polynomials up to degree 7, i.e., functions that have 7 non-vanishing continuous derivatives. The discontinuities get thus canceled by taking suitable linear combinations. Since we use pseudopotentials, our exact wavefunctions are analytic and can locally be represented by a Taylor series. We are thus approximating functions that are approximately polynomials of order 7 and the discontinuities nearly cancel.

Instead of calculating the exact matrix elements we therefore use matrix elements with respect to a smoothed version $\tilde{\phi}$ of the Daubechies scaling functions.

$$\begin{aligned} v_{i,j,k;i',j',k'} &\approx \sum_{l,m,n} \tilde{\phi}_{i',j',k'}(\mathbf{r}_{l,m,n}) v(\mathbf{r}_{l,m,n}) \tilde{\phi}_{i,j,k}(\mathbf{r}_{l,m,n}) \\ &= \sum_{l,m,n} \tilde{\phi}_{0,0,0}(\mathbf{r}_{l-i',m-j',n-k'}) v(\mathbf{r}_{l,m,n}) \\ &\quad \tilde{\phi}_{0,0,0}(\mathbf{r}_{l-i,m-j,n-k}) \end{aligned} \tag{3.55}$$

where the smoothed wave function is defined by

$$\tilde{\phi}_{0,0,0}(\mathbf{r}_{l,m,n}) = \omega_l \omega_m \omega_n$$

and ω_l is the "magic filter". Even though Eq. (3.55) is not a particulary good approximation for a single matrix element it gives an excellent approximation for the expectation values of the local potential energy

$$\int dx \int dy \int dz \psi(x,y,z) v(x,y,z) \psi(x,y,z)$$

and also for matrix elements between different wavefunctions

$$\int dx \int dy \int dz \psi_i(x,y,z) v(x,y,z) \psi_j(x,y,z)$$

in case they are needed. Because of this remarkable achievement of the filter ω we call it the magic filter.

Following the same guidelines as the kinetic energy filters, the smoothed real space values $\tilde{\psi}_{i,j,k}$ of a wavefunction ψ are calculated by performing a product of three one-dimensional convolutions with the magic filters along the x, y and z directions. For the scaling function part of the wavefunction the corresponding formula is

$$\tilde{\psi}_{i_1,i_2,i_3} = \sum_{j_1,j_2,j_3} s_{j_1,j_2,j_3} v^{(1)}_{i_1-2j_1} v^{(1)}_{i_2-2j_2} v^{(1)}_{i_3-2j_3}$$

where $v^{(1)}_i$ is the filter that maps a scaling function on a double resolution grid. Similar convolutions are needed for the wavelet part. The calculation is thus similar to the treatment of the Laplacian in the kinetic energy.

Once we have calculated $\tilde{\psi}_{i,j,k}$ the approximate expectation value ϵ_V of the local potential v for a wavefunction ψ is obtained by simple summation on the double resolution real space grid:

$$\epsilon_v = \sum_{j_1,j_2,j_3} \tilde{\psi}_{j_1,j_2,j_3} v_{j_1,j_2,j_3} \tilde{\psi}_{j_1,j_2,j_3}$$

3.7.4 *Treatment Of The Non-Local Pseudopotential*

The energy contributions from the non-local pseudopotential have for each angular moment l the form

$$\sum_{i,j} \langle \psi | p_i \rangle h_{ij} \langle p_j | \psi \rangle$$

where $|p_i\rangle$ is a pseudopotential projector. Once applying the Hamiltonian operator, the application of one projector on the wavefunctions requires the calculation of

$$|\psi\rangle \to |\psi\rangle + \sum_{i,j} |p_i\rangle h_{ij} \langle p_j | \psi \rangle \, .$$

If we use for the projectors the representation of Eq. (3.52) (i.e., the same as for the wavefunctions) both operations are trivial to perform. Because of the orthogonality of the basis set we just have to calculate scalar products among the coefficient vectors and to update the wavefunctions. The scaling function and wavelet expansion coefficients for the projectors are given by [139]

$$\int p(\mathbf{r}) \, \phi_{i_1,i_2,i_3}(\mathbf{r}) d\mathbf{r} \, , \quad \int p(\mathbf{r}) \, \varphi^{\gamma}_{i_1,i_2,i_3}(\mathbf{r}) d\mathbf{r} \, . \tag{3.56}$$

The Goedecker-Teter-Hutter (GTH) Hartwigsen-Goedecker-Hutter (HGH) pseudopotentials [141, 142] have projectors which are written in terms of gaussians times polynomials. This form of projectors is

particularly convenient for expansion in the Daubechies basis. In other terms, since the general form of the projector is

$$\langle \mathbf{r}|p\rangle = e^{-cr^2} x^{\ell_x} y^{\ell_y} z^{\ell_z} ,$$

the 3-dimensional integrals can be calculated easily since they can be factorized into a product of 3 one-dimensional integrals.

$$\int \langle \mathbf{r}|p\rangle \phi_{i_1,i_2,i_3}(\mathbf{r}) d\mathbf{r} = W_{i_1}(c,\ell_x) W_{i_2}(c,\ell_y) W_{i_3}(c,\ell_x) , \quad (3.57)$$

$$W_j(c,\ell) = \int_{-\infty}^{+\infty} e^{-ct^2} t^{\ell} \phi(t/h - j) dt \quad (3.58)$$

The one-dimensional integrals are calculated in the following way. We first calculate the scaling function expansion coefficients for scaling functions on a one-dimensional grid that is 16 times denser. The integration on this dense grid is done by the well-known quadrature introduced in [188], that coincides with the magic filter [257]. This integration scheme based on the magic filter has a convergence rate of h^{16} and we gain therefore a factor of 16^{16} in accuracy by going to a denser grid. This means that the expansion coefficients are for reasonable grid spacings h accurate to machine precision. After having obtained the expansion coefficients with respect to the fine scaling functions we obtain the expansion coefficients with respect to the scaling functions and wavelets on the required resolution level by one-dimensional fast wavelet transformations. No accuracy is lost in the wavelet transforms and our representation of the projectors is therefore typically accurate to nearly machine precision. In order to treat with the same advantages other pseudopotentials which are not given under the form of gaussians it would be necessary to approximate them by a small number of gaussians.

3.7.5 *The Poisson Operator*

Solving the Poisson equation for an arbitrary charge distribution is a non-trivial task, and is of major importance in many field of science, especially in the field of computational chemistry. A huge effort has been put into making efficient Poisson solvers, and usual real-space approaches include FD and finite element (FE) methods. FD is a grid-based method, which is solving the equations iteratively on a discrete grid of points, while FE is expanding the solution in a basis set, usually by dividing space into cubic cells and allocating a polynomial basis to each cell.

It is well-known fact that the electronic density in molecular systems is rapidly varying in the vicinity of the atomic nuclei, and a usual problem with real-space methods is that an accurate treatment of the system requires high resolution of grid points (FD) or cells (FE) in

the nuclear regions. Keeping this high resolution uniformly throughout space is overkill in the interatomic regions, and the solution of the Poisson equation for molecular systems requires a *multiresolution* framework in order to achieve numerical efficiency. This chapter is concerned with a way of doing DFT and TD-DFT calculations, one where the multiresolution character is inherent in the theory, namely using wavelet bases.

In order to evaluate the Hartree potential, we need to rewrite the standard Poisson equation in integral form. The equation, in its differential form, is given as

$$\nabla^2 v(\mathbf{x}) = 4\pi\rho(\mathbf{x}), \tag{3.59}$$

where $\rho(\mathbf{x})$ is the known (charge) distribution, and $v(\mathbf{x})$ is the unknown (electrostatic) potential. It is a standard textbook procedure to show that the solution can be written as the integral

$$v(\mathbf{x}) = \int G(\mathbf{x},\mathbf{y})\rho(\mathbf{y})d\mathbf{y}, \tag{3.60}$$

where $G(\mathbf{x},\mathbf{y})$ is the Green's function which is the solution to the *fundamental* equation with *homogeneous* (Dirichlet) boundary conditions

$$\begin{aligned} \nabla^2 G(\mathbf{x},\mathbf{y}) &= \delta(\mathbf{x}-\mathbf{y}) \\ G(\mathbf{x},\mathbf{y}) &= 0\,, \mathbf{x} \in \text{boundary} \end{aligned} \tag{3.61}$$

This equation can be solved analytically and the Green's function is given (in three dimensions) simply as

$$G(\mathbf{x},\mathbf{y}) = \frac{1}{\|\mathbf{x}-\mathbf{y}\|}, \tag{3.62}$$

This is the well-known potential arising from a point charge located in the position $\mathbf{y}$, which is exactly what Eq. (3.61) describes.

3.7.6 *Numerical Separation Of The Kernel*

The Green's function kernel as it is given in Eq. (3.62) is not separable in the cartesian coordinates. However, since we are working with finite precision we can get by with an *approximate* kernel as long as the error introduced with this approximation is less than our overall accuracy criterion. If we are able to obtain such a *numerical* separation of the kernel, the operator can be applied in one direction at a time, allowing us to use the expressions derived above for one-dimensional integral operators to solve the three-dimensional Poisson equation. This is of great importance because it reduces the scaling behavior to linear in the dimension of the system.

The Poisson kernel can be made separable by expanding it as a sum of Gaussian functions, specifically

$$\frac{1}{r} \simeq \sum_{k=1}^{M_\epsilon} \omega_k e^{-p_k r^2}. \tag{3.63}$$

where ω_k and p_k are parameters that needs to be determined, and the number of terms M_ϵ, called the separation rank, depends on the accuracy requirement and on what interval this expression needs to be valid. Details of how to obtain this expression can be found in [132, 133], and will not be treated here, but it should be mentioned that the separation rank is usually in the order of 100, e.g, it requires $M_\epsilon = 89$ to reproduce $\frac{1}{r}$ on the interval $[10^{-9}, 1]$ in three dimensions with error less than $\epsilon = 10^{-8}$.

Finally, figure 3.6 summarizes this complete section into a flow-chart type diagram. This kind of explanation is necessary for beginners because there are different functions used for the different operations in BIGDFT. As one can see from the figure, The KS wavefunctions $|\psi\rangle$ are expressed in terms of Daubechies wavelets and the projection of Hamiltonian $v_{nl}|\psi\rangle$ and of pseudopotential operators $|H\psi\rangle$ also expressed using Daubechies wavelets. The rest of the operations such as kinetic energy $|\nabla^2\psi\rangle$, potential energy operator $v(x)\psi(x)$, and the local densities $\rho(x)$ are all expressed using interpolating scaling functions, in which the Hartree $v_H(x)$, local part potential energy $v_{loc}(x)$ and xc operations $v_{xc}(x)$ were performed in real space. The interconnecting lines between different operations represents the transformation between Daubechies wavelets-to-ISF or the transformation of real space-to-fourier space representation.

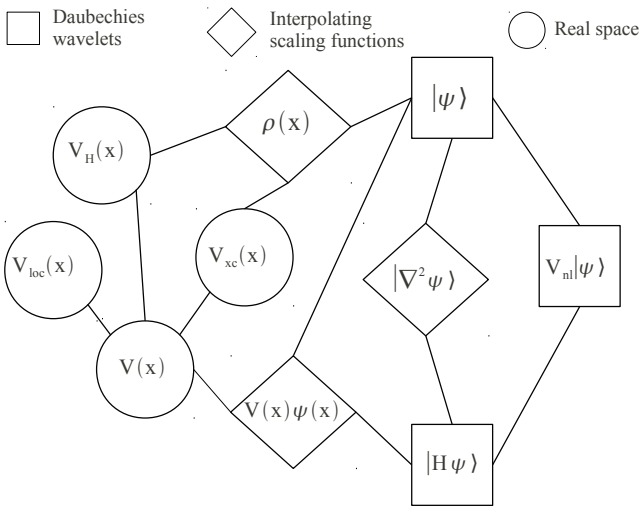

Figure 3.6: Operations performed in BIGDFT

3.8 BIGDFT AND TD-DFT

We want to solve Casida's equation [60],

$$\left[\begin{pmatrix} \mathbf{A}(\omega) & \mathbf{B}(\omega) \\ \mathbf{B}^*(\omega) & \mathbf{A}^*(\omega) \end{pmatrix} - \omega \begin{pmatrix} 1 & 0 \\ 0 & -1 \end{pmatrix}\right] \begin{pmatrix} \vec{X} \\ \vec{Y} \end{pmatrix} = 0\,, \qquad (3.64)$$

where $\vec{X}$ and $\vec{Y}$ represents the pseudoeigenvectors; the matrices **A** and **B** are defined as

$$\mathbf{A}_{ai\sigma,bj\tau} = \delta_{ab}\delta_{ij}\delta_{\sigma\tau}(\epsilon_a - \epsilon_i) + \mathbf{K}_{ai\sigma,bj\tau}(\omega)\,, \tag{3.65}$$

and,

$$\mathbf{B}_{ai\sigma,bj\tau} = \mathbf{K}_{ai\sigma,jb\tau}(\omega)\,, \tag{3.66}$$

in which the integral form of the coupling matrix **K** is given by,

$$\mathbf{K}_{pq\sigma,rs\tau} = \int\int \Psi^*_{p\sigma}(\vec{r})\Psi_{q\sigma}(\vec{r}) \left[\frac{1}{|\vec{r}-\vec{r}'|} + \frac{\partial^2 E_{xc}[\rho]}{\partial\rho_\sigma(\vec{r})\partial\rho_\tau(\vec{r}')}\right]\Psi_{r\tau}(\vec{r}')\Psi^*_{s\tau}(\vec{r}')d\vec{r}d\vec{r}'\,. \tag{3.67}$$

The universal adiabatic approximation is applied to Eq. (3.67) to remove the frequency dependence of the kernel.

The electronic transitions occur with an infinitesimal perturbation obtains the above described non-Hermitian eigenvalue Eq. (3.64). Where the response is due to a real spin independent external perturbation, and the actual response is described as the real density response. However, an unitary transformation is necessary to convert Eq. (3.64) into the real eiganvalue problem. In Eq. (3.64), all occupied-occupied and virtual-virtual element contributions are zero whereas only the elements that are from virtual-occupied and occupied-virtual parts are taken into account. Moreover if we only restricted to virtual-occupied elements and neglecting the occupied-virtual elements of Eq. (3.64) leads to a Hermitian eigenvalue equation of the dimension one-half of that TD-DFT working equation is said to be TDA and it is written as,

$$\mathbf{A}\vec{X} = \omega\vec{X}\,, \tag{3.68}$$

where **A** is as same as in Eq. (3.42). The matrix **A** is just restricted to number of single excitations.

3.8.1 *Calculation Of Coupling Matrix*

We are now in a position to understand the construction of the coupling matrix Eq. (3.67) in our implementation of TD-DFT in BIGDFT, which we split into the Hartree and xc parts,

$$\mathbf{K}_{ai\sigma,bj\tau} = \mathbf{K}^{H}_{ai\sigma,bj\tau} + \mathbf{K}^{xc}_{aj\sigma,bj\tau}\,. \tag{3.69}$$

Instead of calculating the Hartree part of coupling matrix directly as,

$$\mathbf{K}^{H}_{ai\sigma,bj\tau} = \int\int \psi^*_{a\sigma}(\mathbf{r})\psi_{i\sigma}(\mathbf{r})\frac{1}{|\mathbf{r}-\mathbf{r}'|}\psi_{b\tau}(\mathbf{r}')\psi^*_{j\tau}(\mathbf{r}')\,d\mathbf{r}d\mathbf{r}'\,, \tag{3.70}$$

we express the coupling matrix element as,

$$\mathbf{K}^{H}_{ai\sigma,bj\tau} = \int \psi^{*}_{a\sigma}(\mathbf{r})\psi_{i\sigma}(\mathbf{r})v_{bj\tau}(\mathbf{r})\,d\mathbf{r}\,, \tag{3.71}$$

where,

$$v_{ai\sigma}(\mathbf{r}) = \int \frac{\rho_{ai\sigma}(\mathbf{r})}{|\mathbf{r}-\mathbf{r}'|}\,d\mathbf{r}'\,, \tag{3.72}$$

and,

$$\rho_{ai\sigma}(\mathbf{r}) = \psi^{*}_{a\sigma}(\mathbf{r})\psi_{i\sigma}(\mathbf{r})\,. \tag{3.73}$$

The advantage of doing this is that, although $\rho_{ai\sigma}$ and $v_{ai\sigma}$ are neither real physical charge densities nor real physical potentials, they still satisfy the Poisson equation,

$$\nabla^2 v_{ai\sigma}(\mathbf{r}) = -4\pi\rho_{ai\sigma}(\mathbf{r})\,, \tag{3.74}$$

and we can make use of whichever of the efficient wavelet-based Poisson solvers already available in BIGDFT, is appropriate for the boundary conditions of our physical problem.

Once the solution of Poisson's equation, $v_{ai\sigma}(\mathbf{r})$, is known, we can then calculate the Hartree part of the kernel according to Eq. (3.71). Inclusion of the xc kernel is accomplished by evaluating,

$$K_{ai\sigma,bj\tau} = \int M_{ai\sigma}(\mathbf{r})\rho_{bj\tau}(\mathbf{r})\,d\mathbf{r}\,, \tag{3.75}$$

where,

$$M_{ai\sigma}(\mathbf{r}) = v_{ai\sigma}(\mathbf{r}) + \int \rho_{ai\sigma}(\mathbf{r}')f^{\sigma,\tau}_{xc}(\mathbf{r},\mathbf{r}')\,d\mathbf{r}'\,. \tag{3.76}$$

We note that $f^{\sigma,\tau}_{xc}(\mathbf{r},\mathbf{r}') = f^{\sigma,\tau}_{xc}(\mathbf{r},\mathbf{r}')\delta(\mathbf{r}-\mathbf{r}')$ for the LDA, so that no integral need actually be carried out in evaluating $M_{ai\sigma}(\mathbf{r})$. The integral in Eq. (3.75) is, of course, carried out numerically in practice as a discrete summation.

3.9 RESULTS

We now wish to illustrate a bit how wavelet calculations work in the BIGDFT program. Comparison will be made against results obtained with the GTO-based program DEMON2K. This work is very similar to our previous work reporting the first implementation of wavelet-based TD-DFT with illustration for N_2 and application to the absorption spectrum of a medium-sized organic molecule of potential biomedical use as a fluorescent probe [256]. Here however we will present new BIGDFT results for a different small molecule, namely carbon monoxide. Though CO is roughly isoelectronic with N_2, CO has the interesting feature of having a low-lying bright state in its absorption spectrum.

3.9.1 *Computational Details*

Calculations were carried out with DEMON2K and BIGDFT with the LDA-optimized bond length of 1.129 Å.

3.9.1.1 DEMON2K

DEMON2K resembles a typical GTO-based quantum chemistry program in that all the integrals other than the xc-integrals, can be evaluated analytically. In particular, DEMON2K has the important advantage that it accepts the popular GTO basis sets common in quantum chemistry and so can benefit from the experience in basis set construction of a large community built up over the past 50 years or so. In the following, we have chosen to use the well-known correlation-consistent basis sets for this study [114, 285]. (Note, however, that the correlation-consistent basis sets used in DEMON2K lack f and g functions but are otherwise exactly the same as the usual ones.) The advantage of using these particular basis sets is that there is a clear hierarchy as to quality.

An exception to the rule that integrals are evaluated analytically in DEMON2K are the xc-integrals (for the xc-energy, xc-potential, and xc-kernel) which are evaluated numerically over a Becke atom-centered grid. This is important because the relative simplicity of evaluating integrals over a grid has allowed the rapid implemenation of new functionals as they were introduced. We made use of the fine fixed grid in our calculations.

As described so far, DEMON2K should have $\mathcal{O}(N^4)$ scaling because of the need to evaluate 4-center integrals. Instead DEMON2K uses a second atom-centered auxiliary GTO basis to expand the charge density. This allows the the elimination of all 4-center integrals so that only 3-center integrals remain for a formal $\mathcal{O}(N^3)$ scaling. In practice, integral prescreening leads to $\mathcal{O}(N^M)$ scaling where M is typically between 2 and 3. We made use of the A3 auxiliary basis set from the DEMON2K automated auxiliary basis set library.

All calculations were performed using standard DEMON2K default criteria. The implementation of TD-DFT in DEMON2K is described in Ref. [181]. (The charge density conservation constraint is no longer used in DEMON2K TD-DFT calculations.) Although full TD-LDA calculations are possible with DEMON2K, the TD-LDA calculations reported here all made use of the TDA.

3.9.1.2 BIGDFT

The main thing to vary in BIGDFT is the grid which is of more profound importance than in DEMON2K because it is the grid which supports the wavelets. Figures 3.7, 3.8, and 3.9 give an idea of what the grid looks like for the small familiar molecule of water. Conceptually the molecule is in a very large box (Fig. 3.7.) A fine grid is placed

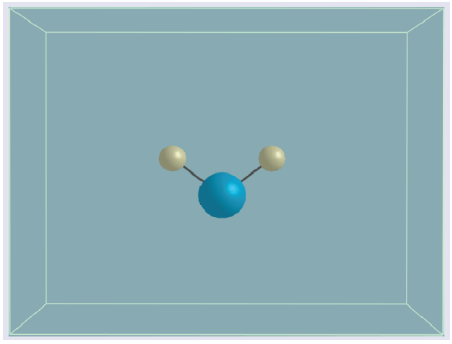

Figure 3.7: Example: H_2O in a simulation box

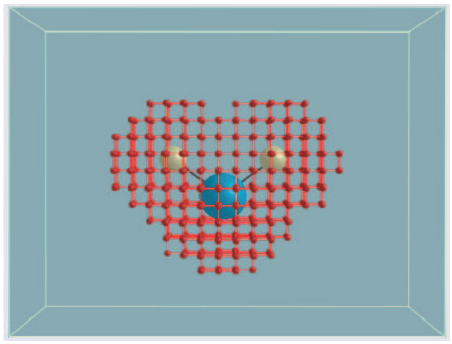

Figure 3.8: Example: H_2O in a simulation box showing fine grid resolution

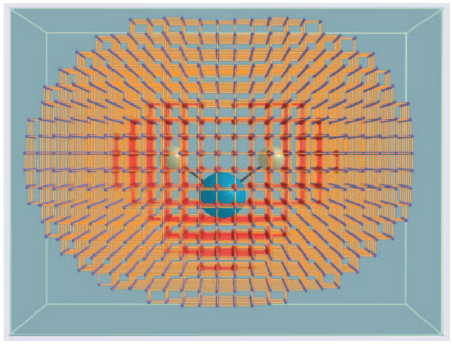

Figure 3.9: Example: H_2O in a simulation box showing coarse grid resolution

in the regions of high electron density around the molecule (Fig. 3.8.) A coarse grid is used in a larger region where the electron density varies more slowly (Fig. 3.9.) The BIGDFT grid is characterized by the triple h_g/crmult/frmult. The first number in the triple (h_g) is a real number which specifies the nodes of the grid in a.u. The second number (the integer-valued crmult) is the coarse grid multiplier. And the third number (the integer-valued frmult) is the fine grid multiplier. Two points must be clearly understood when looking at Figs. 3.7, 3.8, and 3.9. The first is that, while the box may determine the limits of the grid, the grid does not have the shape of the box and there are no basis functions where there are no grid points. This means that we are not dealing with box boundary conditions, but rather with effective boundary conditions which reflect the shape of the molecule. The other point which is not brought out by our explanation is that the BIGDFT grid is adaptive in the sense that additional fine grid points are added during the calculation as they are needed to maintain and improve numerical precision.

The implementation of TD-DFT in BIGDFT is described in Ref. [256].

3.9.2 *Orbital Energies*

Possibly the most remarkable property of wavelets is how rapidly they converge to the basis set limit. Let us illustrate this by comparing HOMO and LUMO energies calculated with DEMON2K and BIGDFT. The difference of these two energies is the HOMO-LUMO gap, $\Delta\epsilon_{\mathrm{HOMO-LUMO}}$.

Consider first how DEMON2K calculations of $\Delta\epsilon_{\mathrm{HOMO-LUMO}}$, evolve as the basis set is improved (Table 5.1.) Convergence to the true HOMO-LUMO LDA gap is expected with systematic improvement within the series:

- Double zeta plus valence polarization (DZVP) → triple zeta plus valence polarization (TZVP)
- Augmented correlation-consistent double zeta plus polarization plus diffuse on all atoms (AUG-CC-PCVDZ) → AUG-CC-PCVTZ (triple zeta) → AUG-CC-PCVQZ (quadruple zeta) → AUG-CC-PCV5Z (quintuple zeta)
- Augmented correlation-consistent valence double zeta plus polarization plus diffuse (AUG-CC-PVDZ) → AUG-CC-PVTZ → AUG-CC-PVQZ → AUG-CC-PV5Z
- Correlation-consistent double zeta plus polarization plus tight core (CC-PCVDZ) → CC-PCVTZ → CC-PCVQZ → CC-PCV5Z
- Correlation-consistent valence double zeta plus polarization on all atoms (CC-PVDZ) → CC-PVTZ → CC-PVQZ → CC-PV5Z.

Table 3.1: Basis set dependence of the HOMO and LUMO energies and of the HOMO-LUMO gap (eV) calculated using DEMON2K.

Basis Set	$-\epsilon_{HOMO}$	$-\epsilon_{LUMO}$	$\Delta\epsilon_{HOMO-LUMO}$
STO-3G	-5.5350	1.2428	4.2922
DZVP	-8.9271	-2.0942	6.8329
TZVP	-9.0287	-2.1902	6.8385
CC-PVDZ	-8.6729	-1.7823	6.8906
CC-PVTZ	-9.0419	-2.1195	6.9224
CC-PVQZ	-9.0944	-2.1971	6.8973
CC-PV5Z	-9.1169	-2.2400	6.8769
CC-PCVDZ	-8.6905	-1.7922	6.8983
CC-PCVQZ	-9.0957	-2.1988	6.8969
CC-PCVTZ	-9.0371	-2.1165	6.9206
CC-PCV5Z	-9.1172	-2.2401	6.8771
AUG-CC-PVDZ	-9.0910	-2.2345	6.8565
AUG-CC-PVQZ	-9.1286	-2.2567	6.8719
AUG-CC-PVTZ	-9.1306	-2.2535	6.8771
AUG-CC-PV5Z	-9.1289	-2.2606	6.8683
AUG-CC-PCVDZ	-9.0987	-2.2371	6.8616
AUG-CC-PCVTZ	-9.1316	-2.2554	6.5776
AUG-CC-PCVQZ	-9.1293	-2.2574	6.8719
AUG-CC-PCV5Z	-9.1291	-2.2607	6.8684

Table 3.2: Basis set dependence of the HOMO and LUMO energies and of the HOMO-LUMO gap (eV) calculated using BIGDFT.

$h_g{}^a/m^b/n^c$	$-\epsilon_{HOMO}$	$-\epsilon_{LUMO}$	$\Delta\epsilon_{HOMO-LUMO}$
0.4/6/8	-9.0976	-2.1946	6.9029
0.4/7/8	-9.1014	-2.2028	6.8985
0.4/8/8	-9.1017	-2.2044	6.8971
0.4/9/8	-9.1017	-2.2049	6.8967
0.4/10/8	-9.1017	-2.2049	6.8966
0.3/7/8	-9.1022	-2.2056	6.8964
0.3/8/8	-9.1025	-2.2073	6.8950

[a]Grid spacing of the cartesian grid in atomic units.
[b]Coarse grid multiplier (crmult).
[c] Fine grid multiplier (frmult).

There is a clear tendency in the correlation-consistent basis sets to tend towards values of -9.13 eV for the HOMO energy, -2.26 eV for the LUMO energy, and 6.87 eV for $\Delta\epsilon_{HOMO-LUMO}$, with adequate convergance achieved with the AUG-CC-PVQZ basis set.

Now let us turn to BigDFT (Table 5.2). Calculations were done for several different grids, including the high-resolution combination 0.3/8/8 and the low-resolution combination of 0.4/6/8. Remarkably, except for the very lowest quality grid 0.4/6/8, there is essentially no difference between results obtained with the two grids (and even the 0.4/6/8 grid gives nearly converged results.) The results are also quite close to, but not identical to those obtained with the DEMON2K program. The reason for the small differences between the converged results obtained with the two programs is more difficult to trace as it might be due to the auxiliary basis approximation in DEMON2K or to the use of pseudopotentials in BIGDFT or perhaps to still other program differences. The important point is that differences are remarkably small.

3.9.3 *Excitation Energies*

Orbital energy differences provide a first estimate for excitation energies. In this case, we would expect to see the HOMO $\rightarrow$ LUMO excitation at $\Delta\epsilon_{HOMO-LUMO} \approx 6.9$ eV (6.87 eV for DEMON2K and 6.90 eV for BIGDFT.) A better estimate is provided by the TOTEM [60, 71, 64, 65] for the singlet (S) and triplet (T) transition from orbital i to orbital a,

$$\begin{aligned} \hbar\omega^T_{i\to a} &= \Delta\epsilon_{i\to a} + (ia|f_{xc}^{\alpha,\alpha} - f_{xc}^{\alpha,\beta}|ai) \\ \hbar\omega^S_{i\to a} &= \Delta\epsilon_{i\to a} + (ia|2f_H + f_{xc}^{\alpha,\alpha} + f_{xc}^{\alpha,\beta}|ai)\,, \end{aligned} \tag{3.77}$$

Table 3.3: Comparison of lowest excitation energies of CO (in eV) calculated using BIGDFT and DEMON2K and with experiment.

State	BIGDFT[a]	DEMON2K[b]	Experiment[c]
$1^3\Sigma^-$	9.84	9.85	9.88
$1^3\Delta$	9.17	9.21	9.36
$1^1\Pi$	8.94	8.42	8.51
$1^3\Sigma^+$	8.94	8.54	8.51
$1^3\Pi$	6.47	6.05	6.32

[a] Present work (TD-LDA/TDA) using AUG-CC-PCQZ basis set.
[b] Present work (TD-LDA/TDA) using 0.3/8/8 grid.
[c] Taken from Ref. [66].

where

$$\Delta\epsilon_{i\to a} = \epsilon_a - \epsilon_i \,. \tag{3.78}$$

The TOTEM often works surprisingly well for small molecules because, unlike the HF approximation which is better adapted to describe electron ionization and attachment, pure DFT KS orbitals are preprepared to describe excitation energies in the sense that the occupied and unoccupied orbitals see the same potential, thus minimizing orbital relaxation effects. Inspection of the sizes and signs of the integrals in Eq. (3.77) indicates that we should expect,

$$\hbar\omega^T_{i\to a} \leqslant \Delta\epsilon_{i\to a} \leqslant \hbar\omega^S_{i\to a} \,. \tag{3.79}$$

These is confirmed in Table 3.3 where the $1^3\Pi$ and $1^1\Pi$ excitations are, respectively, the triplet and singlet states corresponding to the HOMO $\to$ LUMO transition.

Assuming that $f_{xc}^{\alpha,\alpha}$ dominates over $f_{xc}^{\alpha,\beta}$, we may even go a bit further to estimate $(ia|f_H|ai)$ and $(ia|f_{xc}^{\alpha,\alpha}|ai)$ (Fig. 3.10.) The calculations are show in Table 3.4. Comparison of $(ia|f_{xc}^{\alpha,\alpha}|ai)^{(1)}$ and $(ia|f_{xc}^{\alpha,\alpha}|ai)^{(2)}$ provides an indication of the quality of the approximation of neglecting the $(ia|f_{xc}^{\alpha,\beta}|ai)$ integral which in this case appears to be excellent. The $(ia|f_H|ai)$ integrals calculated with the two programs are reasonably close. Interestingly the $(ia|f_{xc}^{\alpha,\alpha}|ai)$ disagree by about 0.4 eV which, though small, is not negligible.

Let us now examine the issue of the collapse of the continuum. In Ref. [70], it was shown that the TD-DFT ionization continuum begins at $-\epsilon_{HOMO}$. In exact KS DFT, this should be the ionization potential. However typical approximate density functionals underbind electrons and so lead to an artificially-early on-set of the TD-DFT ionization continuum. This is first illustrated using the DEMON2K program and different basis sets. Indeed Fig. 3.11 shows that the states above $-\epsilon_{HOMO}$ tend to collapse towards $-\epsilon_{HOMO}$ rather than converging

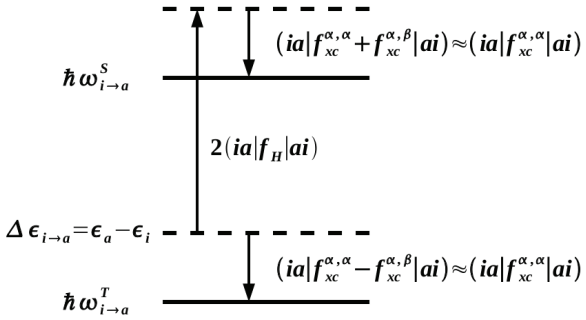

$$(ia|f_H|ai)\approx\frac{\hbar\omega_{i\to a}^{S}-\hbar\epsilon_{i\to a}^{T}}{2}$$
$$(ia|f_{xc}^{\alpha,\alpha}|ai)^{(1)}\approx\hbar\omega_{i\to a}^{T}-\Delta\epsilon_{i\to a}$$
$$(ia|f_{xc}^{\alpha,\alpha}|ai)^{(2)}\approx\hbar\omega_{i\to a}^{S}-\left[\Delta\epsilon_{i\to a}+2(ia|f_H|ai)\right]$$

Figure 3.10: Estimation of integrals within the TOTEM model.

Table 3.4: Estimations of integrals (in eV) within the TOTEM.

Program	DEMON2K	BIGDFT
Input Data		
$1^1\Pi$	8.42	8.94
$\Delta\epsilon_{i\to a}$	6.87	6.90
$1^3\Pi$	6.05	6.47
Derived Results		
$(ia\|f_H\|ai)$	1.19	1.24
$(ia\|f_{xc}^{\alpha,\alpha}\|ai)^{(1)}$	-0.82	-0.43
$(ia\|f_{xc}^{\alpha,\alpha}\|ai)^{(2)}$	-0.83	-0.44

as they should. This is simply because we are trying to describe a continuum which should not be there with a finite basis set. Also seen in the figure is a slight splitting of the $1^1\Pi$ excitation energy. This small effect is due to the fact that the grid used to calculate xc-integrals in DEMON2K has only roughly break the symmetry of the molecule.

Now let us turn to BIGDFT calculations. Figure 3.12 shows a similar collapse of the continuum as the fineness of the grid increases. Interestingly there is no evidence of symmetry breaking of the doubly-degenerate $1^1\Pi$ state.

3.9.4 *Oscillator Strengths*

Carbon monoxide is very unusual for small molecules in that absolute oscillator strengths have been well studied [78] over a significant

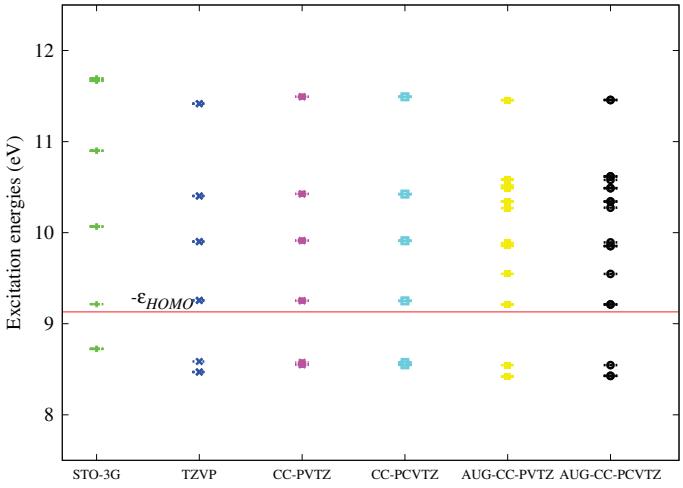

Figure 3.11: Singlet and triplet excitation energies for CO calculated using deMon2k

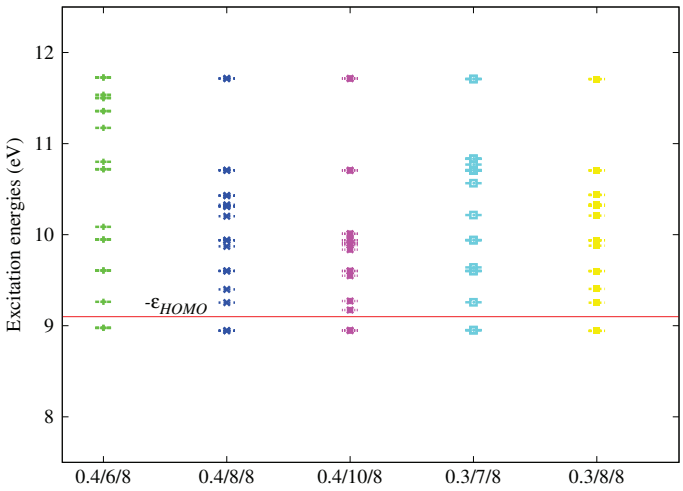

Figure 3.12: Singlet and triplet excitation energies for CO calculated using BigDFT

energy range and the $A^1\Pi$ ($1^1\Pi$ in Table 3.3) is bright and has an accurately determined oscillator strength. See Fig. 2 of Ref. [78] (as well as other references in the same paper) for a graph of measured absolute optical oscillator strengths against absorption energy in eV. Table 3.5 reports our calculated TD-LDA/TDA oscillator strengths. As the TDA violates the Thomas-Reiche-Kuhn (TRK) f-sum rule [60] it should only be used very cautiously to estimate oscillator strengths. Nevertheless the deMon2k value of $f = 0.232$ is in good agreement with the experimental value of $f = 0.1762$. As shown in Ref. [66], full TD-LDA calculations with asymptotically corrected potentials give smaller oscillator strengths (0.136 for TD-LDA/LB94 and 0.156 for TD-LDA/AC-LDA

Table 3.5: Comparison of experimental $A^1\Pi$ energies (eV) and oscillator strengths with TD-LDA/TDA experimental $A^1\Pi$ energies (eV) and degeneracy-weighted oscillator strengths (unitless.)

	deMon2k	BigDFT	Experiment[a]
$\hbar\omega_S$	8.43	8.95	8.4
f	0.232	0.853	0.1762

[a] See Table VIII of Ref. [66].

calculations [66].) (Coincidently our own deMon2k full TD-LDA calcuations without asymptotic corrections give a degeneracy-weighted oscillator strength of 0.1752 (bang on the experimental value) but an excitation energy of 8.19 eV.) Since oscillator strengths are quite sensitive to configuration mixing with nearby states, the fact that the BigDFT oscillator strength is larger than the deMon2k oscillator strength may be due to the relatively small energy separation between the BigDFT $A^1\Pi$ state and the artificially-low TD-LDA ionization continuum.

3.10 CONCLUSION

In this chapter we have tried to give an informative elementary review of a subject largely unfamiliar to most theoretical chemists and physicists. Wavelets, once an obscure ripple at the exterior of engineering applications, grew to become a regular tsumani in engineering circles in the 1990s as the similarity to and superiority over Fourier transform methods for multiresolution problems with arbitrary boundary conditions became increasingly recognized. Though the first applications of wavelet theory to solving the Schrödinger equation may be traced back to the mid-1990s [25, 123, 57], the theory is still not well known among quantum mechanicians. Here we have tried to remedy this aberrant situation by trying to "make some *waves* about *wavelets* for *wave* functions."

In particular we have reviewed the theory behind the wavelet code BigDFT for ground-state DFT and our recent implementation of wavelet-based TD-DFT in BigDFT. Rapid progress is being made towards making BigDFT a high performance computing order-N code for applications to large systems. Right now applications to 400 or 500 atoms are routine for ground-state calculations with BigDFT. Our implementation of TD-DFT in BigDFT is by comparison only a rudementary beginning, but it shows that the basic method is viable and we are confident that there are no insurmountable obstacles to making high performance computing order-N wavelet-based TD-DFT code for large systems.

Part II

PUBLISHED ARTICLES

4

SPIN-FLIP LR-TD-DFT

The aim of this chapter of the thesis is to test the implementation of spin-flip TD-DFT in deMon2k and explore SF-TD-DFT based on the noncollinear formalism presented in [324].

4.1 COLLINEAR TD-DFT

The most common application of KS DFT is to spin-independent external potentials so that

$$[\hat{h}_s, \hat{S}_z] = 0\,, \tag{4.1}$$

That means that the orbitals may be chosen as simultaneous eigen functions of $\hat{h}_s$ and $\hat{S}_z$ with the spin of the spin orbitals aligned collinearly either up or down along the z-axis everywhere in space. It follows that

$$\rho = \begin{bmatrix} \rho_\alpha \\ \rho_\beta \end{bmatrix} = \begin{bmatrix} \rho_\uparrow \\ \rho_\downarrow \end{bmatrix}. \tag{4.2}$$

is a 2-component vector and spin-independent perturbations cannot change spin so that the LR-TD-DFT problem partitions as

$$\begin{bmatrix} \mathbf{A}_{\uparrow,\uparrow} & \mathbf{A}_{\uparrow,\downarrow} \\ \mathbf{A}_{\downarrow,\uparrow} & \mathbf{A}_{\downarrow,\downarrow} \end{bmatrix} \begin{pmatrix} \vec{X}_\uparrow \\ \vec{X}_\downarrow \end{pmatrix} = \omega \begin{pmatrix} \vec{X}_\uparrow \\ \vec{X}_\downarrow \end{pmatrix}. \tag{4.3}$$

in the TDA. For closed-shell ground-states,

$$\begin{aligned} \mathbf{A}_{\uparrow,\uparrow} &= \mathbf{A}_{\downarrow,\downarrow}\,, \\ \mathbf{A}_{\downarrow,\uparrow} &= \mathbf{A}_{\downarrow,\downarrow}\,, \end{aligned} \tag{4.4}$$

so a unitary transformation brings the TDA equation to the form,

$$\begin{bmatrix} \mathbf{A}_T & \mathbf{0} \\ \mathbf{0} & \mathbf{A}_S \end{bmatrix} \begin{pmatrix} \vec{X}_T \\ \vec{X}_S \end{pmatrix} = \omega \begin{pmatrix} \vec{X}_T \\ \vec{X}_S \end{pmatrix}, \tag{4.5}$$

where

$$\mathbf{A}_T = \mathbf{A}_{\uparrow,\uparrow} - \mathbf{A}_{\uparrow,\downarrow}$$

is the triplet matrix and

$$\mathbf{A}_S = \mathbf{A}_{\uparrow,\uparrow} + \mathbf{A}_{\uparrow,\downarrow}$$

is the singlet matrix. Hence SP TD-DFT has only triplet-coupled and singlet-coupled solutions.

4.2 NONCOLLINEAR TD-DFT

In this case, the KS operator contains a component which can rotate spin, possibly differently in different parts of space. Now

$$[\hat{h}_s, \hat{S}_z] \neq 0\,, \tag{4.6}$$

and so spin-orbitals may not be chosen as purely spin up or spin down but rather the orbitals is a 2-component

$$\psi_i(\mathbf{r}) = \begin{pmatrix} \psi_{i\alpha}(\mathbf{r}) \\ \psi_{i\beta}(\mathbf{r}) \end{pmatrix} = \begin{pmatrix} \psi_{i\uparrow}(\mathbf{r}) \\ \psi_{i\downarrow}(\mathbf{r}) \end{pmatrix}, \tag{4.7}$$

It follows that the density matrix is no longer a vector in spin, but a matrix

$$\rho(\mathbf{r}) = \begin{bmatrix} \rho_{\uparrow\uparrow}(\mathbf{r}) & \rho_{\uparrow\downarrow}(\mathbf{r}) \\ \rho_{\downarrow\uparrow}(\mathbf{r}) & \rho_{\downarrow\downarrow}(\mathbf{r}) \end{bmatrix}. \tag{4.8}$$

spin-dependent perturbation may rotate spins and the kernels

$$f_{xc}^{\sigma_1\sigma_2,\tau_1\tau_2}(\mathbf{r}_1,\mathbf{r}_2) = \frac{\delta^2 E_{xc}[\rho]}{\delta\rho_{\sigma_1,\sigma_2}(\mathbf{r}_1)\delta\rho_{\tau_1,\tau_2}(\mathbf{r}_2)}\,, \tag{4.9}$$

has 4-spin indices. The general TDA problem is correspondingly larger

$$\begin{bmatrix} \mathbf{A}_{\uparrow\uparrow,\uparrow\uparrow} & \mathbf{A}_{\uparrow\uparrow,\downarrow\downarrow} & \mathbf{A}_{\uparrow\uparrow,\uparrow\downarrow} & \mathbf{A}_{\uparrow\downarrow,\downarrow\uparrow} \\ \mathbf{A}_{\downarrow\downarrow,\uparrow\uparrow} & \mathbf{A}_{\downarrow\downarrow,\downarrow\downarrow} & \mathbf{A}_{\downarrow\downarrow,\uparrow\downarrow} & \mathbf{A}_{\downarrow\downarrow,\downarrow\uparrow} \\ \mathbf{A}_{\uparrow\downarrow,\uparrow\uparrow} & \mathbf{A}_{\uparrow\downarrow,\downarrow\downarrow} & \mathbf{A}_{\uparrow\downarrow,\uparrow\downarrow} & \mathbf{A}_{\uparrow\downarrow,\downarrow\uparrow} \\ \mathbf{A}_{\downarrow\uparrow,\uparrow\uparrow} & \mathbf{A}_{\downarrow\uparrow,\downarrow\downarrow} & \mathbf{A}_{\downarrow\uparrow,\uparrow\downarrow} & \mathbf{A}_{\downarrow\uparrow,\downarrow\uparrow} \end{bmatrix} \begin{pmatrix} \vec{X}_{\uparrow\uparrow} \\ \vec{X}_{\downarrow\downarrow} \\ \vec{X}_{\uparrow\downarrow} \\ \vec{X}_{\downarrow\uparrow} \end{pmatrix} = \omega \begin{pmatrix} \vec{X}_{\uparrow\uparrow} \\ \vec{X}_{\downarrow\downarrow} \\ \vec{X}_{\uparrow\downarrow} \\ \vec{X}_{\downarrow\uparrow} \end{pmatrix}. \tag{4.10}$$

In principle, noncollinear response theory then allows us to flip spin even when starting from a collinear unperturbed state. However this only works for functionals which allow spin flips. Only two SF functionals are so far known to allow spin flips. The earliest is that of hybrid functionals including some Hartree-Fock exchange. The more recent noncollinear spin-flip functional considered in this paper comes from relativistic DFT and works nominally even for the LDA. Our objective here is to subject it to more demanding tests with critical points on potential energy surfaces in mind.

4.3 COMMENTS ON MY CONTRIBUTION TO THIS ARTICLE

The chapter is structured in the following way. The first section (4.4) of the included article consists of an introduction to the theories underlying the TD-DFT method; it is dedicated to the presentation of the nature of excitations in LR-TD-DFT. Section (4.5), a full description of

the SF-TD-DFT is proposed including the numerical implementation of SF-TD-DFT in DEMON2K, and the SF-TD-DFT method applied to the problem of H_2 dissociation. Section (4.6) explains the different computational approaches used in various different programs in the article. In section 4.7, we applied SF-TD-DFT method to study the mechanism of C_{2v} ring-opening (subsection 4.7.1) of oxirane. In order to test the SF-TD-DFT method on this particular aspect, futher investigation on photochemical pathway of oxirane is studied in detail, (subsections 4.7.2 and 4.7.3) the values are compared with values obtained by other methods such as DMC, CIS and CASSCF. Finally conclusions are summarized in the last section (4.8) along with an outlook for further studies on SF-TD-DFT method.

My contribution in this article is to work on the last part involving the calculation (requiring hundreds of SF-TD-DFT calculations!!!) of the SF-TD-DFT PES for locating the CX in the photochemical ring opening of oxirane.

ASSESSMENT OF NONCOLLINEAR SPIN-FLIP TAMM-DANCOFF APPROXIMATION TIME-DEPENDENT DENSITY-FUNCTIONAL THEORY FOR THE PHOTOCHEMICAL RING-OPENING OF OXIRANE

M. HUIX-ROTLLANT, BHAARATHI NATARAJAN, ANDREI IPATOV, C. MUHAVINI WAWIRE, THIERRY DEUTSCH, AND MARK E. CASIDA

- Published in *Phys. Chem. Chem. Phys.*, **12**, 12811–12825 (2010).
- http://pubs.rsc.org/en/Content/ArticleLanding/2010/CP/c0cp00273a.

4.4 INTRODUCTION

Due to its rigorous formal foundations and computational efficiency, TD-DFT is currently a method of choice for treating electronic excited states. It is thus one of several tools to be found in today's photochemical modeling kit (see e.g., Refs. [99, 100, 97, 296]). Nevertheless applications of TD-DFT are limited by a number of problems due to the inevitable use of approximate functionals in practical applications. Overcoming these limitations is important for extending the domain of applicability of TD-DFT. Here we investigate the ability of spin-flip SF TD-DFT to overcome problems encountered by ordinary TD-DFT near funnel regions, namely avoided crossings (AX) and conical intersections (CX). This is especially important in light of the recent development of Tully-type [313, 314] mixed TD-DFT/classical trajectory surface-hopping dynamics [103, 84, 301, 302, 328, 250]. Surface-hopping dynamics may also have inspired very recent work by Minezawa and Gordon [249] focusing on characterizing the CXs of ethylene using one formulation of SF-TD-DFT [291, 295] and the BHHLYP functional (50% Hartree-Fock plus 50% Becke exchange [41] plus Lee-Yang-Parr correlation [216]). In the present study, we have chosen the photochemical ring opening of oxirane [(I) in Fig. 4.1] as a test case for evaluating the ability of a different formulation of SF-TD-DFT [322, 325] in describing funnel regions because oxiranes are an important class of compounds in photochemistry (see Ref. [163] and the brief review in Appendix B of Ref. [82] as well as Ref. [128] where the photochemical ring-opening of diphenyloxirane has been studied, not by TD-DFT, but by a different DFT approach) and because of the availability of high-quality comparison results [82, 302].

Let us review the fundamental problems encountered by DFT for such applications. Hohenberg, Kohn, and Sham showed that the static ground state properties of a real system of interacting electrons could

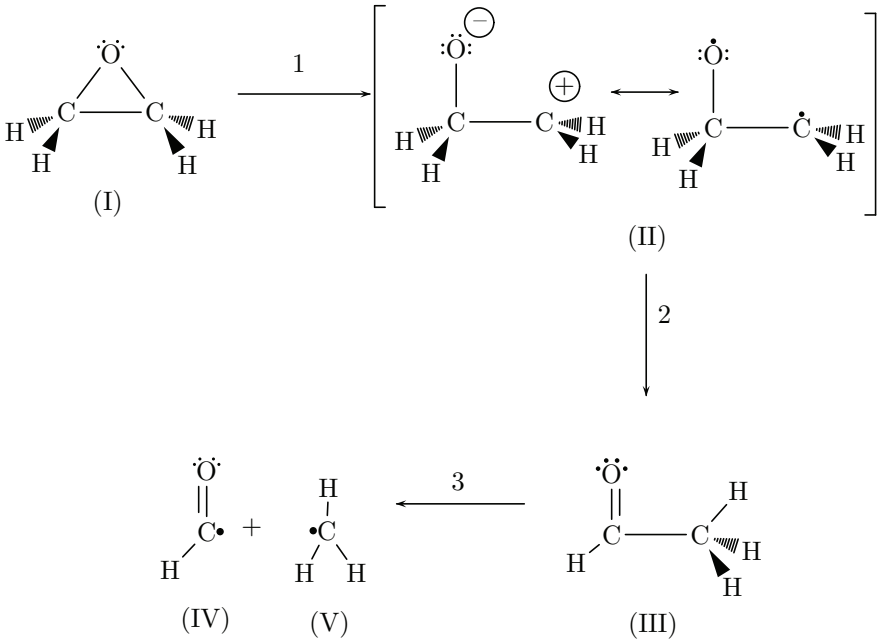

Figure 4.1: Gomer-Noyes mechanism for the ring-opening of oxirane (I). [144]

in principle be treated exactly by replacing it with a fictitious system of noninteracting electrons [172, 206]. In the absence of degeneracies, the wave function of the noninteracting system is single determinantal in nature. The orbitals obey the well-known Kohn-Sham equation,

$$\left(\hat{h}_C + v_H + v_{xc}^{\sigma}\right)\psi_p^{\sigma} = \epsilon_{p\sigma}\psi_p^{\sigma}\,, \tag{4.11}$$

where $\hat{h}_C^{\sigma}$ is the usual core (i.e., kinetic energy plus external potential, v_{ext}^{σ}), v_H is the Hartree (i.e., Coulomb) potential, and (assuming a pure spin-density functional) the exchange-correlation (xc) potential,

$$v_{xc}^{\sigma}[\rho_\alpha, \rho_\beta](\mathbf{r}) = \frac{\delta E_{xc}[\rho_\alpha, \rho_\beta]}{\delta \rho_\sigma(\mathbf{r})}\,, \tag{4.12}$$

is the functional derivative of the xc-energy, E_{xc}. (Hartree atomic units are used throughout this paper: $\hbar = m_e = e = 1$.) While the Hohenberg-Kohn-Sham DFT is formally exact in principle, it is limited in practice by the use of approximate xc-functionals. The result is that DFT, whose equations resemble those of Hartree-Fock (HF) theory, "inherits" some of the problems of HF theory, notably molecular orbital symmetry breaking when describing the rupture of covalent bonds. Indeed simple arguments show that no symmetry breaking should occur for a closed-shell molecule when the xc-functional is exact [82]. In practice, the broken symmetry solution becomes lower in energy than the unbroken symmetry solution beyond some critical bond distance (Coulson-Fischer point) because of the use of approximate functionals. The above arguments rest on the supposition of NVR, which means that the energy is minimized with the *Aufbau* filling of

the KS orbitals. Interestingly there is some indication that NVR fails for biradicals [302], indicating the need for an ensemble formalism which, however, is beyond the scope of the present paper.

Modern TD-DFT is based upon the formalism of Runge and Gross who presented Hohenberg-Kohn-like theorems for the time-dependent (TD) case and a TD-KS equation, [280]

$$\left(\hat{h}_C^\sigma + v_H + v_{xc}^\sigma\right)\psi_p^\sigma = i\frac{\partial}{\partial t}\psi_p^\sigma\,, \tag{4.13}$$

in which the xc-potential is, in principle, a functional of the TD density, $\rho_\sigma(\mathbf{r},t)$, and the wave functions of the interacting and noninteracting systems at some initial time. However the first Hohenberg-Kohn (HK) theorem tells us that these wave functions are also functionals of the initial density, meaning that the xc-potential depends only on the density for the case of a system initially in its ground stationary state perturbed by a TD applied potential [172]. Linear response (LR) theory may then be used to extract information about excited states. This leads, in Casida's formulation [60], to the LR-TD-DFT equation,

$$\begin{bmatrix} \mathbf{A}(\omega) & \mathbf{B}(\omega) \\ \mathbf{B}^*(\omega) & \mathbf{A}^*(\omega) \end{bmatrix} \begin{pmatrix} \vec{X} \\ \vec{Y} \end{pmatrix} = \omega \begin{bmatrix} \mathbf{1} & \mathbf{0} \\ \mathbf{0} & -\mathbf{1} \end{bmatrix} \begin{pmatrix} \vec{X} \\ \vec{Y} \end{pmatrix}, \tag{4.14}$$

which has paired excitation and de-excitation solutions,

$$\begin{pmatrix} \vec{X}_I \\ \vec{Y}_I \end{pmatrix} \leftrightarrow \omega_I = E_0 - E_I = -\omega_I \leftrightarrow \begin{pmatrix} \vec{Y}_I \\ \vec{X}_I \end{pmatrix} \tag{4.15}$$

Here

$$\begin{aligned} \mathbf{A}_{ia,jb}^{\sigma,\tau} &= \delta_{a,b}\delta_{i,j}\delta_{\sigma,\tau}\left(\epsilon_{a\sigma} - \epsilon_{i\sigma}\right) + \mathbf{K}_{ia,jb}^{\sigma,\tau}(\omega) \\ \mathbf{B}_{ia,jb}^{\sigma,\tau} &= \mathbf{K}_{ia,bj}^{\sigma,\tau}(\omega)\,, \end{aligned} \tag{4.16}$$

and the coupling matrix,

$$\mathbf{K}_{ia,bj}^{\sigma,\tau}(\omega) = (ia|f_H + f_{xc}^{\sigma,\tau}(\omega)|bj)\,, \tag{4.17}$$

where,

$$f_H(\mathbf{r}_1,\mathbf{r}_2) = \frac{1}{r_{12}}\,, \tag{4.18}$$

is the Hartree kernel and,

$$f_{xc}^{\sigma,\tau}(\mathbf{r}_1,\mathbf{r}_2;\omega) = \int_{-\infty}^{+\infty} e^{i\omega(t_1-t_2)}\frac{\delta v_{xc}^\sigma(\mathbf{r}_1,t_1)}{\delta\rho_\tau(\mathbf{r}_2,t_2)}\,d(t_1-t_2)\,, \tag{4.19}$$

is the xc-kernel. Integrals are written in Mulliken charge-cloud notation,

$$(pq|f|rs) = \int\int \psi_p^*(\mathbf{r}_1)\psi_q(\mathbf{r}_1)f(\mathbf{r}_1,\mathbf{r}_2)\psi_r^*(\mathbf{r}_2)\psi_s(\mathbf{r}_2)\,d\mathbf{r}_1\,d\mathbf{r}_2\,. \tag{4.20}$$

Since LR-TD-DFT is the primary application of TD-DFT and the only one treated in the present article, we will normally just refer to LR-TD-DFT as TD-DFT. Like conventional DFT, the underlying formalism of TD-DFT has been the subject of much healthy criticism (e.g., Refs. [283, 234, 284]). Nevertheless is our expectation that, like the static ground-state formalism, formal TD-DFT—either as is or suitably modified—will stand the test of time, for at least some time to come. The reader interested in further information about TD-DFT is referred to a recent book [241] and two special journal issues [240, 67] devoted to TD-DFT.

Problems arise in practice because of the use of approximate functionals. These have been extensively reviewed in the literature (e.g., Refs. [61] and [64]). Suffice it to say that the normal domain of validity of TD-DFT with existent approximate xc-functionals is low-lying 1-electron excitations which are not too delocalized in space and do not involve too much charge transfer.

The present paper is primarily concerned with the limitation to 1-electron excitations. This limitation arises from the basic adiabatic approximation (AA) which is almost universally used in practice. This approximation assumes that the xc-potential reacts instantaneously and without memory to any temporal change of the charge density. Mathematically, the AA means that the xc-potential,

$$v_{xc}^{\sigma}(\mathbf{r},t) = \frac{\delta E_{xc}[\rho_{\alpha}^{t},\rho_{\beta}^{t}]}{\delta\rho_{\sigma}^{t}(\mathbf{r})}\,, \tag{4.21}$$

may be evaluated in terms of the xc-functional of static ground-state DFT. Here $\rho_{\sigma}^{t}(\mathbf{r})$ means $\rho_{\sigma}(\mathbf{r},t)$ regarded as a function of the spatial coordinate $\mathbf{r}$ at fixed time t. It is easily seen that the AA limits TD-DFT to 1-electron excitations (albeit "dressed" to include some electron correlation effects). In particular, the AA implies that the coupling matrix is frequency-independent and hence that the number of excitation solutions obtained from the LR-TD-DFT equation is exactly equal to the number of 1-electron excitations. This is a problem for some applications, such as excitations in polyenes and open-shell molecules, and an active area of research is aimed at going beyond the AA by explicit inclusion of 2- and higher-electron excitations through the frequency-dependence of the xc-kernel [74, 233, 62, 243, 278, 149]. The limitation to 1-electron excitations is *a priori* also a problem for photochemical reactions passing through biradicals since the conventional description of biradical formation involves the mixing of the ground state configuration with a doubly-excited state. Thus for the breaking of the σ bond in H_2,

$$H_A\text{-}H_B \rightarrow [H_A\uparrow + H_B\downarrow \leftrightarrow H_A\downarrow + H_B\uparrow]\,, \tag{4.22}$$

the final state corresponds to the wave function,

$$\frac{1}{2}\left(|s_A,\bar{s}_B| + |s_B,\bar{s}_A|\right) = \frac{1}{2}\left(|\sigma,\bar{\sigma}| - |\sigma^*,\bar{\sigma}^*|\right)\,. \tag{4.23}$$

The 2-electron excited state, $|\sigma^*, \bar{\sigma}^*|$, is excluded by the AA. A subtler, but important point, is that mixing of the ground and excited configurations is also forbidden by the AA but is rigorously necessary to have a CX [218, 82, 302].

The present and previous work applying TD-DFT to oxirane photochemistry [302, 82] also makes use of the TDA [170]. [The work of Friedrichs and Frank on the photochemical dynamics of diphenyloxirane uses a different (non-TD-DFT) DFT approach [128].] The TDA consists of neglecting the **B** matrix to obtain just,

$$\mathbf{A}\vec{X} = \omega\vec{X}. \tag{4.24}$$

While the TDA is simpler than full LR-TD-DFT and so is both a bit easier to interpret as well as being computationally a bit simpler, the main advantage of the TDA is that it bypasses the triplet instability problem — that is, symmetry breaking in the ground state occurs if and only if an imaginary triplet excitation energy is found in TD-DFT [61, 71, 72, 82]. The reason, of course, is that TD-DFT excitation energies obtained by LR theory are intrisically limited by the quality of the DFT description of the ground state which in the NVR case should not show any symmetry breaking. Underestimates of corresponding singlet excitation energies are also often associated with triplet instabilities. However when the TDA is applied to LR-TD-HF, then the fully variational CIS is obtained, indicating that the excited-state problem has been decoupled from the ground-state problem in a way that avoids the problem of variational collapse. The situation in TD-DFT is similar and TD-DFT TDA calculations give much improved excited-state PES compared to full TD-DFT calculations [71, 72, 82].

(It may be worth noting that use of the TDA comes with a cost. TD-DFT absorption spectra are derived using linear response theory from the poles of the dynamic polarizability [60]. This implies that the spectral intensities should be reasonably correct. For example, it is known that the Thomas-Reiche-Kuhn (TRK) "f-sum" rule holds in a sufficiently extended basis set [186]. However the f-sum rule is lost and the reliability of calculated spectral intensities is diminished when making the TDA with potentially important effects on spectra. Consequently the TDA should be used with extreme caution when calculating oscillator strength distributions [153]. Here however we are interested in potential energy surfaces not oscillator strengths.)

Though it yields improved PESs, the TDA does not solve the problem that mixing of the ground and excited configurations is forbidden by the AA but is rigorously necessary to have a CX, nor does the TDA provide the 2-electron excited states needed for describing biradialoïd intermediates. At first thought such an absence of CX might seem fatal for photodynamics applications. Though the situation is not actually as dark as might at first seem [302], it would be nice to find a way to recover a true CX.

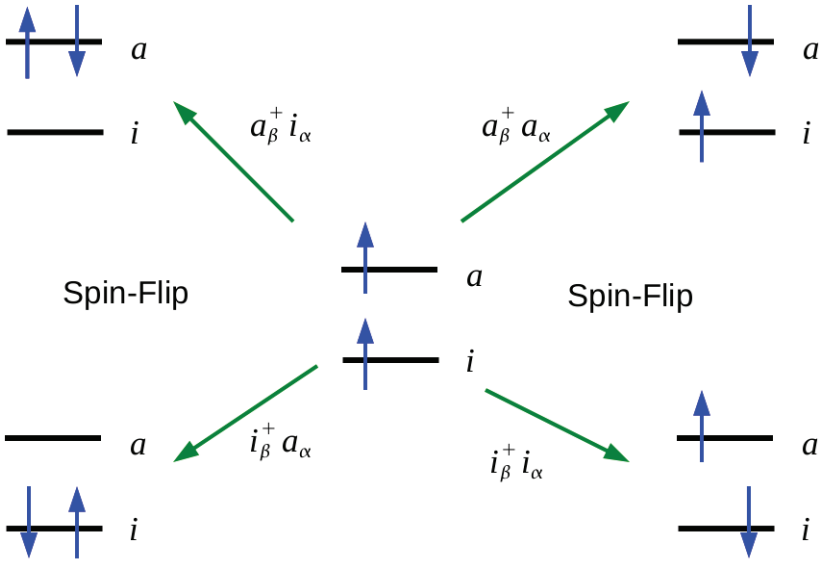

Figure 4.2: Two-orbital model of TD-DFT excitations with a triplet reference configuration.

Levine *et al*. suggest that SF-TD-DFT might be good for this purpose [218]. The main idea of SF-TD-DFT is shown in Fig. 4.2. We must first make the common pragmatic assumption that DFT applies not only to the ground state but also to the lowest energy state of a given spin-symmetry. This assumption is especially plausible if a single-determinant provides a reasonable first approximation to the state in question. Excited states normally excluded from TD-DFT are included in SF-TD-DFT by beginning from the lowest triplet state and flipping spins while exciting electrons from one orbital to another. In this manner we arrive at exactly the ground configuration and the doubly-excited configuration needed to describe bond breaking. Ideally then H_2 will dissociate correctly without recourse to symmetry breaking and this is indeed the case [322] (Fig. 4.3). Moreover the problem of an effective failure of NVR is very much reduced leading to much improved convergence. Historically designing an appropriate functional for SF-TD-DFT has proven to be not entirely straightforward. This problem is reviewed in some detail the next section.

Computational details and a brief description of our own implementation of SF-TD-DFT are given in Sec. 4.6. In Sec. 4.7, we report results pertinent to oxirane photochemistry. Section 4.8 summarizes our main conclusions about the effectiveness of SF-TD-DFT for describing photochemical funnels.

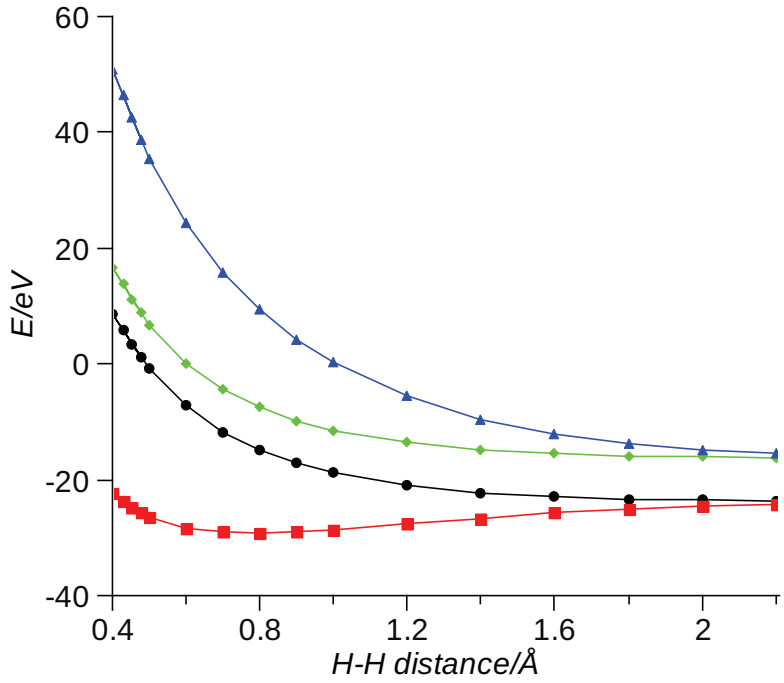

Figure 4.3: Dissociation of H_2 obtained with the present implementation of SF-TD-DFT. The black $1\,^3\Sigma_u$ curve (circles) is the triplet SCF reference state from which excitations are taken. It is nearly degenerate with the $M_S = 0$ triplet state (not shown) generated by SF-TD-DFT. The red $1\,^1\Sigma_g$ ground state curve (squares) is a mixture of $|\sigma, \bar{\sigma}|$ and $|\sigma^*, \bar{\sigma}^*|$ configurations, with the $|\sigma, \bar{\sigma}|$ dominating at the equilibrium geometry. The $1\,^1\Sigma_g$ and $1\,^3\Sigma_u$ states dissociate to the same neutral "diradical" limit, namely $[H\uparrow + H\downarrow \leftrightarrow H\downarrow + H\uparrow]$. The blue $2\,^1\Sigma_g$ state curve (triangles) is also a mixture of $|\sigma, \bar{\sigma}|$ and $|\sigma^*, \bar{\sigma}^*|$ configurations, but the "doubly-excited" $|\sigma^*, \bar{\sigma}^*|$ configuration dominates at the ground state equilibrium geometry. The green curve (diamonds) is the $1\,^1\Sigma_u(\sigma \rightarrow \sigma^*)$ singly-excited state. The $2\,^1\Sigma_g$ and $1\,^1\Sigma_u(\sigma \rightarrow \sigma^*)$ states dissociate to the same ionic limit, namely $[H^+ + H^- \leftrightarrow H^- + H^+]$.

4.5 SPIN-FLIP TD-DFT

No new solution to the SF-TD-DFT problem is proposed in the present paper, but this section reviews existent solutions to the problem of developing appropriate functionals for SF-TD-DFT. We do this partly to keep this paper self-contained, but also to point out that some aspects of present SF solutions might also be improved if the goal is complete compatibility between SF-TD-DFT and conventional TD-DFT.

The most basic requirement of the SF method is the generalization of the one-component collinear approach in which each orbital is associated with either spin α or spin β aligned along an arbitrary z-axis, to a two-component noncollinear approach in which each orbital is a linear combination of spin α and spin β components. Lifting of the collinear requirement is needed to allow spins to rotate in response to an external spin-dependent perturbation and hence to be able to flip. Orbitals become two-component spinors,

$$\psi_p(\mathbf{r}) = \begin{pmatrix} \psi_p^\alpha(\mathbf{r}) \\ \psi_p^\beta(\mathbf{r}) \end{pmatrix}, \tag{4.25}$$

which are obtained by solving the 2×2 matrix equation in spin,

$$\begin{bmatrix} \hat{h}_C^{\alpha,\alpha} + v_{Hxc}^{\alpha,\alpha} & \hat{h}_C^{\alpha,\beta} + v_{Hxc}^{\alpha,\beta} \\ \hat{h}_C^{\beta,\alpha} + v_{Hxc}^{\beta,\alpha} & \hat{h}_C^{\beta,\beta} + v_{Hxc}^{\beta,\beta} \end{bmatrix} \begin{pmatrix} \psi_p^\alpha(\mathbf{r}) \\ \psi_p^\beta(\mathbf{r}) \end{pmatrix} = \epsilon_p \begin{pmatrix} \psi_p^\alpha(\mathbf{r}) \\ \psi_p^\beta(\mathbf{r}) \end{pmatrix}. \tag{4.26}$$

Note that the core hamiltonian may now have a spin-dependence due to a spin-dependent external potential. The density is also a 2×2 matrix in spin,

$$\rho(\mathbf{r}) = \begin{bmatrix} \rho_{\alpha,\alpha}(\mathbf{r}) & \rho_{\alpha,\beta}(\mathbf{r}) \\ \rho_{\beta,\alpha}(\mathbf{r}) & \rho_{\beta,\beta}(\mathbf{r}) \end{bmatrix}. \tag{4.27}$$

Consequently the xc-kernel has four spin indices,

$$f_{xc}^{\sigma,\sigma';\tau,\tau'}(\mathbf{r}_1, \mathbf{r}_2; \omega) = \int_{-\infty}^{\infty} e^{i\omega(t-t')} \frac{\delta v^{\sigma,\sigma'}(\mathbf{r}, t_1)}{\delta \rho_{\tau,\tau'}(\mathbf{r}_2, t_2)} \, d(t_1 - t_2), \tag{4.28}$$

or, in the AA,

$$f_{xc}^{\sigma,\sigma';\tau,\tau'}(\mathbf{r}_1, \mathbf{r}_2) = \frac{\delta^2 E_{xc}[\rho]}{\delta \rho_{\sigma,\sigma'}(\mathbf{r}_1) \delta \rho_{\tau,\tau'}(\mathbf{r}_2)}. \tag{4.29}$$

Naturally the TD-DFT coupling matrix also has four spin indices.

Normal practice is to apply SF-TD-DFT using orbitals and orbital energies obtained from an ordinary one-component collinear calculation, rather than as a post two-component noncollinear calculation. Thus the assumption is that the one-component noncollinear calculation is an adequate approximation at the SCF level to a full two-component noncollinear SCF calculation. In the end, the noncollinear model only

serves in deriving the SF-TD-DFT formalism, not in actually carrying it out.

Applying the SF-TD-DFT formalism to the usual collinear pure xc-functionals leads to nothing new because,

$$f_{xc}^{\sigma,\sigma';\tau,\tau'} = \delta_{\sigma,\sigma'}\delta_{\tau,\tau'}f_{xc}^{\sigma,\tau}\,. \tag{4.30}$$

This however is not true in HF because the kernel of the exchange operator, $\hat{\Sigma}_x^{\sigma,\tau}$, is given by,

$$\Sigma_x^{\sigma,\tau}(\mathbf{r}_1,\mathbf{r}_2) = -\frac{\gamma_{\sigma,\tau}(\mathbf{r},\mathbf{r}')}{r_{12}}\,, \tag{4.31}$$

where $\gamma_{\sigma,\tau}(\mathbf{r},\mathbf{r}')$ is the one-electron reduced density matrix. Consequently,

$$\begin{aligned} f_x^{\sigma,\tau;\sigma',\tau'}(\mathbf{r}_1,\mathbf{r}_2;\mathbf{r}_1',\mathbf{r}_2') &= \frac{\delta\Sigma_x^{\sigma,\tau}(\mathbf{r}_1,\mathbf{r}_2)}{\delta\gamma_{\sigma',\tau'}(\mathbf{r}_1',\mathbf{r}_2')} \\ &= -\delta_{\sigma,\sigma'}\delta_{\tau,\tau'}\frac{\delta(\mathbf{r}_1-\mathbf{r}_1')\delta(\mathbf{r}_2-\mathbf{r}_2')}{r_{12}}\,, \end{aligned} \tag{4.32}$$

and the exchange-part of the HF coupling matrix is,

$$K_{pq,rs}^{\sigma,\tau;\sigma',\tau'} = -\delta_{\sigma,\sigma'}\delta_{\tau,\tau'}(ps|f_H|rq)\,. \tag{4.33}$$

This means that hybrid functionals allow SF because they include a portion of HF exchange. This in fact was the first form of SF-TD-DFT. It was proposed by Anna Krylov and coworkers who used their approach to study the ground and excited states of diradicals [291, 295]. In order to get good agreement with experiment, they found it necessary to use a significantly higher amount of HF exchange (50%) than is typically used for ground state properties (~ 25%). Even higher percentages of HF exchange (> 50%) have been reported to be necessary for calculating second hyperpolarizabilities of diradical systems by this spin-flip method [199]. Although the use of a different functional for ground and excited states is disturbing, the basic idea is admirable and this method continues to be used [199, 308, 212]. In particular, this is the SF-TD-DFT approach mentioned in the introduction in the context of its recent use by Minezawa and Gordon who found the method to give a relatively good description of CXs in ethylene [249].

The next and most recent major advance in SF-TD-DFT came with an article by Wang and Ziegler [322]. (See also Ref. [325].) It is intimately related to work by Wenjian Liu and coworkers on relativistic four-component TD-DFT [131]. Basing their approach on ideas from relativistic two-component DFT [111, 319], Wang and Ziegler proposed that any pure spin-density xc-functional, $E_{xc}[\rho_\alpha,\rho_\beta]$, could be used

to make a noncollinear xc-functional suitable for SF calculations by making the substitution,

$$\begin{aligned} \rho_\alpha &\rightarrow \rho_+ = \frac{1}{2}(\rho + s) \\ \rho_\beta &\rightarrow \rho_- = \frac{1}{2}(\rho - s) \,, \end{aligned} \tag{4.34}$$

involving two quantities which are invariant under a unitary transformation of the spin coordinates. These are the total charge density,

$$\rho = \rho_{\alpha,\alpha} + \rho_{\beta,\beta} \,, \tag{4.35}$$

and the magnetization, s, whose square is given by,

$$s^2 = \left(\rho_{\alpha,\alpha} - \rho_{\beta,\beta}\right)^2 + 2\left(\rho_{\alpha,\beta}^2 + \rho_{\beta,\alpha}^2\right) \,. \tag{4.36}$$

The collinear limit of s is just the spin-polarization,

$$s \rightarrow \rho_\alpha - \rho_\beta \,, \tag{4.37}$$

after an appropriate choice of phase. The factor of $1/2$ has been introduced by us so that,

$$\begin{aligned} \rho_+ &\rightarrow \rho_\alpha \\ \rho_- &\rightarrow \rho_\beta \,, \end{aligned} \tag{4.38}$$

in the same limit. After taking derivatives and the noncollinear limit, the xc-kernel becomes,

$$\begin{aligned} &\begin{bmatrix} f_{xc}^{\alpha,\alpha;\alpha,\alpha} & f_{xc}^{\alpha,\alpha;\beta\beta} & f_{xc}^{\alpha,\alpha;\alpha,\beta} & f_{xc}^{\alpha,\alpha;\beta,\alpha} \\ f_{xc}^{\beta,\beta;\alpha,\alpha} & f_{xc}^{\beta,\beta;\beta,\beta} & f_{xc}^{\beta,\beta;\alpha,\beta} & f_{xc}^{\beta,\beta;\beta,\alpha} \\ f_{xc}^{\alpha,\beta;\alpha,\alpha} & f_{xc}^{\alpha,\beta;\beta,\beta} & f_{xc}^{\alpha,\beta;\alpha,\beta} & f_{xc}^{\alpha,\beta;\beta,\alpha} \\ f_{xc}^{\beta,\alpha;\alpha,\alpha} & f_{xc}^{\beta,\alpha;\beta\beta} & f_{xc}^{\beta,\alpha;\alpha,\beta} & f_{xc}^{\beta,\alpha;\beta,\alpha} \end{bmatrix} \\ = &\begin{bmatrix} f_{xc}^{\alpha,\alpha} & f_{xc}^{\alpha,\beta} & 0 & 0 \\ f_{xc}^{\beta,\alpha} & f_{xc}^{\beta,\beta} & 0 & 0 \\ 0 & 0 & \frac{v_{xc}^\alpha - v_{xc}^\beta}{\rho_\alpha - \rho_\beta} & 0 \\ 0 & 0 & 0 & \frac{v_{xc}^\alpha - v_{xc}^\beta}{\rho_\alpha - \rho_\beta} \end{bmatrix} . \end{aligned} \tag{4.39}$$

This approach to SF-TD-DFT has been applied to the dissociation of H_2 [322] and to calculate the spectra of open-shell molecules [323, 289, 154]. Very recent work has used the Wang-Ziegler approach to treat the reaction path for the *cis-trans* photochemical isomerization of 4-styrylpyridine [215, 214]. The Wang-Ziegler approach has also been proposed as the basis of a more general spin-coupled TD-DFT [317].

At first glance, Eq. (4.39) is very pretty because it contains ordinary TD-DFT for spin-preserving (SP) transitions. However we can be more

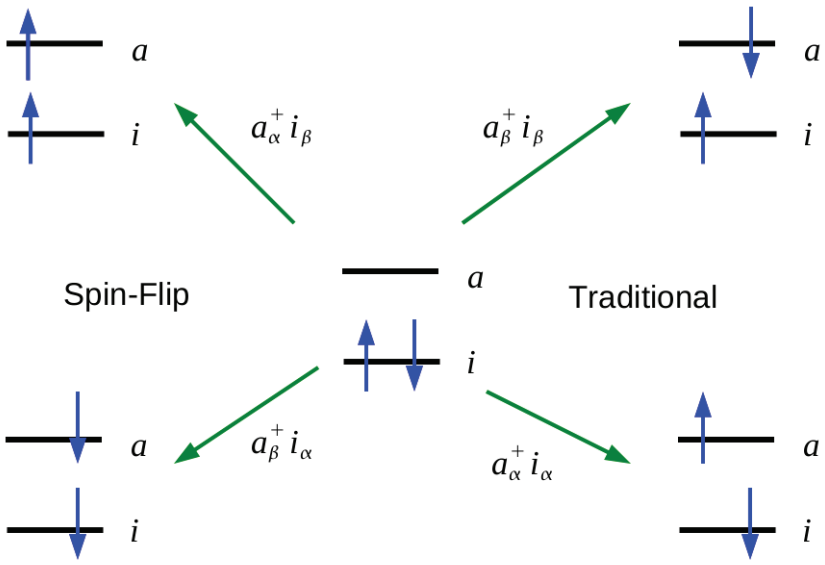

Figure 4.4: Two-orbital model of TD-DFT excitations with a closed-shell singlet reference configuration.

demanding. For example, we can require that the three triplets which are generated from the singlet referenced two-orbital model shown in Fig. 4.4 be strictly degenerate. In the TDA, ordinary TD-DFT gives the $M_S = 0$ triplet excitation energy,

$$\omega_T = \epsilon_a - \epsilon_i + (ia|f_{xc}^{\alpha,\alpha} - f_{xc}^{\alpha,\beta}|ia)\,. \tag{4.40}$$

Also in the TDA, SF-TD-DFT gives the $M_S = \pm 1$ triplet excitation energies,

$$\omega_T = \epsilon_a - \epsilon_i + (ia|\frac{v_{xc}^{\alpha} - v_{xc}^{\beta}}{\rho_\alpha - \rho_\beta}|ia)\,. \tag{4.41}$$

Since $\rho_\alpha = \rho_\beta$, the right-hand-side of Eq. (4.41) can only be interpreted as a derivative. That is, we set $\rho_\alpha = \rho_\beta + \delta$ and take the limit that the function $\delta \to 0$. Then,

$$\begin{aligned} &\frac{v_{xc}^{\alpha}(\mathbf{r}) - v_{xc}^{\beta}(\mathbf{r})}{\rho_\alpha(\mathbf{r}) - \rho_\beta(\mathbf{r})} \\ = &\lim_{\delta\to 0} \frac{v_{xc}^{\alpha}[\rho_\beta + \delta, \rho_\beta](\mathbf{r}) - v_{xc}^{\beta}[\rho_\beta + \delta, \rho_\beta](\mathbf{r})}{\delta(\mathbf{r})} \\ = &\lim_{\delta\to 0} \frac{\int f_{xc}^{\alpha,\alpha}(\mathbf{r},\mathbf{r}')\delta(\mathbf{r}')\,d\mathbf{r}' - \int f_{xc}^{\beta,\alpha}(\mathbf{r},\mathbf{r}')\delta(\mathbf{r}')\,d\mathbf{r}'}{\delta(\mathbf{r})}\,, \end{aligned} \tag{4.42}$$

which is rigorously only equal to $f_{xc}^{\alpha,\alpha} - f_{xc}^{\alpha,\beta}$ for the local density approximation (LDA), in which case Eqs. (4.40) and (4.41) reduce to

the same thing. That, of course, is quite good (probably even adequate for most applications), but it would have been nice to have a theory which was completely general.

As emphasized in the introduction, the case that most interests us in practice is when we begin with a triplet reference configuration as in the two-orbital model of Fig. 4.2 and look at $\Delta M_S = -1$ transitions. This leads to a triplet-triplet SF-TD-DFT TDA excitation energy which is equal to zero when orbital relaxation is neglected. The demonstration involves making use of the identity,

$$F^{\alpha}_{p,q} - F^{\beta}_{p,q} = (pq|\frac{v^{\alpha}_{xc} - v^{\beta}_{xc}}{\rho_{\alpha} - \rho_{\beta}}|aa) + (pq|\frac{v^{\alpha}_{xc} - v^{\beta}_{xc}}{\rho_{\alpha} - \rho_{\beta}}|ii)\,. \tag{4.43}$$

However the usual SP-TD-DFT excited singlet-triplet energy difference formula,

$$\omega_S - \omega_T = 2(ia|f_H + f^{\alpha,\beta}_{xc}|ia)\,, \tag{4.44}$$

cannot be recovered in the SF-TD-DFT formalism where instead is found,

$$\omega_S - \omega_T = 2(ii|\frac{v^{\alpha}_{xc} - v^{\beta}_{xc}}{\rho_{\alpha} - \rho_{\beta}}|aa)\,. \tag{4.45}$$

The ground to triplet excitation energy formulae obtained from the two formalisms are equally different. Furthermore there is no analogue of Brillouin's theorem in the sense that the coupling between the ground configuration (lower left in Fig. 4.2) and the singly excited configurations (right hand side of Fig. 4.2) is nonzero in this formalism. Of course, a sort of Brillouin's theorem still holds by construction in the sense that there is no coupling in this formalism between the reference triplet (center in Fig. 4.2) and any of the excited states (left and right sides in Fig. 4.2).

While the above comments suggest that there are grave problems in harmonizing the formulae of the two different TD-DFT formalisms, they do not suggest any fatal problems since different looking formulae can lead to nearly similar numerical results. It will, however, turn out that the SF-TD-DFT triplet energy is lower than the corresponding SP-TD-DFT triplet energy because orbital relaxation in the triplet is more easily described when beginning from a triplet reference than from a singlet reference. Thus the two formalisms are at least shifted with respect to one another.

Despite these unresolved problems, *we have chosen to use the Wang-Ziegler functional in the present paper for our noncollinear SF-TD-DFT calculations.* This is because we believe pure density-functionals, rather than HF exchange, to be at the heart of DFT. It thus seems more attractive to us to use the LDA or a generalized gradient approximation (GGA) in conjunction with the Wang-Ziegler noncollinear spin-flip approach than not to use potentially different amounts of HF exchange

in hybrid functionals for ground and excited states while completely ignoring the pure DFT part of the hybrid functional as implied by the pioneering SF-TD-DFT approach of Krylov and coworkers.

4.6 COMPUTATIONAL DETAILS

The benchmark geometries and electronic structure calculations used in the present work are taken from the literature. For the C_{2v} CC ring-opening pathway, we used the geometries and quantum Monte Carlo (QMC) potential energy curves given in Appendix C of Ref. [82]. The idea behind QMC is to use statistical techniques to go beyond typical high-quality *ab initio* calculations, such as CASSCF and CI, through the use of more general types of wave functions. The QMC calculations of Ref. [82] began with a conventional CASSCF calculation. This was then reoptimized by variational Monte Carlo in the presence of a Jastrow factor to include dynamical correlation. Finally diffusion Monte Carlo was used to further improve on the result of the variational Monte Carlo calculation. Suffice it to say that the result is an electronic structure calculation of very high quality (certainly better than the CASSCF starting point or multireference CI.) Geometry optimizations are not presently possible with QMC, so the benchmark geometries are those obtained by C_{2v} structure optimization at fixed ring-opening angle using DFT with the B3LYP functional [1]. For asymmetric CO ring-opening, we used the geometries and QMC potential energy curves from Appendix C of Ref. [302]. The QMC calculations in this reference are similar to those of Ref. [82], but are carried out along a typical pathway for CO ring-opening obtained by mixed TD-DFT/classical surface hopping photodynamics calculations. They pass close to a CX which was characterized at the CASSCF level in Ref. [302]. While exact CXs with the ground state are impossible in conventional TD-DFT [218], it was shown in Ref. [302] that the CX is described to a reasonably good approximation by TD-DFT in the form of an interpenetrating double cone.

Calculations for the present work were performed with the Grenoble development version of deMon2k (density of Montreal 2000) [9]. Where needed additional calculations were carried out with Gaussian 03 [11] in order to fix orbital symmetry assignments since the particular version of deMon2k used here did not yet have automatic symmetry assignments. The deMon2k program makes use of two Gaussian-type basis sets. In addition to the usual orbital basis set, there is a second auxiliary charge-density fitting basis set. Its use permits the elimination of all four-center integrals. As with other DFT programs, deMon2k uses a grid to evaluate xc-integrals. A description of the implementation of standard (spin-preserving) TD-DFT in deMon2k has been published elsewhere [181]. The present work is the first reported use of our implementation of Wang-Ziegler SF-TD-DFT

in DEMON2K. Results were compared against those obtained from the Amsterdam density-functional (ADF) [307] package and were found to be acceptably close.

The DEMON2K calculations in the present work were carried out using the Vosko-Wilk-Nusair parameterization of the LDA [320]. Density-fitting was carried out *without* imposing the charge conservation constraint [181] using the GEN-A3* density-fitting basis. The orbital basis was the extensive 6-311++G**(2d,2p) basis set [209, 80]. The SCF convergence was set at 10^{-7} and the FIXED FINE option was always used for the grid. Our SF-TD-DFT calculations used the TDA and the reference state was always the lowest energy triplet. Full advantage was taken of DEMON2K keywords allowing convergence of excited state configurations to explore alternative triplet reference configurations for SF-TD-DFT.

4.7 RESULTS

We are interested in the ability of TD-DFT to describe funnel regions. These are regions where potential energy surfaces (PESs) come close enough together that surface hopping becomes possible. Typical funnels are AXs and CXs.

Rather than being distinct phenomena, AXs and CXs are actually very closely related. The PESs of a molecule with f (15 in the case of oxirane) nuclear internal degrees of freedom, $\mathbf{R}$, is an f-dimensional hypersurface in an $(f+1)$-dimensional hyperspace. The condition that the Ith and Jth PESs cross,

$$E_I(\mathbf{R}) = E_J(\mathbf{R}), \tag{4.46}$$

reduces the dimensionality of the intersection to an $(f-1)$-dimensional hyperline. If this were all that there were to it, then we could talk about "surfaces that cross without seeing each other." However quantum mechanics typically also requires zeroing out a CI like coupling matrix element,

$$A_{I,J}(\mathbf{R}) = 0, \tag{4.47}$$

denoted $\mathbf{A}$ here to indicate that it could be the linear response matrix in the TDA. (However we could equally well have called it $\mathbf{H}$ for the CI matrix in a CASSCF calculation.) This second condition reduces the dimensionality of the intersection to an $(f-2)$-dimensional hyperpoint. CXs are impossible for diatomics for states belonging to different irreducible representations of the molecular point group because $f = 1$ and $f - 2 = -1$ is impossible. So only AXs are seen for diatomics in this case. [Crossings may occur for states belonging to different irreducible representations because Eq. (4.47) is then a consequence of symmetry and so no longer useful as a condition defining the intersection space.] However, in general, there will be two coordinates

in hyperspace along which the two intersecting PESs will separate. These two branching coordinates are normally defined by the DC,

$$h_q^{(I,J)} = \mathbf{X}_I^\dagger \frac{\partial \mathbf{H}}{\partial q} \mathbf{X}_J \,, \tag{4.48}$$

and the UGD vector,

$$g_q^{(I,J)} = \mathbf{X}_I^\dagger \frac{\partial \mathbf{H}}{\partial q} \mathbf{X}_I - \mathbf{X}_J^\dagger \frac{\partial \mathbf{H}}{\partial q} \mathbf{X}_J \,, \tag{4.49}$$

and there is quite a literature on finding and characterizing them (see e.g., Ref. [105]). Within the 3-dimensional space defined by the two branching coordinates plus the energy coordinate, a CX takes on the form of a double cone. Choosing a one-dimensional slice within the space of branching coordinates means that we will typically pass near but not through the CX and so see an AX.

In this section we report the results of our calculations to see to what extent SF-TD-DFT calculations give a better than ordinary SP-TD-DFT description of funnel regions in oxirane photochemistry in comparison with the results of previously reported-high benchmark calculations [82]. Results are divided into two parts. In the first part we look at C_{2v} ring opening which involves breaking the CC single bond. This is a one-dimensional slice and so any funnel region will appear as an AX. However it has two advantages: firstly that it represents our "normal" picture of how bonds break and secondly that we can analyze it in great detail. In the second part we look at the CX region for asymmetric CO ring opening along the typical photochemical pathway. Here we are restricted to using CASSCF branching coordinates because we are not yet able to find CXs within TD-DFT. From this point of view, our conclusions cannot be as conclusive as those of the recent study of Minezawa and Gordon [249], but nevertheless we believe the present calculations to be indicative of some of the strengths and weaknesses of Ziegler-Wang SF-TD-DFT for this type of application.

4.7.1 C_{2v} *Ring Opening*

The present SF-TD-DFT work is perhaps best understood in the light of previous work which is now briefly reviewed. Aryl substitution of oxirane favors symmetric ring opening via CC bond cleavage. Cordova *et al*. investigated the ability of TD-DFT to describe C_{2v} as well as conrotatory and disrotatory ring opening of oxirane, by comparing TD-DFT results against results from high-quality quantum Monte Carlo (QMC) calculations [82]. The high symmetry C_{2v} ring-opening pathway allowed a particularly detailed analysis. Investigation of conrotatory and disrotatory ring opening was inspired by the Woodward-Hoffmann theory of electrocyclic ring-opening reactions. The three principal UV absorption peaks were assigned to Rydberg excitations from the

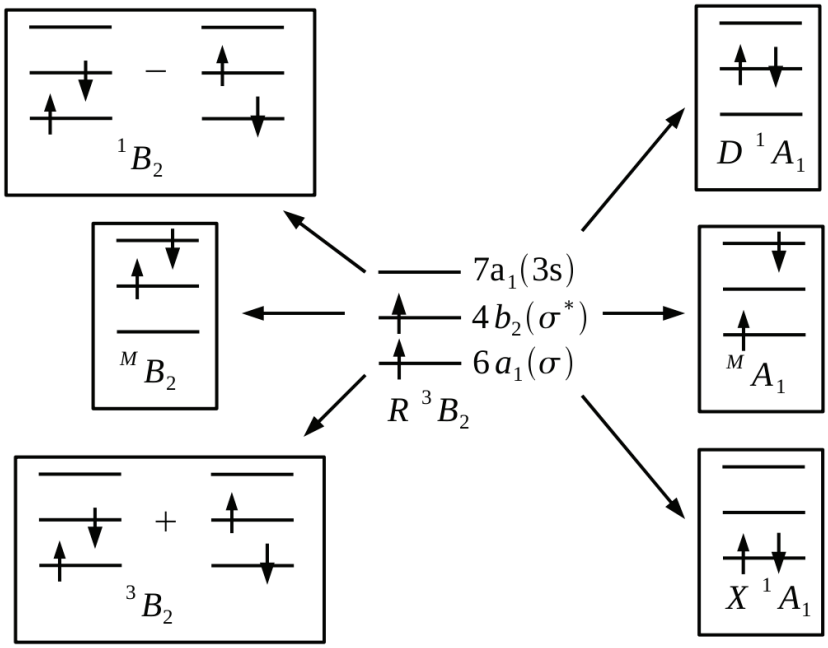

Figure 4.5: Principal frontier molecular orbital spin-flip transitions involved in the C_{2v} ring-opening of oxirane beginning from the $R\,^3B_2[6a_1(\sigma) \rightarrow 4b_2(\sigma^*)]$ reference state.

oxygen nonbonding orbital, which are difficult to describe quantitatively because of the well-known problem of underestimation of the ionization threshold [70], but which can nevertheless be described qualitatively correctly even with the simple local density approximation (LDA). The C_{2v} ring-opening pathway showed a cusp in the ground state potential energy surface when the occupied $6a_1(\sigma)$ and unoccupied $4b_2(\sigma^*)$ orbitals became quasidegenerate. This region also showed an "effective failure of NVR," which is to say that the energy of the LUMO fell below that of the HOMO. A consequence of this effective failure are severe SCF convergence problems when using a program which tries to enforce the *Aufbau* principle. Triplet instabilities were found to be omnipresent for all the symmetric ring-opening pathways investigated. It was pointed out that the TDA is a practical necessity for avoiding triplet instabilities and singlet near instabilities. With the TDA, the excited-state potential energy surfaces were found to be energetically reasonable even during bond breaking. In principle, SF-TD-DFT can improve upon the previous SP-TD-DFT calculations in two ways: first by removing the cusp along the C_{2v} ring-opening pathway through an improved description of the AX, and second through the use of a triplet reference which bypasses the effective failure of NVR in the ground singlet state and so may lead to improved convergence.

The reference in our SF-TD-DFT calculations is the lowest triplet. While the configuration of oxirane at the intial equilibrium geometry [82],

$$\cdots [6a_1(\sigma)]^2 [2b_1(\pi)]^2 [7a_1(3s)]^0 [4b_2(\sigma^*)]^0 \cdots . \tag{4.50}$$

suggests that the reference is the $1\,^3B_1[2b_1(\pi) \rightarrow 7a_1(3s)]$ state, this is at most true below a ring-opening angle of about 75°. Beyond this angle the reference triplet is the $1\,^3B_2[6a_1(\sigma) \rightarrow 4b_2(\sigma^*)]$ state. This is true not only in the range 75-120° when the configuration is,

$$\cdots [2b_1(\pi)]^2 [6a_1(\sigma)]^2 [4b_2(\sigma^*)]^0 [7a_1(3s)]^0 \cdots , \tag{4.51}$$

but also beyond 120° when the σ and σ^* orbitals change order,

$$\cdots [2b_1(\pi)]^2 [4b_2(\sigma^*)]^2 [6a_1(\sigma)]^0 [7a_1(3s)]^0 \cdots , \tag{4.52}$$

Figure 4.5 shows the frontier molecular orbitals in our SF-TD-DFT calculations (which however make use of all, not just the of the frontier, molecular orbitals). Both the ground $X\,^1A_1$ and doubly excited $D\,^1A_1$ configurations are accessible by spin-flip from the $R\,^3B_2$ reference state. Taking the symmetric and antisymmetric combinations of the $6a_1(\sigma)$ and $4b_2(\sigma^*)$ SF configurations leads to B_2 states, the triplet of which is expected to be degenerate with the $R\,^3B_2$ reference state. Two states of mixed spin symmetry ($^MB_2$ and $^MA_1$) are also formed. These states are unphysical and yet are necessarily present in any SF-TD-DFT calculation (including in the Krylov approach to SF-TD-DFT). They are readily identifiable in our calculations and have been excluded from the following discussion.

Figure 4.6 shows the results of the SF-TD-DFT calculations. The four states predicted in our qualitative discussion are all present. The $R\,^3B_2$ SCF reference curve and the corresponding $^3B_2$ SF-TD-DFT curve are not identical, but they are indistinguishable on the scale of the figure. The figure also shows a very important feature, namely the classic avoided crossing corresponding to the breaking of the CC σ bond. The traditional picture is that of H_2 described in the introduction where mixing of the σ^2 and $(\sigma^*)^2$ configurations is necessary for bond breaking. In order to confirm this two-orbital model, we isolated the part of the SF-TD-DFT corresponding to the $4b_2(\sigma^*) \rightarrow 6a_1(\sigma)$ and $6a_1(\sigma) \rightarrow 4b_2(\sigma^*)$ SF transitions. Diagonalizing this 2×2 matrix gives the two-orbital model adiabatic curves in Fig. 4.6, which are seen to be in semiquantitative agreement with the results of the full SF-TD-DFT calculation. The diagonal elements of the 2×2 matrix give the corresponding diabatic curves. These show how the σ^2 ground state configuration at small angles continues on at large angles to become an excited state and how the $(\sigma^*)^2$ excited state configuration at small angles continues on at large angles to become the ground state at large angles. Thus it would seem that SF-TD-DFT can correctly describe avoided crossings associated with bond breaking.

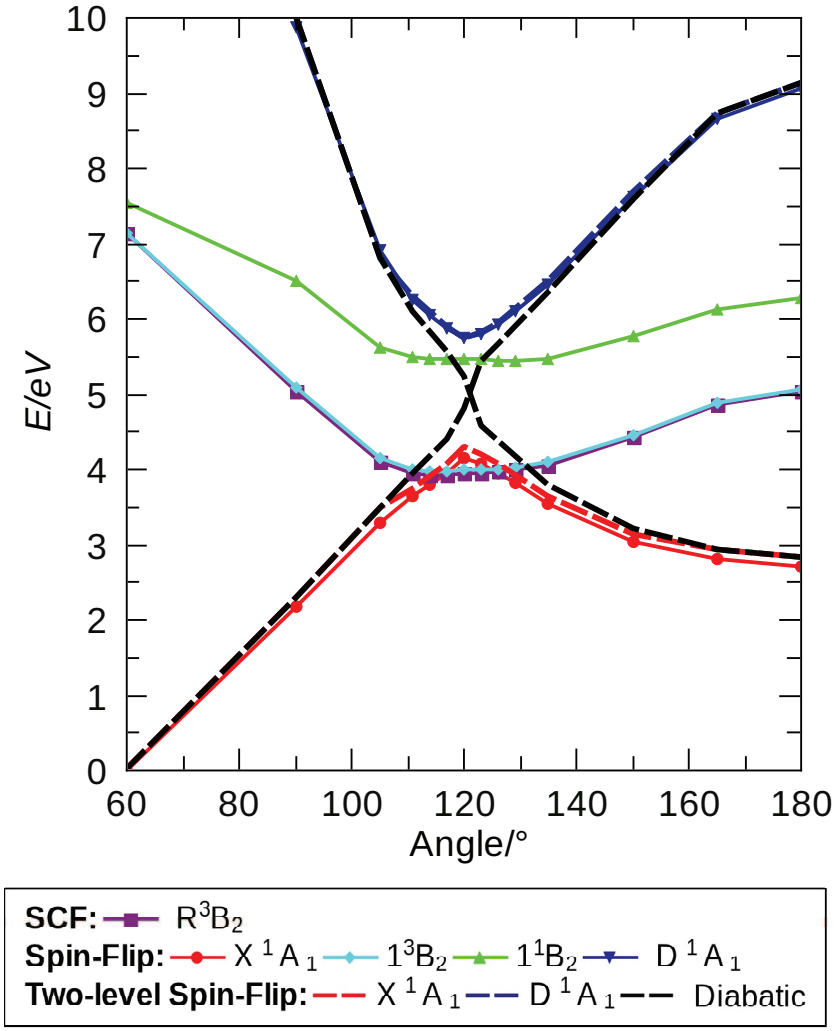

Figure 4.6: C_{2v} potential energy curves: full calculation (solid lines), two-orbital model (dashed lines).

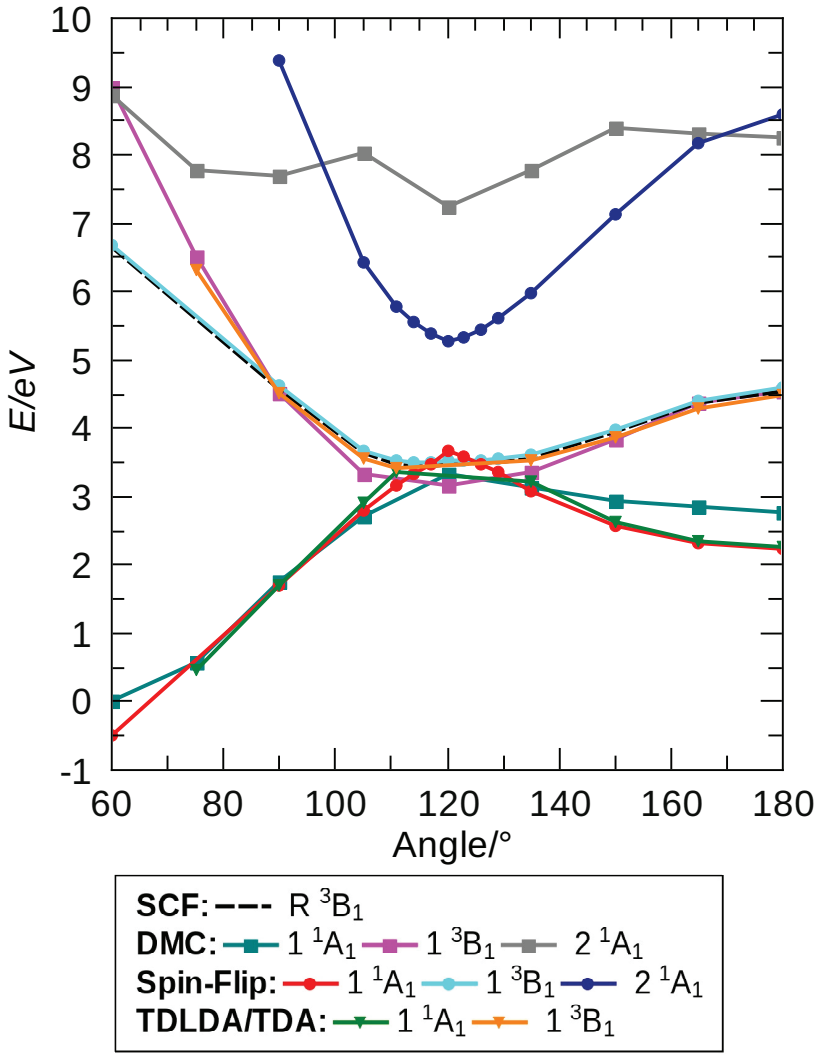

Figure 4.7: Comparison between different methods for the X^1A_1, 1^3B_2, and D^1A_1 C_{2v} ring-opening potential energy curves: SF-TD-DFT triplet SCF reference state (black dashed line), SF-TD-DFT (circles), SP-TD-DFT (squares), and DMC (triangles). All curves have been shifted to give the same ground state energy at a ring-opening angle of 80°.

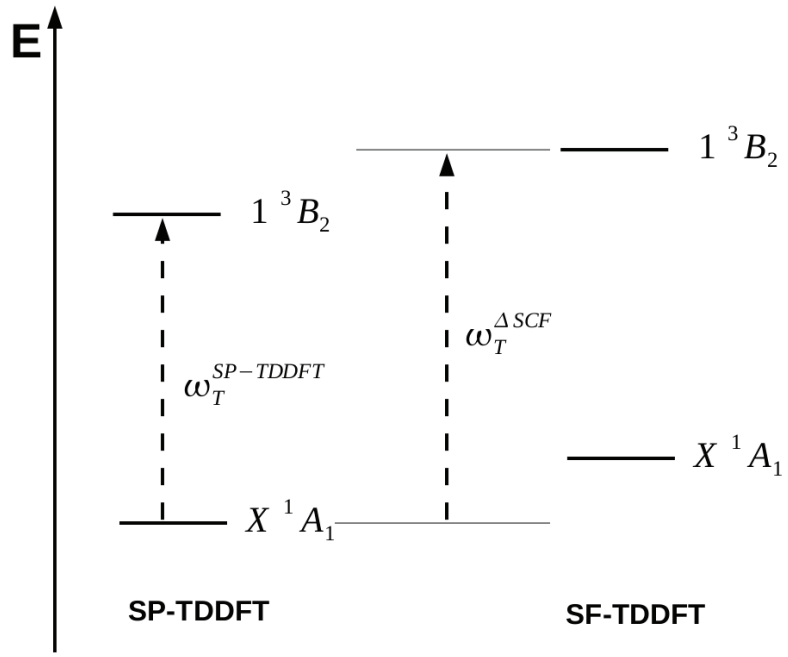

Figure 4.8: Illustration of orbital relaxation effects in SF versus SP TD-DFT.

Figure 4.7 compares the present SF-TD-DFT calculations with both ordinary SP-TD-DFT calculations obtained with the LDA functional and the TDA (Ref. [82]) and with the QMC benchmark calculations. Let us begin first with the comparison with SP-TD-DFT calculations. As explained in Ref. [82], the bond-breaking region around 120° is an example of effective failure of NVR where the LUMO falls lower in energy than the HOMO. The result is that "normal" DFT programs which insist on filling the Kohn-Sham orbitals according to the *Aufbau* principle will inevitably fail to converge in this region. This is why there are neither SCF ground state nor SP-TD-DFT results near 120° in the figure. Very significantly, few convergence difficulties are encountered for the triplet reference state. This would seem to be very good news for those who would like to carry out routine photodynamics calculations where SCF convergence failures can be highly inconvenient if not fatal to the calculations.

In the region where the SCF ground state does converge the *shape* of the ground $X\,^1A_1$ and excited $1\,^3B_2$ curves are very similar for SF-TD-DFT and SP-TD-DFT calculations. Before shifting the SF-TD-DFT curves are actually 0.41 eV in energy higher than the corresponding SP-TD-DFT curves. Differences between SCF and TD-DFT triplet excitation energies have been previously discussed by Casida *et al*. [71] who gave an analysis within a two-level model. The result is that the SF-TD-DFT triplet reference is expected to be higher in energy than the SP-TD-

DFT triplet by the charge-transfer correction (really a density-transfer correction or relaxation effect),

$$\omega_T^{\Delta SCF} - \omega_T^{SP\text{-}TDDFT} \approx \frac{1}{2}(\Delta\rho|f_H + f_{xc}^{\alpha,\alpha}|\Delta\rho) > 0\,. \tag{4.53}$$

This is illustrated in Fig. 4.8. Simultaneously there is a problem describing the ground state with orbitals optimized for a triplet. The result is that the SF-TD-DFT method overestimates the ground state energy. However energy differences do appear to be similar in SF-TD-DFT and in SP-TD-DFT when the same configurations are concerned, so that a rigid shift of energy levels is reasonable.

Having established the similarity and differences of the DFT approaches, let us now compare against the QMC benchmark calculations. Just as relaxation effects lead to the underestimation of the SP-TD-DFT $1\,^3B_2[6a_1(\sigma) \rightarrow 4b_2(\sigma^*)]$ state with respect to the SF-TD-DFT SCF reference state, so we can expect the SF-TD-DFT $D\,^1A_1\{[6a_1(\sigma)]^2 \rightarrow [4b_2(\sigma^*)]^2\}$ to be underestimated with respect to an SCF calculation with the doubly-excited configuration. This may help to explain why the SF-TD-DFT $D\,^1A_1$ is significantly below the corresponding QMC curve. Consequently we may also expect important differences between the SF-TD-DFT and QMC description of the ground state curve in the region of the avoided crossing. Nevertheless, except for the point at 60°, the shape of the QMC and DFT ground state curves agree reasonably well below about 100°. Significant differences only really appear in Fig. 4.7 between the DFT and QMC ground state curves at higher angles. We must conclude that SF-TD-DFT is not able to capture all of the correlation effects present in QMC at these angles. Note that the QMC $D\,^1A_1$ also seems to be mixing with one or more singly-excited states (see Table II of Ref. [82]), none of which are accessible to the SF-TD-DFT formalism used here. The result is a QMC $D\,^1A_1$ curve which is rather flatter than its SF-TD-DFT counterpart.

4.7.2 *Photochemical Pathway*

Alkyl substitution of oxirane and indeed oxirane itself does not undergo symmetric ring opening. Rather photochemical ring-opening of oxirane is believed to proceed via the three step Gomer-Noyes mechanism shown in Fig. 4.1. In Ref. [302], Tapavicza *et al.* carried out Tully-type TD-DFT/classical trajectory surface-hopping photodynamics calculations using the TDA. This study confirmed and detailed the Gomer-Noyes mechanism. It was shown that the $^1(n, 3p_z)$ Rydberg state is directly linked to a $^1(n, \sigma^*)$ valence CO antibonding state. Initial excitation leads within 100 femtoseconds or so to population of the $^1(n, 3p_z)$ state and thereby to spontaneous ring-opening (step 1 in Fig. 4.1). Structure (II) of Fig. 4.1 is a CX with mixed zwitterionic and biradical character permitting electronic de-excitation directly to a vibrationally hot (4000 K) electronic ground state. At this point

there is enough energy for several things to happen, one of which is hydrogen abstraction (III) followed by CC bond breaking. High-quality QMC calculations were carried out along a typical trajectory and used for comparison purposes. Once again an effective failure of NVR was encountered, but difficulties with SCF convergence problems are minimized in dynamics calculations by restarting the SCF for each new geometry from the converged result of the previous geometry, so that orbital-following rather than *Aufbau* filling is enforced.

In this subsection we compare the results of our SF-TD-DFT calculations with results of other methods along this trajectory. The trajectory involves the following "events": Only the initial geometry has C_{2v} symmetry, so we fall back on a more chemical nomenclature for key molecular orbitals. The first excited singlet state, S_1, is initially assigned as $1\,^1B_1[b_1(\pi) \rightarrow a_1(3s)]$ and thereafter as simply $^1(\pi, 3s)$. This state remains of Rydberg character throughout the photoreaction. However the second excited singlet state, S_2, does not. Instead, S_2 is initially $2\,^1B_1[b_1(\pi) \rightarrow a_1(3p_z)]$, remains of $^1(\pi, 3p_z)$ Rydberg type for only a short time, soon falling in energy to become the new S_1 as it takes on valence-type CO antibonding character, $^1(\pi, \sigma^*_{CO})$. At that point $^1(\pi, 3s)$ is the new S_2. In fact, what happens is qualitatively very much in-line with the Woodward-Hoffmann orbital correlation scheme described in Ref. [82] (Fig. 1 of that reference) for the C_{2v} ring-opening reaction but without the symmetry. The trajectory finally passes through (or near) a CX where surface hopping takes place. The nature of this CX has been discussed in Ref. [302]. Suffice it to say that it is probably best described by the resonance structure II shown in Fig. 4.1, which has both biradicaloid and zwitterionic character.

Results are shown in Fig. 4.9 alongside those from the QMC and SP-TD-DFT calculations of Ref. [302]. Configuration interaction singles (CIS) calculations obtained using GAUSSIAN [11] and the same basis set have also been included in the figure. It appears from this figure that the S_1/S_0 CX is perhaps a bit better described by SP-TD-DFT than by SF-TD-DFT and, as expected, that both are significantly better than the CIS description of the same CX. Most dramatic however is the difference between the behavior of the SP-TD-DFT S_2 state, which is in relatively good agreement with the QMC S_2 state and in qualitatively reasonable agreement with the CIS S_2 state, and the SF-TD-DFT S_2 state which takes an energetic dive as the ring opens. This latter state is in fact highly spin-contaminated and hence unphysical.

It is clear from both the SP-TD-DFT and SF-TD-DFT calculations that the S_1 state is predominantly of $^1(\pi, \sigma^*_{CO})$ character. This confers a partial CO σ biradicaloid character by reducing the bond index to 1/2. The SF-TD-DFT reference configuration is geometry dependent but for most geometries is,

$$\begin{aligned} \text{spin } \alpha\text{:} \quad & \cdots \pi^1 \sigma^1_{CO} (\sigma^*_{CO})^1 \cdots \\ \text{spin } \beta\text{:} \quad & \cdots \sigma^1_{CO} \pi^0 (\sigma^*_{CO})^0 \cdots . \end{aligned} \tag{4.54}$$

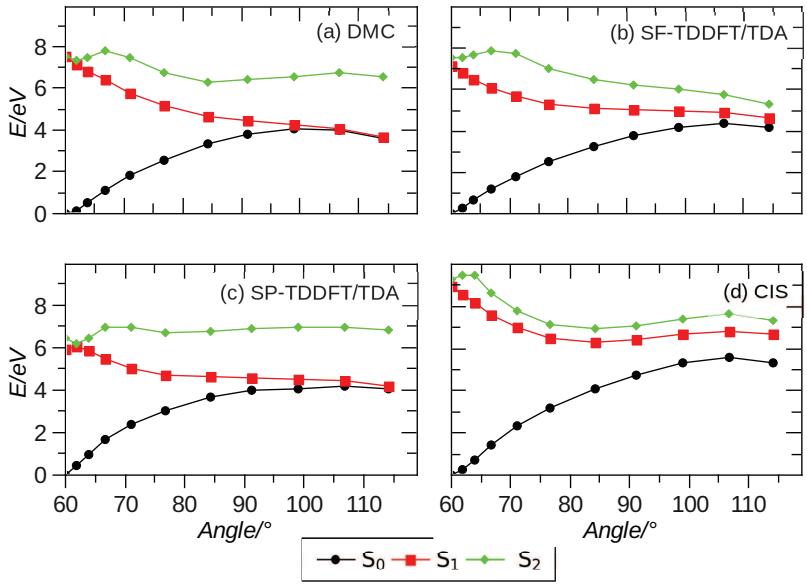

Figure 4.9: Potential energy curves for asymmetric ring-opening in oxirane calculated with various methods.

Formation of the $\sigma^2_{CO} \rightarrow (\sigma^*_{CO})^2$ is thus impossible. Rechoosing the orbital occupations as,

$$\begin{aligned} \text{spin } \alpha\text{:} \quad & \cdots n^1 \sigma^1_{CO} (\sigma^*_{CO})^1 \cdots \\ \text{spin } \beta\text{:} \quad & \cdots n^1 \sigma^0_{CO} (\sigma^*_{CO})^0 \cdots , \end{aligned} \tag{4.55}$$

makes the usual $\sigma^2_{CO}/(\sigma^*_{CO})^2$ description of a biradical possible but explicit calculations (not shown here) show S_0 and S_1 potential energy surfaces which are misshapen and much too high in energy, something we can only partly attribute to the use of orbitals optimized for a triplet excited state. As the electronic configuration around the CX likely has both some $^1(n, \sigma^*_{CO})$ and some $\sigma^2_{CO}/(\sigma^*_{CO})^2$, it is remarkable that SP-TD-DFT and SF-TD-DFT with reference configuration (4.54) do as well as they do.

4.7.3 *Conical Intersection*

Let us now take a closer look at what is happening around the CX, first reviewing some of the conclusions of Ref. [302]. Earlier Levine *et al*. had noted that a true CX could not exist between S_0 and S_1 because condition (4.47) is a consequence of the formalism and hence cannot serve as a criterion for fixing the dimensionality of the intersection space [218]. Tapavicza *et al*. verified this point but showed that an approximate CX did exist in adiabatic TD-DFT for the asymmetric ring opening of oxirane, provided appropriate care was taken in treating convergence problems. These convergence problems result from an effective failure of NVR near the CX as shown schematically in

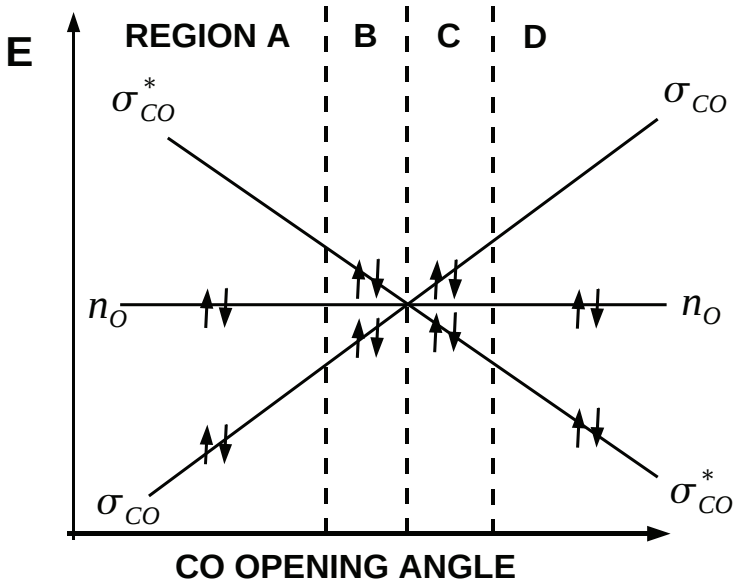

Figure 4.10: Schematic Walsh diagram showing how the orbital fillings during asymmetric ring-opening in a normal TD-DFT calculation. Regions B and C show effective violation of NVR.

Fig. 4.10. The representation can only be schematic because the orbitals mix and their energetic ordering varies with the mixing. However this representation, while simplified, is as close as possible to what emerged during lengthy discussions between one of us (MEC) and Enrico Tapavicza [304]. However Tapavicza *et al*. were able to maintain the lower energy solution with its "hole below the Fermi level" by a sort of "orbital following." The result is an approximate TD-DFT CX in the form of interpenetrating double cones as shown in Fig. 4.11. The similarity between the behavior of the TD-DFT and CASSCF PESs is perhaps even more clear in Fig. 4.12 where the $S_0 \rightarrow S_1$ excitation energy is shown for the CASSCF branching plane.

Given the results obtained in the case of the symmetric C_{2v} CC ring-opening reaction, we expected that SF-TD-DFT would give a rather good description of the asymmetric CO ring-opening reaction by mixing configurations with doubly occupied σ_{CO} and doubly occupied σ^*_{CO} orbitals. Levine *et al*. also suggested that SF-TD-DFT might be the solution to the CX problem in TD-DFT [218]. Figures 4.11 and 4.12 show that the situation is not so simple. These results do seem to confirm what is expected theoretically, namely that SF-TD-DFT is able to produce a CX by coupling ground and excited states. However the SF-TD-DFT S_0/S_1 intersection is located at a position between that found in CIS and that found with CASSCF (and approximately by SP-TD-DFT).

It is worth taking a closer look. Figure 4.11 shows that, while not identical, the SF-TD-DFT ground state more closely resembles the CIS ground state than the CASSCF ground state. In particular both the

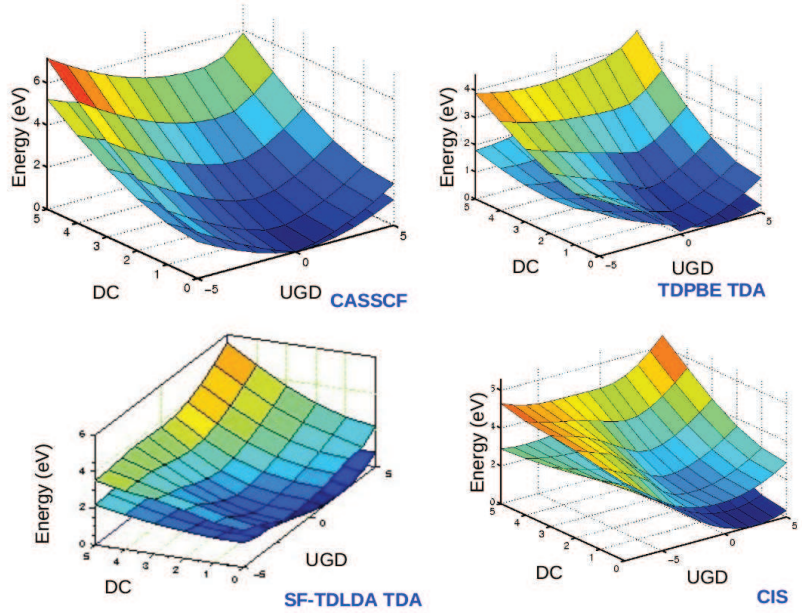

Figure 4.11: Comparison of the S_0 and S_1 PESs calculated using different methods for the CASSCF branching coordinate space. All but the SF-TD-DFT part of the figure have been adapted from Ref. [302]. See also that reference for a detailed description of the branching coordinates.

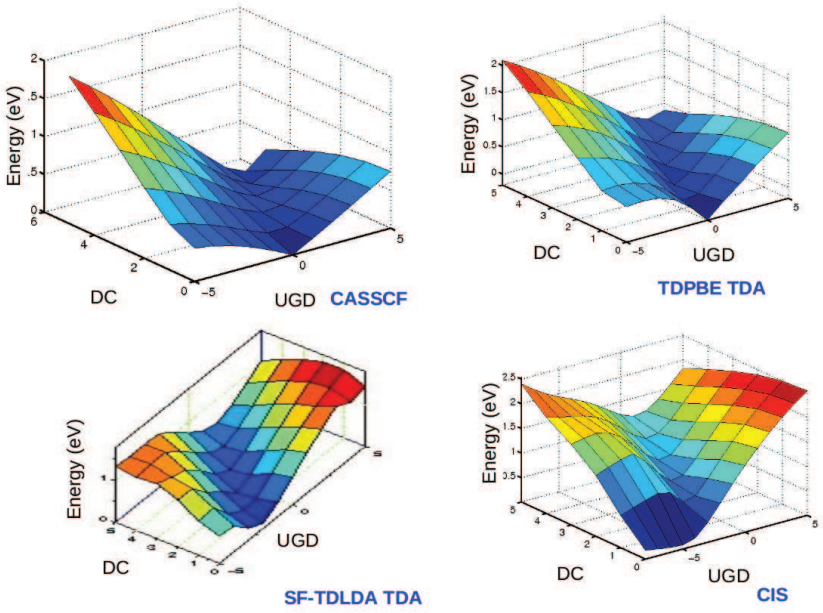

Figure 4.12: Comparison of the $S_0 \rightarrow S_1$ excitation energy surfaces calculated using different methods for the CASSCF branching coordinate space. See Ref. [302] for a detailed description of the branching coordinates.

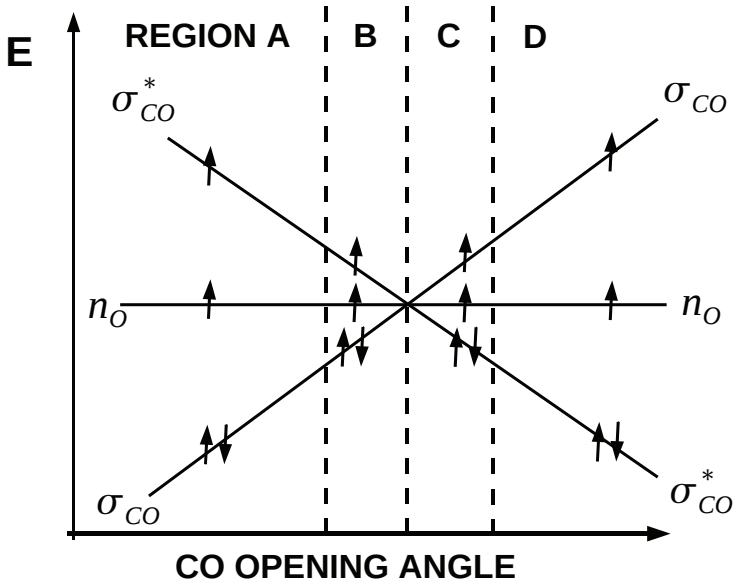

Figure 4.13: Schematic Walsh diagram showing how the orbital fillings vary during asymmetric ring-opening in a SF-TD-DFT calculation.

SF-TD-DFT and the CIS PESs have a minimum at (DC,UGD)=(0,2) while the CASSCF PES has its minimum at the origin. This indicates that it is highly unlikely that $(\sigma_{CO})^2$-$(\sigma^*_{CO})^2$ configuration mixing is actually occuring near (DC,UGD)=(0,0). (As might be expected, straight DFT also gives a result similar to SF-TD-DFT for the ground state.) Our explanation is shown schematically in Fig. 4.13 which shows how the reference triplet configuration evolves with ring-opening angle. Though the spin α and β orbitals have different energies in our spin-unrestricted calculation and significant orbital remixing occurs, this explanation could still be confirmed by explicit orbital visualization. Conclusions based upon Fig. 4.13 explain our results rather well, because there is no geometry where SF-TD-DFT can simultaneously lead to both the $(\sigma_{CO})^2$ and $(\sigma^*_{CO})^2$ configurations.

We have carried out SF-TD-DFT by enforcing an initial $\sigma^1_{CO}(\sigma^*_{CO})^1$ triplet state Eq. (4.55), with significant degradation of results compared to the CASSCF and SP-TD-DFT curves. This is in line with our above mentioned observations for the asymmetric ring opening pathway when the reference configuration was rechosen as (4.55).

4.8 CONCLUSION

The present paper is a contribution to our understanding of how well TD-DFT, and SF-TD-DFT in particular, is able to describe critical funnels in photochemical reactions. We have chosen the small molecule oxirane for our study because of the availability of previously reported high-quality *ab initio* results [82, 302] for comparison and have investi-

gated the avoided crossing (AX) in the C_{2v} ring-opening pathway, the more physical CO ring-opening pathway, and the associated conical intersection (CX).

As pointed out in the introduction, the recent development of mixed TD-DFT/classical trajectory SH photodynamics [103, 84, 301, 302, 328, 250] is fueling investigations of the ability of TD-DFT to describe critical funnel regions [79, 29, 218, 174, 82, 175, 302, 306, 305]. Such regions often correspond to the formation of diradicals through bond breaking. Traditional wisdom tells us that a correct description of such regions requires mixing of the ground-state configuration with doubly-excited configurations, which are not normally available to ordinary spin-preserving (SP) TD-DFT. In particular, Levine *et al*. argued convincingly that CXs cannot exist between the ground and excited states in SP-TD-DFT in the usual case where the TD-DFT adiabatic approximation is employed [218]. This is counter to the idea that exact TD-DFT should be able to describe this coupling [82] and that an approximate CX has been found in practice [302]. Nevertheless it is highly desirable to find a way to include double excitations so as to obtain a more rigorous description of funnel regions. One active area of research which may lead to a better understanding of the problem, if not a solution, is the explicit inclusion of 2- and higher-electron excitations through the frequency-dependence of the xc-kernel [74, 233, 62, 243, 278, 149]. In the meantime, spin-flip (SF) TD-DFT [291, 295, 322, 323, 289, 154, 325, 199, 317, 308, 212, 215, 214] offers an attractive alternative. Indeed this was also recognized by Levine *et al* [302]. The present work reports our implementation of Wang-Ziegler noncollinear SF-TD-DFT in the program deMon2k and constitutes a test of the usefulness of SF-TD-DFT for photochemical funnels.

We know of only two previous works on this subject. One is unpublished work by Lawson Daku, Linares, and Boillot who used Wang-Ziegler SF-TD-DFT to investigate the *cis*/*trans* photoisomerization of 4-styrylpyridine [215, 214]. The other is recent work by Minezawa and Gordon who characterized CXs in ethylene using the Krylov variant of SF-TD-DFT [249]. While both of those applications appeared to be successful, they are both restricted to *cis*/*trans* isomerization around a double bond. Here we treat something very different, namely photochemical ring-opening and are only able to report mixed success.

We first applied SF-TD-DFT to study the AX along the C_{2v} ring-opening pathway. A few problems show up which are not present in the obligatory test of dissociation of H_2 (Fig. 4.3). One problem is the presence of unphysical states of mixed spin symmetry (Fig. 4.5). Fortunately these were readily identifiable and so could be appropriately ignored. A second problem arises in comparing the results of SP-TD-DFT beginning from the ground-state singlet determinant reference and SF-TD-DFT beginning from the lowest triplet determinant reference. The different choice of reference immediately implies the

possible presence of an orbital relaxation energy correction and indeed the SF-TD-DFT potential energy curves are shifted by about 0.4 eV from the corresponding SP-TD-DFT curves. Nevertheless SF-TD-DFT is to be quite successful in describing the interesting AX.

This is especially true when it is realized that the usual SP-TD-DFT calculations run into serious convergence problems in the vicinity of the AX [82]. This is exactly a region of effective violation of noninteracting v-representability [302]. Minimizing the total energy with integer occupation number leads to a violation of the *Aufbau* principle with the LUMO below the HOMO or (to put it in more solid-state physics language) with a hole below the Fermi level. Most quantum chemistry programs seek to enforce the *Aufbau* principle even in this case with the result that convergence is not possible at this geometry. In contrast, no particular convergence problems were encountered using SF-TD-DFT and the triplet reference.

The question arises as to what can be done in order to remove the unphysical mixed spin-symmetry states in the SF-TD-DFT calculations. Vahtras and Rinkevicius have proposed what appears to be a very elegant formal solution [317]. They propose a reformulation of TD-DFT which makes use from the very beginning of explicit spin-coupled excitation and de-excitation operators. This requires using the same orbitals for different spin (i.e., a spin-restricted formalism) which is often viewed as at odds with the variational principle in density-functional theory, but this perhaps is a small price to pay. (Note however that our own experience in the present work is that spin-restricted calculations can be significantly more difficult to converge than spin-unrestricted calculations. This is one reason why all of our calculations have been done in the spin-unrestricted formalism.) More importantly putting the Vahtras-Rinkvicius scheme into practice still means finding explicit ways to include matrix elements involving 2-electron and higher excitations. We have already mentioned research aimed at the explicit inclusion of 2- and higher-electron excitations through the frequency-dependence of the xc-kernel [74, 233, 62, 243, 278, 149]. Another approach which should be mentioned is to handle these states by a transformed reference via an intermediate configuration Kohn-Sham TD-DFT procedure proposed by Seth and Ziegler with its very appropriate acronym "TRICKS-TD-DFT" [289]. The basic idea is to combine SF-TD-DFT with different reference states using ideas from the Ziegler-Rauk-Baerends multiplet sum method to make first-order estimates of the pure spin-states corresponding to the mixed states. [340] Thus, in the case of the ${}^{M}(a_1 \rightarrow b_1)$ mixed state on the right hand side of Fig. 4.5 obtained from SF-TD-DFT, we could calculate the energy for the corresponding ${}^{3}(a_1 \rightarrow b_1)$ triplet state from conventional SP-TD-DFT and then use the multiplet sum formula

$$\omega_S^{\text{TRICKS-TDDFT}} = 2\omega_M^{\text{SF-TDDFT}} - \omega_T^{\text{SP-TDDFT}}, \tag{4.56}$$

to estimate the energy of the $^1(a_1 \rightarrow b_1)$ singlet state. Similar ideas have been used to advantage in the recent study of the reaction path for the *cis*/*trans* photochemical isomerization of 4-styrylpyridine [215, 214]. The main drawback, and the reason that this approach was not considered here, is that finding corresponding spin α and β orbitals is not only not always easy but also not always possible in the spin-unrestricted (i.e., different-orbitals-for-different-spins) approach. It turns out that this is especially true in the funnel regions which interest us most.

Perhaps the most interesting and important result in this paper came when we pursued the CO ring-opening path way and examined the physically-important CX. The situation is very different than the case of *cis*/*trans* photoisomerization. In that case, the HOMO and LUMO are typically the π and π^* orbitals associated with the double bond around which rotation is occuring. It is also true that the HOMO and LUMO involved in the C_{2v} ring-opening reaction are the σ and σ^* orbitals associated with breaking the CC bond. The oxygen lone pair (n) is tightly enough bound that it stays out of the way. However along the physical CO ring-opening reaction route, elementary chemical arguments indicate that the oxygen lone pair intercedes as HOMO between the relevant CO σ and σ^* orbitals. This means that taking the lowest triplet as reference does not necessarily lead to an optimal description of the biradical present at the CO ring-opening CX. In particular, attempts to include the doubly-excited $\sigma^2 \rightarrow (\sigma^*)^2$ configuration exclude the possibility of the $^1(n, \sigma^*)$ configuration whose importance is well-established, and did not prove useful. Nevertheless S_0/S_1 coupling exists in SF-TD-DFT meaning that a CX is theoretically possible. Indeed such a feature is seen in our lowest energy triplet SF-TD-DFT calculations roughly half-way between the location of the CASSCF CX and the CIS seam.

We conclude that, depending upon the molecule and the CX, the lowest triplet state may or may not be the optimal choice of reference for SF-TD-DFT. However the asymmetric ring-opening reaction in oxirane should be taken as a warning that choosing a suitable triplet reference for SF-TD-DFT may require a nontrivial use of chemical intuition. This is likely to be especially problematic for larger molecules and is unlikely to be practical for on-the-fly photodynamics calculations. Thus, for the moment, SF-TD-DFT remains an *ad hoc* solution for particular problems rather than a universal panacea.

5

WAVELETS FOR TD-DFT

As theoretical methods have improved and available computing power has increased there has been a continuing trend towards DFT studies on larger size systems [20]. One of the modern methodological trends in the development of computational methods includes the wavelet-based DFT program, BIGDFT. This pseudopotential code for bigger systems [136] based as it is on traditional Hohenberg-Kohn-Sham DFT, could only calculate ground-state properties with an eye to order-N DFT. As a step to increase the feasibility of the code we have formulated wavelet-based LR-TD-DFT and the article that is included in this chapter presents our first implementation for calculating electronic excitation spectra [60, 186] in BIGDFT for the well-studied test case N_2. In this work we also present first calculated spectra of one of the biologically important molecule from the flugi family using our implemented TD-DFT calculations with the aim of providing the spectral details of these fluorescent molecules.

Density functional theory is widely used in the computations of materials properties. It has a demonstrated ability to produce results that, whose predictive value for ground-state electronic structure are competitive with the best traditional methods of quantum chemistry. In addition, DFT has superior scaling properties [23], and so can be applied to much larger systems than can the traditional methods. Although several general-purpose computer codes for DFT-based calculations of molecular and solid structures have become commercially available [129, 13, 46], the writing of such codes remains largely an effort pursued in several research groups, working in collaboration. Such groups focus on the solution of problems of physics and chemistry, and tend to establishing the limits of accuracy of the underlying methods. Within the accuracies of the KS approach the only remaining limitations on the types and sizes of systems which can be tackled are the efficiency of the computations, the choice of basis set, and the availability of sufficient computing power. Today, even the difficulty of dealing with thousands of atoms has been circumvented due the joint advance of computer and theoretical methods. However, another difficulty – conceptual difficulty still stand. One recent contribution towards this computational and also as an alternative way to deal with the conceptual difficulties is the massively parallel BIGDFT code which uses a wavelet basis set on a real-space grid to obtain essentially basis-set limit results for DFT.

Several extensions to DFT that allow for the treatment of excited states have recently been developed and implemented. The imple-

mentation of TD-DFT in Gaussian [129] had led to an explosion in the number of calculations using this particular variant of excited-state DFT. The performance of TD-DFT for vertical excitation energies to valance excited states is often quite good [311, 35, 298], with an apparent accuracy similar to some of the best ab initio methods. When the excited state of interest has significant Rydberg character, there are often problems related to the improper asymptotic properties of most functionals [311, 66]. An efficient approximate formulation of TD-DFT has been presented [170] that makes the computational cost almost identical to the CIS method. These considerations make TD-DFT a very attractive method in the context of first-principles photodynamics calculations.

5.1 COMMENTS ON MY CONTRIBUTION TO THIS ARTICLE

We begin in section 5.2 with a small introduction to LR-TD-DFT and importance of wavelet theory in computational science. We continue in section 5.3 by introducing the time-dependent density-functional theory and explaining our implementation details in section 5.4. Before showing the results, it is important to validate our implementation in the wavelet-based code BIGDFT by comparing the test case results against GTO-based program DEMON2K in section 5.5. Next we turn our attention in section 5.6 to our actual application, excited-state calculations of a fluorescent molecule Flugi **6** (See figure 5.1) .

This is also one of the projects which interest me a lot because a) when I was working on this project, I started to realize the real objective of my thesis by bringing ideas from two different quantum mechanics comunities. b) I had a chance to interact with experimentalists. It was right on time when we just finished the implementation on BIGDFT, Olga came to us with the details of structure and spectrum of Flugi **6**. Among several authors in the article, Luigi was the one helped with the implementation part, Olga and Max were responsible for this beautiful collaborative work, and Christian did the X-ray crystallography to get the structural details. Most of my preliminary knowledge about wavelets were come from Thierry who is really helpful throughout this project whereas Mark helped me to interpreting the results and with my writing.

WAVELET-BASED LINEAR-RESPONSE TIME-DEPENDENT DENSITY-FUNCTIONAL THEORY

BHAARATHI NATARAJAN, LUIGI GENOVESE, MARK E. CASIDA, THIERRY DEUTSCH, OLGA N. BURCHAK, CHRISTIAN PHILOUZE AND MAXIM Y. BALAKIREV

- Submitted (under review) to *Chemical Physics*.
- http://arXiv:1108.3475v1.

5.2 INTRODUCTION

The last century witnessed the birth, growth, and increasing awareness of the importance of quantum mechanics for describing the behavior of electrons in atoms, molecules, and solids. One key to unlocking the door to widespread applications was the advent of scientific computing in the 1960s. New computational methods had to be developed — and continue to be developed — to make use of the increasing computational power. Wavelet-based methods are a comparative newcomer to the world of electronic structure algorithms (Refs. [25, 143] provide useful, if dated, reviews) but offer increasing accuracy for grid-based DFT calculations of molecular properties. Although DFT is a theory of the ground stationary state, excited states may be treated by the complementary time-dependent (TD) theory. This paper reports the first implementation of TD-DFT in a wavelet-based code — namely our implementation of linear response TD-DFT in the BIGDFT [2] program. TD-DFT results obtained with our implementation in BIGDFT and with the GTOs based program DEMON2K [9] are compared and BIGDFT is used to calculate and analyse the absorption spectrum of a recently-synthesized small organic molecule [51].

Modern computing requires discretization and this has been historically treated in DFT and non-DFT *ab initio* [6] electronic structure calculations by basis set expansions. Because the basis set is necessarily finite, electronic structure algorithms for solids and molecules have developed as refinements on physically-sensible zero-order systems, based upon the reasonable idea that fewer basis functions should be needed when the underlying physics is already approximately correct. Thus computations on solids used plane-wave basis sets partly because of analogies with the free-electron model of metals and partly for other reasons (ease of integral evaluation and Bloch's theorem taking explicit account of crystal symmetry.) Similarly computations on molecules are typically based upon the LCAO approximation to

molecular orbitals, with split-valence, polarization, and diffuse functions added as needed to go beyond this crude first approximation. A key feature of finite-basis-set calculations has been the use of the variational principle in order to guarantee smooth convergence from above to the true ground-state energy.

Meanwhile a different set of methods developed within the larger context of engineering applications, where model-independent methods are important for treating a variety of complex systems. These methods involve spatial discretization over a grid of points and include finite-difference (FD) methods, finite-element (FE) methods, and (more recently) wavelet methods. Use of these methods in solid-state electronic structure calculations is particularly natural in areas such as materials science where physics meets engineering [44], in real-time applications [73] and also in chemical engineering [252].

Although one of the first applications of computers to scientific problems was to solve the Schrödinger equation by direct numerical integration using the Cooley-Cashion-Zare approach [81, 59, 338] and this method soon became the preferred way to find atomic orbitals [121, 237, 122], quantum chemists have been slow to accept grid-based methods. There have been at least three reasons for this. The first is the principle that any two quantum chemistry programs should give the same answer to machine precision when the same calculation is performed. Historically this principle has been essential for debugging and assuring the consistency of the multiple sophisticated GTO-based programs common in quantum chemistry. The second reason is the fear that numerical noise would undermine the variational principle and make chemical accuracy (1 kcal/mol) impossible to achieve for realistic chemical problems. The first principle has gradually been abandoned with the wide-spread adoption in quantum chemistry of DFT and its associated grid-based algorithms. The second reason is simply an obsolete fear as grid-based methods are now more precise and free of numerical error than ever before. A third reason for the slow acceptance of grid-based methods in quantum chemistry is the conviction that the continuum-like unoccupied orbitals typically produced by grid-based methods are not the most efficient orbital-basis set to use when large CI or MBPT type expansions are needed for the accurate description of electron correlation. Rather it is more useful to replace continuum-like unoccupied orbitals with natural orbitals or with other orbitals localized in the same region of space as the occupied orbitals since this is where electron correlation occurs. We discuss this problem further in Sec. 5.5.

Wavelet-based codes represent some of the latest evolutions in grid-based methods for the problem of electronic structure calculations. Daubechies classic 1992 book [89] helped to establish wavelet theory as the powerful, flexible, and still-growing toolbox we know today. Wavelet theory has deep roots in applied mathematics and computa-

tional theory, and has benefited from the various points of view and expertises of researchers in markedly different but complementary disciplines. (Ingrid Daubechies describes this aspect of wavelet theory rather well in a 1996 viewpoint article [90].) Wavelet theory somewhat resembles the older Fourier theory in its use of continuous and discrete transforms and underlying grids. However wavelet theory is designed to embody the powerful idea of MRA that coarse features are large-scale objects while fine-scale features tend to be more localized. Computationally, a low resolution description is afforded by a set of so-called "scaling functions" placed at nodes of a coarse spatial grid. Note that scaling functions are typically only placed where they are needed on this grid. Wavelets or "detail functions" are then added adaptively on a finer grid in regions of space where more resolution is needed. This provides yet another attractive feature for grid-based calculations, namely flexible boundary conditions. A subtler, and also highly desirable feature, is that the coefficients of the scaling and wavelet expansions are of comparable size and so properly reflect an even balance between different length scales. The reader interested in more information about wavelets is referred to the classic book of Daubechies [89] and for applications in theoretical physics is referred to Refs. [143, 146].

The first applications of wavelet theory to solving the Schrödinger equation began in the mid-1990s [25]. (Interest was also expressed by quantum chemists at around the same time [123, 57].) At least two important wavelet-based codes have been developed for solving the Kohn-Sham equation of the traditional Hohenberg-Kohn-Sham ground-state DFT [172, 206]. These are MADNESS [161] and BIGDFT [2]. This paper concerns BIGDFT.

Since Hohenberg-Kohn-Sham DFT is a ground-state theory, a different theory is needed to treat electronic excited states and, in particular, to calculate absorption spectra. The TD-DFT formalism [280] complements that of DFT by laying the ground work for calculating the time-dependent response of the charge density to an applied perturbation. Excitation spectra may then be calculated through linear response theory using, for example, the equations developed by one of us [60]. Implementing these equations in a wavelet code is not entirely straightforward since integral evalulation is performed differently than in traditional TD-DFT codes. Thus a key point in the present paper is how we handle integral evaluation in our implementation of TD-DFT in BIGDFT.

Our implementation is first validated by comparison against TD-DFT calculations with the GTO-based program DEMON2K for the historically-important test case of N_2 [186, 70]. This allows us to see and discuss some of the pros and cons of wavelets versus GTOs. We then go on to apply the method to a real-world application, namely the calculation of the absorption spectrum of a molecule of poten-

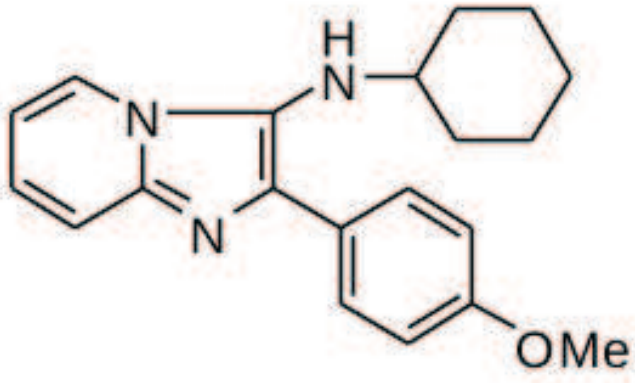

Figure 5.1: N-cyclohexyl-2-(4-methoxyphenyl)imidazo[1,2-α] pyridin-3-amine (Flugi **6**).

tial interest as a fluorescent probe in biological applications. This molecule, N-cyclohexyl-2-(4-methoxyphenyl)imidazo[1,2-α]pyridin-3-amine (Fig. 5.1), will simply be referred to as Flugi **6** [51]. Since this molecule has not been thoroughly characterized before we have included an experimental section describing our determination of its X-ray crystal structure.

This paper is organized as follows: The basic equations of TD-DFT are reviewed in the next section. In Sec. 5.4, we briefly review the idea of wavelets, explain how we handle the integral evaluation in our implementation of TD-DFT, and Section 5.5 discuss the pros and cons of the wavelet implementation in the context of N_2 calculations with BIGDFT and the GTO-based code DEMON2K. Section 5.6 reports the X-ray crystal structure, and experimental and calculated UV/visible absorption spectrum of Flugi **6**. An assignment is also made of the peaks appearing in the spectrum. The final section contains our concluding discussion.

5.3 TIME-DEPENDENT DENSITY-FUNCTIONAL THEORY

As evidenced by the numerous review articles [110, 150, 60, 151, 52, 318, 307, 61, 88, 238, 239, 53, 107, 73, 63, 64, 65] and books [231, 241, 152] written on the subject, TD-DFT is now such a well-established formalism that little additional review seems necessary. Nevertheless the purpose of this section is to recall a few key equations in order to keep the present paper reasonably self-contained and to introduce notation.

Time-dependent DFT builds upon the KS formulation of ground-state DFT [206]. In its modern formulation, Kohn-Sham DFT is spin-DFT so that the total energy involves an exchange-correlation (xc) energy which depends upon the density ρ_α of spin-α electrons and the density

ρ_β of spin-β electrons. These are obtained as the sum of the densities of the occupied orbitals of each spin,

$$\rho_\sigma(\mathbf{r}) = e \sum_p n_{p\sigma} |\psi_{p\sigma}(\mathbf{r})|^2 , \tag{5.1}$$

where $n_{p\sigma}$ is the occupation number of orbital $\psi_{p\sigma}$ and, the total charge density is given as the sum of the charge densities of two spin components. The Kohn-Sham orbitals are obtained by solving the Kohn-Sham equation,

$$\left(-\frac{\hbar^2}{2m_e} \nabla^2 + v_s^\sigma[\rho_\alpha, \rho_\beta](\mathbf{r}) \right) \psi_{p\sigma}(\mathbf{r}) = \epsilon_{p\sigma} \psi_{p\sigma}(\mathbf{r}) . \tag{5.2}$$

This involves a single-particle potential,

$$v_s^\sigma[\rho_\alpha, \rho_\beta](\mathbf{r}) = v_{ext}(\mathbf{r}) + v_H[\rho](\mathbf{r}) + v_{xc}^\sigma[\rho_\alpha, \rho_\beta](\mathbf{r}) . \tag{5.3}$$

which is the sum of the external potential v_{ext} (i.e., the interaction of the electrons with the nuclei and any applied electronic fields), the Hartree potential,

$$v_H[\rho](\mathbf{r}) = \int \frac{\rho(\mathbf{r}')}{|\mathbf{r} - \mathbf{r}'|} \, d\mathbf{r}' , \tag{5.4}$$

which may alternatively be obtained as the solution of Poisson's equation,

$$\nabla^2 v_H[\rho](\mathbf{r}) = -4\pi\rho(\mathbf{r}) , \tag{5.5}$$

and the xc-potential which is just the functional derivative of the xc-energy,

$$v_{xc}^\sigma[\rho_\alpha, \rho_\beta](\mathbf{r}) = \frac{\delta E_{xc}[\rho_\alpha, \rho_\beta]}{\delta \rho_\sigma(\mathbf{r})} . \tag{5.6}$$

Together $v_H[\rho]$ and $v_{xc}^\sigma[\rho_\alpha, \rho_\beta]$ constitute the self-consistent field (SCF), $v_{Hxc}^\sigma[\rho_\alpha, \rho_\beta]$. Modern DFT often uses a type of generalized Kohn-Sham formalism where the SCF may contain some orbital dependence due to (say) inclusion of some fraction of Hartree-Fock exchange and the external potential may even include a nonlocal part. In particular this latter generalization is the case when nonlocal pseudopotentials are employed, as is the case in BIGDFT.

The external potential is time-dependent in TD-DFT, and the TD-KS potential has the form,

$$\left(-\frac{\hbar^2}{2m_e} \nabla^2 + v_s^\sigma[\rho_\alpha, \rho_\beta; \Phi_0; \Psi_0](\mathbf{r}, t) \right) \psi_{p\sigma}(\mathbf{r}, t) = i\hbar \frac{\partial}{\partial t} \psi_{p\sigma}(\mathbf{r}, t) , \tag{5.7}$$

where the external potential,

$$v_s^\sigma[\rho_\alpha, \rho_\beta; \Phi_0; \Psi_0](\mathbf{r}, t) = v_{ext}(\mathbf{r}, t) + v_H[\rho](\mathbf{r}, t) + v_{xc}^\sigma[\rho_\alpha, \rho_\beta; \Phi_0; \Psi_0](\mathbf{r}, t) .$$

(5.8)

The dependence of the XC part on the initial interacting (Ψ_0) and noninteracting (Φ_0) wave functions may be eliminated by using the first HK theorem [172] if the initial state is the ground stationary state. This is the case when seeking the linear response of the ground stationary state to an applied electronic field. The TD charge density,

$$\rho(\mathbf{r}, t) = e \sum_{p\sigma} n_{p\sigma} |\psi_{p\sigma}(\mathbf{r}, t)|^2 , \tag{5.9}$$

then suffices to calculate the induced dipole moment (at least for finite systems such as molecules) and hence the dynamic polarizability,

$$\alpha(\omega) = \sum_{I}^{I\neq 0} \frac{e^2 f_I}{m_e(\omega_I^2 - \omega^2)} , \tag{5.10}$$

whose poles give the excitation energies of the system,

$$\hbar\omega_I = E_I - E_0 , \tag{5.11}$$

and whose residues give the corresponding oscillator strengths,

$$f_I = \frac{2\omega_I m_e}{\hbar} |\langle \Psi_I | \mathbf{r} | \Psi_0 \rangle|^2 . \tag{5.12}$$

The excitation energies and oscillator strengths are often presented in the form of a stick spectrum consisting of lines of height f_I located at the associated ω_I. What is actually measured is the molar extinction coefficient ϵ, in Beer's law. To a first approximation, this is related to the spectral function,

$$S(\omega) = \sum_{I} f_I \delta(\omega - \omega_I) , \tag{5.13}$$

by,

$$\epsilon(\omega) = \frac{\pi N_A e^2}{2\epsilon_0 m_e c \ln(10)} S(\omega) , \tag{5.14}$$

in SI units [168, 169, 167]. Finite spectrometer resolution, finite-temperature vibrational, and solvent effects are traditionally approximated by replacing the Dirac delta functions in Eq. (5.13) with a Gaussian whose full-width at half-maximum (FWHM) is selected to match the experimental spectrum and we will do the same. Solvent effects may also shift excitation energies [37, 38, 225, 228, 245, 34, 45] and affect oscillator strengths [77, 254, 259, 227, 36, 14, 246, 15, 24, 160, 31]. While these effects are not necessarily small (*vide infra*), we will simply ignore them when comparing with experimental data as this is a reasonable first approximation.

Practical TD-DFT calculations typically make use of the TD-DFT adiabatic approximation,

$$v_{xc}^{\sigma}[\rho_\alpha, \rho_\beta](\mathbf{r}, t) = \frac{\delta E_{xc}[\rho_\alpha^t, \rho_\beta^t]}{\delta \rho_\sigma^t(\mathbf{r})}, \tag{5.15}$$

because even less is known about the exact xc-potential in TD-DFT than is the case for regular DFT. Here $\rho_\sigma^t(\mathbf{r})$ is $\rho(\mathbf{r}, t)$ regarded at fixed t as a function of $\mathbf{r} = (x, y, z)$. If in addition, the xc-energy functional is of the local density approximation (LDA) or generalized gradient approximation (GGA) type, the TD-DFT adiabatic approximation is typically found to work well for low-energy excitations of dominant one-hole/one-particle character which are not too delocalized in space and do not involve too much charge transfer. Several extensions of classic TD-DFT have been found to be useful for going beyond these restrictions (see for example Ref. [64, 65] for a review).

One of us used a density-matrix formalism to develop a random-phase approximation (RPA) like formalism for the calculation of absorption spectra from the dynamic polarizability Eq. (5.10) [60]. This allowed the calculation of TD-DFT spectra to be quickly implemented in a wide variety of quantum chemistry programs since most of the available computational framework was already in place. The precise equation that needs to be solved is, within the TD-DFT adiabatic approximation,

$$\begin{bmatrix} \mathbf{A} & \mathbf{B} \\ \mathbf{B}^* & \mathbf{A}^* \end{bmatrix} \begin{pmatrix} \vec{X} \\ \vec{Y} \end{pmatrix} = \hbar\omega \begin{bmatrix} \mathbf{1} & \mathbf{0} \\ \mathbf{0} & -\mathbf{1} \end{bmatrix} \begin{pmatrix} \vec{X} \\ \vec{Y} \end{pmatrix}. \tag{5.16}$$

Here,

$$\begin{aligned} \mathbf{A}_{ai\sigma,bj\tau} &= \delta_{ab}\delta_{ij}\delta_{\sigma\tau}(\epsilon_a - \epsilon_i) + \mathbf{K}_{ai\sigma,bj\tau} \\ \mathbf{B}_{ai\sigma,bj\tau} &= \mathbf{K}_{ai\sigma,jb\tau}, \end{aligned} \tag{5.17}$$

and the coupling matrix is given by,

$$\mathbf{K}_{pq\sigma,rs\tau} = e^2 \int\int \psi_{p\sigma}^*(\mathbf{r})\psi_{q\sigma}(\mathbf{r}) \left[\frac{1}{|\mathbf{r}-\mathbf{r}'|} + \frac{\delta^2 E_{xc}}{\delta\rho_\sigma(\mathbf{r})\delta\rho_\tau(\mathbf{r}')}\right] \psi_{r\tau}(\mathbf{r}')\psi_{s\tau}^*(\mathbf{r}')\,d\mathbf{r}d\mathbf{r}', \tag{5.18}$$

where we are making use of the index convention that orbitals $a, b, \cdots, g, h$ are unoccupied, orbitals i, j, k, l, m, n are occupied, and orbitals $o, p, \cdots, x, y, z$ are free to be either occupied or unoccupied. In the case of an LDA or GGA, Eq. (5.16) may be rearranged to give the lower-dimensional matrix equation,

$$\Omega\vec{F} = \hbar^2\omega^2\vec{F}, \tag{5.19}$$

where

$$\Omega_{ia\sigma,jb\tau} = \delta_{ia}\delta_{jb}\delta_{\sigma\tau}(\epsilon_{a\sigma} - \epsilon_{i\sigma})^2 + 2\sqrt{(\epsilon_{a\sigma} - \epsilon_{i\sigma})}\mathbf{K}_{ia\sigma,jb\tau}\sqrt{(\epsilon_{a\sigma} - \epsilon_{i\sigma})}.$$

(5.20)

Alternatively the TDA is sometimes found to be useful [170],

$$\mathbf{A}\vec{X} = \omega\vec{X}. \tag{5.21}$$

This is particularly the case when it is necessary to attenuate the effect of spin-instabilities on potential energy surfaces when investigating photoprocesses [68].

5.4 IMPLEMENTATION IN BIGDFT

Our implementation of the equations of the previous section in BIGDFT is described in this section and their validation by comparison against calculations with DEMON2K is described in the next section.

BIGDFT solves the Kohn-Sham equation [Eq. (5.2)] in the pseudopotential approximation. The main difference is that the external potential part, v_{ext}, of the Kohn-Sham potential, v_s^σ, is manipulated so as to smooth the behavior of the KS orbitals in the core region near the nuclei while preserving the form of the KS orbitals outside the core region. This is done through the use of GTH pseudopotentials [141] in order to avoid "wasting" wavelets on describing the nuclear cusp. These include both a local and nonlocal part and are used for all atoms (even hydrogen). Several different functionals are available for the xc-energy. However we will only be considering the LDA functional with Teter's Pade approximation [141] of Ceperley and Alder's quantum Monte Carlo results [76] since the xc-kernel, f_{xc}, is thus far only implemented in BIGDFT at the LDA level.

There are two fundamental functions in Daubechies family: the scaling function $\phi(x)$ and the wavelet $\varphi(x)$ (see Fig. 5.2.) Note that both types of function are localized with compact support. The full basis set can be obtained from all translations by a certain grid spacing h of the scaling and wavelet functions centered at the origin. These functions satisfy the fundamental defining equations,

$$\begin{aligned} \phi(x) &= \sqrt{2}\sum_{j=1-m}^{m} h_j \phi(2x-j)\,, \\ \varphi(x) &= \sqrt{2}\sum_{j=1-m}^{m} g_j \phi(2x-j)\,. \end{aligned} \tag{5.22}$$

which relate the basis functions on a grid with spacing h and another one with spacing $h/2$. The coefficients, h_j and g_j, constitute the so-called "filters" which define the wavelet family of order m. These coefficients satisfy the relations, $\sum_j h_j = 1$ and $g_j = (-1)^j h_{-j+1}$. Equation (5.22) is very important since it means that a scaling-function basis defined over a fine grid of spacing $h/2$ may be replaced by combining a scaling-function basis over a coarse grid of spacing h

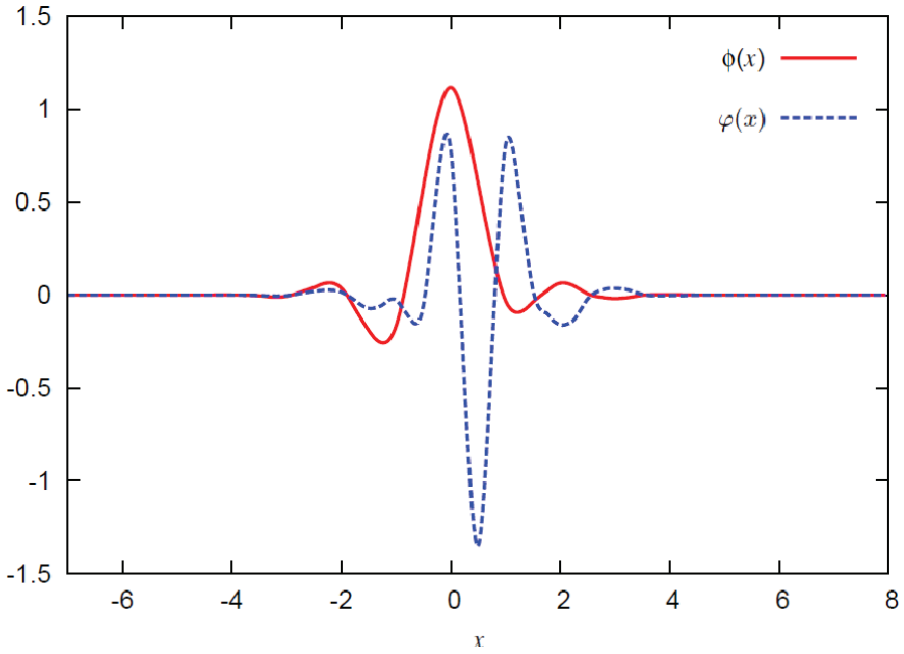

Figure 5.2: Daubechies scaling function $\phi(x)$ and wavelet $\varphi(x)$ of order 16.

with a wavelet basis defined over the fine grid of spacing $h/2$. This then gives us the liberty to begin with a coarse description in terms of scaling functions and then add wavelets only where a more refined description is needed. In principle the refined wavelet description may be further refined by adding higher-order wavelets where needed. However in BIGDFT we restricted ourselves to just two levels: coarse and fine-associated respectively with scaling functions and wavelets.

For a three-dimensional description, the simplest basis set is obtained by a tensor product of one-dimensional basis functions. For a two resolution level description, the coarse degrees of freedom are expanded by a single three dimensional function, $\phi^0_{i_1,i_2,i_3}(\mathbf{r})$, while the fine degrees of freedom can be expressed by adding another seven basis functions, $\phi^\nu_{j_1,j_2,j_3}(\mathbf{r})$, which include tensor products with one-dimensional wavelet functions. Thus, the Kohn-Sham wave function $\psi(\mathbf{r})$ is of the form

$$\psi(\mathbf{r}) = \sum_{i_1,i_2,i_3} c^0_{i_1,i_2,i_3}\phi^0_{i_1,i_2,i_3}(\mathbf{r}) + \sum_{j_1,j_2,j_3}\sum_{\nu_1}^{7} c^\nu_{j_1,j_2,j_3}\phi^\nu_{j_1,j_2,j_3}(\mathbf{r})\,. \tag{5.23}$$

The sum over i_1,i_2,i_3 runs over all the grid points contained in the low-resolution regions and the sum over j_1,j_2,j_3 runs over all the points contained in the (generally smaller) high resolution regions. Each wave function is then described by a set of coefficients $\{c^\nu_{j_1,j_2,j_3}\}$, $\nu = 0,...,7$. Only the nonzero scaling function and wavelet coefficients are stored. The data is thus compressed. The basis set being orthogonal, several operations such as scalar products among different orbitals and

between orbitals and the projectors of the nonlocal pseudopotential can be directly carried out in this compressed form. In addition to raw Daubechies scaling functions, practical applications make use of autocorrelated functions to make ISF [94]. In particular, as shown by A. Neelov and S. Goedecker [257], the local potential matrix elements approximated using the linear combination of such ISF is exact for polynomial expansions up to 7th order and the corresponding KS densities can be calculated by the real-valued coefficients on the grid points.

Although not every grid point is associated with a basis function and the fine grid is only used in some regions of space, the Daubechies basis set is still very large. This means that full diagonalization of the KS orbital Hamiltonian is not possible. Instead the direct minimisation method [92, 255] is used to obtain the occupied orbitals. This is in contrast with the GTO-based DEMON2K program which will be described below in which full diagonalization of the Kohn-Sham orbital Hamiltonian matrix is carried out within the finite GTO basis set.

A key point to review because of its importance for our implementation of TD-DFT in BIGDFT is the Poisson solver used to treat the Hartree part of the potential, v_H. Although this Poisson solver has been discussed elsewhere [132, 133], we briefly review how it works in order to keep this article somewhat self-contained. The Hartree potential is evaluated as,

$$v_H(\mathbf{r}) = \int G(|\mathbf{r}-\mathbf{r}'|)\rho(\mathbf{r}')\,d\mathbf{r}', \tag{5.24}$$

where $G(r) = 1/r$ is the Green's function for the Poisson equation, namely just the Coulomb potential. The density and potential are expanded in a set of interpolating scaling functions,

$$\begin{aligned} \rho(\mathbf{r}) &= \sum_{i_1,i_2,i_3} \tilde{\phi}_{i_1}(x)\tilde{\phi}_{i_2}(y)\tilde{\phi}_{i_3}(z)\rho_{i_1,i_2,i_3} \\ v_H(\mathbf{r}) &= \sum_{i_1,i_2,i_3} \tilde{\phi}_{i_1}(x)\tilde{\phi}_{i_2}(y)\tilde{\phi}_{i_3}(z)v_{i_1,i_2,i_3}\,, \end{aligned} \tag{5.25}$$

associated with the same grid of points, $\mathbf{r}_{i_1,i_2,i_3}$, in real space. In particular, the charge density coefficients, $\rho_{i_1,i_2,i_3} = \rho(\mathbf{r}_{i_1,i_2,i_3})$. Then,

$$v_{i_1,i_2,i_3} = \sum_{j_1,j_2,j_3} G_{j_1-i_1,j_2-i_2,j_3-i_3}\rho_{j_1,j_2,j_3}\,, \tag{5.26}$$

where the quantity,

$$G_{j_1-i_1,j_2-i_2,j_3-i_3} = \int \frac{\tilde{\phi}_{j_1}(x')\tilde{\phi}_{j_2}(y')\tilde{\phi}_{j_3}(z')}{|\mathbf{r}_{i_1,i_2,i_3}-\mathbf{r}'|}\,d\mathbf{r}', \tag{5.27}$$

is translationally invariant by construction. Since Eq. (5.26) has the form of a three dimensional convolution, it may be efficiently evaluated by using appropriate parallelized fast Fourier transform algorithms at the cost of only $\mathcal{O}(N \ln N)$ operations. The calculation of matrix elements of the Green's function $G(r) = 1/r$ is simplified by using a separable approximation in terms of Gaussians,

$$\frac{1}{r} \approx \sum_k e^{-p_k r^2} c_k \,, \tag{5.28}$$

so that all the complicated 3-dimensional integrals are reduced to products of simpler 1-dimensional integrals. For more information about BIGDFT, the reader is referred to the program website [2] and to various publications [132, 133, 135, 20, 136, 138].

We are now in a position to understand the construction of the coupling matrix in our implementation of TD-DFT in BIGDFT, which we split into the Hartree and exchange-correlation parts,

$$K_{ai\sigma,bj\tau} = K^{H}_{ai\sigma,bj\tau} + K^{xc}_{aj\sigma,bj\tau} \,. \tag{5.29}$$

Instead of calculating the Hartree part of coupling matrix directly as,

$$K^{H}_{ai\sigma,bj\tau} = \int\int \psi^{*}_{a\sigma}(\mathbf{r})\psi_{i\sigma}(\mathbf{r}) \frac{1}{|\mathbf{r}-\mathbf{r}'|} \psi_{b\tau}(\mathbf{r}')\psi^{*}_{j\tau}(\mathbf{r}')\, d\mathbf{r}d\mathbf{r}' \,, \tag{5.30}$$

we express the coupling matrix element as,

$$K^{H}_{ai\sigma,bj\tau} = \int \psi^{*}_{a\sigma}(\mathbf{r})\psi_{i\sigma}(\mathbf{r})v_{bj\tau}(\mathbf{r})\, d\mathbf{r} \,, \tag{5.31}$$

where,

$$v_{ai\sigma}(\mathbf{r}) = \int \frac{\rho_{ai\sigma}(\mathbf{r})}{|\mathbf{r}-\mathbf{r}'|}\, d\mathbf{r}' \,, \tag{5.32}$$

and,

$$\rho_{ai\sigma}(\mathbf{r}) = \psi^{*}_{a\sigma}(\mathbf{r})\psi_{i\sigma}(\mathbf{r}) \,. \tag{5.33}$$

The advantage of doing this is that, although $\rho_{ai\sigma}$ and $v_{ai\sigma}$ are neither real physical charge densities nor real physical potentials, they still satisfy the Poisson equation,

$$\nabla^2 v_{ai\sigma}(\mathbf{r}) = -4\pi\rho_{ai\sigma}(\mathbf{r}) \,, \tag{5.34}$$

and we can make use of whichever of the efficient wavelet-based Poisson solvers already available in BIGDFT, is appropriate for the boundary conditions of our physical problem.

Once the solution of Poisson's equation, $v_{ai\sigma}(\mathbf{r})$, is known, we can then calculate the Hartree part of the kernel according to Eq. (5.31).

Inclusion of the exchange-correlation kernel is accomplished by evaluating,

$$K_{ai\sigma,bj\tau} = \int M_{ai\sigma}(\mathbf{r})\rho_{bj\tau}(\mathbf{r})\,d\mathbf{r}\,, \tag{5.35}$$

where,

$$M_{ai\sigma}(\mathbf{r}) = v_{ai\sigma}(\mathbf{r}) + \int \rho_{ai\sigma}(\mathbf{r}')f_{xc}^{\sigma,\tau}(\mathbf{r},\mathbf{r}')\,d\mathbf{r}'\,. \tag{5.36}$$

We note that $f_{xc}^{\sigma,\tau}(\mathbf{r},\mathbf{r}') = f_{xc}^{\sigma,\tau}(\mathbf{r},\mathbf{r}')\delta(\mathbf{r}-\mathbf{r}')$ for the LDA, so that no integral need actually be carried out in evaluating $M_{ai\sigma}(\mathbf{r})$. The integral in Eq. (5.35) is, of course, carried out numerically in practice as a discrete sum.

5.5 VALIDATION

Having implemented TD-DFT in BIGDFT we now desire to validate our implementation by testing it against another program in which TD-DFT is already implemented, namely the all-electron GTO-based program DEMON2K [9]. DEMON2K resembles a typical GTO-based quantum chemistry program in that all the integrals other than the xc-integrals, can be evaluated analytically. In particular, DEMON2K has the important advantage that it accepts the popular GTO basis sets common in quantum chemistry and so can benefit from the experience in basis set construction of a large community built up over the past 50 years or so. In the following, we have chosen to use the well-known correlation-consistent basis sets for this study [114, 285]. (Note, however, that the correlation-consistent basis sets used in DEMON2K lack f and g functions but are otherwise exactly the same as the usual ones.) The advantage of using these particular basis sets is that there is a clear hierarchy as to quality.

An exception to the rule that integrals are evaluated analytically in DEMON2K are the xc-integrals (for the xc-energy, xc-potential, and xc-kernel) which are evaluated numerically over a Becke atom-centered grid. This is important because the relative simplicity of evaluating integrals over a grid has allowed the rapid implementation of new functionals as they were introduced. We made use of the fine fixed grid in our calculations.

As described so far, DEMON2K should have $\mathcal{O}(N^4)$ scaling because of the need to evaluate 4-center integrals. Instead DEMON2K uses a second atom-centered auxiliary GTO basis to expand the charge density. This allows the the elimination of all 4-center integrals so that only 3-center integrals remain for a formal $\mathcal{O}(N^3)$ scaling. In practice, integral prescreening leads to $\mathcal{O}(N^M)$ scaling where M is typically between 2 and 3. We made use of the A3 auxiliary basis set from the DEMON2K automated auxiliary basis set library.

All calculations were performed using standard deMon2k default criteria. Although full TD-LDA calculations are possible with deMon2k, the TD-LDA calculations reported here all made use of the TDA. The chosen test molecule was N_2 with an optimized bond length of 1.115 Å. This molecule was chosen partly because of its small size but also because of the large number of excited states which are well characterized (see Refs. [186, 70] and references therein.)

Unlike TD-HF (or configuration interaction singles) calculations, TD-LDA calculations are prepared to describe excitation processes in the sense that the occupied and unoccupied orbitals both see the same number of electrons (because they come from the same local potential). This means that there is often little relaxation — at least in small molecules — and a two orbital model [60, 63, 65, 71] often provides a good first approximation to the singlet ($\hbar\omega^{S}_{i\to a}$) and triplet ($\hbar\omega^{T}_{i\to a}$) excitation energies,

$$\begin{aligned} \hbar\omega^{T}_{i\to a} &= \epsilon_a - \epsilon_i + (ia|f^{\alpha,\alpha}_{xc} - f^{\alpha,\beta}_{xc}|ai) \\ \hbar\omega^{S}_{i\to a} &= \epsilon_a - \epsilon_i + (ia|2f_H + f^{\alpha,\alpha}_{xc} + f^{\alpha,\beta}_{xc}|ai)\,. \end{aligned} \tag{5.37}$$

Consideration of typical integral signs and magnitudes then implies that

$$\hbar\omega^{T}_{i\to a} \leqslant \epsilon_a - \epsilon_i \leqslant \hbar\omega^{S}_{i\to a}\,, \tag{5.38}$$

with the singlet-triplet splitting going to zero for Rydberg states (in which case the electron repulsion integrals become negligible due to the diffuse nature of the target orbital ψ_a.)

Since orbital energy differences provide an important first estimate of TD-DFT excitation energies, we wished to see how rapidly they converged for BigDFT and deMon2k as the quality of the basis set was improved. Tables 5.1 and 5.2 show how HOMO – LUMO energy gap ($\Delta\epsilon_{HOMO-LUMO}$) varies for each program.

Consider first how deMon2k calculations of $\Delta\epsilon_{HOMO-LUMO}$ evolve as the basis set is improved (Table 5.1). Jamorski, Casida, and Salahub had earlier shown that LUMO is bound for reasonable basis sets [186]. (Small differences between the present calculations and those in Ref. [186] are due to gradual improvements in the grid, auxiliary basis sets, and convergence criteria used in the deMon programs). Convergence to the true HOMO-LUMO LDA gap is expected with systematic improvement within the series:

- Double zeta plus valence polarization (DZVP) → triple zeta plus valence polarization (TZVP),
- Augmented correlation-consistent double zeta plus polarization plus diffuse on all atoms (AUG-CC-PCVDZ) → AUG-CC-PCVTZ (triple zeta) → AUG-CC-PCVQZ (quadruple zeta) → AUG-CC-PCV5Z (quintuple zeta)

Table 5.1: Basis set dependence of the HOMO and LUMO energies and of the HOMO-LUMO gap (eV) calculated using deMon2k.

Basis Set	$-\epsilon_{\text{HOMO}}$	$-\epsilon_{\text{LUMO}}$	$\Delta\epsilon_{\text{HOMO-LUMO}}$
STO-3G	7.6758	0.0297	7.6461
DZVP	10.1824	2.2616	7.9208
TZVP	10.2142	2.2894	7.9248
CC-PVDZ	9.8656	1.8993	7.9663
CC-PVTZ	10.2978	2.2868	8.0110
CC-PVQZ	10.3545	2.3527	8.0018
CC-PV5Z	10.3786	2.3886	7.9900
CC-PCVDZ	9.9197	1.9314	7.9883
CC-PCVQZ	10.3555	2.3532	8.0023
CC-PCVTZ	10.2372	2.2718	8.0154
CC-PCV5Z	10.3793	2.3891	7.9902
AUG-CC-PVDZ	10.3534	2.3785	7.9749
AUG-CC-PVQZ	10.3987	2.4127	7.9860
AUG-CC-PVTZ	10.3953	2.4010	7.9943
AUG-CC-PV5Z	10.3984	2.4137	7.9847
AUG-CC-PCVDZ	10.3732	2.3879	7.9847
AUG-CC-PCVTZ	10.3972	2.4015	7.9957
AUG-CC-PCVQZ	10.3990	2.4124	7.9866
AUG-CC-PCV5Z	10.3985	2.4136	7.9849

Table 5.2: Basis set dependence of the HOMO and LUMO energies and of the HOMO-LUMO gap (eV) calculated using BIGDFT.

h_g[1]/m[2]/n[3]	$-\epsilon_{HOMO}$	$-\epsilon_{LUMO}$	$\Delta\epsilon_{HOMO-LUMO}$
Low resolution			
0.4/6/8	10.3910	2.3815	8.0095
0.4/7/8	10.3964	2.3922	8.0042
0.4/8/8	10.3971	2.3945	8.0027
0.4/9/8	10.3972	2.3951	8.0022
0.4/10/8	10.3973	2.3953	8.0020
0.4/11/8	10.3972	2.3953	8.0019
High resolution			
0.3/7/8	10.3977	2.3932	8.0043
0.3/8/8	10.3984	2.3957	8.0027
0.3/9/8	10.3985	2.3963	8.0022
0.3/10/8	10.3985	2.3965	8.0021
0.3/11/8	10.3985	2.3965	8.0020

[1] Grid spacing of the cartesian grid in atomic units.
[2] coarse grid multiplier (crmult)
[3] fine grid multiplier (frmult)

- Augmented correlation-consistent valence double zeta plus polarization plus diffuse (AUG-CC-PVDZ) → AUG-CC-PVTZ → AUG-CC-PVQZ → AUG-CC-PV5Z
- Correlation-consistent double zeta plus polarization plus tight core (CC-PCVDZ) → CC-PCVTZ → CC-PCVQZ → CC-PCV5Z
- Correlation-consistent valence double zeta plus polarization on all atoms (CC-PVDZ) → CC-PVTZ → CC-PVQZ → CC-PV5Z.

There is a clear tendency in the correlation-consistent basis sets to tend towards values of 10.40 eV for the HOMO energy, 2.42 eV for the LUMO energy, and 8.01 eV for $\Delta\epsilon_{\text{HOMO–LUMO}}$, with adequate convergance already achieved with the CC-PVTZ basis set.

Now let us turn to BigDFT (Table 5.2). Calculations were done for two different grid values, denoted by h_g = 0.3, 0.4. (These values are the nodes of the grid in a.u which serve as centers for the scaling function/wavelet basis.) The simulation "box" has the shape of the molecule and its size is expressed in the units of the coarse grid multiplier (crmult) and the fine grid multiplier (frmult) which determines the radius for the low/high resolution sphere around the atom. Results using 16 unoccopied orbitals with the different wavelet basis sets are essentially identical, with no significant variation in the HOMO energy, the LUMO energy, and the $\Delta\epsilon_{\text{HOMO–LUMO}}$ value of 8.00 eV between the high resolution combination of 0.3/11/8 and the low resolution combination of 0.4/6/8.

The remaining differences for the HOMO energy, LUMO energy, and $\Delta\epsilon_{\text{HOMO–LUMO}}$ calculated by the two programs, deMon2k and BigDFT, is more difficult to trace. For example, it might be due to the auxiliary basis approximation in deMon2k or to the use of pseudopotentials in BigDFT or perhaps to still other program differences. The important point is that differences are remarkably small.

We now come to the calculation of the actual excited states of N_2 and the third reason alluded to in the introduction that quantum chemists have been slow to adapt grid-based methods. This is the concern that the very large size of basis sets in grid-based methods would lead to impractically-large configuration interaction expansions. Put differently, this concerns the basic problem of how to handle the continuum. A correct inclusion of the continuum in the formalism of Sec. 5.3 would seem to require at least approximate integrals over a quasicontinuum of unoccupied orbitals. Clearly this is impractical and our method only uses the first several unoccupied orbitals. This is perhaps reasonable for the lower excited states, given the anticipated dominance of the two-orbital model [Eq. (5.37)], but may fail to be quantitative when relaxation or state mixing starts to become important and the two-orbital model breaks down. This problem is avoided in quantum chemistry where the virtual orbitals in the

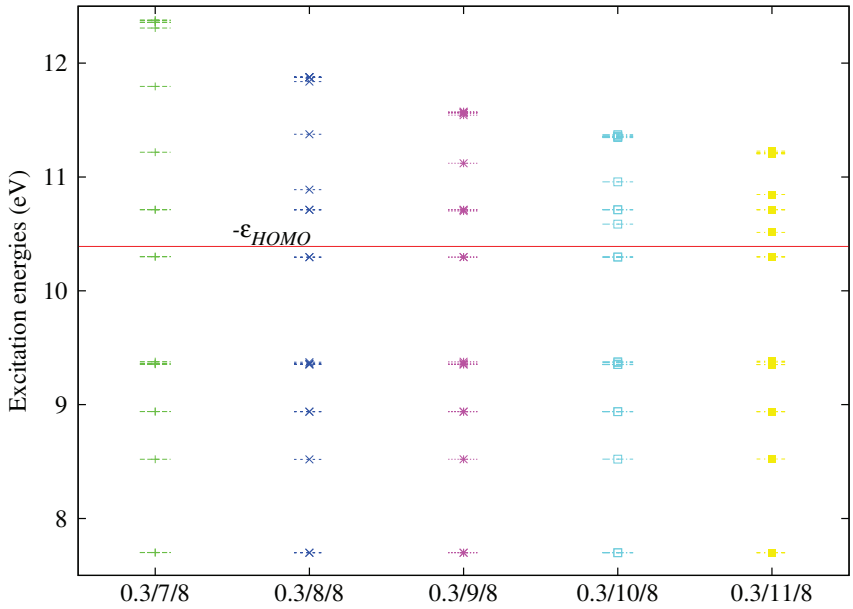

Figure 5.3: Singlet and triplet excitation energies for N_2 calculated using BIGDFT

Table 5.3: Comparison of the nine lowest excitation energies of N_2 (in eV) calculated using different programs and with experiment.

State	BIGDFT[1]	DEMON2K[2]	ABINIT[3]	Experiment[4]
$1^3\Sigma_g^+$	10.71	10.39	9.91	12.0
$1^3\Pi_u$	10.58	10.38	10.79	11.19
$1^1\Delta_u$	10.29	9.99	10.46	10.27
$1^1\Sigma_u^-$	9.37	9.36	9.92	9.92
$1^3\Sigma_u^-$	9.36	9.36	9.16	9.67
$1^1\Pi_g$	9.35	9.10	9.47	9.31
$1^3\Delta_u$	8.93	8.60	9.08	8.88
$1^3\Pi_g$	7.69	7.83	7.85	7.75
$1^3\Sigma_u^+$	8.52	8.43	8.16	8.04

[1] Present work (TD-LDA/TDA).
[2] Present work (TD-LDA/TDA).
[3] From [5] (TD-LDA).
[4] Taken from Ref.([42]).

TD-DFT calculation have an altogether different meaning: they are simply there to describe the dynamic polarizability of the ground-state charge density and need not describe the continuum well. This is why fewer unoccupied orbitals are normally needed in quantum chemical applications of TD-DFT than is the case when using, say, plane waves. In Fig. 5.3 the lowest few excited-states are calculated using BIGDFT. This figure shows that the excited states calculated with different grids are essentially the same up to $-\epsilon_{\text{HOMO}}$. After $-\epsilon_{\text{HOMO}}$, increasing the quality of the basis set by varying the simulation box sizes leads to an increasing collapse of the higher excited-states. This is a reflection of the fact that the TD-LDA ionization continuum starts at $-\epsilon_{\text{HOMO}}$ which is about 5 eV low because of the incorrect asymptotic behavior of the xc-potential [70]. Of course, as indicated by the estimate (5.37), the excitation energy is not exactly a simple orbital energy difference, but they are closely related.

With these caveats, let us see how well our implementation of TD-DFT does in BIGDFT. Table 5.3, lists the lowest nine excited states of N_2 calculated with DEMON2K and BIGDFT. For comparison, Table 5.3 also contains full TD-LDA (i.e, non-TDA) excitation energies obtained from ABINIT [145] using the Perdew-Wang 92 parameterisation of the LDA functional [264] along with the experimental values from the literature [42]. The slight differences which occur between the $1^1\Sigma_u^-$ and $1^3\Sigma_u^-$ excitation energies in the BIGDFT and ABINIT calculations are an indication of residual numerical errors since these two states are rigorously degenerate by symmetry when using the TD-LDA and TD-LDA/TDA approximations: Aside from this tiny difference, it is certainly reassuring that excitation energies calculated with BIGDFT, DEMON2K, and ABINIT are quite similar. Nevertheless differences as large as 0.3 eV or more are found for some states. Such differences are large enough to be potentially problematic for determining the ordering of near-lying states.

Finally since a large number of excited states have been calculated, it is interesting to test the assertion that the oscillator strength distribution should be approximately correct even above the TD-LDA ionization threshold at $-\epsilon_{\text{HOMO}}$ [70]. This is especially true since the transitions given in Table 5.3 are all dark and we would like to see how the oscillator strengths of bright states compare. The high-energy spectra are compared in Fig. 5.4 using Eq. (5.14). Clearly the spectra are in reasonable qualitative agreement.

The above results show that this first implementation of BIGDFT is quantitative — especially when results are dominated by bound-bound transitions — and our discussion may eventually suggest ways to go further towards improving the method. In the meantime, we have a method that can be used for moderate-size molecules and this is illustrated in the next section.

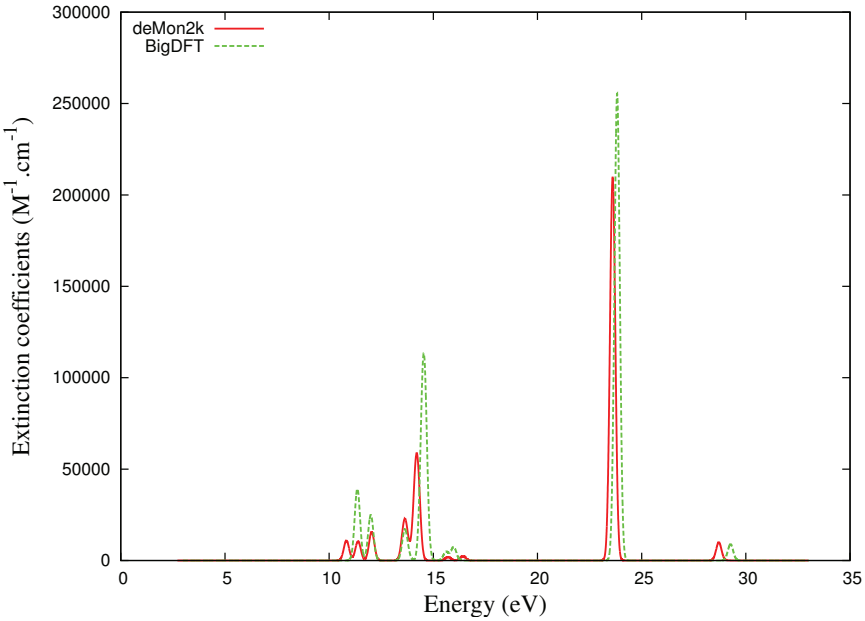

Figure 5.4: Comparison of deMon2k and BigDFT N_2 spectra at higher energies.

5.6 APPLICATION

A large series of fluorescent molecules of potential interest as biological markers [147] has recently been synthesized by combinatorial chemistry [51]. This is a method whereby large sets of similar reactions are conducted in parallel in arrays of spots on a single plate, thus dramatically increasing throughput when searching for molecules with a particular property — in this case fluorescence. We have chosen to calculate the absorption spectrum of one of these fluorescent molecules in preparation for future more in-depth theoretical studies of their fluorescence properties using BigDFT. This molecule, which we will simply refer to as Flugi **6** (because it is molecule 6 [51] among the fluorescent molecules prepared by the UGI reaction [316]) rather than by its full name of N-cyclohexyl-2-(4-methoxyphenyl)imidazo[1,2-a]pyridin-3-amine is shown in Fig. 5.1. The synthesis and partial characterization of Flugi **6** has been described in Ref. [51]. However we go further here and report the experimental determination of its crystal structure. We then go on to compare the spectrum calculated with BigDFT with the measured spectrum and discuss the problem of peak assignment.

5.6.1 *X-Ray Crystal Structure*

Crystals of Flugi **6** ($C_{20}H_{23}N_3O$, M = 321.42 g/mol) were obtained out of recrystallisation in ethyl acetate (EtOAc) as colorless needles suitable for X-ray diffraction. A 0.38 mm × 0.28 mm × 0.01 mm crystal

was mounted on a glass fiber using grease and centered on a Bruker Enraf Nonius kappa charge-coupled device (CCD) detector working at 200 K and at the monochromated (graphite) Mo K_α radiation λ = 0.71073 Å. The crystal was found to be orthorhombic, $Pna2_1$, a = 27.912(4) Å , b = 5.876(2)Å, c = 10.297(2) Å, V = 1688.7(6) $Å^3$, Z = 4, D_x = 1.264 $g.cm^{-3}$, m = 0.080 mm^{-1}. A total of 17700 reflections were collected using ϕ and ω scans; 2853 independent reflections (R_{int} = 0.1557). The data were corrected for the Lorentz and polarization effects. The structure was solved by direct methods with SIR92 [18] and refined against F by leastsquare method implemented by TeXsan [4]. C, N, and O atoms were refined anisotropically by the full matrix least-squares method. H atoms were set geometrically and recalculated before the last refinement cycle. The final R values for 1964 reflections with $I > 2\sigma$ (I) and 217 parameters are R1 = 0.0617, wR2 = 0.0657, goodness of fit (GOF) = 1.78 and for all 2854 unique reflections R1 = 0.0923 , wR2 = 0.0829, GOF = 1.85. The resultant crystal geometry is given in 5.4

The data have been deposited with the Cambridge Crystallographic Data Centre (Reference No. CCDC 8200007). This material is available free of charge via www.ccdc.can.ac.uk/conts/retrieving.html (or from the Cambridge Crystallographic Data Centre, 12 Union Road, Cambridge CB2 1EZ, UK. Fax: +44-1223-336033. E-mail: deposit@ccdc.cam.ac.uk).

5.6.2 *Spectrum*

The experimental UV/Vis spectrum was determined in dimethyl sulphur dioxide (DMSO) as described in the supplementary material of Ref. [51] The first step to calculating the spectrum of Flugi **6** is to optimize the geometry. This was done with BIGDFT using the 0.4/8/8 grid, beginning with the experimental crystal geometry shown in Fig. 5.5. Our optimized geometry is given in Table 5.5. The largest change 0.15 Å from the initial guess is for the 18th atom of hydrogen. It was verified that the optimized geometry is indeed a minimum by explicit calculation of vibrational frequencies. However the experimental geometry is not identical to our calculated gas phase geometry as confirmed by the presence of three imaginary vibrational frequencies calculated for the (unoptimized) experimental geometry.

The TD-LDA absorption spectrum of Flugi **6** was then calculated at the optimized geometry using our new implementation of TD-DFT in BIGDFT. In addition to the previously mentioned computational details, the calculation used 60 unoccupied orbitals within the TDA. The excited-states were obtained using full-matrix diagonalization of the TD-DFT part. The theoretical spectrum was calculated using Eq. (5.14) using a FWHM of 0.25 eV and then transformed to a wavelength scale using our spectrum convolution program [12]. Because we were

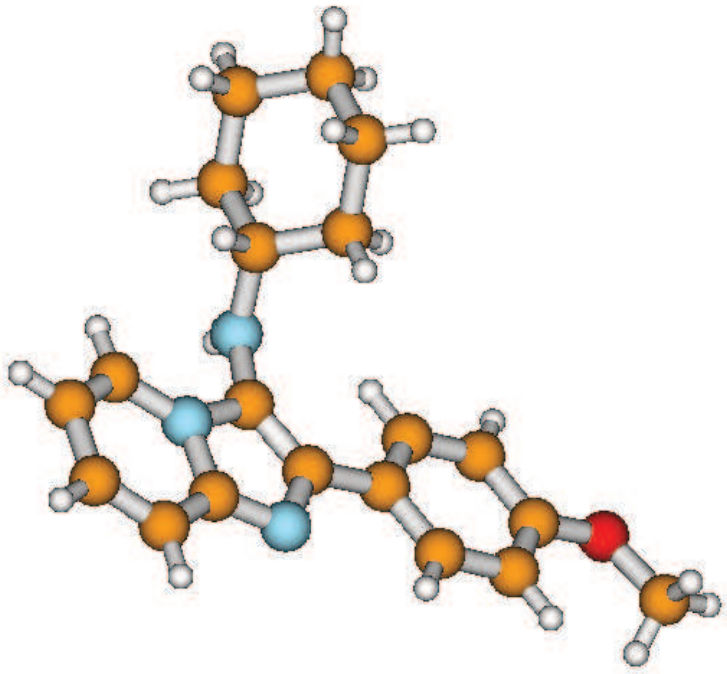

Figure 5.5: Experimental geometry: carbon, orange; nitrogen, blue; oxygen, red; hydrogen, white. This geometry consists of two nearly planar entities, namely a nearly planar cyclohexane (C_6H_{11}-) ring and the rest of the molecule which rests in a plane perpendicular to the plane of the cyclohexane

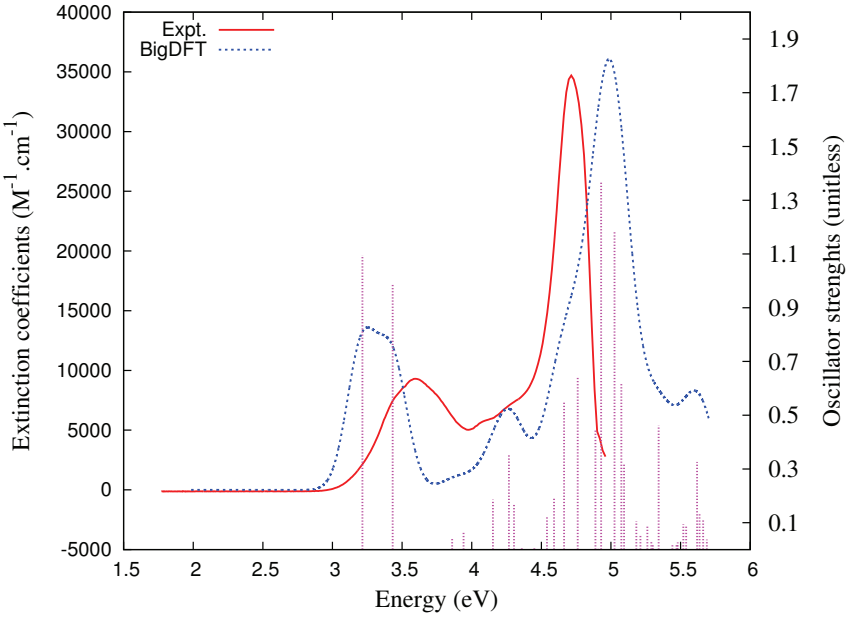

Figure 5.6: Comparison of theoretical and measured absorption spectra for Flugi **6** (left y-axis). The magnitude of the BIGDFT curve has been divided by a factor of ten (see text). Both theoretical and experimental curves show qualitative agreement with the oscillator strength stick-spectra which however is in different units (right y-axis).

restricted to a more limited number of unoccupied orbitals than in the N_2 test case, there is some concern that our calculated spectrum might change if a larger number of unoccupied orbitals is included. However the comparison of the theoretical and experimental results shown in Fig. 5.6 is reasonable. This is especially true when it is kept in mind that we are comparing gas-phase theory with an experimental spectrum measured in a polar solvent DMSO. Notice the presence of a larger peak at 4.6-5.0 eV, a smaller peak at 3.2-3.5 eV, and a shoulder inbetween near 4.3 eV.

In contrast to experience with ruthenium complexes (to name but one example), Eq. (5.14) with gaussian broadening does *not* suffice in the present case to give good agreement between theoretical and experimental molar extinction coefficinets. This is why the theoretical curve has been divided *magnitude by a factor of ten*. We believe that this discrepancy is in part due to the aforementioned solvent effects on excitation energies and oscillator strengths which we have chosen to neglect and in part due to the possible presence of multiple conformers in the room temperature experiment. This latter hypothesis might be tested by expensive dynamics calculations, but this far beyond the scope of the present work. Nevertheless, even without dynamics we find this level of agreement to be encouraging and now go on to further analyze our calculated spectrum. The calculated stick spectrum is also shown in Fig. 5.6. It is now clear that the small peak at 3.2-

3.5 eV corresponds to two transitions, that the shoulder near 4.3 eV corresponds to three transitions, and that the large peak at 4.6-5.0 eV corresponds to several electric excited states. Table 5.6 provides a more detailed analysis. All of the transitions are below the onset of TD-LDA ionization continuum at $-\epsilon_{HOMO} = 4.8713$ eV, which is artificially low compared to the true ionization energy [70]. As mentioned in Sec. 5.4, unlike TD-HF (or configuration interaction singles) calculations, TD-LDA calculations are prepared to describe excitation processes in the sense that the occupied and unoccupied orbitals both see the same number of electrons (because they come from the same local potential.) This means that there is often little relaxation — at least in small molecules — and a two orbital model [60] provides a good first approximation to the excitation energy Eqs. (5.37) and (5.38). The TDA configuration interaction coefficient is then determined by spin coupling and is given by $1/\sqrt{2} = 0.707$. Table 5.6 shows significant deviations from this theoretical value, suggesting significant relaxation effects may be taking place. Visualization of the HOMO and LUMO suggests that relaxation is important here and might help to explain why the first peak is at slightly too low an energy compared to the first experimental peak in the absorption spectrum [71]. Nevertheless, the energy of HOMO $\rightarrow$ LUMO dominated singlet transition at 3.21 eV exceeds the simple difference of HOMO and LUMO molecular orbital energies of 2.80 eV as expected from the domination of the Hartree term $(ia|f_H|ai)$ over the two xc terms. Two interesting features, which will not be pursued in the present paper, are the absence of oscillator strength for the $^1(H, L+1)$ transition and the indication of significant configuration mixing for the first and seventh transitions which both borrow from $^1(H, L)$ and for the third and fifth transitions which both borrow from $^1(H, L+2)$.

5.7 CONCLUSION

Grid-based methods have long been regarded with skepticism by the quantum chemistry community, but have now been accepted in the form of the grids used to evaluate xc-integrals in the DFT part of most quantum chemistry codes. We believe that an even greater acceptance of grid-based methods may prove useful as theoretical solid-state and chemical physics strive to meet on "neutral ground" at the nanometer scale. Acceptance will be aided by continuing advances in grid-based methods with wavelets being of particular interest here. At the same time, new features should be added to grid-based electronic structure codes in order to make them more useful for chemical applications. This paper represents a small step in that direction. In particular, we have presented the first implementation of TD-DFT in a wavelet-based code, namely in BIGDFT.

While BIGDFT is designed for routine calculations on systems containing many hundreds of atoms, this first implementation of TD-DFT in BIGDFT is not yet ready for these more ambitious applications. Rather, we wished to bring out the pros and cons of wavelet-based TD-DFT by comparing against a GTO-based quantum chemistry code (in this case, DEMON2K) and by an example application showing how our implementation in BIGDFT can be useful in analyzing the spectrum of a molecule of contemporary experimental interest.

A factor in favor of the wavelet-based approach is the rapidity of convergence of the bound orbitals and orbital energies with respect to refinements of the wavelet basis and associated grid. While orbital results from the all-electron DEMON2K code are not (and should not) be in exact agreement with those of the pseudopotential BIGDFT code, the results are really quite close when sufficiently large basis sets are used. In the case of the GTO-based code, tight basis set convergence typically requires going beyond at least the triple-zeta-valence-plus-polarization (TZVP) level. In contrast, adequate orbital convergence is easily obtained with BIGDFT using the default wavelet basis set and grid, with further refinements leading to only minor improvement. This comes close to the quantum chemists' dream of calculations free of errors due to basis set incompleteness.

Interestingly, problems which could be envisioned with this first implementation of TD-DFT in BIGDFT either did not arise or did not seem to be serious. The worry was that the unbound orbitals of the molecule are continuum orbitals whose description is apparently only limited by the boundaries of the box defined by the coarse grid. In principle, for an infinitely large box, there are an infinite number of unoccupied orbitals in even a small energy band and all of these would seem to need to be taken into account even for describing transitions below the TD-DFT ionization threshold at $-\epsilon_{HOMO}$. This is a doubly large worry because the number of unoccupied orbitals to be calculated is limited by an input parameter, making a double convergence problem (number of virtuals and box size.) Nevertheless our calculations show that the implementation in BIGDFT works correctly, giving quite reasonable results when compared with DEMON2K and with experimental results for transitions below $-\epsilon_{HOMO}$. There are at least two probable reasons that the anticipated problems are not seen here. The first is the tendency, at least for small molecules, for excitations to be dominated by bound-to-bound transitions involving two or only a few orbitals. This is especially true for the LDA and GGA, but will gradually breakdown with the inclusion of Hartree-Fock exchange where orbital relaxation becomes more important. The second reason that we may not see the expected problems associated with continuum-type unoccupied orbitals is that putting the molecule in a box acts much like atom-centered GTOs in the sense that it keeps wavelet basis functions close to those regions of space where electron density is high and

so can be efficiently used to describe the dynamic response of the charge density, whose description is the fundamental key to extracting spectra in TD-DFT. Nevertheless it should be mentioned that there are alternative algorithms in TD-DFT such as the modified Sternheimer equation and the Green's function approach which avoid explicit reference to unoccupied orbitals [231]. These may be worth exploring in future development work of wavelet-based TD-DFT. However our first priority will be to implement analytic derivatives for TD-DFT excited states which are needed in modeling fluorescence.

It should also be mentioned that implementing TD-DFT is a step along the way to implementing MBPT methods from solid-state physics, namely the *GW* one-particle Green's function approximation and the Bethe-Salpeter equation approach to the two-particle Green's function [261]. Such work is already in progress in BIGDFT. Of course, the expected collapse of the TD-DFT continuum [70] was seen above - ϵ_{HOMO} (Fig. 5.3) with increasing box size, though the spectrum remains qualitatively correct (Fig. 5.4).

The application to Flugi **6** presented in this paper provides a concrete reality check on the usefulness of TD-DFT for practical applications. Geometry optimization was simplified by beginning with an X-ray structure, but solvent and dynamics effects were ignored. All in all the final result may be qualified as semiquantitative but useful. In fact, we have also carried out preliminary calculations of absorption spectra for five other members of the Flugi combinatorial chemistry series (not reported here.) For these molecules, trends in the energies of the first experimental absorption peaks do parallel trends in the calculated first absorption peak as well as the HOMO-LUMO energy difference. However, in the absence of X-ray crystal data, the large number of possible molecular configurations merits further exploration, especially since the LDA may not correctly order these states. Hydrogen bonding with the solvent should also be considered in some cases. For these reasons it seems best to reserve the calculation of these spectra, comparison with experimental spectra, and assignment of transitions for a future paper.

Table 5.4: Experimental geomentry (Cartesian coordinates in Å) for the Flugi **6**

Atom	x	y	z
O	14.0340	1.5882	2.9552
N	7.7362	0.5932	7.4268
N	9.1303	2.5361	7.6402
N	8.7184	-0.6003	5.8202
C	8.8581	1.3112	7.0430
C	7.6978	-0.5625	6.6613
C	6.7910	0.8587	8.3836
C	5.8275	-0.0445	8.6210
C	9.4459	0.5452	6.0467
C	12.4814	2.2280	4.5690
C	9.6943	2.5959	8.9709
C	12.2450	0.0746	3.5887
C	12.9311	1.2651	3.6923
C	11.3663	2.0047	5.3306
C	11.1149	-0.1284	4.3608
C	10.6426	0.8232	5.2590
C	5.7504	-1.2331	7.8594
C	6.6706	-1.4857	6.8881
C	11.0628	2.0293	9.0805
C	14.5914	0.5796	2.1251
C	9.6456	4.0228	9.4571
C	10.1882	4.1778	10.8473
C	11.6027	2.1400	10.5019
C	11.5598	3.5428	10.9936
H	6.8178	1.6727	8.8752
H	5.1910	0.1163	9.3101
H	12.9482	3.0519	4.6478
H	9.1307	2.0846	9.5420
H	12.5454	-0.6011	2.9948
H	11.0776	2.6830	5.9322
H	10.6436	-0.9486	4.2766
H	5.0541	-1.8576	8.0282
H	6.6161	-2.2802	6.3725
H	11.0384	1.1132	8.8327
H	11.6406	2.5025	8.4958
H	10.1595	4.5627	8.8705
H	8.7422	4.3165	9.4511
H	10.2551	5.1036	11.0519
H	9.5907	3.7627	11.4607
H	11.0761	1.5956	11.0779
H	12.5025	1.8356	10.5174
H	12.1865	4.0570	10.5007
H	11.8007	3.5496	11.9149
H	15.3192	0.9409	1.6353
H	14.8996	-0.1395	2.6665
H	13.9283	0.2626	1.5256
H	8.9445	3.3408	7.1731

Table 5.5: DFT optimized geometries (Cartesian coordinates in Å) of Flugi **6**. Calculations performed at the LDA level of theory.

Atom	x	y	z
O	14.0374	1.5760	2.9779
N	7.75774	0.5820	7.4296
N	9.14347	2.5138	7.6339
N	8.73705	-0.581	5.7976
C	8.85269	1.3197	7.0273
C	7.73253	-0.574	6.6557
C	6.82855	0.8581	8.3749
C	5.83564	-0.044	8.6043
C	9.44155	0.5586	6.0148
C	12.4807	2.2541	4.5863
C	9.66483	2.5868	8.9771
C	12.2472	0.0755	3.6050
C	12.9348	1.2789	3.7031
C	11.3530	2.0325	5.3457
C	11.1111	-0.130	4.3645
C	10.6388	0.8366	5.2444
C	5.77383	-1.232	7.8551
C	6.70657	-1.492	6.8869
C	11.0671	2.0245	9.0831
C	14.5517	0.5791	2.1429
C	9.63546	4.0197	9.4485
C	10.1799	4.1615	10.852
C	11.5902	2.1260	10.497
C	11.5622	3.5584	10.985
H	6.94062	1.8172	8.8855
H	5.08962	0.1718	9.3696
H	13.0361	3.1924	4.6593
H	9.01856	1.9925	9.6670
H	12.5948	-0.707	2.9284
H	11.0089	2.7962	6.0486
H	10.5470	-1.064	4.2928
H	4.97202	-1.948	8.0454
H	6.68074	-2.397	6.2775
H	11.0746	0.9834	8.7183
H	11.7169	2.5999	8.3962
H	10.2520	4.6168	8.7465
H	8.60472	4.4110	9.3825
H	10.1918	5.2227	11.149
H	9.49548	3.6524	11.557
H	10.9656	1.5016	11.164
H	12.6112	1.7164	10.558
H	12.2802	4.1561	10.392
H	11.9013	3.6190	12.032
H	15.4016	1.0289	1.6155
H	14.9021	-0.292	2.7251
H	13.8030	0.2392	1.4055
H	8.94041	3.3910	7.1600

Table 5.6: Singlet excitation energies ($\hbar\omega_I$, in eV) up to $-\epsilon_{HOMO}$ = 4.8713 eV, oscillator strength (f_I, unitless) and assignment.

$\hbar\omega_I$	f_I	Dominant transition[1]	Coefficient[2]
4.83006	0.047	$^1(H, L+7)$	0.698419
4.81870	0.890	$^1(H-2, L+3)$	0.402878
4.77478	0.054	$^1(H, L+6)$	0.662945
4.72164	0.373	$^1(H-1, L+4)$	0.423823
4.63424	0.665	$^1(H-1, L+2)$	0.308510
4.58075	0.572	$^1(H-1, L+3)$	0.279673
4.50552	0.048	$^1(H, L+5)$	0.654877
4.47587	0.012	$^1(H-5, L)$	0.396204
4.38722	0.037	$^1(H-2, L+2)$	0.496849
4.33889	0.005	$^1(H, L+4)$	0.550260
4.29785	0.007	$^1(H-1, L)$	0.332720
4.24700	0.221	$^1(H, L+3)$	0.418216
4.12777	0.495	$^1(H, L+2)$	0.358160
3.92056	0.116	$^1(H-2, L)$	0.431698
3.78973	0.042	$^1(H, L+2)$	0.418160
3.50331	0.883	$^1(H-1, L)$	0.523227
3.21284	1.386	$^1(H, L)$	0.615044

Part III

WORK IN PROGRESS

6

MOLECULAR ORBITAL SYMMETRY LABELLING

Unlike the rest of the thesis, this chapter is organized in a little different way because of the nature of the work presented here. Even though the main idea of this article to validate our implementation of symmetry orbital labelling in deMon2k (whose theoretical details are given in appendix A and its implementation details in appendix B) to a real-time application, being a begineer to the field of applied chemical physics, I think it is necessary to introduce some of the vocabularies from the field of ligand field theory (LFT) and crysal field theory (CFT).

Since 1951, [300, 189, 190, 191] LFT has been applied to the absorption spectra of octahedral complexes with partly filled d-shells and found to give very good agreement with the observed energy levels, provided that reasonable values are chosen for the ligand field parameter Δ (also denoted by $(E_1 - E_2)$ or 10 Dq or $\frac{10}{21}K$), the energy difference between the high energy orbitals and the low orbitals containing at most four and six electrons, respectively, for an octahedral complex.

Studies on symmetry of molecules is an application of mathematical group theory. The symmetry of a molecule can be described by listing all the symmetry elements of the molecule and this allows one to classify the molecule. This classification plays a vital role in the variety of coordination complexes. A simple, yet complicated, example is complexes of the two oxidation states of elemental iron: Fe(II) (ferrous, $3d^6$) and Fe(III) (ferric, $3d^5$). While the half-integer spin ferric ion is generally amendable to experimental and theoretical studies, the integer spin ferrous ion presents a considerable challenge to spectroscopists. When in the low-spin form (S=0), it is diamagnetic, however it is paramagnetic in the intermediate (S=1) spin, or more commonly, high spin (S=2). Prediction of high-spin configurations may be difficult or even impossible to validate experimentally. This is because in reduced symmetry environments anisotropic orbital angular momentum contributions cause the phenomenon of zero-field splitting (ZFS).

Thus LFT is the standard theory used to describe the physical properties of transition metal complexes [119]. However LFT is very limited in at least two respects: (i) its abilities to describe differences in geometries due to changes in spin state, and (ii) excited states involving ligand orbitals. DFT offers an attractive alternative, but its application is not entirely evident. This is primarily because ΔSCF and TD-DFT may give different answers for some excited states (though they should agree when both are applicable). Not every excited state may be

described by TD-DFT. We address these issues in detail for the small well-studied complex $[Fe(H_2O)_6]^{2+}$ and then go on to extract to show how information about LFT may be extracted from DFT.

6.0.1 *Transition Metal Coordination*

A transition metal is defined as an element whose atom has an incomplete d-sub-shell or which can give rise to cations with an incomplete d-sub-shell. Whereas a transition metal compound is a structure of a central transition metal atom, coordinated to one or more ligands. These compounds may be brightly coloured and some are paramagnetic, due to the partially filled d-shells. The variety of transition metal compounds originate from the diversity of available oxidation states (for the transition metal) and their ability to form complexes with a wide-range of ligands. This results in a wide range of coordination numbers and geometries. The total number of other atoms directly linked to the central element is termed the coordination number [3] and this can vary from 2 to as many as 16, of which 4 and 6 are the most common.

- Coordination number 2 (ML_2) : This coordination number is relatively rare for transition metals, since the two ligands will have to be oriented 180° apart. The coordination geometry is linear ($D_{\infty h}$).

Figure 6.1: Linear [$D_{\infty h}$](Image found on the web [8])

- Coordination number 3 (ML_3) : The most important 3-coordinate arrangements are trigonal planar (D_{3h}) and trigonal pyramidal (C_{3v}) in which the three ligands are oriented 120° apart.

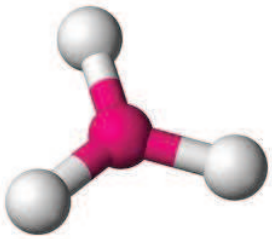

Figure 6.2: Trigonal planar [D_{3h}] (Image found on the web [8])

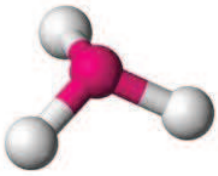

Figure 6.3: Trigonal pyramidal [C_{3v}] (Image found on the web [8])

- Coordination number 4 (ML_4) : This is a very important number. The best known 4-coordinate arrangements are square planar (D_{4h}) and tetrahedral (T_d). The tetrahedral arrangement is the more common while the square planar arrangement is found almost exclusively with metal ions having a d^8 electronic configuration.

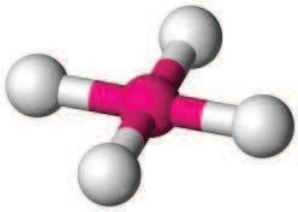

Figure 6.4: Square planar [D_{4h}] (Image found on the web [8])

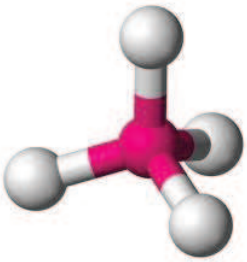

Figure 6.5: Tetrahedral [T_d] (Image found on the web [8])

- Coordination number 5 (ML_5) : This coordination number is less common than four or six, but is still very important. The most important 5-coordinate arrangements are trigonal bipyramidal (D_{3h}) and square pyramidal (C_{4v}). For the trigonal bipyramidal, a substitution of one of the axial ligands typically would lower the symmetry to C_{3v} whereas a subsitution of one of the quatorial ligands would lower the symmetry to C_{2v}. It is interesting to note that these trigonal bipyramidal and square pyramidal geometries usually differ little in energy and thus the one may

become converted into the other by small changes in bond angles.

Figure 6.6: Trigonal bipyramidal [D_{3h}] (Image found on the web [8])

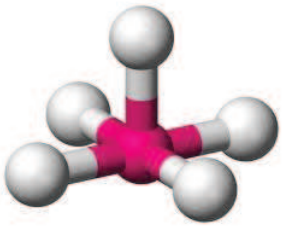

Figure 6.7: Square pyramidal [C_{4v}] (Image found on the web [8])

- Coordination number 6 (ML_6) : This coordination number is most important of them all, since nearly all cations form 6-coordinated complexes. The octahedron is often distorted, even in cases where all ligands are chemically the same. There are three principal forms of distortion of an octahedron. The tetragonal distortion (symmetrical distortion along one C_4-axis) gives a D_{4h} symmetry, the rhombic distortion (unsymmetrical distortion along one C_4-axis) gives a D_{2h} symmetry and the trigonal distortion gives a D_{3d} symmetry.

Figure 6.8: Octahedral [D_{4h}] (Image found on the web [8])

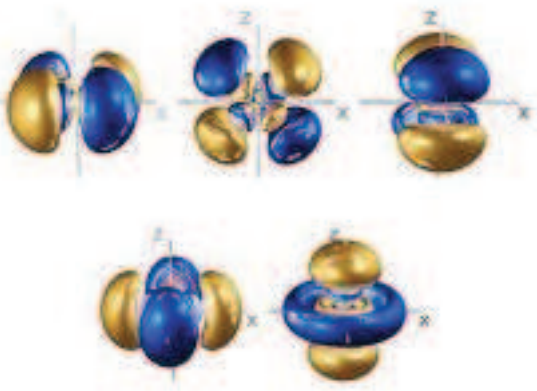

Figure 6.9: The five atomic d-orbitals on the Cartesian axis. There are two atomic d-orbitals that point direct along the Cartesian axis: d_{x^2} (which points along the z-axis) and $d_{x^2-y^2}$ (which has lobes on both x- and y-axes.) The other three atomic d-orbitals (d_{xy}, d_{xz} and d_{yz}), have lobes in between the Cartesian axis. A 45° rotation of d_{xy} along the z-axis results in $d_{x^2-y^2}$, and a 90° rotation of d_{xz} along the z-axis results in d_{yz}. Image found on the web [7]

6.0.2 *Crystal Field Theory*

There are different approaches to explain the bonding in transition metal complexes. One very familier approach is the crystal field theory (CFT). CFT is an electrostatic model that uses the negative charge on the non-bonding ligand electrons to create an electric field around the positively charged metal centre. The CFT focues on the energy changes (splitting) of the five degenerate atomic d-atomic orbitals (Figure 6.9) on the metal centre, when surrounded by the point charges from the ligands. For alkali metal ions containing a symmetric sphere of charge, calculations of energies are generally quite successful. However, for transition metal cations that contain varying numbers of d-electrons in orbitals that are not spherically symmetric, the situation is quite different. Despite above, CFT still provides a remarkably good qualitative explanation of many of the transition metal properties. The most common type of metal complex is octahedral, although tetrahedral and other complex geometries can also be described by CFT.

The splitting is affected by the following factors:

- The nature of the metal ion.
- The metal's oxidation state - a higher oxidation state leads to a larger splitting.
- The arrangement of the ligands around the metal ion.

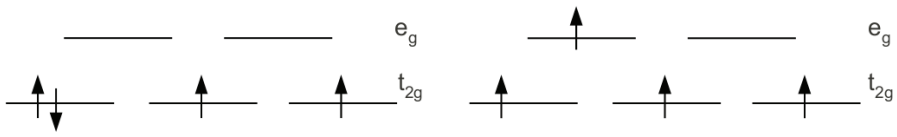

Figure 6.10: Illustration of a LS and HS d^4 system in an octahedral environment

The nature of the ligands surrounding the metal ion - the stronger the effect of the ligands, the greater the difference between the high and low energy 3d groups.

6.0.3 *Octahedral Crystal Field*

Consider a first row metal cation surrounded by six identical ligands, placed on the Cartesian axis at the vertices of an octahedron. As mentioned before, each ligand is treated as a negative point charge and there is an electrostatic attraction between the metal ion and ligands. However, there is also a repulsive interaction between the electrons in the atomic d-orbitals (Fig. 6.9) and the ligand point charges, due to the repulsion between similar charges. As the distance between the ligands and the metal ion decreases, the electrons from the ligands will be closer to the $d_{x^2-y^2}$ and d_{z^2} atomic orbitals and further away from the d_{xy}, d_{xz} and d_{yz} atomic orbitals. Thus the d-electrons closer to the ligands will have a higher energy than those further away, which results in the atomic d-orbitals splitting in energy. This means that the $d_{x^2-y^2}$ and d_{z^2} atomic orbitals are destabilized while the d_{xy}, d_{xz} and d_{yz} atomic orbitals are stabilized. From the O_h character table [83], it can be deduced that the $d_{x^2-y^2}$ and d_{z^2} atomic orbitals have an e_g symmetry and the d_{xy}, d_{xz} and d_{yz} atomic orbitals possess a t_{2g} symmetry. The energy separation between them is called Δ_{oct}. To maintain an energy equilibrium, the e_g level lies $3/5\Delta_{oct}$ above and the t_2g level lies $2/5\Delta_{oct}$ below the energy of the unsplit atomic d-orbitals. This pattern of splitting, in which the algebraic sum of all energy shifts of all atomic orbitals is zero, is said to "preserve the centre of gravity" of the set of levels and is called the crystal field stabilization energy (CFSE). The magnitude of Δ_{oct} is determined by the strength of the crystal field. Factors governing the magnitude are the identity and oxidation state of the metal ion and the nature of the ligands.

6.0.4 *High-Spin (HS) And Low-Spin (LS)*

Let us have a look at the effects of different numbers of electrons occupying the atomic d-orbitals in an octahedral crystal field. For a

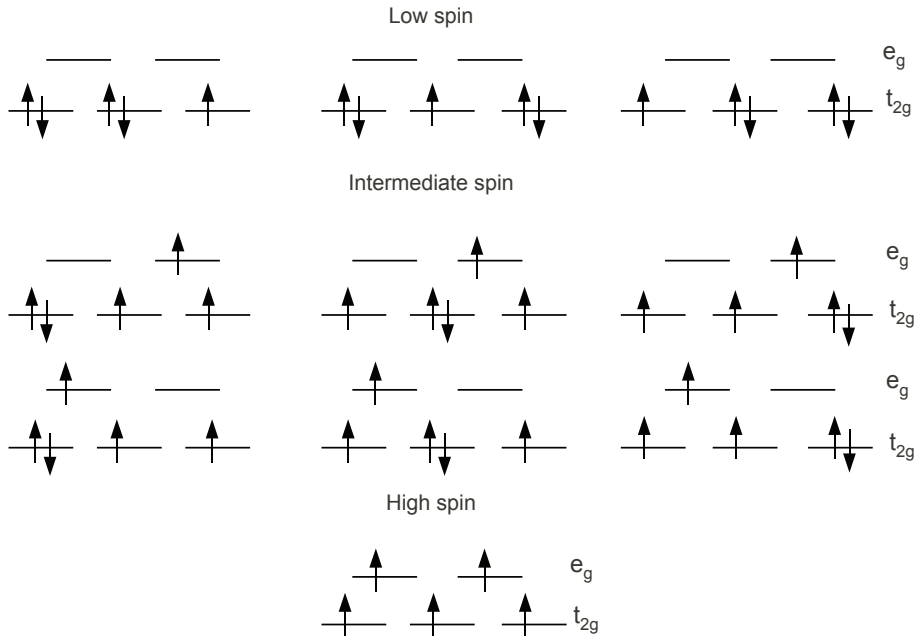

Figure 6.11: Illustration of alternative spin states: LS, intermediate spin and HS of a d^5 system in an octahedral environment

d^1 system, only one state is possible, which is t_{2g}^1. For a d^4 system, two arrangements are available: the four electrons may occupy the t_{2g} set with the configuration t_{2g}^4 (large Δ_{oct} Figure 6.10 left) or may singly occupy four atomic d-orbitals with the configuration $t_{2g}^3 e_g^1$ (small Δ_{oct} Figure. 6.10 right). This corresponds to LS (Fig. 6.10 left) and HS (Fig. 6.10 right) respectively. The distinction between the LS and HS configuration is governed by the size of the pairing energy (E_p) *versus* the crystal field splitting energy (Δ). For the LS configuration, the next question arises - where is the paired electron? Is it $d_{xy}^2 d_{xz}^1 d_{yz}^1$,$d_{xy}^1 d_{xz}^2 d_{yz}^1$ or $d_{xy}^1 d_{xz}^1 d_{yz}^2$? The preferred configuration is that with the lowest energy and depends on where it is energitically preferable to place the fourth electron. Thus for a d^5 system, ten different arrangement (3 LSs, 6 intermediate-spins and 1 HS) are possible (Fig. 6.11). These different arrangements are called alternative spin states and will be used in this study.

6.0.5 *Jahn-Teller Distortions*

Octahedral complexes of d^9 and HS d^4 ions are often distorted in such a way that the axial metal-ligand bonds (along the z-axis) are of different lengths from the remaining four equatorial metal-ligand bonds (x- and y-axis). This is illustration in Fig. 6.12. For a HS d^4

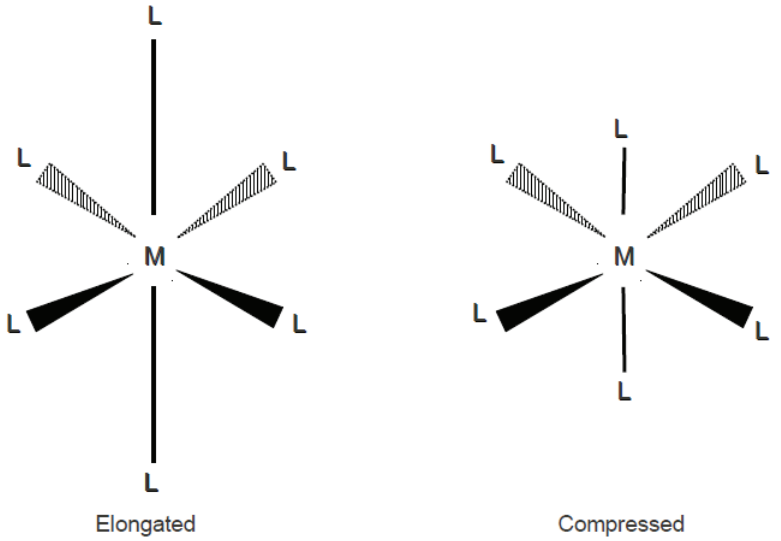

Figure 6.12: Jahn-Teller distortions along the z-axis. The Jahn-Teller theorem states that any non-linear molecule system in a degenerate electronic state will be unstable and will undergo distortion to form a system of low symmetry and low energy, thereby removing the degeneracy

ion, one of the e_g atomic orbitals contains one electron while the other is vacant. If the singly occupied orbital is in the d_{z^2} atomic orbital, most of the electron density in this orbital will be concentrated between the cation and the two ligands on the z-axis. Thus, there will be a greater electrostatic repulsion associated with these ligands than with the other four and the complex suffers elongation (Fig. 6.12 left). On the other hand, if the singly occupied orbital is in the $d_{x^2-y^2}$ atomic orbital, it would lead to elongation along the x- and y-axis (Fig. 6.12 right). A similar argument applies for a d^9 system where the two atomic orbtials in the e_g set are singly and doubly occupied respectively. Distortions of this kind are called Jahn-Teller distortions.

6.0.6 *Molecular Orbital Theory*

Another approach to explain the bonding in transition metal complexes is the molecular orbital (MO) theory. In MO theory, electrons are not assigned to individual bonds, but are treated as moving under the influence of the nuclei in the whole molecule. The probable position of the electrons can be described by an MO wave function which describes the different MOs of a molecule. MOs can be arranged in energy levels that account for the stability of various molecules.

Consider an octahedral ML_6 complex where the ligands have only σ-orbitals (no π-orbitals) directed toward the metal ion. The six σ-

orbitals are designated σ_x and σ_{-x} (along the x-axis), σ_y and σ_{-y} (along the y-axis), and σ_z and σ_{-z} (along the z-axis). These six orbitals combine to make six distinct linear combinations called ligand group orbitals (LGOs). Each LGO has a symmetry that is correctly oriented to overlap with one of thes−, p− or d−orbitals of the metal. This method is called the linear combination of atomic orbitals approximation and is used in computational chemistry.

Each such overlap between one of the six LGOs and a metal orbital results in the formation of a bonding MO and an antibonding MO. If this orbital is of a type in which the electron in the orbital has a higher probability of being between nuclei than elsewhere, the orbital will be a bonding orbital and will tend to hold the nuclei together. If the electrons tend to be present in a molecular orbital in which they spend more time elsewhere than between nuclei, the orbital will function as an antibonding orbital and will actually weaken the bond.

MO theory can further be generalized by including π-orbitals. One must differentiate between two types of ligands: π-donor and π-acceptor ligands. A π-donor ligand donates electrons to the metal centre in an interaction that involves a filled ligand orbital and an empty metal orbital, whereas a π-acceptor ligand accepts electrons from the metal centre in an interaction that involves a filled metal orbital and an empty ligand orbital. The ligand group π-orbitals are filled and lie above (but relatively close to) the ligand group σ-orbitals. The π-orbitals can overlap with the d_{xy}, d_{yz} and d_{xz} atomic orbitals of the metal and this leads to bonding (t_{2g}) and antibonding (t^*_{2g}) MOs. The positions of these sets of t_{2g} and t^*_{2g} orbitals in the MO energy-level diagram are variable depending on the nature of the ligand π-orbitals.

The following important differences between octahedral ML_6 complexes containing σ-donar, π-donar and π-acceptor ligands exist:

- Δ_{oct} decreases in going from a σ-complex to one containing π-donor ligands.
- For a complex with π-donor ligands, increased π-donation stabilizes the t_{2g} level and destabilizes the t^*_{2g}, thus decreasing Δ_{oct}.
- Δ_{oct} values are relatively large for complexes containing π-acceptor ligands and such complexes are likely to be LS.
- For a complex with π-acceptor ligands, increased π-acceptance stabilizes the t_{2g} level, thus increasing Δ_{oct}.

6.0.7 *Ligand Field Theory*

Ligand field theory (LFT) is an extension of CFT that assigns certain parameters as variables rather than taking them as equal to the values

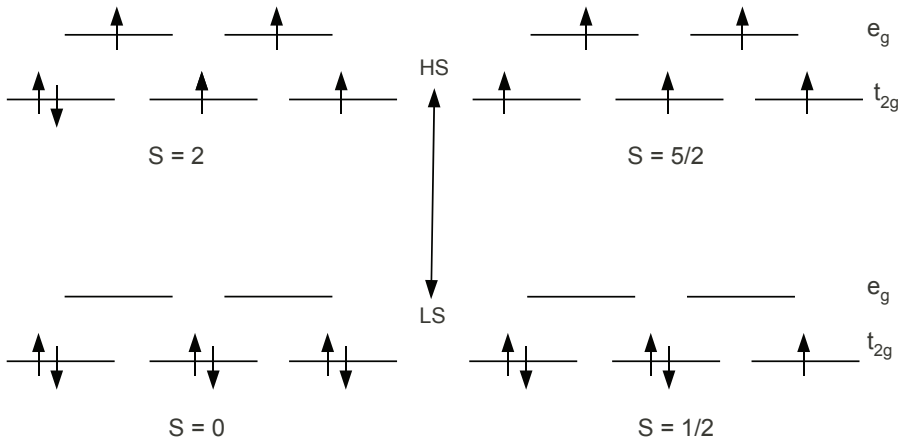

Figure 6.13: Schematic representation of the two possible spin states for iron(II) and iron(III) coordination compounds in an octahedral environment

found for free ions, thereby taking into account the potential covalent character of the metal-ligand bond. In other words, LFT (like CFT) is confined to the role of atomic d-orbitals, but (unlike CFT) the LFT approach is not purely electrostatic model. It is a freely parameterized model and uses Δ_{oct} along with the Racah parameters, which are obtained from electronic spectroscopic data. LFT is more powerful than either CFT or MO theory, but unfortunately it is also more abstract.

6.0.8 *Spin Crossover*

The choice between a LS and HS configurations for d^4 to d^7 complexes is not always unique and a spin crossover (SCO) sometimes occurs. The electronic ground state of these SCO complexes may be reversibly interchanged under external stimuli such as temperature, pressure, magnetic field or light irradiation. This type of molecular magnetism is one of the most spectacualr examples of molecular bistability driven by external constraints leading to molecular switches or memory.

The atomic d-orbitals of an octahedral complex split into the t_{2g} and e_g sets with an energy separation of Δ_{oct} and therefore the complexes can either exist in LS or HS states. As an example, Fig. 6.13 illustrates the possible spin states for iron(II) and iron(III) complexes. This spin

state is influenced by the nature of the ligand field surrounding the metal centre. In weak fields, HS is the ground state (corresponding to the highest possible spin multiplicity) and the d-electrons are distributed over the t_{2g} and e_g sets. Strong fields again stabilize the LS state with minimum multiplicity. In this case, Fig. 6.13, the t_{2g} set is completely occupied before electrons are added to the e_g set. The energy gap between these orbitals (Δ_{oct}) varies subject to the ligands used to generate the metal coordination compounds. If the appropriate energy gap is achieved by the application of an external stimulus, the d-electron(s) transfers from the t_{2g} set to the e_g set and the compound passes from one configuration to the other. This phenomenon is called spin crossover.

TESTING SYMMETRY IMPLEMENTATION IN DEMON@GRENOBLE: SPIN STATE ASSIGNMENT FOR THE GROUND AND EXCITED STATES OF $[FE(H_2O)_6]^{2+}$

BHAARATHI NATARAJAN AND MARK E. CASIDA

6.1 INTRODUCTION

The importance of transition metal complexes—whether it be in the active sites of biomolecules or in intelligent materials—has given them a well-merited place in the curriculum of every well-trained chemist. We are particularly interested in transition metal complexes belonging to the spin-crossover regime. In these complexes, the high-spin (HS) and low-spin (LS) states are close in energy with the LS state a little lower in energy. As the equilibrium,

$$LS = HS, \tag{6.1}$$

with

$$K = \frac{[HS]}{[LS]}, \tag{6.2}$$

is determined by the well-known thermodynamic relation,

$$-RT \ln K = \Delta G = \Delta E + P\Delta V - T\Delta S \approx \Delta E - T\Delta S, \tag{6.3}$$

and

$$\begin{aligned} \Delta E &= E_{HS} - E_{LS} > 0 \\ \Delta S &= S_{HS} - S_{LS} > 0, \end{aligned} \tag{6.4}$$

it is possible to change the color, magnetism, as well as still other properties (such as the dielectric constant), of the complex by a change of temperature. This gives us an optomagnetic molecular switch. When it is possible to induce the spin-crossover transition by light, we speak of light-induced excited spin-state trapping (LIESST).

Up until about 10 years ago, LFT was pretty much the only model used to describe complexes in the spin-crossover regime, despite the limitations associated with the relative simplicity of the spin-crossover model [119]. The DFT has shown itself to be useful for studying the ground states of these complexes. In order to go further in modeling the light-induced excited spin-state trapping (LIESST) phenomenon, one could imagine using a generalization of DFT, namely TD-DFT [241]. The LIESST effect is a general phenomenon in the sense that it is

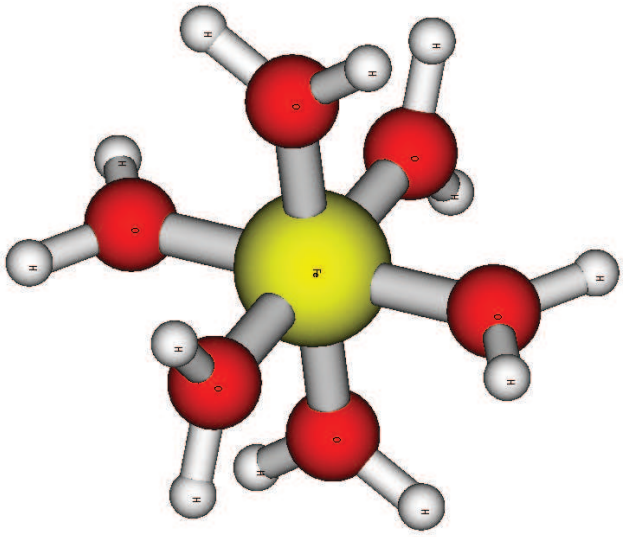

Figure 6.14: Starting geometry for optimizations for S=5/2,3/2 and 1/2 spin states of $[Fe(H_2O)_6]^{2+}$

the photoinduced population of the HS state of any transition metal complex with a LS ground state. However there may be problems associated with TD-DFT state assignments due to spin-contamination when the ground state is open-shell [182].

6.2 STRUCTURAL DETAILS

Figure 6.14 shows the initial geometry for the hexaaquo iron(II) complex used for all calculations. All the Fe-O distances have been regularized to the same initial value of 1.75 Å and the oxygen atoms placed along the octahedral axes. (Slight deviations from octahedral symmetry are present in the crystal structure they appear to be the result of intermolecular hydrogen-bonding interactions between water molecules or between water and the counterions.) The dispositions of the hydrogens of the waters closest to one another in this structure are of a "staggered" nature with the hydrogens of waters "anti" to one another in the same plane. However, the mean deviation of the hydrogen positions are fixed throughout the calculations relative to the oxygen to which they are bonded and the Fe-O bond. The point group characterizing the complete structure of the complex is T_h.

6.2.1 *Basis Sets*

For Fe we employed a triple-zeta-valance polarization (TZVP) contracted Gaussian type orbital basis. The basis set used for H_2O was a double-zeta-valance polarization (DZVP) Gaussian set.

6.2.2 *Computational Details*

All calculations were performed using the symmetry implemented version of DEMON2K. All DFT and TD-DFT calculations were performed using the PBE91 functional and 'fine' integration grid was employed. The guess 'core' option was used for all SCF calculations with the tolerance of $10^{-}5$ a.u. TD-DFT calculations were performed within TDA.

6.3 RESULTS

In a mononuclear transition metal complex, the central ion is surrounded by the ligands in a specific three-dimentional arrangement. The metal-ligand bonds involved are of the dative type, that is the metal interacts as a Lewis acid with the ligand, which in turn acts as a Lewis base.

In T_h symmetry, the metallic d_{z^2} and $d_{x^2-z^2}$ orbitals form a basis set for the e_g irreducible representation, while the d_{xy}, d_{yz} and d_{xz} orbitals constitue a basis for the t_{2g} irreducible representation. All five 3d orbitals are degenerate in the free metal iron. The ligand orbitals, also can be combined linearly to form a basis set for the irreducible representations in T_h. Those belonging to e_g and t_{2g} can interact with the metal d orbitals of corresponding symmetry.

Molecular orbitals thus formed from the σ interaction between the metal e_g orbitals and the correspondingly combined ligand e_g orbitals result in antibonding e_g^* and bonding e_g MOs. The former are metal-centered because the metallic contributions (the d_{x^2} and $d_{x^2-z^2}$) are higher in energy than those from the corresponding ligand e_g orbitals. The metalic t_{2g} orbitals remain mostly non-bonding because their symmetry is not appropriate to have interactions with the orbitals of the ligands, except for usually small π interactions which can be either antibonding character in the case of π base ligands. The six σ bonding molecular orbitals result from the combination of the symmetry adapted linear combinations (SALC) of the ligands with the metal orbitals of the same symmetry.

The splitting of the d orbitals upon complex formation is often discussed in terms of crystal field theory (CFT) in which the ligands are considered as point charges with which the d electrons interact electrostatically. Thus the metal e_g orbitals pointing towards the ligands are destabilized with respect to the metal t_{2g} orbitals. The energy difference between the metal-centered e_g^* and t_{2g} levels is called the ligand field splitting and is expressed by the ligand field parameter Δ=10Dq. Its value depends on the chemical properties of the ligands and the metal iron. Thus 10Dq can be regarded as a measure of the metal-ligand interaction.

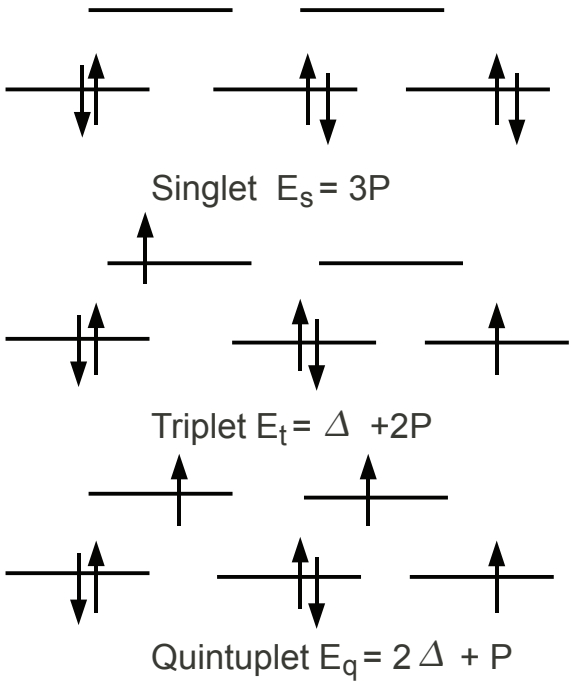

Figure 6.15: Elementary pairing energy argument

6.3.1 *Optimized Geometries And Breathing Coordinates*

Table 6.1: Average Fe-O bond lengths of the three spin states.

State	R(Fe-O)/Å
S=5/2	2.15
S=3/2	2.10
S=1/2	2.00

Table 6.1 and 6.2 lists the Fe-O distances for the optimized $[Fe(H_2O)_6]^{2+}$ structures resulting in T_h symmetry and their corresponding energies in the three spin states respectively. The average value of the Fe-O distance decreases with decreasing spin multiplicity: $R_{Fe-O}(S = 5/2)_{avg} > R_{Fe-O}(S = 3/2)_{avg} > R_{Fe-O}(S = 1/2)_{avg}$.

The optimized singlet and quintet geometries have been discussed in Ref. [125]. According to LFT the triply degenerate t_{2g} orbital is expected to be nonbonding while the doubly degenerate e_g orbital is expected to be antibonding with respect to the ligands. Going to higher spin states means populating the antibonding orbital and

Table 6.2: Energies of High, Intermediate, and Low Spin State Complexes at Optimized Geometries .

State	E(Ha)
S=5/2	-1721.11678
S=3/2	-1721.08743
S=1/2	-1721.09407
E(3/2) - E(5/2)	6441.41908
E(1/2) - E(5/2)	4984.20717

hence is expected to lead to longer bonds. The calculated average equilibrium Fe-O bond lengths are shown in Table 6.1. Not only are the complexes not exactly octahedral because the water molecules are not exactly spherical, but the triplet and quintet states undergo Jahn-Teller distortions to remove their electronic degeneracies. This is why we speak of average bond lengths. However the distortion is small.

6.3.2 *Ground State And Excited-State Curves*

The efficient control of spin-state transitions depends on an in-depth understanding of the relationship between the structural and energetic factors which rule the relaxation kinetics.

Although its nature and the spectroscopic constants are known, our results will be included here for sake of validation. The total energies of the low-lying states as a function of metal ligand distance (R Å) are depicted in figure 6.16. The increase of the R parameter equilizes the singlet and triplet energies, producing a spin crossover at R $\approx$ 2 Å and the triplet and quintuplet energies, producing an another spin crossover at R $\approx$ 2.1 Å. At higher values of R, the quintuplet remains the ground state.

6.3.2.1 *Excited States Calculations*

The ΔSCF method is based on the extension of the Hohenberg-Kohn theorems to treat the state of lowest energy among states of given spatial and spin symmetry $^{2S+2}\Gamma$. It allows in particular to estimate the energy difference between states of distinct symmetries through regular Kohn-Sham calculations. The method requires the knowledge of the symmetry dependence of the xc functional. This condition is not fulfilled by the current approximate functionals. Despite this, the ΔSCF approach is known to give satisfactory results [340].

The linear-response (LR) method in TD-DFT can be used to characterize the states of interest even if they are not the states of lowest energy in a given symmetry. It allows one to obtain the energies of

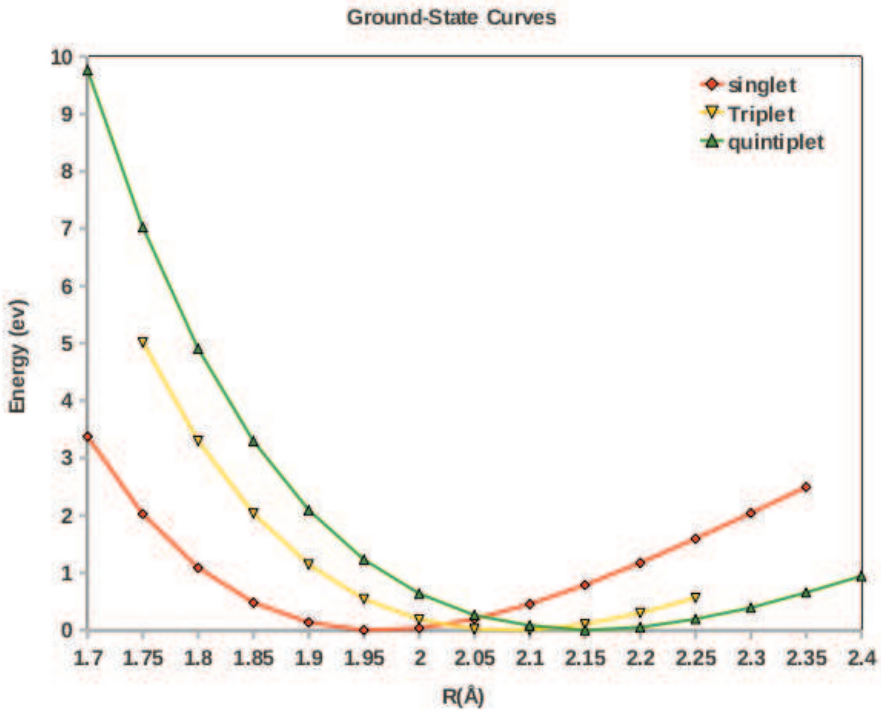

Figure 6.16: Ground-state curves

the excited states upon excitations with respect to a given reference state which could be the ground state or the state of lowest energy for a chosen symmetry. In particular the calculations on transition metal systems involve treating partially filled d shells with one or several unpaired electrons. The reliable determination of the small energy differences between states, which originated from the state or different electronic configurations demands very accurate computational methods. It should be recalled that the first-row transition metal ions have a very compact 3d electron subshell, which makes the treatment of electronic correlation extremely difficult with an decisive choice of the xc-functional.

Figures 6.17, 6.18, and 6.19 presents the Walsh diagrams for the excited state singlet, triplet, and quintuplet respectively. Examination of orbital symmetries using those plots show us the tendency of decrease in energy with respect to decrease in interatomic distance with among the lowest excited states. In case of singlet, the e_g orbital symmetry tend to mix with the lowest a_g state symmetry when the water molecule close to the metal ion. More or less the same trend is observed for the triplet as shown in fig 6.18. When the system is in the high spin state i.e., for quintuplet orbital symmetry behavior seems is not yet quite understood especially in the region where the spin crossover occurs. The observation shows that the orbital with a_g symmetry orbital remains unchanged thoughout the interatomic

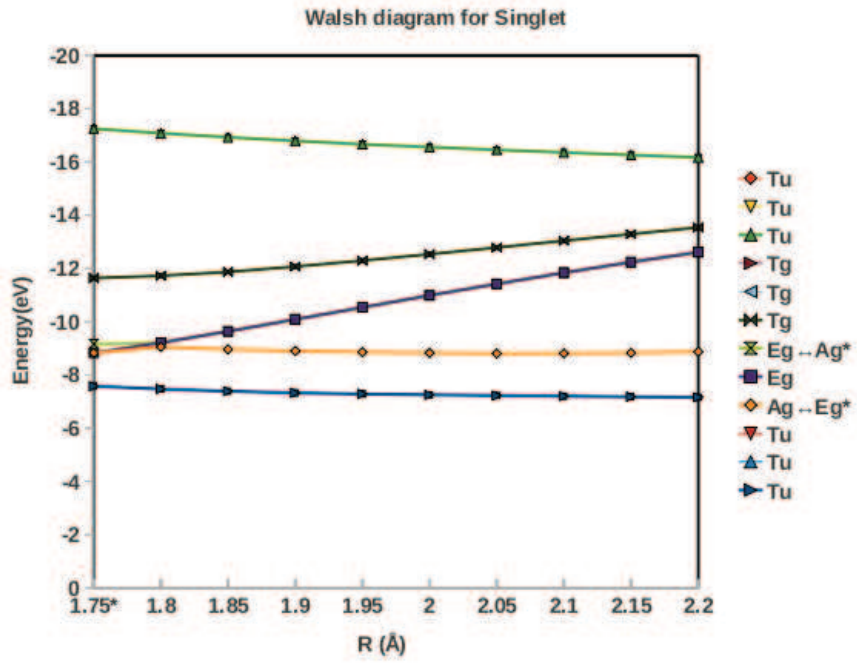

Figure 6.17: Singlet Walsh diagram

distances. However higher orbital symmetries gets lower in energy for the lower distance between metal ion and ligand but not close enough to cross the lower symmetry orbital. Careful studies would be needed to make any further understanding of this spin state behavior.

6.4 CONCLUSION

The optimized structure and spin-state energies of the hexaaquo iron(II) complex, $[Fe(H_2O)_6]^{2+}$, in high (S=5/2), intermediate (S=3/2), and low (S=1/2) spin states were determined from a common structure using unrestricted Kohn-Sham density-functional theoretical (DFT) method. The optimized ground-state geometries were similar to each other and the energy ordering of the spin state was found to be : E(5/2) $<$ E(3/2) $<$ E(1/2). Time-dependent density-functional calculations were performed using symmetry implemented version of deMon2k.

ACKNOWLEDGEMENTS

B. N. would like to acknowledge a scholarship from the *Fondation Nanoscience*. B. N. would also like to acknowledge Berndie Ema Fleurinor, Emilio Cineros, Loic Joubert Doriol and Sébastien Bruneau those who were worked on the preliminary results of this problem as part of their undergraduate research projects. This work has been carried out in the context of the French Rhône-Alpes *Réseau thématique de*

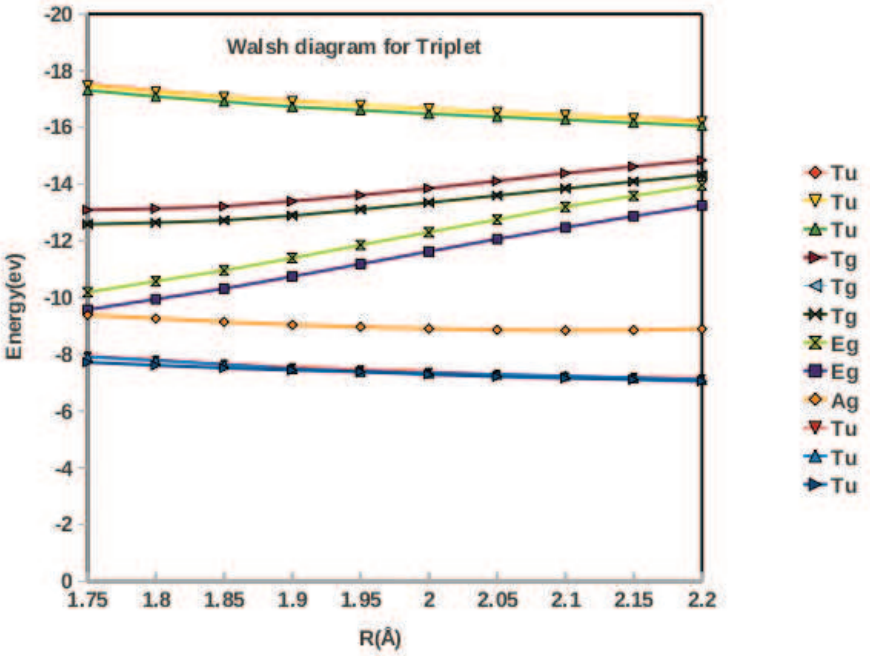

Figure 6.18: Triplet Walsh diagram

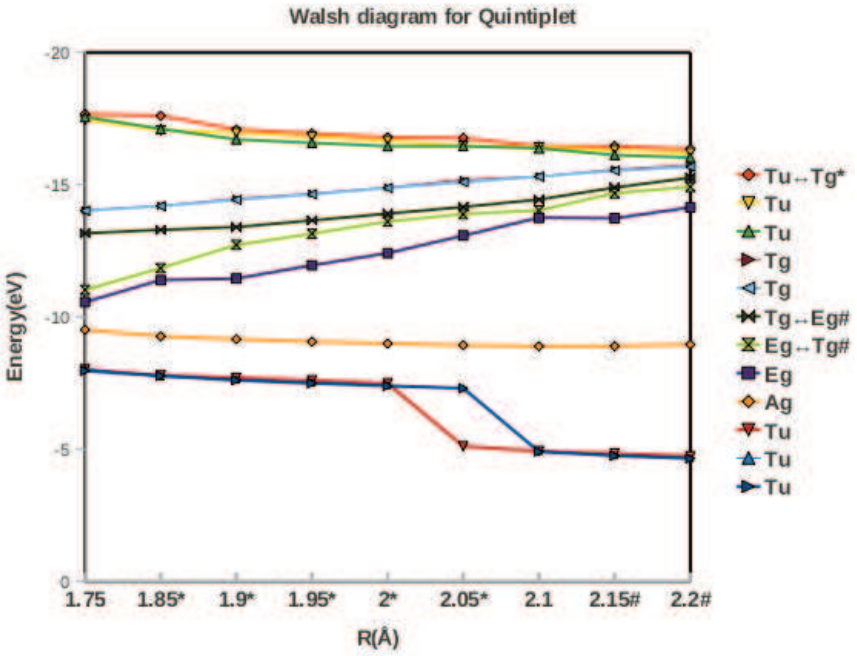

Figure 6.19: Quintet Walsh diagram

recherche avancée (RTRA): Nanosciences aux limites de la nanoélectronique and the Rhône-Alpes Associated Node of the European Theoretical Spectroscopy Facility (ETSF).

Part IV

CONCLUDING REMARKS

7 OVERALL CONCLUSION

7.1 CONCLUSION

My thesis project, *"Implementation, Testing, and Application of Time-Dependent Density-Functional Theory Algorithms for Gaussian- and Wavelet-based Programs"*, is part of a greater NanoSTAR project aimed at developing new, and improving existant methods for the theoretical modeling of nanoelectronic systems. Such systems typically involve large molecules, small solids, or simply molecules on surfaces. Thus the modelling of nanoelectronic systems very much lies at the interface between molecular and solid-state theory.

The NanoSTAR project divides into two parts: one dealing with spectroscopy; the other dealing with conductivity. My project falls within the former part and steps taken to acheive the goal of the project are reported in this thesis.

This thesis is very much a contribution at the interface between molecular and solid-state theory. Many interesting things happen when molecules come in contact with solids – be it heterogeneous catalysis, molecular crystals, or molecules on conducting surfaces designed to carry out applications in nanoelectronics. Very few people are trained to work with the theoretical ideas and the programming of computer codes in both of these areas and I think that my work contributing to improved algorithms for TD-DFT in both these areas opens the way to new algorithms for applications where molecules come into contact with conductors, semiconductors, and even optically-active insulators.

My thesis work began with the quantum chemistry code deMon2k. This was my initiation to many ideas in hard-core theory. Not only did I have to learn about basis sets, grids, convegence criteria, potential energy surfaces, and all the jargon of quantum chemistry so that I could run the programs, but I also helped to implement the molecular orbital symmetry routines in deMon2k and verify that they worked correctly. These routines were subsequently applied to work in progress (chapter 6) on $[Fe(H_2O)_6]^{2+}$ designed to high-light the pros and cons of TD-DFT for potential energy surfaces of open-shell molecules. It is often assumed that, for the characterization of transition metal complexes used for studying the spin crossover (SCO) and light induced excited spin-state trapping (LIESST) phenomena, density-functional theory (DFT) within the Kohn-Sham (KS) formulation is adequate for the description not only of the molecular structure in all spin-states, but also of the energies and photophysics. However

it is also clear that TD-DFT may present not just advantages, but also problems, when used to calculate the excitation spectra and PES of species with open-shell ground states. Such species abound in the field of transition metal coordination complexes. In order to clarify how best to use TD-DFT for such problems. Thus, a spin crossover complex $[Fe(H_2O)_6]^{2+}$ was taken as an example test case. In the study of $[Fe(H_2O)_6]^{2+}$, the main subjects treated were the ability of DFT to describe and predict the molecular structure of such complexes and the difficulties encountered when it comes to calculating the energetics of the different spin states. The calculation of excitation energies for three different spin states were carried out and future studies will be focused on studying the potential energy surfaces (PES) morefully, including with functionals beyond the simple LDA. The modelling of the effect of the environment is very important, especially because it is known that the environment is often important for getting right delicate energy difference between different spin-states.

Early on I was also heavily involved in exploring the spin-flip (SF) approach to TD-DFT to see how it works for describing the conical intersection (CX) in the photochemical pathway of oxirane ring opening. The CX forms a part of the photophysical and photochemical reaction pathway of molecules. In this model, points on the excited state (Franck-Condon region, minima, transition states and conical intersections) are linked by a path of steepest descent. The CX acts as a point from which the reaction may branch, as the population moves from the higher to the lower state. The exact structure of the CX can be used to gain insight regarding the photochemical stability of molecules and regarding how the reaction pathway may branch thus leading to more than one product in different relative ratios. In chapter 4 an attempt is made to test the validity of SF-TD-DFT method for locating CX and to make a comparison of the PES trajectories with that of TD-DFT, CIS and CASSCF for the text book molecule oxirane. The results presented in 4.7.3 suggest that SF-TD-DFT method, though not as good as multi-reference wave function methods, can improve the description of oxirane photochemistry compared to conventional TD-DFT. The generalities of SF-TD-DFT has been reinforced and presented in what we trust is a convincing way.

This was long and tedious but rewarding work which helped to bring out the pros and cons of this attractive and yet not completely satisfactory approach to resolving some fundamental problems of TD-DFT for key regions of photochemistry potential energy surfaces. This project certainly sparked my interest for theoretical photochemistry and helps to explain my contribution both to the book chapter on photodynamics with TD-DFT (chapter 2). In that chapter, two common approaches to quantum-classical (nonadiabatic) dynamics were introduced: wave function-based and density function-based dynamics. After reviewing quantum-classical wave function molecular dynamics,

a method to perform dynamics within TD-DFT was discussed. Such a formulation on the dynamics holds much promise for cases where the dynamics of large molecues.

My work then shifted to the problem of implementing TD-DFT in the wavelet program BIGDFT. Wavelets are very different both from the plane waves typical of solid-state physics programs and from the GTOs typical of quantum chemistry programs. In attacking this problem, I brought with me the knowledge of how TD-DFT is programmed in DEMON2K and how it is used in practice in that program plus the desire to explore the new (both to me and to much of the physics and chemistry communities) technique of wavlets. Learning the basics of wavelets involved a major retraining in modern applied mathematics and this is well reflected in the book chapter that I wrote trying to make wavelet-based DFT and TD-DFT more understandable to the broader physics and chemistry audience. In this chapter 3, we have shown the principal features of an electronic structure pseudopotential method based on Daubechies wavelets. Daubechies wavelets properties make the basis set a powerful tool for electronic structure calculations. The matrix elements, the kinetic energy and nonlocal pseudopotentials operators can be calculated analytically in this basis. The other operations are mainly based on convolutions with short-range filters, which can be highly optimized in order to obtain good computational performances. BIGDFT shows high systematic convergence properties, very good performances for bigger systems and an excellent efficiency for parallel calculations.

Implementation of TD-DFT in BIGDFT as described in chapter 5 was also facilitated by my previous experience in working with DEMON2K in the sense that both programs are very big, professional codes. The final result is a first working version of wavelet-based TD-DFT which was tested and found to work reasonably well – well enough to do an interesting calculation of the Flugi**6** spectrum. The corresponding documentation is given in appendix C. The problems anticipated with the use of unoccupied wavelet-orbitals are there, but turned out to be much less severe than expected. Future work on TD-DFT in BIGDFT should focus on eliminating as much as possible the need for unoccupied orbitals. Making the TD-DFT part of the code robust and user-friendly is also important. Only then should we go on to the very interesting area of excited-state analytical derivatives with applications to luminescence and to photochemical dynamics.

Detailed formula given in appendix D for the TD-DFT analytical derivatives that we had hoped (and still hope) to implement in both the GTO-based DEMON2K and the wavelet-based BIGDFT codes for the future exploitation of TD-DFT beyond Born-Oppenheimer approximation.

Part V

APPENDIX

A

PROJECTORS FOR SYMMETRY BLOCKING

Implementing and debugging a method can be very difficult unless you have a good understanding of the formalism behind the method. The goal of this small document is to help provide the background for symmetry blocking of the Kohn-Sham orbital eiganvalue problem,

$$\hat{F}|i_\sigma\rangle = \epsilon_i^\sigma |i_\sigma\rangle \,, \tag{A.1}$$

Here $|i_\sigma\rangle$ is the ith molecular orbitals (MO) associated with spin σ. The emphasis on how symmetry projectors are defined and used. In particular we will be concerned with $\hat{\mathcal{P}}_\Gamma$, the projector onto the irreducible representation (irrep) Γ.

Most of the time, the MO should belong to an irrep of the space group of the molecule. An exception occurs when there are accidental degeneracies. These are simply MOs with the same energy but belonging to different irreps. Their linear combination is also an eigenfunction of the molecule with the same energy but need not belong to an irrep of the molecule. Far from being rare, accidental degeneracies of 1s core orbitals are likely to be common for large symmetric molecules. Problems may also occur for virtual orbitals with closely-spaced energy levels.

Probably the best way to ensure that the MOs belong to irreps is to set up and solve the projected problem,

$$\hat{F}_\Gamma^\sigma |i_\sigma\rangle = \epsilon_i^\sigma |i_\sigma\rangle \,, \tag{A.2}$$

where,

$$\hat{F}_\Gamma^\sigma = \hat{\mathcal{P}}_\Gamma \hat{F}^\sigma \hat{\mathcal{P}}_\Gamma \,. \tag{A.3}$$

Our ultimate objective is to set up and solve Eq. (A.2) in a finite basis set of atomic orbitals (AO)s, $|\mu\rangle$. That is, we want to find the coefficients $c_{\mu,i}^\sigma$ in the expansion,

$$|i_\sigma\rangle = \sum |\mu\rangle c_{\mu,i}^\sigma \,. \tag{A.4}$$

A.1 REPRESENTATION THEORY

Any operator, $\hat{O}$, may be represented in terms of finite basis sets, $|\mu A\rangle$, $|\nu A\rangle$, etc. Here I have deliberately chosen to use more than one basis set so that we can talk about transformations from one basis set to another.

The operator $\hat{\mathcal{O}}$ may be either represented in a finite basis set by using expansion coefficients, $\left[\hat{\mathcal{O}}\right]_{\mu A,\nu B}$, defining the action of the operator on a basis set,

$$\hat{\mathcal{O}}|\nu B\rangle = \sum |\mu A\rangle \left[\hat{\mathcal{O}}\right]_{\mu A,\nu B} , \tag{A.5}$$

or in terms of its matrix elements,

$$\hat{\mathcal{O}}_{\mu A,\nu B} = \langle \mu A|\hat{\mathcal{O}}|\nu B\rangle . \tag{A.6}$$

The relation between the two is that,

$$\begin{aligned} \hat{\mathcal{O}}_{\mu A,\nu C} &= \sum \langle \mu A|\kappa B\rangle \left[\hat{\mathcal{O}}\right]_{\kappa B,\nu C} \\ \mathbf{O}_{A,C} &= \mathbf{S}_{A,B} \left[\hat{\mathcal{O}}\right]_{B,C} \\ \left[\hat{\mathcal{O}}\right]_{B,C} &= (\mathbf{S}_{A,B})^{-1}\mathbf{O}_{A,C} , \end{aligned} \tag{A.7}$$

where

$$S_{\mu A,\nu B} = \langle \mu A|\nu B\rangle , \tag{A.8}$$

defines the overlap matrix $\mathbf{S}_{A,B}$. I shall assume that sums are over all repeated indices after the sum sign (Einstein convention), unless otherwise indicated.

The action of an operator expressed in terms of a finite basis set is a little tricky. The algebra of expansion coefficients is easiest,

$$\begin{aligned} \sum |\nu A\rangle \left[\hat{X}\hat{Y}\right]^{A,C}_{\mu,\nu} &= \hat{X}\hat{Y}|\mu C\rangle \\ &= \hat{X}\sum |\kappa B\rangle \left[\hat{Y}\right]_{\kappa B,\nu C} \\ &= \sum |\nu A \left[\hat{X}\right]_{\nu A,\kappa B} \left[\hat{Y}\right]_{\kappa B,\nu C} \end{aligned} \tag{A.9}$$

or

$$\left[\hat{X}\hat{Y}\right]_{A,C} = \left[\hat{X}\right]_{A,B} \left[\hat{Y}\right]_{B,C} . \tag{A.10}$$

In fact, the expansion coefficients have the same algebra as the operators!

This is not so far the matrices. Instead we have that

$$(\mathbf{S}_{B,A})^{-1}\,\mathbf{M}_{B,E} = (\mathbf{S}_{B,A})^{-1}\,\mathbf{X}_{B,C}\,(\mathbf{S}_{D,C})^{-1}\,\mathbf{Y}_{D,E} , \tag{A.11}$$

because of Eq. (A.7). Here $\mathbf{M}_{\mu B,\nu E} = \langle \mu B|\hat{X}\hat{Y}|\nu E\rangle$ is the matrix of the product of the operators. Thus

$$\mathbf{M}_{B,E} = \mathbf{X}_{B,C}\left(\mathbf{S}^{-1}_{D,C}\right)\mathbf{Y}_{D,E} . \tag{A.12}$$

We can also arrive at the same result using the projection operator,

$$\hat{\mathcal{P}} = \sum |\mu C\rangle \left(\mathbf{S}^{-1}_{D,C}\right)_{\mu C,\nu D} \langle \nu D| . \tag{A.13}$$

Then

$$\begin{aligned} M_{\mu B,\nu E} &= \langle \mu B|\hat{X}\hat{Y}|\nu E\rangle \\ &\approx \langle \mu B|\hat{X}\hat{\mathcal{P}}\hat{Y}|\nu E\rangle \\ &= \sum \langle \mu B|\hat{X}|\kappa C\rangle \left(\mathbf{S}^{-1}_{D,C}\right)_{\kappa C,\lambda D} \langle D\lambda|\hat{Y}|\nu E\rangle \\ \mathbf{M}_{B,E} &= \mathbf{X}_{B,C}\left(\mathbf{S}_{D,C}\right)^{-1}\mathbf{Y}_{C,E}\,. \end{aligned} \tag{A.14}$$

Notice how Eq. (A.12) assumes that the space spanned by the finite AO basis set is closed under the action of the operators (which may not actually be the case.) Also the projection operator becomes the resolution-of-identity (RI) (i.e., completeness relation) in the limit of a complete basis set.

A.2 SYMMETRY PROJECTION

We want to make symmetry adapted linear combinations (SALCs) by projection. For each irrep, this involves a transformation,

$$|\nu\Gamma\rangle = \sum |\mu\rangle \left[\hat{1}\right]_{\mu,\nu\Gamma}\,, \tag{A.15}$$

Here

$$\left[\hat{1}\right]_{\mu,\nu\Gamma} = A_{\mu,\nu\Gamma}\,, \tag{A.16}$$

(Actually **A** is a work vector in DEMON2K and so does not always refer to the SALCs, but we will use it here as synomymous with the SALC expanstion coefficients.)

The most common way to make SALCs is via the well-known formula of group theory,

$$\Gamma_{\hat{\mathcal{P}}} = \frac{\dim(\Gamma)}{\dim(\mathcal{G})}\sum_{\hat{G}\in\mathcal{G}} \chi_\Gamma(\hat{G})\hat{G}\,. \tag{A.17}$$

However orthonormalization of SALCs belonging to the same irrep provides a potentially different equivalent set of SALCs, so we should not necessarily assume Eq. (A.17). Note that I have made the irrep label a left superscript in Eq. (A.17) to minimize confusion with basis set transformations.

From Eqs. (A.15-A.16), matrix elements of the projector $\hat{\mathcal{P}}$ onto the irrep Γ are given by,

$$\begin{aligned} \mathcal{P}_{\mu,\nu\Gamma} &= \sum \langle \mu|\kappa\rangle A_{\kappa,\nu\Gamma} \\ \mathbf{P}_{-,\Gamma} &= \mathbf{S}_{-,-}\mathbf{A}_{-,\Gamma} \\ \mathbf{A}_{-,\Gamma} &= (\mathbf{S}_{-,-})^{-1}\mathbf{P}_{-,\Gamma}\,. \end{aligned} \tag{A.18}$$

Here $(\_)$ indicates the untransformed AO basis set, while the Γ subscript refers to the SALCs. This is the famous DEMON2K formula for the projector. Also

$$\begin{aligned} \mathcal{P}_{\mu,\Gamma,\nu\Gamma} &= \sum \langle \mu\Gamma|\lambda\rangle \mathbf{A}_{\lambda,\nu\Gamma} \\ &= \sum A^*_{\kappa,\mu\Gamma} \langle \lambda|\lambda\rangle A_{\lambda,\nu\Gamma} \\ \mathbf{P}_{\Gamma,\Gamma} &= \mathbf{A}^\dagger_{-,\Gamma} \mathbf{S}_{-,-} \mathbf{A}_{-,\Gamma} \,. \end{aligned} \tag{A.19}$$

It should be clear that Eq. (A.18) and Eq. (A.19) are representations of the same projector but in different basis sets.

One way to that $|i_\sigma\rangle$ belongs to the irrep Γ is to calculate,

$$\langle i_\sigma|\hat{\mathcal{P}}|i_\sigma\rangle = \sum_{\Gamma!} \langle i_\sigma|\mu\Gamma\rangle \left(\mathbf{S}^{-1}_{\Gamma,\Gamma}\right)_{\mu\Gamma,\nu\Gamma} \langle \nu\Gamma|i_\sigma\rangle \,, \tag{A.20}$$

and compare it with

$$\langle i_\sigma|i_\sigma\rangle = \vec{c}^\dagger_i \mathbf{S}_{-,-} \vec{c}_i \,. \tag{A.21}$$

The $\Gamma!$ indicates *not* to sum over the index Γ. Now

$$\mathbf{S}_{\Gamma,\Gamma} = \mathbf{P}_{\Gamma,\Gamma} = \mathbf{A}^\dagger_{-,\Gamma} \mathbf{S}_{-,-} \mathbf{A}_{-,\Gamma} \,, \tag{A.22}$$

and

$$\begin{aligned} \langle i_\sigma|\mu\Gamma\rangle &= \sum \langle i_\sigma|\nu\rangle A_{\nu,\mu\Gamma} \\ &= \sum \vec{c}^\sigma_{\kappa,i} S_{\kappa,\nu} A_{\nu,\mu\Gamma} \\ \langle i_\sigma|\hat{\mathcal{P}}|i_\sigma\rangle &= \vec{c}^{\sigma,\dagger}_i \mathbf{S}_{-,-} \mathbf{A}_{-,\Gamma} \left(\mathbf{A}^\dagger_{-,\Gamma} \mathbf{S}_{-,-} \mathbf{A}_{-,\Gamma}\right)^{-1} \mathbf{A}^\dagger_{-,\Gamma} \mathbf{S}_{-,-} \vec{c}^\sigma_i \\ &= \vec{c}^{\sigma,\dagger}_i \mathbf{P}^{-1}_{\Gamma,\Gamma} \mathbf{P}_{\Gamma,-} \vec{c}^\sigma_i \,. \end{aligned} \tag{A.23}$$

From this we can deduce that,

$$\mathbf{P}_{-,-} = \mathbf{P}_{-,\Gamma} \mathbf{P}^{-1}_{\Gamma,\Gamma} \mathbf{P}_{\Gamma,-} \,. \tag{A.24}$$

This will often work to assign the irrep of a MO, but not always. The problem is that $|i_\sigma\rangle$ need not belong to an irrep because of accidental degenerecies. That is why symmetry blocking is essential.

A.3 SYMMETRY BLOCKING

Let us now work on blocking the Kohn–Sham eigenvalue problem. Let us write,

$$\begin{aligned} |i_\sigma\rangle &= \sum |\nu\Gamma\rangle d^\sigma_{\nu\Gamma,i} \\ &= \sum |\mu\rangle A_{\mu,\nu\Gamma} d^\sigma_{\nu\Gamma,i} \,. \end{aligned} \tag{A.25}$$

Comparing with Eq. (A.4) gives that,

$$\begin{aligned} c^{\sigma}_{\mu,i} &= \sum A_{\mu,\nu\Gamma} d^{\sigma}_{\nu\Gamma,i} \\ \vec{c}^{\sigma}_{i} &= \mathbf{A}_{-,\Gamma} \vec{d}^{\sigma}_{i} \end{aligned} \tag{A.26}$$

Substituting Eq. (A.25) into Eq. (A.1) gives,

$$\sum \hat{F}^{\sigma} |\nu\Gamma\rangle d^{\sigma}_{\nu\Gamma,i} = \epsilon^{\sigma}_{i} \sum |\nu\Gamma\rangle d^{\sigma}_{\nu\Gamma,i} \,, \tag{A.27}$$

If we want to use the projector of Eq. (A.19), then we should work with

$$\sum \langle \mu\Gamma \hat{F}^{\sigma} |\nu\Gamma\rangle d^{\sigma}_{\nu\Gamma,i} = \epsilon^{\sigma}_{i} \sum \langle \mu\Gamma|\nu\Gamma\rangle d^{\sigma}_{\nu\Gamma,i} \,, \tag{A.28}$$

This becomes

$$\mathbf{A}^{\dagger}_{-,\Gamma} \mathbf{F}^{\sigma}_{-,-} \mathbf{A}_{-,\Gamma} \vec{d}^{\sigma}_{i} = \epsilon^{\sigma}_{i} \mathbf{A}^{\dagger}_{-,\Gamma} \mathbf{S}^{\sigma}_{-,-} \mathbf{A}_{-,\Gamma} \vec{d}^{\sigma}_{i} \,. \tag{A.29}$$

What we have is the matrix of $\hat{F}^{\sigma}_{\Gamma}$ in the representation of SALCs: Making use of $\mathbf{P}_{-,\Gamma}$, we see that,

$$\begin{aligned} \mathbf{F}^{\sigma}_{\Gamma,\Gamma} &= \mathbf{P}_{\Gamma,-} \left(\mathbf{S}_{-,-}\right)^{-1} \mathbf{F}_{-,-}{}^{\sigma} \left(\mathbf{S}_{-,-}\right)^{-1} \mathbf{P}_{-,\Gamma} \\ &= \left(\mathbf{A}^{\dagger}_{-,\Gamma} \mathbf{S}_{-,-}\right) \left(\mathbf{S}_{-,-}\right)^{-1} \mathbf{F}_{-,-}{}^{\sigma} \left(\mathbf{S}_{-,-}\right)^{-1} \left(\mathbf{S}_{-,-} \mathbf{A}_{-,\Gamma}\right) \\ &= \mathbf{A}^{\dagger}_{-,\Gamma} \mathbf{F}_{-,-}{}^{\sigma} \mathbf{A}_{-,\Gamma} \,. \end{aligned} \tag{A.30}$$

Notice that, although we have used the projector $\mathbf{P}_{\Gamma,-} = \mathbf{S}_{-,-}\mathbf{A}_{-,\Gamma}$ in the demonstration, the final result is most easily expressed directly in terms of $\mathbf{A}_{-,\Gamma}$.

B

MOLECULAR ORBITAL SYMMETRY LABELING IN DEMON2K

BHAARATHI NATARAJAN AND MARK E. CASIDA

- Available online at http://sites.google.com/site/markcasida/tddft.

Figure B.1: Example of symmetry: Tamil mandala painted on a roof inside a temple located in Mauritius Island. (Found on the web.)

B.1 INTRODUCTION

"Symmetrize and conquer."

Group theory is a basic part of the training of physical chemists and chemical physicists as evidenced by the large number of texts on the subject. (See for example Refs. [157, 310, 83, 17].) Essentially symmetry both helps us to simplify complex problems and thereby understand them. In fact, molecular orbital (MO) symmetry assignments have become such an essential part of the language of spectroscopy that, at least for small molecules, it is difficult to avoid the use of group theoretic labels. [253] This document describes the implementation of symmetry blocking and of MO symmetry assignments in DEMON2K.

The MOs in question are the solution of the Kohn-Sham equation, [206]

$$\hat{F}^{\sigma}\psi_p^{\sigma}(\mathbf{r}) = \epsilon_p^{\sigma}\psi_p^{\sigma}(\mathbf{r})\,, \tag{B.1}$$

where $\hat{F}$ is the Kohn-Sham analogue of the Fock operator in Hartree-Fock. Here $\sigma = \alpha, \beta$ is the spin index and ψ_p^{α} may be different from ψ_p^{β} for spin-unrestricted calculations. DEMON2K solves the Kohn-Sham

equation by developing each MO as a linear combination of atomic orbitals (AOs),

$$\psi_p^\sigma(\mathbf{r}) = \sum_\mu \chi_\mu(\mathbf{r}) C_{\mu,p}^\sigma \,, \tag{B.2}$$

(Note that χ is also used to denote a character in group theory. However we trust that the distinction will be clear from context.) In reality, rather than the solutions of an atomic Schrödinger equation, the so-called AOs are just convenient atom-centered contracted Gaussian-type orbital basis functions. In this way, the exact differential equation (B.1) is reduced to the approximate matrix equation,

$$\mathbf{F}^\sigma \mathbf{C}_p^\sigma = \epsilon_p^\sigma \mathbf{S} \mathbf{C}_p^\sigma \,. \tag{B.3}$$

where,

$$\begin{aligned} F_{\mu,\nu}^\sigma &= \langle \chi_\mu | \hat{F}^\sigma | \chi_\nu \rangle \\ S_{\mu,\nu} &= \langle \chi_\mu | \chi_\nu \rangle \,, \end{aligned} \tag{B.4}$$

or, in an even more compact notation,

$$\begin{aligned} F_{\mu,\nu}^\sigma &= \langle \mu | \hat{F}^\sigma | \nu \rangle \\ S_{\mu,\nu} &= \langle \mu | \nu \rangle \,. \end{aligned} \tag{B.5}$$

The matrix $\mathbf{S}$ is the AO overlap matrix. These matrices are not in general blocked so, for example,

$$\mathbf{F} = \begin{bmatrix} * & * & * & * & * \\ * & * & * & * & * \\ * & * & * & * & * \\ * & * & * & * & * \\ * & * & * & * & * \end{bmatrix} , \tag{B.6}$$

where the asterisk indicates possibly nonzero matrix elements.

However if a molecule has symmetry, we can form new symmetry adapted linear combinations (SALCs) of the AOs,

$$\phi_\mu^\Gamma(\mathbf{r}) = \sum_\nu \chi_\mu(\mathbf{r}) T_{\mu,\nu}^\Gamma \,, \tag{B.7}$$

or,

$$|\mu, \Gamma\rangle = \sum_\nu |\nu\rangle T_{\mu,\nu}^\Gamma \,. \tag{B.8}$$

Here Γ denotes the irreducible representation or "irrep" of the SALC. Re-expressing the Fock and overlap matrices in the underlying basis of the SALCs, leads to symmetry blocking. In particular,

$$\langle \mu, \Gamma | \hat{F}^\sigma | \nu, \Gamma' \rangle = \delta_{\Gamma,\Gamma'} F_{\mu,\nu}^\Gamma \,, \tag{B.9}$$

where,

$$\begin{aligned} F^{\sigma,\Gamma}_{\mu,\nu} &= \sum_{\mu',\nu'} T^{\Gamma,*}_{\mu',\mu} F^{\sigma}_{\mu',\nu'} T^{\Gamma}_{\nu',\nu} \\ \mathbf{F}^{\sigma}_{\Gamma} &= \mathbf{T}^{\dagger}_{\Gamma} \mathbf{F}^{\sigma} \mathbf{T}_{\Gamma} \,, \end{aligned} \tag{B.10}$$

and similarly for the overlap matrix. Defining a new matrix,

$$\tilde{T}_{\mu,\Gamma;\nu} = T^{\Gamma}_{\mu,\nu} \,, \tag{B.11}$$

allows us to write,

$$\begin{aligned} \tilde{\mathbf{F}}^{\sigma} &= \tilde{\mathbf{T}}^{\dagger} \mathbf{F}^{\sigma} \tilde{\mathbf{T}} \\ &= \begin{bmatrix} \mathbf{F}^{\sigma}_{\Gamma_1} & 0 & 0 \\ 0 & \mathbf{F}^{\sigma}_{\Gamma_2} & 0 \\ 0 & 0 & \mathbf{F}^{\sigma}_{\Gamma_3} \end{bmatrix} \\ &= \begin{bmatrix} * & * & 0 & 0 & 0 \\ * & * & 0 & 0 & 0 \\ 0 & 0 & * & 0 & 0 \\ 0 & 0 & 0 & * & * \\ 0 & 0 & 0 & * & * \end{bmatrix} , \end{aligned} \tag{B.12}$$

say, and similarly for the overlap matrix. This allows us to write, the matrix equation (B.3) as separate equations for each block,

$$\mathbf{F}^{\sigma}_{\Gamma} \mathbf{C}^{\Gamma}_{p,\sigma} = \epsilon^{\sigma}_{p} \mathbf{S}_{\Gamma} \mathbf{C}^{\Gamma}_{p,\sigma} \tag{B.13}$$

The corresponding MO ψ^{σ}_{p} belonging to the irrep Γ is,

$$\begin{aligned} \psi^{\sigma}_{p}(\mathbf{r}) &= \sum_{\nu} \phi^{\Gamma}_{\nu}(\mathbf{r}) C^{\Gamma}_{\nu;p,\sigma} \\ &= \sum_{\mu,\nu} \chi_{\mu}(\mathbf{r}) T^{\Gamma}_{\mu,\nu} C^{\Gamma}_{\nu;p,\sigma} \,. \end{aligned} \tag{B.14}$$

Comparison with Eq. (B.2) shows that,

$$C^{\sigma}_{\mu,p} = \sum_{\nu} T^{\Gamma}_{\mu,\nu} C^{\Gamma}_{\nu;p,\sigma} \,. \tag{B.15}$$

Since equations (B.13) are smaller matrix equations than Eq. (B.3), less work is required to solve each one. However this gain is at least partially counterbalanced by the need to calculate the SALCs. The most important gains are possibly elsewhere:

1. Each MO now has an explicit symmetry label, Γ.
2. Explicit symmetry reduces the number of variational parameters and this may lead to faster convergence of self-consistent field (SCF) calculations.

3. Any small symmetry breaking due, say, to the use of a grid in evaluating exchange-correlation (xc) integrals is neutralized.

The last point turns out to be particularly important in the case of nearly degenerate (such as core and high-lying unoccupied) orbitals. A grid whose symmetry is different from that of the molecule introduces off-diagonal terms which couple different irreps. Although this coupling may be small, elementary perturbation theory,

$$\delta\psi_p(\mathbf{r}) = \sum_q^{q\neq p} \frac{\langle p|\delta v|q\rangle}{\epsilon_p - \epsilon_q}\,, \tag{B.16}$$

tells us that the effect on the MOs can be large when the MO energy difference is also small.

It remains to construct the $\mathbf{T}_\Gamma$ matrices. This involves operations at the heart of group theory itself and the reader is referred to anyone of a number of useful texts for more details. [157, 310, 83, 17] The following review is just a reminder: Given a group $\mathcal{G}$ with group elements that we will represent by g and an underlying vector space upon which g acts, then we can represent the group elements as matrices. The underlying vector space could be the space of AOs of a molecule belonging to group $\mathcal{G}$, in which case the action of g on a AO χ is given by the action of the inverse group element on the spatial coordinate,

$$\hat{g}\chi(\mathbf{r}) = \chi(\hat{g}^{-1}\mathbf{r})\,, \tag{B.17}$$

or the underlying space could be the abstract space composed of linear combinations of group elements or it could be something entirely different. However no matter what the nature of the underlying vector space, the group element representation matrices may be in general simultaneously blocked. It is a fundamental tenant of group theory that these blocks, called irrep matrices, are independent of the underlying vector space used in their construction, except possibly for a trivial unitary transformation of each matrix. The matrices of two irreps, Γ_i and Γ_j, obey the *great orthogonality theorem*,

$$\sum_{g\in\mathcal{G}} [\Gamma_i(g)_{m,n}]\left[\Gamma_j(g)_{m',n'}\right]^* = \frac{h}{\sqrt{l_i l_j}}\delta_{i,j}\delta_{m,m'}\delta_{n,n'}\,, \tag{B.18}$$

where $h = \dim\mathcal{G}$ is the number of elements in the group and the matrices of irrep Γ_i are dimensioned $l_i \times l_i$ (i.e., $l_i = \dim\Gamma_i$). Often it is more convenient to work with characters which are defined as the trace of the irrep matrix,

$$\chi_i(g) = \mathrm{tr}\,\boldsymbol{\Gamma}_i(g)\,. \tag{B.19}$$

This leads to the *lesser orthogonality theorem*,

$$\sum_{g\in\mathcal{G}} \chi_i(g)\chi_j(g) = h\delta_{i,j}\,. \tag{B.20}$$

Characters are so much more convenient than irrep matrices, that we tend to forget the latter in favor of the former. However irrep matrices become important for irreps of dimensionality greater than one if we wish to distinguish between the different elements belonging to the irrep. This is really simpler than it sounds. In acetylene (HCCH), π_x and π_y are the two partners of an irrep of dimension two. However there will in general be several π orbitals in a molecule and we may wish to guarantee that the x- and y-components of the different π orbitals correspond. This requires keeping track of elements by using irrep matrices rather than characters.

The SALCs may be found by projection. In the most general theory, the projection operator, $\hat{P}^i_{s,t}$, for the irrep Γ_i is given by,

$$\hat{P}^i_{s,t} = \frac{l_i}{h} \sum_{g \in \mathcal{G}} [\Gamma_i(g)_{s,t}]^* \, \hat{g} \, . \tag{B.21}$$

Let ϕ^i_s represent the different partners of the irrep Γ_i, then

$$\hat{P}^i_{s,t} \phi^j_{t'} = \delta_{i,j} \delta_{t,t'} \phi^i_s \, . \tag{B.22}$$

If information about partners is not needed, then we may use the simpler character-based projection operator,

$$\hat{P}_i = \frac{l_i}{h} \sum_{g \in \mathcal{G}} \chi_i(g) \hat{g} \, . \tag{B.23}$$

Sometimes this is written in a slightly different notation,

$$\hat{P}_\Gamma = \frac{\dim \Gamma}{\dim \mathcal{G}} \sum_{g \in \mathcal{G}} \chi_\Gamma(g) \hat{g} \, . \tag{B.24}$$

Pages 111-119 of Ref. [83] give a very nice illustration of how to apply this projection operator to obtain SALCs. There are several ways one could imagine to obtain the $\mathbf{T}_\Gamma$ matrices. One could, for example, solve the eigenvalue problem,

$$\mathbf{P}_\Gamma \mathbf{t}_j = \lambda_j \mathbf{S} \mathbf{t}_j \, . \tag{B.25}$$

In principle the λ_j can only be zero for functions orthogonal to the irrep space or one for SALCs belonging to the Γ irrep space. Thus to construct the matrix $\mathbf{T}_\Gamma$ column by column it suffices to take those vectors $\mathbf{t}_j$ whose eigenvalues are unity. A second way, and basically equivalent way, to construct the $\mathbf{T}_\Gamma$ matrix is to project each AO and then orthonormalize the surviving nonzero functions. These will be the columns of the $\mathbf{T}_\Gamma$ matrix. It is the later strategy which is used in deMon-StoBe and in deMon2k.

The rest of this document is organized as follows: The next section (Sec. B.2) describes a bit of the history of the present implementation, gives more details about how symmetry is implemented, and describes some of the limitations. Keywords are described in Sec. B.3 and an example is given in Sec. B.4 of the symmetry parts of deMon2k input and output files.

B.2 PRESENT IMPLEMENTATION

Figure B.2 shows a brief time-line of the development of the deMon suite of programs. By 1995, deMon-StoBe and hence deMon-KS3 had MO symmetry assignments. However deMon2k, which was based upon the AllChem project, did not inherit MO symmetry assignments. This has been a bit of a pain in the side of deMon developers. An initial attempt to transplant deMon-StoBe's symmetry routines into deMon2k was made by Emilio Cisneros under the direction of Alberto Vela at Cinvestav in Mexico City. The task proved very complicated without the direct implication of at least one of the authors of deMon-StoBe. Very recently, Klaus Hermann, one of the co-authors of deMon-StoBe visited Cinvestav and worked with Andreas Köster to transplant key symmetry routines into deMon2k. The work then moved to Grenoble where we have a first working implementation.

A major problem has been the harmonization of the underlying philosophy of deMon-StoBe and of deMon2k. The initial procedure follows the deMon2k philosophy. Molecules are input in any orientation. Their principle moments of inertia are found and used to put the molecule in a standard position, in such a way that the principle symmetry axis is the z-axis. The molecules are then automatically analyzed to determine their symmetry group. This analysis can fail if the three moments of inertia are equivalent (case of low-spin $[Fe(H_2O)_6]^{2+}$), in which case the molecule must be positionned by hand.

The flow of control then passes to the transplanted routines. Most of the important symmetry groups are available. In particular, symmetry blocking is supported for the groups C_i, C_s, C_n, C_{nh}, C_{nv}, D_n, D_{nh}, and D_{nd} where n runs from 1 to 6. The special groups O, T, O_h, T_h, and T_d are also supported. The point group symmetry information was taken from Ref. [17]. Complications arise because of differences in how symmetry-redundant atoms are handled in the two programs and because of different internal ordering of basis functions. These have been harmonized upto certain caveats which appear in italics in the keyword section (Sec.B.3). The result is the $\mathbf{T}$ matrix which contains the $\mathbf{T}_\Gamma$ matrices.

These are then used in the SCF to construct the matrix eigenvalue problem block-by-block. Any symmetry breaking due to the grid is thus zeroed out. MO symmetry labeling is also clear at this point. However the MOs and MO energies must be resorted (taking care not to lose the symmetry labels) so that the MOs continue to be filled according to the usual *Aufbau* principle during the SCF iterations.

Later, during calculations of excitation spectra using time-dependent density-functional theory (TDDFT), the orbital symmetry assignments reappear. *It is left up to the user to deduce the total symmetry of the excited state from the symmetry of the ground state and the symmetries of*

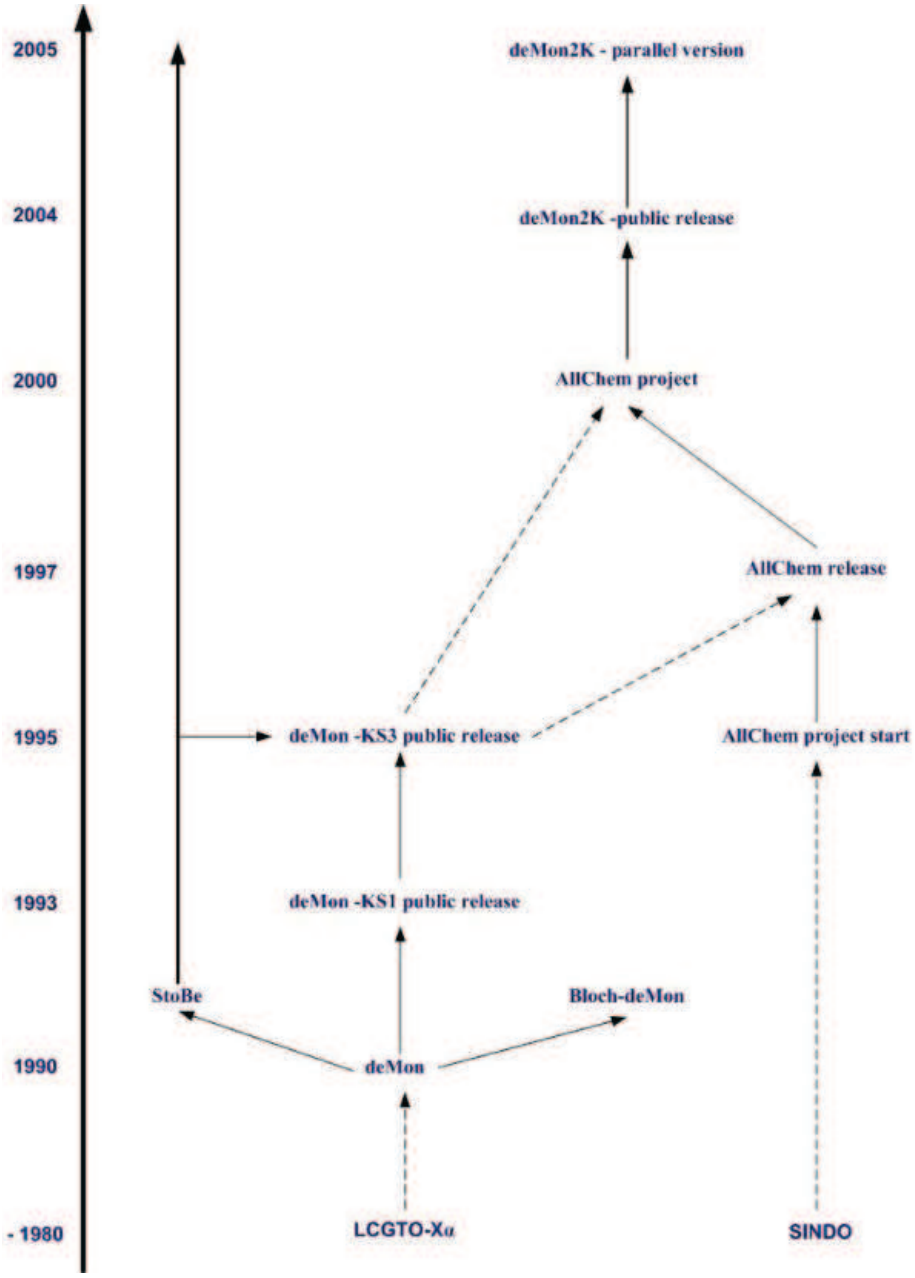

Figure B.2: Brief schematic of the history of the deMon suite of programs. Taken from the web site [10]

Table B.1: C_{2v} group character table. (See for example Ref. [83].)

C_{2v}	E	C_2	$\sigma_v(xz)$	$\sigma'_v(yz)$		
A_1	1	1	1	1	z	x^2, y^2, z^2
A_2	1	1	-1	-1	R_z	xy
B_1	1	-1	1	-1	x, R_y	xz
B_2	1	-1	-1	1	y, R_x	yz

the orbitals involved in the transitions. This is straightforward for abelian groups, but may pose some challenges for nonabelian groups.

B.3 KEYWORDS

The keyword SYMMETRY ON activates spatial-symmetry-based calculations for spin-unrestricted calculations. This keyword must occur in the input before the GEOMETRY keyword.

SYMMETRY ON

B.4 EXAMPLE

We will use the well-known example of H_2O to illustrate how to use symmetry in deMon2k. Table B.1 gives the C_{2v} character table appropriate for this molecule. There are two ways to orient the molecule which are consistent with this group table: Either the molecule is in the (x, z)-plane or it is in th (y, z)-plane. The International Union of Pure and Applied Chemistry (IUPAC) has recommended that the molecule should be aligned in the (y, z)-plane when assigning MO symmetries,

> "**it is recommended** (**REC. 5a**) that, for *planar* C_{2v} molecules, the x-axis always be chosen perpendicular to the plane of the molecule unless there are very exeptionally strong reasons for a different choice; and that the choice of axes used also be explicitly stated" [253].

If the other orientation is chosen then the B_1 and B_2 irreps are interchanged.

B.4.1 *Input*

We have the following input:

```
Title H2O
SYMMETRY ON      ! Turn on symmetry assignments
```

```
GUESS CORE
ORBITAL CARTESIAN
BASIS (STO-3G)
EXCITATION TDA
PRINT SYMMETRY MOS S
GEOMETRY
O  0.00000     0.00000     0.00000
H  0.00000     1.10000     1.20000
H  0.00000    -1.10000     1.20000
```

B.4.2 *Output*

The symmetry part of the output consists of the following parts: Identification of the point group of a molecule, along with its irreducible representations, and the corresponding number of SALCs. For H_2O and the STO-3G basis set,

```
 Orbital basis symmetry decomposition (symm. group C2v )
 Representation  :   A1  A2  B1  B2
 Basis functions :    4   0   1   2
```

Atoms are reordered accordingly to the deMon-StoBe orbital order,

```
 BASIS INFORMATION BEFORE SYMMETRIZATION

   1  1/O S  |  3  2/H  S  |  5  1/O  X  |  7  1/O  Z
   2  1/O S  |  4  3/H  S  |  6  1/O  Y  |
```

The $\mathbf{T}_\Gamma$ matrices are printed out,

```
      IRREDUCIBLE REPRESENTATION A1

 ORBITAL           1        2        3        4

   1  1/O     S    1.0000   0.0000   0.0000   0.0000
   2  1/O     S    0.0000   1.0000   0.0000   0.0000
   3  2/H     S    0.0000   0.0000   0.0000   0.7071
   4  3/H     S    0.0000   0.0000   0.0000   0.7071
   7  1/O     Z    0.0000   0.0000   1.0000   0.0000

      IRREDUCIBLE REPRESENTATION B1
ORBITAL           1

   5  1/O     X    1.0000

      IRREDUCIBLE REPRESENTATION B2
```

```
ORBITAL           1        2

  3  2/H     S    0.0000   0.7071
  4  3/H     S    0.0000  -0.7071
  6  1/O     Y    1.0000   0.0000
```

The symmetry elements of the $\mathbf{T}_\Gamma$ matrices are orthonormalized and the $\mathbf{T}_\Gamma$ matrices are printed out again,

```
 Symmetry orbitals after orthogonalization

    IRREDUCIBLE REPRESENTATION A1

ORBITAL           1        2        3        4

  1  1/O     S    1.0000  -0.2436   0.0000   0.0383
  2  1/O     S    0.0000   1.0292   0.0000  -0.2310
  3  2/H     S    0.0000   0.0000   0.0000   0.7050
  4  3/H     S    0.0000   0.0000   0.0000   0.7050
  7  1/O     Z    0.0000   0.0000   1.0000  -0.1673

    IRREDUCIBLE REPRESENTATION B1

ORBITAL           1

  5  1/O     X    1.0000

    IRREDUCIBLE REPRESENTATION B2
ORBITAL           1        2

  3  2/H     S    0.0000   0.7490
  4  3/H     S    0.0000  -0.7490
  6  1/O     Y    1.0000  -0.1629
```

The SALCs allow the irreps of the MOs to be determined. The irrep label appears when the MO coefficient matrix or MO energies are printed out. The deMon-StoBe ordering is no longer used at this point.

```
                    1         2         3         4         5
                   A1        A1        B2        A1        B1
               -18.28410  -0.91609  -0.37801  -0.19172  -0.07802

                 2.00000   2.00000   2.00000   2.00000   2.00000
```

```
1  1  O  1s   0.99227  -0.21660   0.00000  -0.14898   0.00000
2  1  O  2s   0.03655   0.72078   0.00000   0.71707   0.00000
3  1  O  2px  0.00000   0.00000   0.00000   0.00000   1.00000
4  1  O  2py  0.00000   0.00000   0.64820   0.00000   0.00000
5  1  O  2pz  0.00770   0.27303   0.00000  -0.70607   0.00000

6  2  H  1s  -0.00957   0.18381   0.45249  -0.24480   0.00000

7  3  H  1s  -0.00957   0.18381  -0.45249  -0.24480   0.00000

                    6         7
                   A1        B2
                 0.41527   0.51024

                 0.00000   0.00000
1  1  O  1s    -0.13688   0.00000
2  1  O  2s     1.00837   0.00000
3  1  O  2px    0.00000   0.00000
4  1  O  2py    0.00000   0.98069
5  1  O  2pz    0.86162   0.00000

6  2  H  1s    -0.84429  -0.97835

7  3  H  1s    -0.84429   0.97835
```

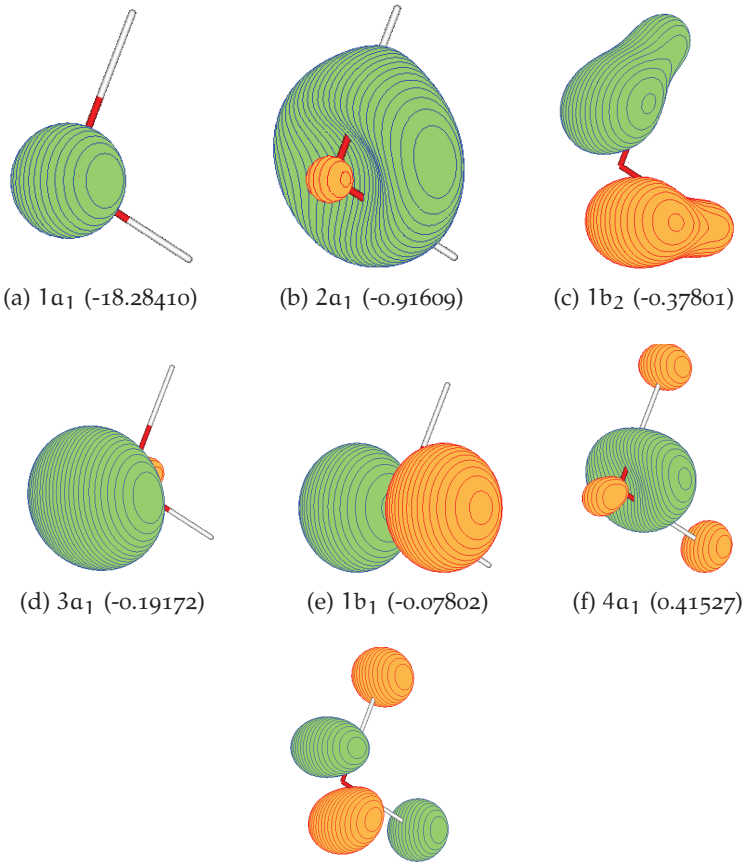

(a) $1a_1$ (-18.28410) (b) $2a_1$ (-0.91609) (c) $1b_2$ (-0.37801)

(d) $3a_1$ (-0.19172) (e) $1b_1$ (-0.07802) (f) $4a_1$ (0.41527)

(g) $2b_2$ (0.51024)

Figure B.3: Molecular orbitals of H_2O

The molecular orbital diagram for H_2O Fig(B.3) displays the orbitals arranged from lowest to highest energy in eVs along with its symmetry labels. Thus, for water molecule, the highest occupied orbital (HOMO) is the $1b_1$ [Fig(B.3e)] orbital and the lowest unoccupied orbital (LUMO) is $4a_1$ [Fig(B.3f)]. The calculated electronic structure of water is $1a_1^2\ 2a_1^2\ 1b_2^2\ 3a_1^2\ 1b_1^2$. This corresponding to a closed-shell $1A_1$ state. we see that the $1b_1$ orbital mainly of p_x character is not involved in (σ) bonding. It represents a lone pair on oxygen.

Excited state calculations are activated by the keyword EXCITATION. The orbital symmetry label are included in the TDDFT output.

```
+=========================================================================+
  1  Transition energy    12.81087 eV : T ! B1 triplet state
+-------------------------------------------------------------------------+
  5(   1 B1  )  -->  6(   4 A1  )  (  13.42216 eV) Coeff = 0.70711E+00
+-------------------------------------------------------------------------+
  5(   1 B1  )  -->  6(   4 A1  )  (  13.42216 eV) Coeff =-0.70711E+00
+=========================================================================+
```

```
  2  Transition energy    14.70036 eV : S ! B1 singlet state
+-------------------------------------------------------------------------+
  5(   1 B1  )  -->  6(   4 A1  )  (  13.42216 eV) Coeff = 0.70711E+00
+-------------------------------------------------------------------------+
  5(   1 B1  )  -->  6(   4 A1  )  (  13.42216 eV) Coeff = 0.70711E+00
+=========================================================================+
  3  Transition energy    15.54388 eV : T ! A2 triplet state
+-------------------------------------------------------------------------+
  5(   1 B1  )  -->  7(   2 B2  )  (  16.00695 eV) Coeff =-0.70711E+00
+-------------------------------------------------------------------------+
  5(   1 B1  )  -->  7(   2 B2  )  (  16.00695 eV) Coeff = 0.70711E+00
+=========================================================================+
  4  Transition energy    15.82217 eV : T ! A1 triplet state
+-------------------------------------------------------------------------+
  4(   3 A1  )  -->  6(   4 A1  )  (  16.51651 eV) Coeff =-0.70518E+00
+-------------------------------------------------------------------------+
  4(   3 A1  )  -->  6(   4 A1  )  (  16.51651 eV) Coeff = 0.70518E+00
+=========================================================================+
  5  Transition energy    16.49019 eV : S ! A2 singlet state
+-------------------------------------------------------------------------+
  5(   1 B1  )  -->  7(   2 B2  )  (  16.00695 eV) Coeff =-0.70711E+00
+-------------------------------------------------------------------------+
  5(   1 B1  )  -->  7(   2 B2  )  (  16.00695 eV) Coeff =-0.70711E+00
+=========================================================================+
  6  Transition energy    17.85242 eV : S ! singlet state
+-------------------------------------------------------------------------+
  3(   1 B2  )  -->  7(   2 B2  )  (  24.17024 eV) Coeff = 0.16180E+00
 4(   3 A1  )  -->  6(   4 A1  )  (  16.51651 eV) Coeff = 0.68766E+00
+-------------------------------------------------------------------------+
  3(   1 B2  )  -->  7(   2 B2  )  (  24.17024 eV) Coeff = 0.16180E+00
  4(   3 A1  )  -->  6(   4 A1  )  (  16.51651 eV) Coeff = 0.68766E+00
+=========================================================================+
```

B.5 FOR THE PROGRAMMER

In this section, we would like to give the list of subroutines that are changed to make the symmetry routines work considering the above explained formalisms and constrains.

B.5.1 *Modified* DEMON2K*(v.2.4.6) Routines*

symdrv.f Driver routine for symmetry analysis. Modification is done to get appropriate redundant elements for the construction of SALCs from the DEMON-STOBE orientation of a molecule.

ksmort.f This is the routine for Kohn-Sham matrix orthogonalization. Implementation of Eq. (B.10) is done here.

doscf.f This routines does the SCF iterations. Implementation of Eq. (B.12) to Eq. (B.15) is done here.

priscf.f This subroutines printing of the SCF matrices. Little modification is done to assign appropriate irreps to MOs.

B.5.1.1 *Routines For Extending MO Symmetry To TD-DFT*

tdini.f This routine initializes the TDDFT calculation. Variables corresponding to MOs symmetry labels are initialized here.

dipspec.f This routine analyses the dipole spectrum and prints it out with symmetry information.

convert.f converts a positive integer into a character string. This is the new routine needed for exporting symmetry information to TDDFT.

scfvec.h This include file is modified for the sake of storing and retriving symmetry labels.

B.6 LIMITATIONS

Although the program works in most cases there are some well characterized limitations. These are listed below as well as possible user pitfalls.

- Since the molecular symmetry orbital implementaion is based on deMon-StoBe, the user should be more careful when looking for the information about symmetry orbitals. Changes in atom order in symmetry orbitals and MOs could confuse the user.
- User should aware of the fact that the symmetry labeling for the excited states is not the final symmetry of the product of occupied and unoccupied irreps.

C

LR-TDDFT CALCULATIONS IN BIGDFT

BHAARATHI NATARAJAN, LUIGI GENOVESE, MARK E. CASIDA AND THIERRY DEUTSCH

C.1 INTRODUCTION

we have arranged an almost-complete code that performs TD-DFT calculations within the linear response formalism. This is not the place to derive the equations that are actually solved; let us just present them very quickly. Let us assume that we have obtained the set of occupied states Ψ_i (in the following, i run over occupied states) and a set of unoccupied states Ψ_a (in the following a run over unoccupied states). In the linear response formalism, the excitation energies may be obtained by solving the following eigenvalue equations (the excitation energies are the square roots of the eigenvalues):

$$\hat{\Omega}(\omega)\vec{F}_I = \omega^2\vec{F}_I\,, \tag{C.1}$$

where

$$\begin{aligned}\Omega_{ia\sigma,jb\tau} &= \delta_{ia}\delta_{jb}\delta_{\sigma\tau}(\epsilon_{a\sigma}-\epsilon_{i\sigma})^2 + \\ &\quad 2\sqrt{(\epsilon_{i\sigma}-\epsilon_{a\sigma})}\mathbf{K}_{ia\sigma,jb\tau}\sqrt{(\epsilon_{i\sigma}-\epsilon_{a\sigma})}\,,\end{aligned} \tag{C.2}$$

where $\epsilon_{i\sigma}-\epsilon_{a\sigma}$ is the energy eigenvalue differences of i^{th} and a^{th} states. Solving Eqs. (C.1) yields TD-DFT excitation energies ω and $\vec{F}_I$'s are the corresponding oscillator strengths which are defined from the transition dipole moments. The key magnitude here is the coupling matrix **K**:

$$\begin{aligned}\mathbf{K}_{pq\sigma,rs\tau} = \int\int \Psi^*_{p\sigma}(\vec{r})\Psi_{q\sigma}(\vec{r}) \quad &\left[\frac{1}{|\vec{r}-\vec{r}'|}+\frac{\partial^2 E_{xc}[\rho]}{\partial\rho_\sigma(\vec{r})\partial\rho_\tau(\vec{r}')}\right] \\ &\Psi_{r\tau}(\vec{r}')\Psi^*_{s\tau}(\vec{r}')d\vec{r}d\vec{r}'\,.\end{aligned} \tag{C.3}$$

Very importantly, in the LDA, the second term of Eq.(C.3) using adiabatic approximation (AA)

$$\frac{\delta v_{xc}[\rho]}{\delta\rho} \approx \frac{\delta^2 E_{xc}[\rho](t)}{\delta\rho(\mathbf{r},\mathbf{t})^2}\,, \tag{C.4}$$

and also of the exchange-correlation energy within LDA is defined as,

$$\epsilon_{xc}[\rho](\vec{r}) = \epsilon_{xc}^{hom}(\rho(\vec{r}))\,. \tag{C.5}$$

as of in the DFT calculations.

C.2 RUNNING TD-DFT

C.2.1 *The Input File "input.tddft"*

If this file exists, BigDFT performs linear response time-dependent calculations and the file should contain the following parameters.

- **tddft_approach** : This character string specifies the method used for the time dependent calculations. For the moment only available keyword is 'TDA'.

C.3 EXAMPLE

Once the ground-state calculations were properly done, one can enable the TDDFT calculations by adding the input file 'input.tddft'. As an example, let us perform a calculation of nitrogen molecule.

C.3.1 *Input*

```
TDA   ! tddft approch that we are using
```

C.3.2 *Output*

If you run the executable *bigdft*, after the ground-state calculations, you will see the message as of following:

```
 Linear-Response TDDFT calculations

 TAMM-DANCOFF APPROXIMATION
~~~~~~~~~~~~~~~~~~~~~~~~~~~~~~~~~~~~~~~~~~~~~~~~~~~~~~~~~~~~~~~~~~~~
     Excitation Energy   Oscillator Strength
~~~~~~~~~~~~~~~~~~~~~~~~~~~~~~~~~~~~~~~~~~~~~~~~~~~~~~~~~~~~~~~~~~~~
  1     7.7258             1.269E-31
  2     7.7258             9.263E-32
....
...
================================================
  1  Transition energy     7.72582 eV
------------------------------------------------
   5----->  1   Coeff )=-7.07084E-01
------------------------------------------------
   5----->  1   Coeff )= 7.07084E-01
================================================
  2  Transition energy     7.72583 eV
....
..
------------------------MEMORY CONSUMPTION REPORT--------
```

...
...

During TD-DFT calculations, we have calculated the excitation energies of nitrogen and the results are tubulated in the outfile along with the oscillator strengths. After this, detailed description of the transitions are listed. In the above example, the first transition from the ground-state occupied orbital (HOMO i.e. 5) to the first unoccupied orbital (LUMO i.e. 1) with a coefficient 0.70708. The corresponding excitation energiy is 7.72582 eV with an oscillator strength of null intensity. The upper part in the transition energy description with an minus coefficient (-0.70708 eV) defines the transition of occupied orbital(5) β-electron with a down-spin to the unoccupied orbital(1) whereas the lower part defines the transition of occupied orbital(5) α-electron with a up-spin to the unoccupied orbital(1).

C.3.3 *Plotting The Absorption Spectra*

At the end of the TD-DFT calculations, the program creates the file 'td_spectra.txt' which contains the first 100 values of excitation energies and oscillator strength. Using the plotting program SPECTRUM.PY [12], one can convolute the theoretical values to compare with the appropriate experimental spectra.

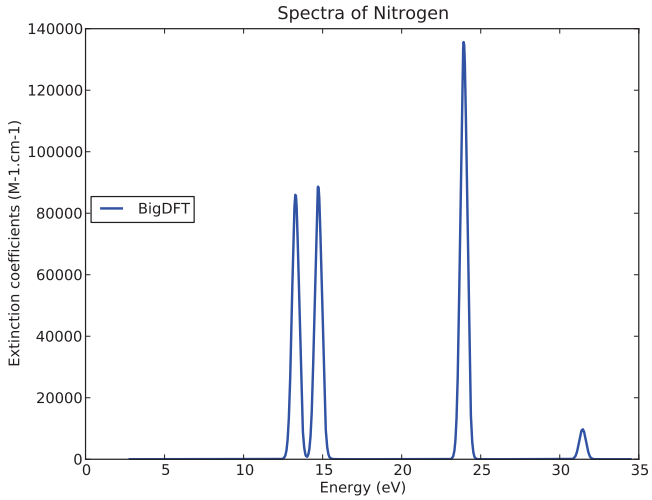

Figure C.1: Absorbtion spectrum of Nitrogen

D

ANALYTICAL DERIVATIVES FOR THE EXCITED STATES USING TD-DFT/TDA APPROACH

BHAARATHI NATARAJAN AND MARK E. CASIDA

Time dependent density functional theory (TD-DFT) become one of the most accepted method for the treatment of excitation energies [280, 60] though it has some known problems like charge transfer [71] and double excitations [171]. Indeed, as we have seen in the earlier chapter of this thesis, TD-DFT is one of the promising approach to obtain potential energy surfaces (PES) for the excited states as the function of molecular geometry by simply adding the ground state DFT energies to the excited state energy. Moreover, the excited state properties such as dipole moments, vibrational spectra calculations which are of interest can be expressed via Hellman-Feynmann theorem as first derivatives of the excited states.The pioneering work for the calculation of analytical gradients and their implementations has long history [273, 274, 185, 262].

Analytical gradient calculations plays an important role for the exploration of very many interesting chemical phenomena. But the problem in using TD-DFT is that we can get excitation energies but its wave functions are not properly defined. But from the practical point of view, examples can be found from the literature to do the geometry optimization of excited states using density functional approach was made recently by van Caillie and Amos [56, 55] and practically validated by Furche and Ahrichs [113] and Hutter [180].

Our idea behind this project is to examine the mathematical framework for the calculation of first derivatives of excited states which was presented in [64] and search for the computational requirements for the general equation set of excited state analytical gradients for the implementation in deMon2k and in BigDFT. Importance is given to the theoretical aspect of implementation in this part of the thesis using Z-vector method as suggested by Handy and Schaefer [159] in order to reduce the number of sets of linear equations from $3 \times$ number of nuclei to one which is the necessary equation when evaluating the contribution of orbital changes to the excited stated gradients.

D.1 ANALYTICAL DERIVATIVES

In this article I am using the follwing notations, μ , ν, λ... are all the indices for AO, p, q, r... are the indices for general MO, i, j, k... represents occupied MOs and a, b, c...are for the virtual MOs.

D.1.1 *Preliminaries*

In TD-DFT formalism the excitation energies can be obtained by

$$E_I = E_o + \hbar\omega_I \,, \tag{D.1}$$

Derivative of excited state energy with respect to the geometric parameter η,

$$\frac{\partial E_I}{\partial \eta} = \frac{\partial E_o}{\partial \eta} + \hbar \frac{\partial \omega_I}{\partial \eta} \,, \tag{D.2}$$

The molecular orbitals (MO) are expanded in terms of atomic orbitals (AO)

$$\psi_s(r) = \sum_{\mu}^{AO} C_{\mu,s} \chi_\mu(r) \,, \tag{D.3}$$

Keep the MOs coefficient $C_{\mu,s}$ as constant and the derivative of AOs with respect to η

$$\begin{aligned} \frac{\partial \psi_s}{\partial \eta} &= \sum_{\mu}^{AO} \left\{ \frac{\partial C_{\mu,s}}{\partial \eta} \chi_\mu + C_{\mu,s} \frac{\partial \chi_\mu}{\partial \eta} \right\} \\ &= \sum_{\mu}^{AO} \left\{ \sum_{r}^{MO} U^{\eta}_{s,r} C_{\mu,r} \chi_\mu + C_{\mu,s} \chi^{\eta}_{\mu} \right\} \\ \frac{\partial \psi_s}{\partial \eta} &= \sum_{r}^{MO} U^{\eta}_{s,r} \psi_r + \psi^{\eta}_s \,, \end{aligned} \tag{D.4}$$

where ψ^{η}_s is the core or skeleton term which is defined as

$$\sum_{\mu}^{AO} \left(\frac{\partial \chi_\mu}{\partial \eta} \right)_{C_{\mu,s}}$$

$U^{\eta}_{s,r}$ is the coupled perturbed coefficients which are defined as,

$$\sum_{r} \psi_r U^{\eta}_{sr} = \sum_{\nu} \frac{\partial C_{\nu r}}{\partial \eta} \chi_\nu \,, \tag{D.5}$$

$$U^{\eta}_{sr} = \sum_{\mu\nu} C^{*}_{\mu\nu} S_{\mu\nu} \frac{\partial C_{\nu s}}{\partial \eta} \,, \tag{D.6}$$

in which $S_{\mu\nu}$ is an overlap matrix

$$\begin{aligned}
S_{pq} &= \sum_{\mu\nu}^{AO} C^*_{\mu p} S_{\mu\nu} C_{\nu q} \\
\frac{\partial S_{pq}}{\partial \eta} &= \frac{\partial}{\partial \eta}\left\{\sum_{\mu\nu} C^*_{\mu p} S_{\mu\nu} C_{\nu q}\right\} \\
&= \sum_{\mu\nu}\left\{\frac{\partial C^*_{\mu p}}{\partial \eta} S_{\mu\nu} C_{\nu q} + C^*_{\mu p}\frac{\partial S_{\mu\nu}}{\partial \eta} C_{\nu q} + C^*_{\mu p} S_{\mu\nu}\frac{\partial C_{\nu q}}{\partial \eta}\right\} \\
&= \sum_{\mu\nu}\left\{\sum_r \left\{U^{\eta *}_{rp} C_{\mu r} S_{\mu\nu} C_{\nu q} + C^*_{\mu p} S_{\mu\nu} U^{\eta}_{rq} C_{\nu r}\right\} + C^*_{\mu p} C_{\nu q} S^{\eta}_{\mu\nu}\right\} \\
&= \sum_r \left(U^{\eta *}_{rp} S_{rq} + U^{\eta}_{rq} S_{rp}\right) + S^{\eta}_{pq}\,, \qquad \text{(D.7)}
\end{aligned}$$

D.1.2 *Turn-Over Rule*

Using orthonormality of MOs and their derivative, we can write

$$\begin{aligned}
S_{pq} &= \delta_{pq} \\
\frac{\partial S_{pq}}{\partial \eta} = \frac{\partial^2 S_{pq}}{\partial \eta \partial \eta'} &= 0 \\
\sum_r \left(U^{\eta *}_{rp} S_{rq} + U^{\eta}_{rq} S_{rp}\right) + S^{\eta}_{pq} &= 0 \\
U^{\eta *}_{qp} + U^{\eta}_{pq} + S^{\eta}_{pq} &= 0\,, \qquad \text{(D.8)}
\end{aligned}$$

Rearrangement of Eq. (D.8) leads to

$$U^{\eta *}_{qp} = -U^{\eta}_{pq} - S^{\eta}_{pq}\,, \qquad \text{(D.9)}$$

and finally we arrive at so called 'Turnover rule'. For the diagonal matrix with the assumption MO and AO orbitals are real, the turnover rule is re-written as,

$$U^{\eta}_{pp} = -\frac{1}{2} S^{\eta}_{pp}\,, \qquad \text{(D.10)}$$

D.1.3 *Analytical Gradients For Ground State*

Lets start from the classic Roothan and Hall equation of linear combination of atomic orbitals,

$$\sum_r^{MO} F_{\mu\nu} C_{\mu,r} = \epsilon_r \sum_r^{MO} C_{\mu,r} S_{\mu\nu}\,, \qquad \text{(D.11)}$$

in which the Fock matrix F is

$$F_{\mu\nu} = h_{\mu\nu} + \sum_{\mu\nu\mu'\nu'} P_{\mu'\nu'}\left\{2(\mu\nu|\mu'\nu') - (\mu\mu'|\nu\nu')\right\}\,, \qquad \text{(D.12)}$$

and the overlap matrix S is defined as

$$S_{\mu\nu} = \int \chi^*_\mu(1)\chi_\nu(1)\,dr_1 = \langle \chi_\mu | \chi_\nu \rangle\,, \tag{D.13}$$

where, the density matrix P take the form

$$P_{\mu\nu} = \sum_p C_{\mu,p} n_p C^*_{\nu,p}\,, \tag{D.14}$$

$$F_{\mu\nu} = \sum_{\mu\nu}^{AO} h_{\mu\nu} P_{\mu\nu} + \sum_{\mu\nu\mu'\nu'}^{AO} (\mu\nu|f_H|\mu'\nu') P_{\nu\mu} P_{\nu'\mu'} + E_{xc}(P)\,, \tag{D.15}$$

in which one electron Hamiltonian in atomic orbitals

$$h_{\mu\nu} = \int \chi^*_\mu(1) h(1) \chi_\nu(1)\,dr_1 = \langle \chi_\mu | h | \chi_\nu \rangle\,, \tag{D.16}$$

and two-electron Coulombic atomic orbital integral as

$$(\mu\nu|f_H|\mu'\nu') = \int \chi^*_\mu(1)\chi_\nu(1)\frac{1}{r_{12}}\chi^*_{\mu'}(2)\chi_{\nu'}(2)\,dr_1\,dr_2\,, \tag{D.17}$$

starting again with density matrix P,

$$P_{\mu\nu}(1) = \sum C_{\mu,p}\chi_\mu(1) n_p C^*_{\nu p}\chi^*_\nu(1)\,, \tag{D.18}$$

$$= \sum \chi_\mu(1) P_{\mu\nu} \chi^*_\nu(1)\,, \tag{D.19}$$

$$\frac{1}{2}(P|f_H|P) = \frac{1}{2}\sum (\mu\nu|f_H|\mu'\nu') P_{\mu\nu} P_{\mu'\nu'}\,, \tag{D.20}$$

The exchange-correlation (xc) part of total energy can be rewritten in terms of density matrices,

$$E^{HF}_{xc} = -\frac{1}{2}\int\int \frac{|r(1,2)|^2}{r_{12}}\,dr_1\,dr_2\,, \tag{D.21}$$

where

$$\begin{aligned}
r(1,2) &= \sum \chi_\mu(1) n_p \chi^*_\nu(2) \\
E^{HF}_{xc} &= -\frac{1}{2}\int\int \chi_\mu(1)\chi^*_\nu(2)\frac{1}{r_{12}}\chi^*_{\mu'}(1)\chi_{\nu'}(2) P_{\mu\nu} P^*_{\mu'\nu'}\,dr_1\,dr_2 \\
&= -\frac{1}{2}\sum (\mu'\mu|f_H|\nu\nu') P_{\mu\nu} P^*_{\mu'\nu'} \\
&= -\frac{1}{2}\sum (\mu\nu'|f_H|\mu'\nu) P_{\mu\nu} P_{\nu'\mu'} \\
&= E^{DFT}_{xc}[\rho(P)]\,,
\end{aligned} \tag{D.22}$$

The final form of Fock matrix is,

$$\begin{aligned}
F_{\mu\nu} &= h_{\mu\nu} P_{\mu\nu} + \sum (\mu\nu|f_H|\mu'\nu') P_{\mu\nu} P_{\mu'\nu'} + E_{xc}[\rho(P)] \\
F_{\mu\nu} &= \frac{\partial E}{\partial P_{\mu\nu}} \\
&= h_{\mu\nu} + \sum (\mu\nu|f_H|\mu'\nu') P_{\mu'\nu'} + V^{xc}_{\nu'\mu'}(P) \\
F_{\mu\nu} &= h_{\mu\nu} + v^{SCF}_{\nu'\mu'}\,,
\end{aligned} \tag{D.23}$$

D.1.4 *Density Matrix Derivatives*

To proceed further lets find out the first derivative of density matrix with respect to the geometric parameter η

$$\begin{aligned} P_{\mu\nu} &= \sum C_{\mu p} n_p C^*_{\nu p} \\ \frac{\partial P_{\mu\nu}}{\partial \eta} &= \frac{\partial}{\partial \eta}\left\{\sum_{\mu\nu} C_{\mu p} n_p C^*_{\nu p}\right\} \\ &= \sum_{\mu\nu}\left\{\frac{\partial C_{\mu p}}{\partial \eta} n_p C^*_{\nu p} + C_{\mu p} n_p \frac{\partial C^*_{\nu p}}{\partial \eta}\right\} \\ &= \sum_{\mu\nu}\left\{\sum_q^{MO} U^\eta_{qp} C_{\mu q} n_p C^*_{\nu p} + \sum_q C_{\mu p} n_p U^{\eta *}_{qp} C^*_{\nu q}\right\} \end{aligned} \tag{D.24}$$

and applying orthonormality condition, (D.9)

$$\begin{aligned} &= \sum_{\mu\nu}\left\{\sum_q^{MO} U^\eta_{qp} C_{\mu q} n_p C^*_{\nu p} + \sum_q C_{\mu p} n_p (-U^\eta_{pq} - S^\eta_{pq}) C^*_{\nu q}\right\} \\ &= \sum_{\mu\nu}\left\{\sum_q^{MO} U^\eta_{qp} C_{\mu q} n_p C^*_{\nu p} - \sum_q C_{\mu p} n_p U^\eta_{pq} C^*_{\nu,q} - \sum_q C_{\mu p} n_p S^\eta_{pq} C^*_{\nu q}\right\} \\ &= \sum_{\mu\nu}\left\{\sum_q^{MO} U^\eta_{qp} C_{\mu q} n_p C^*_{\nu p} - \sum_q C_{\mu q} n_q U^\eta_{qp} C^*_{\nu,p}\right. \\ &\quad \left. - \sum_q C_{\mu q} n_q S^\eta_{qp} C^*_{\nu p}\right\}, \end{aligned}$$

$$\frac{\partial P_{\mu\nu}}{\partial \eta} = \sum_{\mu\nu}\sum_q \left\{C_{\mu q}(n_p - n_q) C^*_{\nu p} U^\eta_{qp} - C_{\mu q} n_q S^\eta_{qp} C^*_{\nu p}\right\}, \tag{D.25}$$

Using the derivative of density matrix, the first derivative of ground state energy is given by,

$$\frac{\partial E}{\partial \eta} = E^\eta + \sum \frac{\partial E}{\partial P_{\mu\nu}} . \frac{\partial P_{\mu\nu}}{\partial \eta}, \tag{D.26}$$

and the canonical form of MOs as,

$$F_{pq} = \delta_{pq} \epsilon_q, \tag{D.27}$$

$$\frac{\partial E}{\partial \eta} = E^\eta - \sum F_{pq} n_q S^\eta_{pq} + \sum F_{pq} U^\eta_{qp}(n_p - n_q), \tag{D.28}$$

$$\frac{\partial E}{\partial \eta} = E^\eta - \sum_{\mu\nu} W_{\mu\nu} S^\eta_{\nu\mu}, \tag{D.29}$$

The first term E^{η} in the right hand side of Eq. (D.29) is a Hellmann-Feynman force in which the derivative of the total energy with respect to a parameter relates the expectation value of the derivative of the Hamiltonian with respect to the same parameter. The last term $W_{\mu\nu}S^{\eta}_{\nu\mu}$ is the Pulay force consists of energy weighted density matrix and overlap matrix in AO basis which must be included in order to obtain forces that are properly tangent to the energy surface.

The weighted density matrix W is defined as,

$$W_{\mu\nu} = \sum_{\mu\nu} C_{\mu p} n_p \epsilon_p C^*_{\nu p}\,, \tag{D.30}$$

$$\begin{aligned}\sum F_{pq} n_q S^{\eta}_{qp} &= \sum \epsilon_p n_p S^{\eta}_{qp} \\ &= \sum \epsilon_p n_p C^*_{\nu p} S^{\eta}_{qp} C_{\mu p} \\ &= \sum W_{\mu\nu} S^{\eta}_{qp}\,,\end{aligned} \tag{D.31}$$

Now we are in the way to construct all the pieces necessary to construct coupled perturbed Kohn-Sham equations. Following previous steps, the first derivative of the canonical form of the MOs can be

$$\frac{\partial F_{pq}}{\partial \eta} = \delta_{pq}\frac{\partial \epsilon_q}{\partial \eta}\,, \tag{D.32}$$

$$\begin{aligned}\delta_{pq}\frac{\partial \epsilon_q}{\partial \eta} &= \frac{\partial}{\partial \eta}\left\{\sum_{\mu\nu} C^*_{\mu p} F_{\mu\nu} C_{\nu q}\right\} \\ &= F^{\eta}_{pq} + \sum_{\mu\nu}\left\{\frac{\partial C_{\mu p}}{\partial \eta}^{*} F_{\mu\nu} C_{\nu q} + C^*_{\mu p} F_{\mu\nu}\frac{\partial C_{\nu q}}{\partial \eta} + C^*_{\mu p}\frac{\partial F_{\mu\nu}}{\partial \eta} C_{\nu q}\right\} \\ &= F^{\eta}_{pq} + \sum_{\mu\nu}^{AO}\left\{\sum_{p'}^{MO} U^{\eta *}_{p'p} C^*_{\mu p'} F_{\mu\nu} C_{\nu q} + \sum_{q'} C^*_{\mu p} F_{\mu\nu} U^{\eta}_{q'q} C_{\nu q'}\right. \\ &\quad \left. + C^*_{\mu p}\frac{\partial F_{\mu\nu}}{\partial P_{\nu'\mu'}}\frac{\partial P_{\nu'\mu'}}{\partial \eta} C_{\nu q}\right\}\,,\end{aligned} \tag{D.33}$$

Substituing Eq. (D.25) and define the TD-DFTcoupling matrix $\mathbf{K}$ as $\frac{\partial F_{\mu\nu}}{\partial P_{\nu'\mu'}}$,

$$
\begin{aligned}
\delta_{pq}\frac{\partial \epsilon_q}{\partial \eta} &= F^{\eta}_{pq} + \sum_{\mu\nu}\sum_{p'}\left(-U^{\eta}_{pp'} - S^{\eta}_{pp'}\right) C^{\eta}_{\mu p'} F_{\mu\nu} C_{\nu q} \\
&\quad + \sum_{q'} C^{*}_{\mu p} F_{\mu\nu} U^{\eta}_{q'q} C_{\nu q'} + \sum_{\mu'\nu'} C^{*}_{\mu p} K_{\mu\nu\mu'\nu'} \\
&\quad \left\{ \sum_{q'p'} C_{\nu' q'} (n_{p'} - n_{q'}) U^{\eta}_{q'p'} C^{*}_{\mu' p'} - C_{\nu' q'} n_{q'} S^{\eta}_{q'p'} C_{\mu' p'} \right\} C_{\nu q} \\
&= F^{\eta}_{pq} + \sum \Big\{ -\sum U^{\eta}_{pp'} C^{*}_{\mu p'} F_{\mu\nu} C_{\nu q} - \sum S^{\eta}_{pp'} C^{*}_{\mu p'} F_{\mu\nu} C_{\nu q} \\
&\quad + \sum C^{*}_{\mu p} F_{\mu\nu} U^{\eta}_{q'q} C_{\nu q'} + \sum C^{*}_{\mu p} K_{\mu\nu\mu'\nu'} C_{\nu' q'} \left(n_{p'} - n_{q'}\right) \\
&\quad U^{\eta}_{q'p'} C^{*}_{\mu' p'} C_{\nu q} - \sum C^{*}_{\mu p} K_{\mu\nu\mu'\nu'} C_{\nu' q'} n_{q'} S^{\eta}_{q'p'} C_{\mu' p'} \Big\} C_{\nu q} \\
&= F^{\eta}_{pq} - \sum U^{\eta}_{pp'} F_{p'q} - \sum S^{\eta}_{pp'} F_{p'q} + \sum U^{\eta}_{q'q} F_{pq'} \\
&\quad + \sum K_{pqp'q'} \left(n_{p'} - n_{q'}\right) U^{\eta}_{q'p'} - \sum K_{pqp'q'} n_{q'} S^{\eta}_{q'p'} \\
&= F^{\eta}_{pq} - U^{\eta}_{pq}\epsilon_q - S^{\eta}_{pq}\epsilon_q + U^{\eta}_{pq}\epsilon_p + \sum K_{pqp'q'} \left(n_{p'} - n_{q'}\right) U^{\eta}_{q'p'} \\
&\quad - \sum K_{pqp'q'} n_{q'} S^{\eta}_{q'p'} \\
&= F^{\eta}_{pq} - (\epsilon_q - \epsilon_p) U^{\eta}_{pq} - S^{\eta}_{pq}\epsilon_q + \sum K_{pqp'q'} \left(n_{p'} - n_{q'}\right) U^{\eta}_{q'p'} \\
&\quad - \sum K_{pqp'q'} n_{q'} S^{\eta}_{q'p'}. \qquad \text{(D.34)}
\end{aligned}
$$

for the case $p \neq q$

$$
\begin{aligned}
(\epsilon_q - \epsilon_p) U^{\eta}_{pq} - \sum K_{pqp'q'} \quad & \left(n_{p'} - n_{q'}\right) U^{\eta}_{q'p'} = F^{\eta}_{pq} - S^{\eta}_{pq}\epsilon_q \\
& - \sum K_{pqp'q'} n_{q'} S^{\eta}_{q'p'} \\
\delta_{pp'}\delta_{qq'}(\epsilon_q - \epsilon_p) U^{\eta}_{p'q'} - \sum K_{pqp'q'} \quad & \left(n_{q'} - n_{p'}\right) U^{\eta}_{p'q'} = F^{\eta}_{pq} - S^{\eta}_{pq}\epsilon_q \\
& - \sum K_{pqq'p'} n_{p'} S^{\eta}_{p'q'} \\
\sum \left[\delta_{pp'}\delta_{qq'}(\epsilon_q - \epsilon_p) - K_{pqq'p'} \right. \quad & \left. \left(n_{q'} - n_{p'}\right)\right] U^{\eta}_{p'q'} = F^{\eta}_{pq} - S^{\eta}_{pq}\epsilon_q \\
& - \sum K_{pqq'p'} n_{p'} S^{\eta}_{p'q'} \\
\sum \left[\delta_{pp'}\delta_{qq'} \frac{(\epsilon_q - \epsilon_p)}{(n_q - n_p)} - K_{pqq'p'}\right] \quad & (n_{q'} - n_{p'}) U^{\eta}_{p'q'} = F^{\eta}_{pq} - S^{\eta}_{pq}\epsilon_q \\
& - \sum K_{pqq'p'} n_{p'} S^{\eta}_{p'q'} \qquad \text{(D.35)}
\end{aligned}
$$

Now getting down into exact details, construct the matrix eigenvalue like equations using occupied and unoccupied orbitals as,

$$
\begin{bmatrix} \delta_{ij}\delta_{ab}(\epsilon_a - \epsilon_i) + K_{ia,bj} & -K_{ia,jb} \\ K_{ai,bj} & -\delta_{ij}\delta_{ab}(\epsilon_a - \epsilon_i) - K_{ai,jb} \end{bmatrix} \begin{bmatrix} U^{\eta}_{jb} \\ U^{\eta}_{bj} \end{bmatrix} = \begin{bmatrix} F^{\eta}_{ia} - S^{\eta}_{ia}\epsilon_a - \sum K_{ia,q'p'} n_{p'} S^{\eta}_{p'q'} \\ F^{\eta}_{ai} - S^{\eta}_{ai}\epsilon_i - \sum K_{ai,q'p'} n_{p'} S^{\eta}_{p'q'} \end{bmatrix}. \qquad \text{(D.36)}
$$

$$\begin{bmatrix} \delta_{ij}\delta_{ab}(\epsilon_a - \epsilon_i) + K_{ia,bj} & K_{ia,jb} \\ K_{ai,bj} & \delta_{ij}\delta_{ab}(\epsilon_a - \epsilon_i) + K_{ai,jb} \end{bmatrix} \begin{bmatrix} U^{\eta}_{jb} \\ -U^{\eta}_{bj} \end{bmatrix} = \begin{bmatrix} F^{\eta}_{ia} - S^{\eta}_{ia}\epsilon_a - \sum K_{ia,q'p'}n_{p'}S^{\eta}_{p'q'}i \\ F^{\eta}_{ai} - S^{\eta}_{ai}\epsilon_i - \sum K_{ai,q'p'}n_{p'}S^{\eta}_{p'q'} \end{bmatrix} . \quad (D.37)$$

D.1.5 *Solving Linear Response (LR) Like Equation*

Since we are familiar with the general matrix of the linear-reponse matrix equation, lets start from that.

$$\begin{bmatrix} A & B \\ B^* & A^* \end{bmatrix} \begin{pmatrix} \vec{X} \\ \vec{Y} \end{pmatrix} = \begin{pmatrix} \vec{W} \\ \vec{Z} \end{pmatrix} , \quad (D.38)$$

where

$$\begin{aligned} A\vec{X} + B\vec{Y} &= \vec{W} \\ B^*\vec{X} + A^*\vec{Y} &= \vec{Z} \\ (A+B)(\vec{X}+\vec{Y}) &= (\vec{W}+\vec{Z}) \\ (A-B)(\vec{X}-\vec{Y}) &= (\vec{W}-\vec{Z}) \\ A &= \delta_{ij}\delta_{ab}(\epsilon_a - \epsilon_i) + K_{ia,bj} \\ B &= K_{ia,jb} \\ \vec{X} &= U^{\eta}_{jb} \\ \vec{Y} &= -U^{\eta}_{bj} . \end{aligned} \quad (D.39)$$

Now there are two ways to proceed with. a) Case: 1

$$(A-B)(\vec{X}-\vec{Y}) = (\vec{W}) - \vec{Z}) , \quad (D.40)$$

$$\begin{aligned} \sum \left[\delta_{ij}\delta_{ab}(\epsilon_a - \epsilon_i) + \right. & \left. K_{iabj} - K_{iajb}\right](U^{\eta}_{jb} + U^{\eta}_{bj}) = F^{\eta}_{ia} - F^{\eta}_{ai} \\ & -S^{\eta}_{ia}(\epsilon_a - \epsilon_i) - \sum \left(K_{iaq'p'} - K_{aiq'p'}\right) n_{p'}S^{\eta}_{p'q'} \\ \sum \left[\delta_{ij}\delta_{ab}(\epsilon_a - \epsilon_i) + \right. & \left. K_{iabj} - K_{iajb}\right](-S^{\eta}_{jb}) = -S^{\eta}_{ia}(\epsilon_a - \epsilon_i) \\ & - \sum (K_{iaq'p'} - K_{iap'q'})n_{p'}S^{\eta}_{p'q'} \\ = \; & -S^{\eta}_{ia}(\epsilon_a - \epsilon_i) \\ & - \sum \left\{ (\sum_{ij} K_{iakj} - K_{iajk})S^{\eta}_{jk} \right. \\ & \left. + \sum_{jb} (K_{iabj} - K_{iajb}) \right\} S^{\eta}_{jb} . \end{aligned} \quad (D.41)$$

Case:2

$$(A+B)(\vec{X}+\vec{Y}) = (\vec{W}+\vec{Z})\,, \tag{D.42}$$

$$\sum \left[\delta_{ij}\delta_{ab}(\epsilon_a-\epsilon_i)+K_{iabj}+K_{iajb}\right] \quad (U^{\eta}_{jb}-U^{\eta}_{bj}) = F^{\eta}_{ia}+F^{\eta}_{ai}-S^{\eta}_{ia}(\epsilon_a+\epsilon_i) - \sum (K'_{iaq'p}+K_{aiq'p'})n_{p'}S^{\eta}_{p'q'}\,. \tag{D.43}$$

Using orthonormality condition given in Eq. (D.9)

$$U^{\eta}_{jb}-U^{\eta}_{bj} = 2U^{\eta}_{jb}+S^{\eta}_{jb}\,. \tag{D.44}$$

$$U^{\eta}_{jb}-U^{\eta}_{bj} = -2U^{\eta}_{bj}-S^{\eta}_{bj}\,. \tag{D.45}$$

Substituting Eq. (D.44) in Eq. (D.43) then,

$$\sum \left[\delta_{ij}\delta_{ab}(\epsilon_a-\epsilon_i) \quad +K_{iabj}+K_{iajb}\right](2U^{\eta}_{jb}+S^{\eta}_{jb}) = 2F^{\eta}_{ia}-S^{\eta}_{ia}(\epsilon_a-\epsilon_i) - \sum (K_{iaq'p'}+K_{aip'q'})n_{p'}S^{\eta}_{p'q'}\,.$$

$$\begin{aligned} 2\sum \left[\delta_{ij}\delta_{ab}(\epsilon_a-\epsilon_i)+K_{iabj}+K_{iajb}\right]U^{\eta}_{jb} & \\ +\sum \left[\delta_{ij}\delta_{ab}(\epsilon_a-\epsilon_i)+K_{iabj}+K_{iajb}\right]S^{\eta}_{jb} &= 2F^{\eta}_{ia}-S^{\eta}_{ia}(\epsilon_a-\epsilon_i) \\ &\quad -\sum\{(\sum_{jk} K_{iakj}+K_{iajk})S^{\eta}_{jk} \\ &\quad +\sum (K_{iabj}+K_{iajb})S^{\eta}_{jb}\}\,. \end{aligned}$$

and Substituting Eq. (D.45) in Eq. (D.43)

$$\begin{aligned} \sum \left[\delta_{ij}\delta_{ab}(\epsilon_a-\epsilon_i)\right. & \\ \left.+K_{iabj}+K_{iajb}\right](-2U^{\eta}_{bj}-S^{\eta}_{bj}) &= 2F^{\eta}_{ia}-S^{\eta}_{ia}(\epsilon_a-\epsilon_i)- \\ &\quad \sum\{\sum (K_{iakj}+K_{iajb})S^{\eta}_{jk} \\ &\quad +\sum (K_{iabj}+K_{iajb})\}S^{\eta}_{bj}\,, \end{aligned}$$

$$\begin{aligned} 2\sum \left[\delta_{ij}\delta_{ab}(\epsilon_i-\epsilon_a)-(K_{iabj}+K_{iajb})\right]U^{\eta}_{bj}- & \\ \left[\delta_{ij}\delta_{ab}(\epsilon_a-\epsilon_i)+K_{iabj}+K_{iajb}\right]S^{\eta}_{bj}+ & \\ S^{\eta}_{ia}(\epsilon_a-\epsilon_i)+\sum (K_{iabj}+K_{iajb})S^{\eta}_{bj} &= 2F^{\eta}_{ia}-\sum (K_{iakj}+K_{iajk})S^{\eta}_{jk}\,, \end{aligned}$$

$$\begin{aligned} 2\sum \left[\delta_{ij}\delta_{ab}(\epsilon_i-\epsilon_a)-(K_{iabj}+K_{iajb})\right]U^{\eta}_{bj}+2S^{\eta}_{ia}\epsilon_i &= 2F^{\eta}_{ia}-2\sum K_{iajk}S^{\eta}_{jk} \\ \sum \left[\delta_{ij}\delta_{ab}(\epsilon_i-\epsilon_a)-(K_{iabj}+K_{iajb})\right]U^{\eta}_{bj} &= F^{\eta}_{ia}-S^{\eta}_{ia}\epsilon_i \\ &\quad -\sum K_{iajk}S^{\eta}_{jk}\,. \end{aligned}$$

D.1.6 *Coupled Perturbed Kohn-Sham Equation*

The linear-response like matrix equation is solved and finally end up with what is an linear CP-KS equation

$$\begin{aligned}
A_{ai,bj} &= \delta_{ij}\delta_{ab}(\epsilon_i - \epsilon_a) - (K_{aijb} + K_{aibj}) \\
B^o_{ai} &= F^\eta_{ai} - S^\eta_{ai}\epsilon_i - \sum K_{aikj} S^\eta_{kj} \\
\sum A_{aibj} U^\eta_{bj} &= B^o_{ai} \\
A_{aibj} &= \delta_{ij}\delta_{ab}(\epsilon_i - \epsilon_a) - [2(ai|f_H + f_{xc}|jb)] \\
B^o_{ai} &= F^\eta_{ai} - S^\eta_{ai}\epsilon_i - \sum [(ai|f_H|jk) - (ak|f_H|ji)] S^\eta_{jk},
\end{aligned}$$

with reformulated matrices **A** and **B** which are coupled to U^η .

$$\begin{aligned}
(\epsilon_q - \epsilon_p) U^\eta_{pq} - \sum K_{pqq'p'}(n_{q'} - n_{p'}) U^\eta_{p'q'} &= F^\eta_{pq} - S^\eta_{pq}\epsilon_q \\
&\quad - \sum K_{pqq'p'} n_{p'} S^\eta_{p'q'}
\end{aligned}$$

$$\begin{aligned}
U^\eta_{pq} &= \frac{1}{(\epsilon_q - \epsilon_p)} \Big[F^\eta_{pq} - S^\eta_{pq}\epsilon_q - \\
&\quad \sum K_{pqq'p'} n_{p'} S^\eta_{p'q'} + K_{pqq'p'}(n_{q'} - n_{p'}) U^\eta_{p'q'} \Big],
\end{aligned}$$

$$(\epsilon_q - \epsilon_p) U^\eta_{pq} - (K_{qpbj} + K_{qpjb}) U^\eta_{bj} = F^\eta_{qp} - S^\eta_{qp}\epsilon_q - \sum K_{qpkj} S^\eta_{kj},$$

$$\begin{aligned}
U^\eta_{pq} &= \frac{1}{(\epsilon_q - \epsilon_p)} \Big[F^\eta_{qp} - S^\eta_{qp}\epsilon_q \\
&\quad - \sum K_{qpkj} S_{kj} + \sum (K_{qpbj} + K_{qpjb}) U^\eta_{bj} \Big],
\end{aligned} \tag{D.46}$$

D.1.7 *Analytical Gradients For Excited States Within TDA*

Applying TDA on the matrix formulation of LR-TD-DFT equation can be written as,

$$
\begin{aligned}
A\vec{X} &= \omega\vec{X} \\
\sum A_{iajb}X_{jb} &= \omega X_{jb} \\
A_{iajb} &= \delta_{ij}\delta_{ab}(\epsilon_a - \epsilon_i) + K_{iabj} \\
\omega &= \sum X^*_{ia}A_{iajb}X_{jb} \\
\frac{\partial\omega}{\partial\eta} &= \sum \frac{\partial X^*_{ia}}{\partial\eta}A_{iajb}X_{jb} + \sum X^*_{ia}A_{iajb}\frac{\partial X_{jb}}{\partial\eta} + \sum X^*_{ia}\frac{\partial A_{iajb}}{\partial\eta}X_{jb} \\
&= \sum \frac{\partial X^*_{ia}}{\partial\eta}(\omega X_{jb}) + \sum \omega X^*_{jb}\frac{\partial X_{jb}}{\partial\eta} + \sum X^*_{ia}\frac{\partial A_{iajb}}{\partial\eta}X_{jb} \\
&= \omega\frac{\partial}{\partial\eta}\sum X^*_{ia}X_{jb} + \omega\frac{\partial}{\partial\eta}\sum X_{jb}X^*_{jb} + \sum X_{ia}\frac{\partial A_{iajb}}{\partial\eta}X_{jb} \\
\frac{\partial\omega}{\partial\eta} &= \sum X_{ia}\frac{\partial A_{iajb}}{\partial\eta}X_{jb} \\
A_{iajb} &= \delta_{ij}\delta_{ab}(\epsilon_a - \epsilon_i) + K_{iabj} \\
&= \delta_{ij}F_{ab} - \delta_{ab}F_{ji} + K_{iabj} \\
\frac{\partial A_{iajb}}{\partial\eta} &= A^{\eta}_{iajb} + \sum \frac{\partial A_{iajb}}{\partial P_{qp}}\frac{\partial P_{qp}}{\partial\eta},
\end{aligned}
$$

This is final form of the first derivative of excited state gradients with

$$
\begin{aligned}
\frac{F_{p'q'}}{\partial P_{qp}} &= K_{p'q'pq} \\
\frac{\partial P_{qp}}{\partial\eta} &= (n_p - n_q)U^{\eta}_{qp} - n_q S^{\eta}_{qp} \\
\frac{\partial K_{p'q'pq}}{\partial\eta} &= G_{p'q'p"q"pq},
\end{aligned}
$$

$$
\begin{aligned}
\frac{\partial A_{iajb}}{\partial \eta} &= A^{\eta}_{iajb} + \sum \{ \frac{\partial}{\partial \eta} \left[(\delta_{ij} F_{ab} - \delta_{ab} F_{ji} + K_{iabj}) \right] \\
&\quad [(n_p - n_q) U^{\eta}_{qp} - n_q S^{\eta}_{qp}] \\
&= A^{\eta}_{iajb} + \sum \left[(\delta_{ij} K_{abpq} - \delta_{ab} K_{jipq} + G_{iapqbj}) \right] \\
&\quad [(n_p - n_q) U^{\eta}_{qp} - n_q S^{\eta}_{qp}] \\
&= A^{\eta}_{iajb} + \sum \delta_{ij} K_{abpq} (n_p - n_q) U^{\eta}_{qp} \\
&\quad - \sum \delta_{ab} K_{jipq} (n_p - n_q) U^{\eta}_{qp} + \sum G_{iapqbj} (n_p - n_q) U^{\eta}_{qp} \\
&\quad - \sum \delta_{ij} K_{abpq} n_q S^{\eta}_{qp} + \sum \delta_{ab} K_{jipq} n_q S^{\eta}_{qp} - \sum G_{iapqbj} n_q S^{\eta}_{qp} \\
&= A^{\eta}_{iajb} + \sum \left[\delta_{ij} K_{abpq} (n_p - n_q) - \delta_{ab} K_{jipq} (n_p - n_q) + G_{iapqbj} \right. \\
&\quad \left. (n_p - n_q) \right] U^{\eta}_{qp} - \sum \left[\delta_{ij} K_{abpq} n_q - \delta_{ab} K_{jipq} n_q - G_{iapqbj} n_q \right] S^{\eta}_{qp} \\
&= A^{\eta}_{iajb} + \sum \left[\delta_{ij} K_{abkc} + \delta_{ab} K_{jikc} + G_{iakcbj} \right] U^{\eta}_{kc} \\
&\quad - \sum \left[\delta_{ij} K_{abck} - \delta_{ab} K_{jick} + G_{iackbj} \right] U^{\eta}_{ck} \\
&\quad - \sum \left[\delta_{ij} K_{abkl} - \delta_{ab} K_{jikl} - G_{iaklbj} \right] S^{\eta}_{kl} \\
&= A^{\eta}_{iajb} + \sum \left[\delta_{ij} (K_{abkc} + K_{abck}) - \delta_{ab} (K_{jikc} + K_{jick}) + \right. \\
&\quad \left. (G_{iakcbj} + G_{iackbj}) \right] U^{\eta}_{ck} - \sum \left[\delta_{ij} K_{abkl} - \delta_{ab} K_{jikl} - G_{iaklbj} \right] S^{\eta}_{kl} ,
\end{aligned}
$$

whereas, L_{ck} and M_{kl} would take the form as,

$$
\begin{aligned}
\frac{\partial \omega}{\partial \eta} &= A^{\eta}_{iajb} + \sum L_{ck} U^{\eta}_{ck} - \sum M_{kl} S^{\eta}_{kl} \\
L_{ck} &= \sum X^{*}_{ia} X_{jb} \{ (K_{abkc} + K_{abck}) - (K_{jikc} + K_{jick}) + (G_{iakcbj} + G_{iackbj}) \} \\
M_{kl} &= \sum X^{*}_{ia} X_{jb} \{ K_{abkl} - K_{jikl} - G_{iaklbj} \} \\
\frac{\partial \omega}{\partial \eta} &= \omega^{\eta} + \sum L_{ck} U^{\eta}_{ck} - \sum M_{kl} S^{\eta}_{kl} ,
\end{aligned}
\tag{D.47}
$$

D.1.8 *Ground State Lagrangian Formalism*

Introduce compact notation of ground state energies in terms of reduced density matrices,

$$
\begin{aligned}
\hat{H} &= \sum h_{pq} p^{+} q + \sum V_{pqrs} p^{+} q^{+} s r \\
V_{pqrs} &= \langle pq | rs \rangle - \langle pq | sr \rangle \\
&= (pr | f_H | qs) - (ps | f_H | qr) \\
\hat{H} &= \sum h_{pq} p^{+} q + 2 \sum (pr | f_H | qs) p^{+} q^{+} s r \\
E &= \sum h_{pq} \langle p^{+} q \rangle + 2 \sum (pr | f_H | qs) \langle p^{+} q^{+} s r \rangle \\
E &= \sum h_{pq} \gamma_{qp} + 2 \sum (pr | f_H | qs) \Gamma_{rspq} .
\end{aligned}
\tag{D.48}
$$

Formation of Lagrangian matrices,

$$\begin{aligned}
E_1 &= \sum h_{pq}\langle p^+ q\rangle \\
&= \sum C^*_{\mu p} h_{\mu\nu} C_{\nu q}\gamma_{qp} \\
\frac{\partial E_1}{\partial \eta} &= E_1^\eta + \frac{\partial}{\partial\eta}(\sum C^*_{\mu p} h_{\mu\nu} C_{\nu q}\gamma_{qp}) \\
&= E_1^\eta + \sum\left(\frac{C^*_{\mu p}}{\partial\eta} h_{\mu\nu} C_{\nu q}\gamma_{qp} + C^*_{\mu p} h_{\mu\nu}\frac{\partial C_{\nu q}}{\partial\eta}\gamma_{qp}\right) \\
&= E_1^\eta + \sum\left(\sum_{p'} U^{\eta *}_{p'p} C^*_{\mu p'} h_{\mu\nu} C_{\nu q}\gamma_{qp} + \sum_{q'} C^*_{\mu p} h_{\mu\nu} C_{\nu q'} U^\eta_{q'q}\gamma_{qp}\right) \\
&= E_1^\eta + \sum U^{\eta *}_{p'p} h_{p'q}\gamma_{qp} + \sum U^\eta_{q'q} h_{pq'}\gamma_{qp} \\
&= E_1^\eta + \sum U^{\eta *}_{p'p} L^{1*}_{p'p} + \sum U^\eta_{q'q} L^1_{q'q}\,, \qquad \text{(D.49)}
\end{aligned}$$

where one electron Lagrangian matrix $L^{1*}_{p'p} = h_{p'q}\gamma_{qp}$.

$$\begin{aligned}
E_2 &= 2\sum (pr|f_H|qs)\Gamma_{rs,pq} \\
&= 2\sum C^*_{\mu p} C_{\nu r} C^*_{\mu q} C_{\nu s}(\mu\nu|f_H|\mu'\nu')\Gamma_{rs,pq} \\
\frac{\partial E_2}{\partial\eta} &= E_2^\eta + 2\{\frac{\partial C^*_{\mu p}}{\partial\eta} C_{\nu r} C^*_{\mu q} C_{\nu s} + C^*_{\mu p}\frac{C_{\nu r}}{\partial\eta} C^*_{\mu q} C_{\nu s} + \\
&\quad C^*_{\mu p} C_{\nu r}\frac{\partial C^*_{\mu q}}{\partial\eta} C_{\nu s} + C^*_{\mu p} C_{\nu r} C^*_{\mu q}\frac{\partial C_{\nu s}}{\partial\eta}\}(\mu\nu|f_H|\mu'\nu')\Gamma_{rs,pq} \\
&= E_2^\eta + 2\sum\{\sum_{p'} U^{\eta *}_{p'p} C^*_{\mu p'} C_{\nu r} C^*_{\mu q} C_{\nu s} + \sum_{r'} C^*_{\mu p} U^\eta_{r'r} C_{\nu r'} C^*_{\mu q} C_{\nu s} + \\
&\quad \sum_{q'} C^*_{\mu p} C_{\nu r} U^{\eta *}_{q'q} C^*_{\mu q'} C_{\nu s} + \sum_{s'} C^*_{\mu p} C_{\nu r} C^*_{\mu q} U^\eta_{s's} C_{\nu s'}\}(\mu\nu|f_H|\mu'\nu')\Gamma_{rspq} \\
&= E_2^\eta + 2\sum\{U^{\eta *}_{p'p}(p'r|f_H|qs)\Gamma_{rspq} + U^\eta_{r'r}(pr'|f_H|qs)\Gamma_{rspq} + \\
&\quad U^{\eta *}_{q'q}(pr|f_H|q's)\Gamma_{rspq} + U^\eta_{s's}(pr|f_H|qs')\Gamma_{rspq}\} \\
&= E_2^\eta + 2\sum\{U^{\eta *}_{p'p}(p'r|f_H|qs)\Gamma_{rspq} + U^\eta_{r'r}(pr'|f_H|qs)\Gamma_{rspq} + \\
&\quad U^{\eta *}_{q'q}(qs|f_H|p'r)\Gamma_{rsqp} + U^\eta_{s's}(qs|f_H|pr')\Gamma_{srqp}\} \\
&= E_2^\eta + 4\sum U^{\eta *}_{p'p}(p'r|f_H|qs)\Gamma_{rspq} + 4\sum U^\eta_{r'r}(pr'|f_H|qs)\Gamma_{rspq} \\
&= E_2^\eta + \sum U^{\eta *}_{p'p} L^2_{p'p} + \sum U_{r'r} L^2_{r'r}\,, \qquad \text{(D.50)}
\end{aligned}$$

therefore

$$\begin{aligned}
\frac{\partial E}{\partial\eta} &= (E_1^\eta + E_2^\eta) + \sum U^{\eta *}_{p'p'}(L^{1*}_{p'p} + L^2_{p'p}) + \sum U^\eta_{r'r}(L^1_{q'q} + L^{2*}_{r'r}) \\
&= E^\eta + \sum U^*_{p'p} L_{p'p} + \sum U^\eta_{r'r} L^*_{rr'}\,, \qquad \text{(D.51)}
\end{aligned}$$

D.1.9 *Z-Vector Method*

The Z-vector method reduces this set of 3N equations (one for each nuclear purturbation) to one. For a given gradient expression, all

terms including occupied-virtual orbital response matrices define Lagrangian L of the chemical system.The remaining task is to determine the SCF Lagrangian and subtitute z-vector whenever necessary.

$$\vec{L}^{+}\vec{U}^{\eta} = \vec{Z}^{+}\vec{B}^{\eta}\,. \tag{D.52}$$

WKT,

$$\begin{aligned} A\vec{U}^{\eta} &= \vec{B}^{\eta} \\ \vec{U}^{\eta} &= A^{-1}\vec{B}^{\eta} \\ \vec{L}^{+}A^{-1}\vec{B}^{\eta} &= \vec{Z}^{+}\vec{B}^{\eta} \\ \vec{Z}^{+} &= \vec{L}^{+}A^{-1} \\ \vec{Z}^{+}A &= \vec{L}^{+}\,, \end{aligned} \tag{D.53}$$

so that the final Lagrangian is independent of η.

D.1.10 *Excited State Lagrangian And Z-Vector Method*

$$\begin{aligned} \frac{\partial \omega}{\partial \eta} &= \sum X^{*}_{ia}\frac{\partial A_{iajb}}{\partial \eta}X_{jb} \\ &= \omega^{\eta} + \sum \left[X^{*}_{ia}X_{jb}(K_{abkc}+K_{abck}) - X^{*}_{ia}X_{jb}(K_{jikc}+K_{jick})\right. \\ &\quad \left. + X^{*}_{ia}X_{jb}(G_{iakcbj}+G_{iackbj})\right]U^{\eta}_{ck} - \sum \left[X^{*}_{ia}X_{jb}K_{abkl}\right. \\ &\quad \left. - X^{*}_{ia}X_{jb}K_{jikl} - X^{*}_{ia}X_{jb}G_{iaklbj}\right]S^{\eta}_{kl}\,, \end{aligned} \tag{D.54}$$

$$\sum L_{ck}U^{\eta}_{ck} = \sum Z_{ck}B^{o}_{ik}\,, \tag{D.55}$$

$$\sum \left[\delta_{ij}\delta_{ab}(\epsilon_i - \epsilon_a) - (K_{aijb}+K_{aibj})\right]Z_{bj} = L_{ai}\,. \tag{D.56}$$

$$\sum Z_{ck}B^{o}_{ck} = \sum \left[F^{\eta}_{ai} - S^{\eta}_{ai}\epsilon_i - \sum \left[(ai|f_H|jk) - (ak|f_H|ji)\right]S^{\eta}_{jk}\right]Z_{ai}\,.$$

BIBLIOGRAPHY

[1] "Becke3LYP Method References and General Citation Guidelines" in *Gaussian NEWS*, Vol. **5**, p. 2 (1994).

[2] http://inac.cea.fr/L_Sim/BigDFT/. Wavelets in BigDFT.

[3] Compendium of chemical terminology. http://goldbook.inpuc.org. International Union of Pure and Applied Chemistry (IUPAC), "coordination number".

[4] Molecular Structure Corporation TeXsan. Single Crystal Structure Analysis Software. Version 1.7. MSC, 3200 Research Forest Drive, The Woodlands, TX 77381, USA. 1992-1997.

[5] http://www.abinit.org/documentation/helpfiles/for-v5.8/tutorial/lesson_tddft.html, . TD-DFT in ABINIT.

[6] . Note that DFT is usually considered as *ab initio* in solid-state theory, while chemical physicists often make a distinction between *ab initio* and DFT.

[7] http://winter.group.shef.ac.uk/orbitron/.

[8] http://chemistry.about.com/od/atomicmolecularstructure/ig/VSEPR-Molecular-Geometry/.

[9] deMon2k@Grenoble, the Grenoble development version of deMon2k, Andreas M. Köster, Patrizia Calaminici, Mark E. Casida, Roberto Flores-Morino, Gerald Geudtner, Annick Goursot, Thomas Heine, Andrei Ipatov, Florian Janetzko, Sergei Patchkovskii, J. Ulisis Reveles, Dennis R. Salahub, and Alberto Vela, *The International deMon Developers Community* (Cinvestav-IPN, Mexico, 2006).

[10] http://www.demon-software.com.

[11] M. J. Frisch, G. W. Trucks, H. B. Schlegel, G. E. Scuseria, M. A. Robb, J. R. Cheeseman, J. A. Montgomery, Jr., T. Vreven, K. N. Kudin, J. C. Burant, J. M. Millam, S. S. Iyengar, J. Tomasi, V. Barone, B. Mennucci, M. Cossi, G. Scalmani, N. Rega, G. A. Petersson, H. Nakatsuji, M. Hada, M. Ehara, K. Toyota, R. Fukuda, J. Hasegawa, M. Ishida, T. Nakajima, Y. Honda, O. Kitao, H. Nakai, M. Klene, X. Li, J. E. Knox, H. P. Hratchian, J. B. Cross, C. Adamo, J. Jaramillo, R. Gomperts, R. E. Stratmann, O. Yazyev, A. J. Austin, R. Cammi, C. Pomelli, J. W. Ochterski, P. Y. Ayala, K. Morokuma, G. A. Voth, P. Salvador, J. J. Dannenberg, V. G. Zakrzewski, S. Dapprich, A. D. Daniels, M. C. Strain,

O. Farkas, D. K. Malick, A. D. Rabuck, K. Raghavachari, J. B. Foresman, J. V. Ortiz, Q. Cui, A. G. Baboul, S. Clifford, J. Cioslowski, B. B. Stefanov, G. Liu, A. Liashenko, P. Piskorz, I. Komaromi, R. L. Martin, D. J. Fox, T. Keith, M. A. Al-Laham, C. Y. Peng, A. Nanayakkara, M. Challacombe, P. M. W. Gill, B. Johnson, W. Chen, M. W. Wong, C. Gonzalez, and J. A. Pople, Gaussian 03, Revision B.05, Gaussian, Inc., Pittsburgh PA, 2003.

[12] http://sites.google.com/site/markcasida/tddft. Absorption spectrum plotting program.

[13] TURBOMOLE V6.2 2010, a development of University of Karlsruhe and Forschungszentrum Karlsruhe GmbH, 1989-2007, TURBOMOLE GmbH, since 2007; available from http://www.turbomole.com.

[14] T. Abe. Theory of solvent effects on osillator strengths for molecular electronic transitions. *Bull. Chem. Soc. Jpn.*, 43:625, 1970.

[15] T. Abe and I. Iweibo. Solvent effects on the $n - \pi^*$ and $\pi - \pi^*$ absorption intensities of some organic molecules. *Bull. Chem. Soc. Jpn.*, 59:2381, 1986.

[16] B. K. Alpert. A class of bases in L^2 for the sparse representation of integral operators. *SIAM J. Math. Anal.*, 24:246–262, 1993.

[17] S. L. Altmann and P. Herzig. *Point-Group Theory Tables*. Clarendon Press, Oxford, 1994.

[18] A. Altomare, G. Cascarano, C. Giacovazzo, and A. Guagliardi. Completion and refinement of crystal structures with *SIR92*. *J. Appl. Cryst.*, 26:343, 1993.

[19] R. D. Amos, J. S. Andrews, N. C. Handy, and P. J. Knowles. Open-shell Møller–Plesset perturbation theory. *Chem. Phys. Lett.*, 185:256–264, 1991.

[20] M. Amsler, S. A. Ghasemi, S. Goedecker, A. Neelov, and L. Genovese. Adsorption of small NaCl clusters on surfaces of silicon nanostructures. *Nanotechnology*, 20:445301, 2009.

[21] O. K. Andersen. Linear methods in band theory. *Phys. Rev. B*, 12:3060, 1975.

[22] J. M. Anglada and J. M. Bofill. Reduced-Restricted-Quasi-Newton-Raphson Method for Locating and Optimizing Energy Crossing Points between Two Potential Energy Surfaces. *J. Comput. Chem*, 18:992–1003, 1997.

[23] James F. Annett. Efficiency of algorithms for Kohn-Sham density functional theory. *Comp. Mat. Sci.*, 4:23, 1995.

[24] J. Appleqvist. Theory of solvent effects on the visible absorption spectrum of β-carotene by a lattice-filled cavity model. *J. Phys. Chem.*, 95:3539, 1991.

[25] T. A. Arias. Multiresolution analysis of electronic structure: semicardinal and wavelet bases. *Rev. Mod. Phys.*, 71:267, 1999.

[26] T. A. Arias, R. A. Lippert, and A. Edelman. Multiscale computation with interpolating wavelets. *J. Comput. Phys.*, 140:278–310, 1997.

[27] J. and S. S. Xantheas Atchity, G. and K. Ruedenberg. Potential energy surfaces near intersections. *J. Chem. Phys.*, 95:1862–1876, 1991.

[28] P. W. Atkins and R. S. Friedman. *Molecular Quantum Mechanics*. Oxford University Press, 3rd edition edition, 1999.

[29] R. Baer. Non-adiabatic couplings by time-dependent density functional theory. *Chem. Phys. Lett.*, 364:75, 2002.

[30] E. J. Baerends, D. E. Ellis, and P. Ros. Self-consistent molecular Hartree–Fock–Slater calculations I. The computational procedure. *Chem. Phys.*, 2:41, 1973.

[31] N. G. Bakhshiev, M. I. Gotynyan, and A. V. Kirilova. How the solvent affects the oscillator strengths of the intense vibronic absorption bands of polyatomic organic molecules. *J. Opt. Technol.*, 73:666, 2006.

[32] M. Barbatti, J. Pitner, M. Pederzoli, U. Werner, R. Mitric, V. Bonavcic-Koutecky, and H. Lischka. Non-adiabatic dynamics of pyrrole: Dependence of deactivation mechanisms on the excitation energy. *Chem. Phys.*, 375:26–34, 2010.

[33] S. Baroni, R. Gebauer, O. B. Malcioğlu, Y. Saad, P. Umari, and J. Xian. Harnessing molecular excited states with Lanczos chains. *J. Phys. Condens. Matter*, 22:074204, 2010.

[34] S. Basu. Theory of solvent effects on molecular electronic spectra. *Adv. Quantum Chem.*, 1:145, 1964.

[35] R. Bauernschmitt and R. Ahlrichs. Treatment of electronic excitations within the adiabatic approximation of time dependent density functional theory. *Chem. Phys. Lett.*, 256:454, 1996.

[36] N. S. Bayliss. Solvent effects on the intensities of the weak ultraviolet spectra of ketones and nitroparaffins–I. *Spectrochim. Acta.*, 24A:551, 1968.

[37] N. S. Bayliss and E. G. McRae. Solvent effects in organic spectra: Dipole forces and the Franck–Condon principle. *J. Phys. Chem.*, 58:1002, 1954.

[38] N. S. Bayliss and E. G. McRae. Solvent effects in the spectra of acetone, crotonaldehyde, nitromethane and nitrobenzene. *J. Phys. Chem.*, 58:1006, 1954.

[39] R. Bear. Ground-state degeneracies leave recongnizable topological scars in the electron density. *Phys. Rev. Lett.*, 104:073001–1–4, 2010.

[40] M. J. Bearpark, M. A. Robb, and H. B. Schlegel. Direct method for the location of the lowest energy point on a potential surface crossing. *Chem. Phys. Lett.*, 223:269–274, 1994.

[41] A. D. Becke. Density-functional exchange-energy approximation with correct asymptotic behavior. *Phys. Rev. A*, 38:3098, 1988.

[42] S. B. Ben-Shlomo and U. Kaldor. N_2 excitations below 15 ev by the multireference coupled -cluster method. *J. Chem. Phys.*, 92: 3680, 1990.

[43] G. Beylkin. On the representation of operators in bases of compactly supported wavelets. *SIAM J. Numer. Anal.*, 6:1716, 1992.

[44] C. Bienia, S. Kumar, J. P. Singh, and K. Li. The PARSEC benchmark suite: Characterization and architectural implications. Technical report, in Princeton University, 2008.

[45] R. R. Birge, M. J. Sullivan, and B. E. Kohler. The effect of temperature and solvent environment on the conformational stability of 11-cis-retinal. *J. Am. Chem. Soc.*, 98:358, 1976.

[46] P. Blaha, K. Schwarz, P. Sorantin, and S.B. Trickey. Full-potential, linearized augmented plane wave programs for crystalline systems. *Comp. Phys. Commun.*, 59:399–415, 1990.

[47] N. Bohr. On the constitution of atoms and molecules. I. *Phil. Mag.*, 26:1, 1913.

[48] M. Born and R. Oppenheimer. Zur quantentheorie der molekeln. *Ann. Physik*, 389:457, 1927.

[49] S. G. Brush. *The Kind of Motion We Call Heat*, volume 1. Amsterdam: North Holland, 1976.

[50] S. G. Brush. *The Kind of Motion We Call Heat*, volume 2. Amsterdam: North Holland, 1976.

[51] O. N. Burchak, L. Mugherli, M. Ostuni, J. J. Lacapére, and M. Y. Balakirev. Combinatorial discovery of fluorescent pharmacophores by multicomponent reactions in droplet arrays. *Journal of the American Chemical Society*, 133(26):10058–10061, 2011.

[52] K. Burke and E. K. U. Gross. A guided tour of time-dependent density functional theory. In D. Joubert, editor, *Density Functionals: Theory and Applications*, volume 500 of *Springer Lecture Notes in Physics*, pages 116–146. Springer, 1998.

[53] K. Burke, J. Werschnik, and E. K. U Gross. Time-dependent density functional theory: Past, present, and future. *J. Chem. Phys.*, 123:062206, 2005.

[54] T. Burnus, M. A. L. Marques, and E. K. U. Gross. Time-dependent electron localization function. *Phys. Rev. A*, 71:010501–1–4(R), 2005.

[55] C. Van Caillie and R. D. Amos. Geometric Derivatives of Density Functional Theory Excitation Energies Using Gradient-Corrected Functionals. *Chem. Phys. Lett.*, 317:159–164, 2000.

[56] C. Van Caillie and R. E. Amos. Geometric derivatives of excitation energies using SCF and DFT. *Chem. Phys. Lett.*, 308:249–255, 1999.

[57] J.-L. Calais. Wavelets–Something for quantum chemistry? *Int. J. Quant. Chem.*, 58:541, 1996.

[58] F. Calvayrac, P. -G. Reinhard, and E. Suraud. Coulomb explosion of an Na_{13} cluster in a diabatic electron-ion dynamical picture. *J. Phys. B: At. Mol. Opt. Phys.*, 31:5023–5030, 1998.

[59] J. K. Cashion. Testing of diatomic potential-energy functions by numerical methods. *J. Chem. Phys.*, 39:1872, 1963.

[60] M. E. Casida. Time-dependent density-functional response theory for molecules. In D. P. Chong, editor, *Recent Advances in Density Functional Methods*, page 155, Singapore, 1995. World Scientific.

[61] M. E. Casida. Jacob's ladder for time-dependent density-functional theory: Some rungs on the way to photochemical heaven. In M. R. H. Hoffmann and K. G. Dyall, editors, *Accurate Description of Low-Lying Molecular States and Potential Energy Surfaces*, page 199. ACS Press, Washington, D.C., 2002.

[62] M. E. Casida. Propagator corrections to adiabatic time-dependent density-functional theory linear response theory. *J. Chem. Phys.*, 122:054111, 2005.

[63] M. E. Casida. TDDFT for excited states. In P. Sautet and R. A. van Santen, editors, *Computational Methods in Catalysis and Materials Science*, page 33. Wiley-VCH, Weinheim, Germany, 2008.

[64] M. E. Casida. Review: Time-dependent density-functional theory for molecules and molecular solids. *J. Mol. Struct. (Theochem)*, 914:3, 2009.

[65] M. E. Casida and M. Huix-Rotllant. Progress in time-dependent density-functional theory. *Annu. Rev. Phys. Chem.*, 63:in press, 2012.

[66] M. E. Casida and D. R. Salahub. Asymptotic correction approach to improving approximate exchange-correlation potentials: Time-dependent density-functional theory calculations of molecular excitation spectra. *J. Chem. Phys.*,, 113:8918–8935, 2000.

[67] M. E. Casida, H. Chermette, and D. Jacquemin. Time-dependent density-functional theory for molecules and molecular solids. Special Issue: J. Mol. Struct. (Theochem), **914** (2009), .

[68] M. E. Casida, B. Natarajan, and T. Deutsch. Real-time dynamics and conical intersections. http://arxiv.org/abs/1102.1849, . to appear as a chapter in *Fundamentals of Time-Dependent Density-Functional Theory*, edited by E.K.U. Gross, M. Marques, F. Noguiera, and A. Rubio (Springer: in press).

[69] M. E. Casida, K. C. Casida, and D. R. Salahub. Excited-state potential energy curves from time-dependent density-functional theory: A cross-section of formaldehyde's $^1A_1$ manifold. *Int. J. Quant. Chem.*, 70:933–941, 1998.

[70] M. E. Casida, C. Jamorski, K. C. Casida, and D. R. Salahub. Molecular excitation energies to high-lying bound states from time-dependent density-functional response theory: Characterization and correction of the time-dependent local density approximation ionization threshold. *J. Chem. Phys.*, 108:4439, 1998.

[71] M. E. Casida, F. Gutierrez, J. Guan, F.-X. Gadea, D. R. Salahub, and J.-P. Daudey. Charge-transfer correction for improved time-dependent local density approximation excited-state potential energy curves: Analysis within the two-level model with illustration for H_2 and LiH. *J. Chem. Phys.*, 113:7062, 2000.

[72] M. E. Casida, A. Ipatov, and F. Cordova. Linear-response time-dependent density-functional theory for open-shell molecules. In M.A.L. Marques, C. Ulrich, F. Nogueira, A. Rubio, and E.K.U. Gross, editors, *Time-Dependent Density Functional Theory*. Springer, Berlin, 2006.

[73] A. Castro, M. A. L. Marques, H. Appel, M. Oliveira, C. A. Rozzi, X. Andrade, F. Lorenzen, E. K. U. Gross, and A. Rubio. Octopus: a tool for the application of time-dependent density functional theory. *Physica Status Solidi*, 243:2465, 2006.

[74] R. J. Cave, F. Zhang, N. T. Maitra, and K. Burke. A dressed TDDFT treatment of the 2^1A_g states of butadiene and hexatriene. *Chem. Phys. Lett.*, 389:39, 2004.

[75] L. Cederbaum. *Born-Oppenheimer Approximation and Beyond*. Conical Intersections: Electronic Structure, Dynamics and Spectroscopy. World Scientific, Singapore, 2004.

[76] D. M. Ceperley and B. J. Alder. Ground state of the electron gas by a stochastic method. *Phys. Rev. Lett.*, 45:566, 1980.

[77] N. Q. Chako. Adsorption of light in organic compounds. *J. Chem. Phys.*, 2:644, 1934.

[78] W. F. Chan, G. Cooper, and C. E. Brion. Absolute optical oscillator strengths for discrete and continuum photoabsorption of carbon monoxide (7-200 ev) and transition moments for the $X^1\Sigma^+ \rightarrow A^1\Pi$ system. *Chem. Phys.*, 170:123, 1993.

[79] V. Chernyak and S. Mukamel. Density-matrix representation of nonadiabatic couplings in time-dependent density functional (TDDFT) theories. *J. Chem. Phys.*, 112:3572–3579, 2000.

[80] T. Clark, J. Chandrasekhar, and P. v. R. Schleyer. Efficient diffuse function-augmented basis sets for anion calculations. III. The 3-21+G basis set for first-row elements, Li–F. *J. Comp. Chem.*, 4: 294, 1983.

[81] J. W. Cooley. An improved eigenvalue corrector formula for solving the schrödinger equation for central fields. *Math. Computation*, 15:363, 1961.

[82] F. Cordova, L. Joubert Doriol, A. Ipatov, M. E. Casida, C. Filippi, and Alberto Vela. Troubleshooting time-dependent density-functional theory for photochemical applications: Oxirane. *J. Chem. Phys.*, 127:164111, 2007.

[83] F. A. Cotton. *Chemical Applications of Group Theory*. Wiley-Interscience, New York, second edition, 1971.

[84] C. F. Craig, W. R. Duncan, and O. V. Prezhdo. Trajectory surface hopping in the time-dependent Kohn-Sham approach for electron-nuclear dynamics. *Phys. Rev. Lett.*, 95:163001, 2005.

[85] L. A. Curtiss, P.C. Redfern, and K. Raghavachari. Gaussian–4 theory. *J. Chem. Phys.*, 126:084108, 2007.

[86] D. Rappoport and F. Furche. Analytical time-dependent density functional derivative methods within the RI-J approximation an approach to excited states of large molecules. *J. Chem. Phys.*, 122: 064105, 2005.

[87] W. Dahmen, A. Cohen, and R. DeVore. Adaptive wavelet schemes for elliptic operator equations - convergence rates. *Math. Comput.*, 70:27–75, 2001.

[88] C. Daniel. Electronic spectroscopy and photoreactivity in transition metal complexes. *Coordination Chem. Rev.*, 238-239:141, 2003.

[89] I. Daubechies. *Ten Lectures on Wavelets*, volume 61 of *CBMS-NSF*. SIAM, Philadelphia, 1992.

[90] I. Daubechies. Where do wavelets come from? — A personal point of view. *Proceedings of the IEEE*, 84:510, 1996.

[91] C. Daul. Density-functional theory applied to the excited-states of coordination-compounds. *Int. J. Quantum Chem.*, 52:867, 1994.

[92] E. R. Davidson. The iterative calculation of a few of the lowest eigenvalues and corresponding eigenvectors of large real-symmetric matrices. *J. Comput. Phys.*, 17:87, 1975.

[93] M. S. Daw. Model for energetics of solids based on the density matrix. *Phys. Rev. B*, 47:10895, 1993.

[94] G. Deslauriers and S. Duboc. Symmetric iterative interpolation processes. *Constructive Approx*, 5:49, 1989.

[95] T. Deutsch and L. Genovese. Wavelets for electronic structure calculations. *Journées des Neutrons*, 18:33, 2011.

[96] N. DeYonker, T. Cundari, and A. Wilson. The correlation consistent composite approach (ccCA): An alternative to the Gaussian-n methods. *J. Chem. Phys.*, 124:114104, 2006.

[97] E. W. -G. Diau, C. Kotting, T. I. Solling, and A. H. Zewail. Femtochemistry of Norrish type-I reactions: III. Highly excited ketones – theoretical. *Chem. Phys. Chem*, 3:57, 2002.

[98] E. W.-G. Diau and A. H. Zewail. Femtochemistry of trans-azomethane: A combined experimental and theoretical study. *Chem. Phys. Chem.*, 4:445–456, 2003.

[99] E. W.-G. Diau, C. Kotting, and A. H. Zewail. Femtochemistry of Norrish type-1 reactions: I. Experimental and theoretical studies of acetone and related ketones on the s_1 surface. *Chem. Phys. Chem.*, 2:273, 2001.

[100] E. W.-G. Diau, C. Kotting, and A. H. Zewail. Femtochemistry of Norrish type-1 reactions: II. The anomalous predissociation dynamics of cyclobutanone on the s_1 surface. *Chem. Phys. Chem.*, 2:294, 2001.

[101] P. A. M. Dirac. On the theory of quantum mechanics. *Proc. Roy. Soc. London A*, 112:661, 1926.

[102] P. A. M. Dirac. Note on exchange phenomena in the Thomas atom. *Math. Proc. Cambr. Phil. Soc.*, 26:376, 1930.

[103] N. L. Doltsinis and D. Marx. First principles molecular dynamics involving excited states and nonadiabatic transitions. *J. Theo. Comput. Chem.*, 1:319, 2002.

[104] W. Domcke and G. Stock. Theory of ultrafast nonadiabatic excited-state processes and their spectroscopic detectionin real time. *Adv. Chem. Phys.*, 100:1–169, 1997.

[105] W. Domcke, D. R. Yarkony, and H. Koeppel, editors. *Modern Methods and Algorithms of Quantum Chemistry*, volume 15 of *Advanced Series in Physical Chemistry*. World Scientific, 2004.

[106] R. M. Dreizler and E. K. U. Gross. *Density Functional Theory*. Springer-Verlag, Berlin Heidelberg New York, 1990.

[107] A. Dreuw and M. Head-Gordon. Single-reference *ab initio* methods for the calculation of excited states of large molecules. *Chem. Rev.*, 105:4009, 2005.

[108] T. H. Dunning. Gaussian basis sets for use in correlated molecular calculations. I. The atoms boron through neon and hydrogen. *J. Chem. Phys.*, 90:1007, 1989.

[109] P Ehrenfest. Bemerkung über die agenäherte Gültigkeit der klassichen Mechanik innerhalb der Quantenmechanik. *Z. Physik*, 45:455–457, 1927.

[110] E.K.U.Gross and W.Kohn. Time-dependent density functional theory. *Adv. quantum.Chem.*, 21:225, 1990.

[111] H. Eshrig and V. D. P. Servedio. Relativistic density functional approach to open shells. *J. Comput. Chem.*, 20:23, 1999.

[112] S. Evangelisti, J. P. Daudey, and J. P. Malrieu. Convergence of an improved CIPSI algorithm. *Chem. Phys.*, 75:91, 1983.

[113] F. Furche and R. Ahlrichs. Adiabatic time-dependent density functional methods for excited state properties . *J. Chem. Phys.*, 117:7433, 2002.

[114] D. Feller. The role of databases in support of computational chemistry calculations. *J. Comp. Chem.*, 17:1571, 1996.

[115] E. Fermi. Sulla quantizzazione del gas perfetto monoatomico. *Rend. Lincei*, 3:145, 1926.

[116] E. Fermi. Zur Quantelung des idealen einatomigen Gases. *Z. für physik*, 36:902, 1926.

[117] E. Fermi. Un metodo statistico per la determinazione di alcune prioprietà dell'atomo. *Rend. Accad. Naz. Lincei*, 6:602, 1927.

[118] A. L. Fetter and J. D. Walecka. *Quantum Theory of Many-Particle Systems*. Mc-Graw-Hill, New York, first edition, 1971.

[119] B. N. Figgis and M. A. Hitchman. *Ligand Field Theory and Its Applications*. Wiley-VCH, New York, 2000.

[120] C. F. Fischer. Numerical solution of the hartree-fock equations. *Can. J. Phys.*, 41:1895, 1963.

[121] C. F. Fischer. Average-energy-of-configuration Hartree-Fock results for the atoms helium to radon charlotte froese fischer. *At. Data Nucl. Data Tables*, 4:301, 1972.

[122] C. F. Fischer. Average-energy-of-configuration Hartree-Fock results for the atoms helium to radon. *At. Data Nucl. Data Tables*, 12:87, 1973.

[123] P. Fischer and M. Defranceschi. Looking at atomic orbitals through Fourier and wavelet transforms. *Int. J. Quant. chem.*, 45: 619, 1993.

[124] V. Fock. Näherungsmethode zur Lösung des quantenmechanischen Mehrkörperproblems. *Z. für physik*, 61:126, 1930.

[125] A. Fouqueau, S. Mer, M. E. Casida, L. M. Lawson Daku, A. Hauser, and T. Mineva nd F. Neese. Comparison of density functionals for energy and structural differences between the high $[^5T^{2g} : (t_{2g})^4(e_g)^2]$ and low $[^1A_{1g} : (t_{2g})^6(e_g)^0]$ spin states of the hexaquoferrous cation, $[Fe(H_2O)_6]^{2+}$. *J. Chem. Phys.*, 120:9473, 2004.

[126] I. Frank, J. Hutter, D. Marx, and M. Parrinello. Molecular dynamics in low-spin excited states. *J. Chem. Phys.*, 108:4060–4069, 1998.

[127] J. Frenkel. Zur wellenmechanischen Theorie der metallischen Leitfähigkeit. *Z. für physik*, 47:819, 1928.

[128] J. Friedrichs and I. Frank. Mechanism of electrocyclic ring-opening of diphenyloxirane: 40 years after Woodward and Hoffmann. *Chem. Eur. J.*, 15:10825, 2009.

[129] M. J. Frisch, G. W. Trucks, H. B. Schlegel, G. E. Scuseria, M. A. Robb, J. R. Cheeseman, G. Scalmani, V. Barone, B. Mennucci, G. A. Petersson, H. Nakatsuji, M. Caricato, X. Li, H. P. Hratchian, A. F. Izmaylov, J. Bloino, G. Zheng, J. L. Sonnenberg, M. Hada, M. Ehara, K. Toyota, R. Fukuda, J. Hasegawa, M. Ishida, T. Nakajima, Y. Honda, O. Kitao, H. Nakai, T. Vreven, J. A. Montgomery, Jr., J. E. Peralta, F. Ogliaro, M. Bearpark, J. J. Heyd, E. Brothers, K. N. Kudin, V. N. Staroverov, R. Kobayashi, J. Normand, K. Raghavachari, A. Rendell, J. C. Burant, S. S. Iyengar, J. Tomasi, M. Cossi, N. Rega, J. M. Millam, M. Klene, J. E. Knox, J. B. Cross, V. Bakken, C. Adamo, J. Jaramillo, R. Gomperts, R. E. Stratmann, O. Yazyev, A. J. Austin, R. Cammi, C. Pomelli, J. W. Ochterski, R. L. Martin, K. Morokuma, V. G. Zakrzewski, G. A. Voth, P. Salvador, J. J. Dannenberg, S. Dapprich, A. D. Daniels, Ö. Farkas, J. B. Foresman, J. V. Ortiz, J. Cioslowski, and D. J. Fox.

[130] F. Furche and R. Ahlrichs. Adiabatic time-dependent density functional methods for excited state properties. *J. Chem. Phys.*, 117:7433–7447, 2004.

[131] J. Gao, W. Zou, W. Liu, Y. Xiao, D. Peng, B. Song, and C. Liu. Time-dependent four-component relativistic density functional theory for excitation energies: II. The exchange-correlation kernel. *J. Chem. Phys.*, 123:054102, 2005.

[132] L. Genovese, T. Deutsch, A. Neelov, S. Goedecker, and G. Beylkin. Efficient solution of poisson's equation with free boundary conditions. *J. Chem. Phys.*, 125:074105, 2006.

[133] L. Genovese, T. Deutsch, and S. Goedecker. Efficient and accurate three-dimensional poisson solver for surface problems. *J. Chem. Phys.*, 127:054704, 2007.

[134] L. Genovese, A. Neelov, S. Goedecker, T. Deutsch, S. A. Ghasemi, A. Willand, D. Caliste, O. Zilberberg, M. Rayson, A. Bergman, and R. Schneider. Daubechies wavelets as a basis set for density functional pseudopotential calculations. *J. Chem. Phys.*, 129: 014109, 2008.

[135] L. Genovese, A. Neelov, S. Goedecker, T. Deutsch, S. A. Ghasemi, A. Willand, D. Caliste, O. Zilberberg, M. Rayson, A. Bergman, and R. Schneider. Dabeuchies wavelets as a basis set for density functional pseudopotential calculations. *J. Chem. Phys.*, 129: 014109, 2008.

[136] L. Genovese, M. Ospici, T. Deutsch, J.-F. Méhaut, A. Neelov, and S. Goedecker. Density functional theory calculation on many-cores hybrid CPU-GPU architectures. *J. Chem. Phys.*, 131:034103, 2009.

[137] L. Genovese, B. Videau, M. Ospici, T. Deutsch, S. Goedecker, and J.-F. Méhaut. Daubechies wavelets for high performance electronic structure calculations: The bigdft project. *Comptes Rendus Mécanique*, 339:149–164, 2011.

[138] L. Genovese, B. Videau, M. Ospici, T. Deutsch, S. Goedecker, and J.-F. Mh́aut. Daubechies wavelets for high performance electronic structure calculations. *Comptes Rendus Mécanique*, 339: 149, 2011.

[139] S. Goedecker. *Wavelets and Their Application for the Solution of Partial Differential Equations*. Presses Polytechniques Universitaires et Romandes, Lausanne, Switzerland, 1998.

[140] S. Goedecker and L. Colombo. Efficient linear scaling algorithm for tight-binding molecular dynamics. *Phys. Rev. Lett.*, 73:122, 1994.

[141] S. Goedecker, M. Teter, and J. Hutter. Separable dual-space gaussian pseudopotentials. *Phys. Rev. B*, 54:1703–1710, 1996.

[142] S. Goedecker, M. Teter, and J. Hutter. Relativistic separable dual-space Gaussian pseudopotentials from H to Rn. *Phys. Rev. B*, 58:3641, 1998.

[143] A. Goerling. Exact exchange kernel for time-dependent density functional theory. *Int. J. Quantum Chem.*, 69:265, 1998.

[144] E. Gomer and W. A. Noyes. Photochemical studies. XLII. Ethylene oxide. *J. Am. Chem. Soc.*, 72:101, 1950.

[145] X. Gonze, J. Beuken, R. Caracas, F. Detraux, M. Fuchs, G. Rignanese, L. Sindic, M. Verstraete, G. Zerah, and F. Jollet. First-principles computation of material properties: the ABINIT software project. *Comput. Mat. Sci.*, 25:478–492, 2002.

[146] S. Gopalakrishnan and M. Mitra. *Wavelet Methods for Dynamical Problems*. CRC Press, New York, 2010.

[147] Z. R. Grabowski, K. Rotkiewicz, and W. Rettig. Structural changes accompanying intramolecular electron transfer: Focus on twisted intramolecular charge-transfer states and structures. *Chem. Rev.*, 103:3899–4031, 2003.

[148] S. Grimme and M. Waletzke. A combination of Kohn-Sham density functional theory and multi-reference configuration interaction methods. *J. Chem. Phys.*, 111:5645–5655, 1999.

[149] O. V. Gritsenko and E. J. Baerends. Double excitation effect in non-adiabatic time-dependent density functional theory with an analytic construction of the exchange-correlation kernel in

the common energy denominator approximation. *Phys. Chem. Chem. Phys.*, 11:4640, 2009.

[150] E. K. U. Gross, C. A. Ullrich, and U. J. Gossmann. Density functional theory of time-dependent systems. In E. K. U. Gross and R. M. Dreizler, editors, *Density Functional Theory*, pages 149–171. Plenum, New York, 1994.

[151] E. K. U. Gross, J. F. Dobson, and M. Petersilka. Density-functional theory of time-dependent phenomena. *Topics in Current Chemistry*, 181:81–172, 1996.

[152] E. K. U. Gross, M. Marques, F. Noguiera, and A. Rubio, editors. *Fundamentals of Time-Dependent Density-Functional Theory*. Lecture Notes in Physics. Springer, Berlin, 2011. in press.

[153] M. Grüning, A. Marini, and X. Gonze. Exciton-plasmon states in nanoscale materials: Breakdown of the Tamm-Dancoff approximation. *Nano Lett.*, 9:2820, 2009.

[154] J. Guan, F. Wang, T. Ziegler, and H. Cox. Time-dependent density functional study of the electronic potential energy curves and excitation spectrum of the oxygen molecule. 125:044314, 2006.

[155] A. Haar. Zur Theorie des orthogonalen Funktionensysteme. *Mathematische Annalen*, 69:331, 1910.

[156] C. F. Craig Habenicht, B. F. and O. V. Prezhdo. Time-domain *ab initio* simulation of electron and hole relaxation dynamics in a single-walled semiconducting carbon nanotube. *Phys. Rev. Lett.*, 96:187401–1–4, 2006.

[157] M. Hamermesh. *Group Theory and Its Application to Physical Problems*. Addison-Wesley Publishing Company, Menlo Park, California, 1962.

[158] S. Hammes-Schiffer and J. C. Tully. Proton transfer in solution: Molecular dynamics with quantum transitions. *J. Chem. Phys.*, 101:4657–4667, 1994.

[159] N. C. Handy and H. F. Schaefer. On the evaluation of analytic energy derivatives for correlated wave functions. *J. Chem. Phys.*, 81:5031, 1984.

[160] T. Harder and J. Bendig. Solvent effects on the UV/VIS absorption spectrum of bis-(dimethylamino)-heptamethinium chloride $[(BDH)^{+}Cl^{-}]$. *Chem. Phys. Lett.*, 228:621, 1994.

[161] R. J. Harrison, G. I. Fann, T. Yanai, and G. Beylkin. Multiresolution quantum chemistry in multiwavelet bases. In P. M. A. Sloot *et al.*, editor, *ICCS 2003, LNCS 2660*, pages 103–110. Springer-Verlag, Berlin, 2003.

[162] D. R. Hartree. *The Calculation of Atomic Structures*. Wiley, New York, 1957.

[163] E. Hasegawa and M. Kamata. Photoinduced electron transfer reactions of oxiranes and epoxyketones. In W. Horspool and F. Lenci, editors, *CRC Handbook of Organic Photoreactions and Photobiology, Second Edition*, page 53. CRC Press, New York, 2004.

[164] D. Heinemann, B. Ficke, and D. Kolb. Accurate Hartree-Fock-Slater calculations on small diatomic molecules with the finite-element method. *Chem. Phys. Lett.*, 145:125, 1988.

[165] P. Jørgensen Helgaker, T. and J. Olsen. *Molecular Electronic-Structure Theory*. Wiley, Chichester, 2000.

[166] F. Herman, J. P. Van Dyke, and I. B. Ortenburger. Improved statistical exchange approximation for inhomogeneous many-electron systems. *Phys. Rev. Lett.*, 22:807, 1969.

[167] R. C. Hilborn. Einstein coefficients, cross sections, f values, dipole moments, and all that , an updated version of Am. J. Phys. 50, 982 (1982). http://arxiv.org/abs/physics/020202.

[168] R. C. Hilborn. Einstein coefficients, cross sections, f values, dipole moments and all that. *Am. J. Phys.*, 50:982, 1982.

[169] R. C. Hilborn. Erratum: Einstein coefficients, cross sections, f values, dipole moments and all that" [Am. J. Phys. 50, 982 (1982)]. *Am. J. Phys.*, 51:471, 1983.

[170] S. Hirata and M. Head-Gordon. Time-dependent density functional theory within the Tamm-Dancoff approximation. *Chem. Phys. Lett.*, 314:291, 1999.

[171] S. Hirata and M. Head-Gordon. Time-dependent density functional theory for radicals: An improved description of excited states with substantial double excitation character. *Chem. Phys. Lett.*, 302:375, 1999.

[172] P. Hohenberg and W. Kohn. Inhomogeneous electron gas. *Phys. Rev.*, 136:B864, 1964.

[173] C. Hu and O. Sugino. Average excitation energies from time-dependent density-functional theory. *J. Chem. Phys.*, 127:074112–1–10, 2007.

[174] C. Hu, H. Hirai, and O. Sugino. Nonadiabatic couplings from time-dependent density functional theory: Formulation in the Casida formalism and practical scheme within modified linear response. *J. Chem. Phys.*, 127:064103, 2007.

[175] C. Hu, H. Hirai, and O. Sugino. Nonadiabatic couplings from time-dependent density functional theory. II. Successes and challenges of the pseudopotential approximation. *J. Chem. Phys.*, 128:154111, 2008.

[176] M. Huix-Rollant and M. E. Casida. Formal foundations of dressed time-dependent density-functional theory for many-electron excitations. 2011.

[177] M. Huix-Rotllant, B. Natarajan, A. Ipatov, C. M. Wawire, and M. E. Casida. Assessment of Noncollinear Spin-Flip Tamm-Dancoff Approximation Time-Dependent Density-Functional Theory for the Photochemical Ring-Opening of Oxirane. *Phys. Chem. Chem. Phys.*, 12:12811–12825, 2010.

[178] M. Huix-Rotllant, A. Ipatov, A. Rubio, and M. E. Casida. Assessment of dressed time-dependent density-functional theory for the low-lying valence states of 28 organic chromophores. *Chem. Phys.*, 2011.

[179] B. Huron, J. P. Malrieu, and P. Rancurel. Iterative perturbation calculations of ground and excited state energies from multiconfigurational zeroth-order wavefunctions. *J. Chem. Phys.*, 58:5745, 1973.

[180] J. Hutter. Excited state nuclear forces from the Tamm-Dancoff approximation to time-dependent density functional theory within the plane wave basis set framework. *J. Chem. Phys.*, 118:3928–3934, 2003.

[181] A. Ipatov, A. Fouqueau, C. Perez del Valle, F. Cordova, M. E. Casida, A. M. Köster, A. Vela, and C. Jödicke Jamorski. Excitation energies from an auxiliary-function formulation of time-dependent density-functional response theory with charge conservation constraint. *J. Mol. Struct. (Theochem)*, 762:179, 2006.

[182] A. Ipatov, F. Cordova, and M. E. Casida. Excited-state spin-contamination in time-dependent density-functional theory for molecules with open-shell ground states. *J. Molec. Struct. (Theochem)*, 914:60–73, 2009.

[183] S. Ismail-Beigi and T. A. Arias. New algebraic formulation of density functional calculation. *Comp. Phys. Comm.*, 128(1-2):1–45, 2000.

[184] R. Izzo and M. Klessinger. Optimization of conical intersections using the semiempirical mndoc-ci method with analytic gradients. *J. Comp. Chem.*, 21:52–62, 2000.

[185] N. C. Handy J. D. Goddard and H. F. Schaefer. Gradient techniques for open-shell restricted Hartree–Fock and multiconfiguration self-consistent-field methods. *J. Chem. Phys.*, 71:1525, 1979.

[186] C. Jamorski, M. E. Casida, and D. R. Salahub. Dynamic polarizabilities and excitation spectra from a molecular implementation of time-dependent density-functional response theory: N_2 as a case study. *J. Chem. Phys.*, 104:5134, 1996.

[187] T. K. Jensen. *On adaptive wavelet-based methods for the Maxwell equations*. PhD thesis, Department of Mathematics, Technical University of Denmark, 2003.

[188] B. R. Johnson, J. P. Modisette, P. J. Nordlander, and J. L. Kinsey. Quadrature integration for orthogonal wavelet systems. *J. Chem. Phys.*, 110:8309, 1999.

[189] K. C. Jörgensen. Studies of Absorption Spectra. IV. Some New Transition Group Bands of Low Intensity. *Acta. Chem. Scand.*, 8: 1502, 1954.

[190] K. C. Jörgensen. Comparative Crystal Field Studies of some Ligands and the Lowest Singlet State of Paramagnetic Nickel(II) Complexes. *Acta. Chem. Scand.*, 9:1362, 1955.

[191] K. C. Jörgensen. Complexes of the 4d- and 5d-Groups. I. Crystal Field Spectra of Rhodium(III) and Iridium(III). *Acta. Chem. Scand.*, 10:500, 1956.

[192] P. Jørgensen, H. J. A. Hensen, and J. Olsen. Linear response calculations for large scale multiconfiguration self-consistent field wave functions. *J. Chem. Phys.*, 89:3654, 1988.

[193] B. Kaduk and T. Van Voorhis. Communication: Conical intersections using constrained density functional theory–configuration interaction. *J. Chem. Phys.*, 133:061102–1–4, 2010.

[194] T. Kato. On the eigenfunctions of many particle systems in quantum mechanics. *Comm. Pure Appl. Math*, 10:151, 1957.

[195] Y. Kawashita, T. Nakatsukasa, and K. Yabana. Time-dependent density-functional theory simulation for electron-ion dynamics in molecules under intense laser pulses. *J. Phys. Condens. Matter*, 21:064222–1–6, 2009.

[196] W. Keal, T. A. Koslowski, and W. Thiel. Comparison of algorithms for conical intersection optimisation using semiempirical methods. *Theor. Chem. Acc.*, 118:837–844, 2007.

[197] F. Keinert. *Wavelets and Multiwavelets*. Chapman and Hall/CRC, 2003.

[198] R. A. Kendall, T. H. Dunning, and R. J. Harrison. Electron affinities of the first-row atoms revisited. Systematic basis sets and wave functions. *J. Chem. Phys.*, 96:6796, 1992.

[199] R. Kishi, M. Nakano, S. Ohta, A. Takebe, M. Nate, H. Takahashi, T. Kubo, K. Kamada, K. Ohta, B. Champagne, and E. Botek. Finite-field spin-flip configuration interaction calculation of the second hyperpolarizabilities of singlet diradical systems. *J. Chem. Theory Comput.*, 3:1699, 2007.

[200] P. Knowles and P. Werner. An efficient method for the evaluation of coupling coefficients in configuration interaction calculations. *Chem. Phys. Lett.*, 145:514–522, 1988.

[201] P. J. Knowles and N. C. Handy. A new determinant-based full configuration interaction method. *Chem. Phys. Lett.*, 111:315–321, 1984.

[202] P. J. Knowles, J. S. Andrews, R. D. Amos, N. C. Handy, and J. A. Pople. Restricted Møller–Plesset theory for open-shell molecules . *Chem. Phys. Lett.*, 186:130–136, 1991.

[203] P. J. Knowles, C. Hampel, and H.-J. Werner. Coupled cluster theory for high spin, open shell reference wave functions. *J. Chem. Phys.*, 99:5219–5227, 1993.

[204] N. Koga and K. Morokuma. Determination of the lowest energy point on the crossing seam between two potential surfaces using the energy gradient. *Chem. Phys. Lett.*, 119:371–374, 1985.

[205] W. Kohn. Density functional and density matrix method scaling linearly with the number of atoms. *Phys. Rev. Lett.*, 76:3168, 1996.

[206] W. Kohn and L. J. Sham. Self-consistent equations including exchange and correlation effects. *Phys. Rev.*, 140:A1133, 1965.

[207] T. Kreibich and E. K. U. Gross. Multicomponent density-functional theory for electrons and nuclei. *Phys. Rev. Lett.*, 86: 2984–2987, 2000.

[208] T. Kreibich, R. van Leeuwen, and E. K. U. Gross. Multicomponent density-functional theory for electrons and nuclei. *Phys. Rev. A*, 78:022501–1–22, 2008.

[209] R. Krishnan, J. S. Binkley, R. Seeger, and J. A. Pople. Self-consistent molecular orbital methods. XX. A basis set for correlated wave functions. *J. Chem. Phys.*, 72:650, 1980.

[210] A. Krylov. Spin-flip equation-of-motion coupled-cluster electronic structure method for a description of excited states, bond breaking, diradicals, and triradicals. *Acc. Chem. Res.*, 39:83, 2006.

[211] L. D. Landau. On the theory of transfer of energy at collisions II. *Phys. Z. Sowjetunion*, 2:46–51, 1932.

[212] A. De La Lande, , H. Gérard, and O. Parisel. How to optimize a CH cleavage with a mononuclear copper-dioxygen adduct? *Int. J. Quant. Chem.*, 108:1898, 2008.

[213] K.-A. Lau and Q. Sun. Asymptotic regularity of Daubechies scaling functions. *Proc. Am. Math. Soc.*, 128:1087, 2000.

[214] L. M. Lawson Daku. personal communication.

[215] L. M. Lawson Daku, J. Linares, and M.-L. Boillot. *Ab initio* static and molecular dynamics study of the absorption spectra of the 4-styrylpyridine photowitch in its *cis* and *trans* forms, 2010.

[216] C. Lee, W. Yang, and R. G. Parr. Development of the Colle-Salvetti correlation-energy formula into a functional of the electron density. *Phys. Rev. B*, 37:785, 1988.

[217] L. Lehtovaara, V. Havu, and M. Puska. All-electron density functional theory and time-dependent density-functional theory with high-order finite elements. *J. Chem. Phys.*, 131:054103, 2009.

[218] B. G. Levine, C. Ko, J. Quenneville, and T. J. Martinez. Conical intersections and double excitations in time-dependent density functional theory. *Mol. Phys.*, 104:1039, 2006.

[219] B. G. Levine, J. D. Coe, and T. J. Martínez. Optimizing conical intersections without derivative coupling vectors: Application to mutistate multireference second-order perturbation theory (MS-CASPT2). *J. Phys. Chem. B*, 112:405–413, 2008.

[220] M. Levy. Universal variational functionals of electron densities, first-order density matrices, and natural spin-orbitals and solution of the v-representability problem. *Proc. Natl. Acad. Sci. USA*, 76:6062, 1979.

[221] M. Levy. Electron densities in search of hamiltonians. *Phys. Rev. A*, 26:1200, 1982.

[222] M. Levy and J. P. Perdew. *The constrained search formulation of density functional theory*. New York: Plenum, 1985.

[223] X.-P. Li, R. W. Nunes, and D. Vanderbilt. Density-matrix electronic-structure method with linear system-size scaling. *Phys. Rev. B*, 47:10891, 1993.

[224] E. H. Lieb. *Density Functionals for Coulomb systems*. Cambridge:MIT Press, feshbach, m. and shimony, a. eds edition, 1982.

[225] E. Lippert. Spectroscopic determination of the dipole moment of aromatic compounds in the first excited singlet state. *Z. Elektrochem.*, 61:962, 1957.

[226] R. A. Lippert, T. A. Arias, and A. Edelman. Multiscale computation with interpolating wavelets. *J. Comput. Phys.*, 140:278, 1998.

[227] W. Liptay. Solvent-dependence of the wave number of electron bands and physicochemical fundamentals. *Z. Naturforsch.*, 21A: 1605, 1966.

[228] H. C. Longuet-Higgins and J. A. Pople. Electronic spectral shifts of nonpolar molecules in nonpolar solvents. *J. Chem. Phys.*, 27: 192, 1957.

[229] S. Maeda, K. Ohna, and K. Morokuma. Automated global mapping of minimal energy points on seams of crossing by the anharmonic downward distortion following method: A case study of H_2CO. *J. Phys. Chem. A*, 113:1704–1710, 2009.

[230] S. Maeda, K. Ohno, and K. Morokuma. Updated branching plane for finding conical intersections without coupling derivative vectors. *J. Chem. Theo. Comput.*, 6:1538–1545, 2010.

[231] G. D. Mahan and K. R. Subbaswamy. *Local Density Theory of Polarizability*. Plenum, New York, 1990.

[232] N. T. Maitra. On correlated electron-nuclear dynamics using time-dependent density functional theory. *J. Chem. Phys.*, 125: 014110–1–4, 2006.

[233] N. T. Maitra, F. Zhang, R. J. Cave, and K. Burke. Double excitations within time-dependent density functional theory linear response. *J. Chem. Phys.*, 120:5932, 2004.

[234] N. T. Maitra, K. Burke, and R. van Leeuwen. Comment on "Critique of the foundations of time-dependent density functional theory". *Phys. Rev. A*, 78:056501, 2008.

[235] O. B. Malcioğlu, R. Gebauer, D. Rocca, and S. Baroni. TURBOTDDFT – A code for the simulation of molecular spectra using the Liouville-Lanczos approach to time-dependent density-functional perturbation theory. *Comp. Phys. Comm.*, 182:1744, 2011.

[236] M. R. Manaa and D. R. Yarkony. On the Intersection of Two Potential Energy Surfaces of the Same Symmetry. Systematic Characterization Using a Lagrange Multiplier Constrained Procedure. *J. Chem. Phys.*, 99:5251–5256, 1993.

[237] J. B. Mann and J. T. Waber. Self-consistent relativistic Dirac-Hartree-Fock calculations of lanthanide atoms. *At. Data Nucl. Data Tables*, 5:201, 1973.

[238] M. A. L. Marques and E. K. U. Gross. Time-dependent density functional theory. In C. Fiolhais, F. Nogueira, and M. A. L. Marques, editors, *A Primer in Density Functional Theory*, volume 620 of *Springer Lecture Notes in Physics*, pages 144–184. Springer, 2003.

[239] M. A. L. Marques and E. K. U. Gross. Time-dependent density-functional theory. *Annu. Rev. Phys. Chem.*, 55:427, 2004.

[240] M. A. L. Marques and A. Rubio. Time-dependent density-functional theory. Special Issue: Phys. Chem. Chem. Phys. **11**, issue 22, pp. 4421-4688 (2009).

[241] M. A. L. Marques, C. A. Ullrich, F. Nogueira, A. Rubio, K. Burke, and E. K. U. Gross, editors. *Time-dependent Density Functional Theory*, volume 706 of *Lecture Notes of Physics*. Springer, Berlin, 2006.

[242] R. M. Martin. *Electronic Structure*. Cambridge University Press, Cambridge, first edition, 2004.

[243] G. Mazur and R. Włodarczyk. Application of the dressed time-dependent density functional theory for the excited states of linear polyenes. *J. Comput. Chem.*, 30:811, 2009.

[244] G. Mazur, R. Włodarczyk M. Marcin, and Y. Aoki. Dressed TDDFT study of low-lying electronic excited states in selected linear polyenes and diphenylopolyenes. *Int. J. Quant. Chem.*, 111: 810–825, 2010.

[245] E. G. McRae. Theory of solvent effects on molecular electronic spectra. frequency shifts. *J. Phys. Chem.*, 61:562, 1957.

[246] A. B. Meyers and R. R.. Birge. The effect of solvent environment on molecular electronic oscillator strengths. *J. Chem. Phys.*, 73: 5314, 1980.

[247] J. Michl and V. Bonačić-Koutecký. *Electronic Aspects of Organic Photochemistry*. Wiley, New York, 1990.

[248] J. M. Millam and G. E. Scuseria. Linear scaling conjugate gradient density matrix search as an alternative to diagonalization for first principles electronic structure calculations. *J. Chem. Phys.*, 106:5569, 1997.

[249] N. Minezawa and M. S. Gordon. Optimizing conical intersections by spin-flip density functional theory: Application to ethylene. *Phys. Chem. A*, 113:12749, 2009.

[250] R. Mirić, U. Werner, and V. Bonačić-Koutecký. Nonadiabatic dynamics and simulation of time resolved photoelectron spectra within time-dependent density functional theory: Ultrafast photoswitching in benzylideneaniline. *J. Chem. Phys.*, 129:164118–1–9, 2008.

[251] R. Mitrić, U. Werner, M. Wohlgemuth, G. Seifert, and V. Bonačić-Koutecký. Nonadiabatic dynamics within time-dependent density functional tight binding method. *J. Phys. Chem. A*, 113: 12700–12705, 2009.

[252] R. L. Motard and B. Joseph, editors. *Wavelet Applications in Chemical Engineering*. Kluwer Academic Publishers, Boston, 1994.

[253] R. S. Mulliken. Report on notation for the spectra of polyatomic molecules. *J. Chem. Phys.*, 23:1997, 1955. *Erratum*, **24**, 118 (1956).

[254] R. S. Mulliken and C. A. Rieke. Molecular electronic spectra, dispersion and polarization: The theoretical interpretation and computation of osciallator strengths and intensities. *Rep. Prog. Phys.*, 8:231, 1941.

[255] C. W. Murray, S. C. Racine, and E.R. Davidson. Improved algorithms for the lowest few eigenvalues and eigenvectors of large matrices. *J. Comput. Phys.*, 103:382, 1991.

[256] B. Natarajan, L. Genovese, M. E. Casida, T. Deutsch, O. N. Burchak, C. Philouze, and M. Y. Balakirev. Wavelet-based linear-response time-dependent density-functional theory. http://arxiv.org/abs/1108.3475.

[257] A. I. Neelov and S. Goedecker. An efficient numerical quadrature for the calculation of the potential energy of wavefunctions expressed in the daubechies wavelet basis. *J. Comput. Phys.*, 217: 055501, 2006.

[258] O. M. Nielsen. *Wavelets in scientific computing*. PhD thesis, Department of Mathematical Modelling, Technical University of Denmark, 1998.

[259] Jr. O. E. Weigang. Solvent field corrections for electric dipole and rotatory strengths. *J. Chem. Phys.*, 41:1435, 1964.

[260] C. Ochsenfeld and M. Head-Gordon. A reformulation of the coupled perturbed self-consistent field equations entirely within a local atomic orbital density matrix-based scheme. *Chem. Phys. Lett.*, 270:399, 1997.

[261] G. Onida, L. Reining, and A. Rubio. Electronic excitations: density-functional versus many-body Green's-function approaches. *Rev. Mod. Phys.*, 74:601, 2002.

[262] Y. Osamura, Y. Yamaguchi, and H. F. Schaefer. Generalization of analytic configuration interaction (CI) gradient techniques for potential energy hypersurfaces, including a solution to the coupled perturbed Hartree–Fock equations for multiconfiguration SCF molecular wave functions . *J. Chem. Phys.*, 77:383, 1982.

[263] M. C. Payne, M. P. Teter, D. C. Allan, T. A. Arias, and J. D. Johannopoulos. Iterative minimization techniques for *ab initio* total-energy calculations: Molecular dynamics and conjugate gradients. *Rev. Mod. Phys.*, 64:1045, 1992.

[264] J. P. Perdew and Y. Wang. Accurate and simple analytic representation of the electron-gas correlation energy. *Phys. Rev.B*, 45: 13244, 1992.

[265] J. P. Perdew and A. Zunger. Self-interaction correction to density-functional approximations for many-electron systems. *Phys. Rev.B*, 23:5048, 1981.

[266] J. P. Perdew, K. Burke, and M. Ernzerhof. Generalized gradient approximation made simple. *Phys. Rev. Lett.*, 77:3865, 1996.

[267] M. Petersilka, U. J. Gossmann, and E. K. U. Gross. Excitation energies from time-dependent density-functional theory. *Phys. Rev. Lett.*, 76:1212, 1996.

[268] F. L. Pilar. *Elementary Quantum Chemistry*. McGraw-Hill, New York, 2001.

[269] J. Pipek and I. Varga. Statistical electron densities. *Int. J. Quant. Chem.*, 64:85, 1997.

[270] R. Poirier, R. Kari, and I. G. Csizmadia. *Handbook of Gaussian Basis sets*. Elsevier, Amsterdam, 1970.

[271] D. Polli, P. Altoè, O. Weingart, K. M. Spillane, C. Manzoni, D. Brida, G. Tomasello, G. Orlandi, P. Kurkura, R. A. Mathies, M. Garavellli, and G. Cerullo. Conical intersection dynamics in the primary photoisomerization event in vision. *Nature*, 467: 440–443, 2010.

[272] J. A. Pople and D. L. Beveridge. *Approximate Molecular Orbital Theory*. McGraw-Hill, New York, 1970.

[273] P. Pulay. *Ab initio* calculation of force constants and equilibrium geometries in polyatomic molecules I. Theory. *Mol. Phys.*, 17: 197, 1969.

[274] P. Pulay. *Ab initio* calculation of force constants and equilibrium geometries in polyatomic molecules II. Force constants of water. *Mol. Phys.*, 18:473, 1970.

[275] P. Pulay. Convergence acceleration of iterative sequences. The case of SCF iteration. *Chem. Phys. Lett.*, 73:393, 1980.

[276] N. Ragazos, I. A. Robb M. F. Bernardi, and M. Olivucci. Optimization and characterization of the lowest energy point on a conical intersection using an MC-SCF lagrangian. *Chem. Phys. Lett.*, 197:217–223, 1992.

[277] D. Rocca, R. Gebauer, Y. Saad, and S. Baroni. Turbo charging time-dependent density-functional theory with Lanczos chains. *J. Chem. Phys.*, 128:154105, 2008.

[278] P. Romaniello, D. Sangalli, J. A. Berger, F. Sottile, L. G. Molinari, L. Reining, and G. Onida. Double excitations in finite systems. *J. Chem. Phys.*, 130:044108–1–11, 2009.

[279] C. C. J. Roothan. New developments in molecular orbital theory. *Rev. Mod. Phys.*, 23:69, 1951.

[280] E. Runge and E. K. U. Gross. Density-functional theory for time-dependent systems. *Phys. Rev. Lett.*, 52:997, 1984.

[281] E. Rutherford. The scattering of α and β particles by matter and the structure of the atom. *Phil. Mag.*, 21:669, 1911.

[282] G. Scalmani, M. J. Frisch, B. Mennucci, J. Tomasi, R. Cammi, and V. Barone. Geometries and properties of excited states in the gas phase and in solution: Theory and application of a time-dependent density functional theory polarizable continuum model. *J. Chem. Phys.*, 124:094107–1–15, 2006.

[283] J. Schirmer and A. Dreuw. Critique of the foundations of time-dependent density-functional theory. *Phys. Rev. A*, 75:022513, 2007.

[284] J. Schirmer and A. Dreuw. Reply to "comment on 'critique of the foundations of time-dependent density functional theory' ". *Phys. Rev. A*, 78:056502, 2008.

[285] K. L. Schuchardt, B. T. Didier, T. Elsethagen, L. Sun, V. Gurumoorthi, J. Chase, J. Li, and T. L. Windus. Basis set exchange: A community database for computational sciences. *J. Chem. Inf. Model.*, 47:1045, 2007.

[286] M. Schütz, G. Hetzer, and H. -J. Werner. Low-order scaling local electron correlation methods. I. Linear scaling local MP2. *J. Chem. Phys.*, 111:5691, 1999.

[287] G. E. Scuseria and P. Y. Ayala. Linear scaling coupled cluster and perturbation theories in the atomic orbital basis. *J. Chem. Phys.*, 111:8330, 1999.

[288] R. Send and F. Furche. First-order nonadiabatic couplings from time-dependent hybrid density functional response theory: Consistent formalism, implementation, and performance. *J. Chem. Phys.*, 132:044107–1–12, 2010.

[289] M. Seth and T. Ziegler. Calculation of excitation energies of open-shell molecules with spatially degenerate ground states. I. Transformed reference via an intermediate configuration Kohn-Sham density-functional theory and applications to d^1 and d^2 systems with octahedral and tetrahedral symmetries. *J. Chem. Phys.*, 123:144105, 2005.

[290] M. Seth, G. Mazur, and T. Ziegler. Time-dependent density functional theory gradients in the amsterdam density functional package: Geometry optimizations of spin-flip excitations. *Theor. Chim. Acta.*, 129:331–342, 2010.

[291] Y. Shao, M. Head-Gordon, and A. I. Krylov. The spin-flip approach within time-dependent density functional theory: Theory and applications to diradicals. *J. Chem. Phys.*, 118:4807, 2003.

[292] F. Sicilia, L. Blancafort, M. J. Bearpark, and M. A. Robb. New algorithms for optimizing and linking conical intersection points. *J. Chem. Theor. Comput.*, 4:257–266, 2008.

[293] J. C. Slater. Note on Hartree's method. *Phys. Rev.*, 35:210, 1930.

[294] J. C. Slater. *Quantum Theory of Atomic Structure*. McGraw-Hill, New York, 1960.

[295] L. V. Slipchenko and A. I. Krylov. Electronic structure of the trimethylenemethane diradical in its ground and electronically excited states: Bonding, equilibrium geometries, and vibrational frequencies. *J. Chem. Phys.*, 118:6874, 2003.

[296] T. I. Solling, E. W.-G. Diau, C. Kotting, S. De Feyter, and A. H. Zewail. Femtochemistry of Norrish type-I reactions: IV. Highly excited ketones–experimental. *Chem. Phys. Chem.*, 3:79, 2002.

[297] A. Sommerfeld. Zur Elektronentheorie der Metalle auf Grund der Fermischen Statistik I. Teil: Allgemeines, Strömungs- und Austrittsvorgänge. *Z. für physik*, 47:1, 1928.

[298] R. E. Stratmann, G. E. Scuseria, and M. J. Frisch. An efficient implementation of time-dependent density-functional theory for the calculation of excitation energies of large molecules. *J. Chem. Phys.*, 109:8218, 1998.

[299] A. Szabo and N. S. Ostlund. *Modern Quantum Chemistry*. Dover Publications, 1996.

[300] Y. Tanabe and S. Sugano. On the Absorption Spectra of Complex Ions. I. *J. Phys. Soc. Japan*, 9:753–766, 1954.

[301] E. Tapavicza, I. Tavernelli, and U. Rothlisberger. Trajectory surface hopping within linear response time-dependent density-functional theory. *Phys. Rev. Lett.*, 98:023001–1–19, 2007.

[302] E. Tapavicza, I. Tavernelli, U. Rothlisberger, C. Filippi, and M. E. Casida. Mixed time-dependent density-functional theory/classical surface hopping study of oxirane photochemistry. *J. Chem. Phys.*, 129:124108–1–19, 2008.

[303] E. Tapavicza, A. M. Meyer, and F. Furche. Unravelling the details of vitamin D photosynthesis by non-adiabatic molecular dynamics simulations. *Phys. Chem. Chem. Phys.*, 2011.

[304] Enrico Tapavicza. Personal Communication.

[305] I. Tavernelli, E. Tapavicza, and U. Rothlisberger. Non-adiabatic dynamics using time-dependent density functional theory: Assessing the coupling strengths. *J. Molec. Struct. (Theochem)*, 914: 22, 2009.

[306] I. Tavernelli, E. Tapavicza, and U. Rothlisberger. Nonadiabatic coupling vectors within linear response time-dependent density functional theory. *J. Chem. Phys.*, 130:124107, 2009.

[307] G. te Velde, F. M. Bickelhaupt, E. J. Baerends, C. Fonseca, C. Guerra, S. J. A. van Gisbergen, J. G. Snijders, and T. Ziegler. Chemistry with ADF. *J. Comput. Chem.*, 22:931, 2001.

[308] A. Thomas, K. Srinivas, Ch. Prabhakara, K. Bhanuprakasha, and V. J. Rao. Estimation of the first excitation energy in diradicaloid croconate dyes having absorption in the near infra red (NIR): A DFT and SF-TDDFT study. *Chem. Phys. Lett.*, 454:36, 2008.

[309] L. H. Thomas. The calculation of atomic fields. *Proc. Cambridge Phil. Soc.*, 23:542, 1926.

[310] M. Tinkham. *Group Theory and Quantum Mechanics*. McGraw-Hill Co., New York, 1964.

[311] D. J. Tozer and N. C. Handy. On the determination of excitation energies using density functional theory. *Phys. Chem. Chem. Phys.*, 2:2117, 2000.

[312] C. Tully, J. *"Nonadiabatic Dynamics", in* Modern Methods in Multidimensional Dynamics Computations in Chemistry. World Scientific, Singapore, 1998.

[313] J. C. Tully. Molecular dynamics with electronic transitions. *J. Chem. Phys.*, 93:1061–1071, 1990.

[314] J. C. Tully. Nonadiabatic dynamics. In D. L. Thompson, editor, *Modern Methods for Multidimensional Dynamics Computations in Chemistry*, page 34, Singapore, 1998. World Scientific.

[315] C. J. Tymczak and X.-Q. Wang. Orthonormal wavelet bases for quantum molecular dynamics. *Phys. Rev. Lett.*, 78:3654, 1997.

[316] I. Ugi. The α-addition of immonium ions and anions to isonitriles accompanied by secondary reactions. *Ang. Chemie Int.*, 1: 8–21, 1962.

[317] O. Vahtras and Z. Rinkevicius. General excitations in time-dependent density functional theory. *J. Chem. Phys.*, 126:114101, 2007.

[318] R. van Leeuwen. Key concepts in time-dependent density-functional theory. *Int. J. Mod. Phys. B*, 15:1969, 2001.

[319] C. van Wüllen. Spin densities in two-component relativistic density functional calculations: Noncollinear versus collinear approach. *J. Comput. Chem.*, 23:779, 2002.

[320] S. H. Vosko, L. Wilk, and M. Nusair. Accurate spin-dependent electron liquid correlation energies for local spin density calculations: a critical analysis. *Can. J. Phys.*, 58:1200, 1980.

[321] B. Walker, A. M. Saitta, R. Gebauer, and S. Baroni. Efficient approach to time-dependent density-functional perturbation theory for optical spectroscopy. *Phys. Rev. Lett.*, 96:113001, 2006.

[322] F. Wang and T. Ziegler. Time-dependent density functional theory based on a noncollinear formulation of the exchange-correlation potential. *J. Chem. Phys.*, 121:12191–12196, 2004.

[323] F. Wang and T. Ziegler. The performance of time-dependent density functional theory based on a noncollinear exchange-correlation potential in the calculation of excitation energies. *J. Chem. Phys.*, 122:074109, 2005.

[324] F. Wang and T. Ziegler. The performance of time-dependent density functional theory based on a noncollinear exchange-correlation potential in the calculation of excitation energies. *J. Chem. Phys.*, 122:074109, 2005.

[325] F. Wang and T. Ziegler. Use of noncollinear exchange-correlation potentials in multiplet resolutions by time-dependent density functional theory. *Int. J. Quant. Chem.*, 106:2545, 2006.

[326] S. Wei and M. Y. Chou. Wavelets in self-consistent electronic structure calculations. *Phys. Rev. Lett.*, 76:2650, 1996.

[327] P. Werner and P. Knowles. An efficient internally contracted multiconfiguration–reference configuration interaction method. *J. Chem. Phys.*, 89:5803–5814, 1988.

[328] U. Werner, R. Mitrić, T. Suzuki, and V. Bonačić-Koutecký. Nonadiabatic dynamics within the time dependent density functional theory: Ultrafast photodynamics in pyrazine. *Chem. Phys.*, 349: 319–324, 2008.

[329] E. Wimmer, H. Krakauer, M. Weinert, and A. J. Freeman. Full-potential self-consistent linearized-augmented-plane-wave method for calculating the electronic structure of molecules and surfaces: O_2 molecule. *Phys. Rev. B*, 24:864, 1981.

[330] C. Wittig. The Landau-Zener formula. *J. Phys. Chem. B*, 109: 8428–8430, 2005.

[331] D. E. Woon and T. H. Dunning. Gaussian basis sets for use in correlated molecular calculations. III. The atoms aluminum through argon. *J. Chem. Phys.*, 98:1358, 1993.

[332] Q. Wu, L. Cheng C. and T. Van Voorhis. Configuration interaction based on constrained density functional theory: A multireference method. *J. Chem. Phys.*, 127:164119–1–9, 2007.

[333] K. Yabana and G. F. Bertsch. Time-dependent local-density approximation in real time. *Phys. Rev. B*, 54:4484, 1996.

[334] K. Yabana and G. F. Bertsch. Time-dependent local-density approximation in real time: Application to conjugated molecules. *Int. J. Quant. Chem.*, 75:55–66, 1999.

[335] K. Yabana, T. Tazawa, Y. Abe, and P. Bozek. Time-dependent mean-field description for multiple electron transfer in slow ion-cluster collisions. *Phys. Rev. A*, 57:R3165–R3168, 1998.

[336] D. R. Yarkony. Diabolical conical intersections. *Rev. Mod. Phys.*, 68:985–1013, 1996.

[337] D. R. Yarkony. Conical intersections: The new conventional wisdom. *J. Phys. Chem. A*, 105:6277–6293, 2001.

[338] R. N. Zare. Calculation of intensity distribution in the vibrational structure of electronic transitions: The $B^3\Pi_{O^+u} - X^1\Sigma_{O^+g}$ resonance series of molecular iodine. *J. Chem. Phys.*, 40:1934, 1964.

[339] C. Zener. Non-adiabatic crossing of energy levels. *Proc. R. Soc. London A*, 137:696–702, 1932.

[340] T. Ziegler, A. Rauk, and E. J. Baerends. On the calculation of multiplet energies by the hartree-fock-slater method. *Theoretical Chemistry Accounts: Theory, Computation, and Modeling (Theoretica Chimica Acta)*, 43:261–271, 1977. ISSN 1432-881X. URL http://dx.doi.org/10.1007/BF00551551. 10.1007/BF00551551.